Capillary flow of dense colloidal suspensions

Lucio Isa

A thesis submitted in fulfilment of the requirements
for the degree of Doctor of Philosophy
to the
University of Edinburgh

2007

Abstract

The purpose of this thesis is to study the flow of dense colloidal suspensions into micron-sized capillaries at the particle level. Understanding the flow of complex fluids in terms of their constituents (colloids, polymers, or surfactants) poses deep fundamental challenges, and has wide applications in many industrial processes. Through the use of a novel experimental procedure we find results contrasting with the predicted bulk rheological behaviour of dense colloidal systems and propose an alternative approach based on the analogy with granular systems. Quantitative predictions which successfully explain the data are obtained.

In order to obtain quantitative information on the dynamics of the system, we image the flow using a fast confocal microscope and identify the trajectories of each particle. Due to the nature of the flow, conventional techniques for locating and tracking the particles fail to yield satisfactory results. To overcome this limitation, we have developed a novel technique which allows us to successfully track the particles in strongly non-uniform flow fields (published, 2006).

We focus our attention on three main aspects of the flow: concentration gradients, velocity profiles and time behaviour.

We initially discuss the occurrence of concentration gradients along the flow direction and relate them to the local flow profiles. We observe high density regions where the velocity is uniform across the channel (complete plugs) and lower density regions where shear is present. The observed concentration profiles can be qualitatively explained by considering the relative flow between the solvent and the suspended particles.

The flow profiles in the presence of shear consist of a plug in the centre while shear occurs localized adjacent to the channel walls, reminiscent of yield-stress fluid behaviour. However, the observed scaling of the velocity profiles with the flow rate strongly contrasts yield-stress fluid predictions. Instead, the velocity profiles can be captured by a theory of stress fluctuations originally developed for chute flow of dry granular media (published ,2007). We extend the model to our case and discuss it as a function of a series of parameters (boundary conditions, volume fraction, channel size, etc.) highlighting differences and similarities with granular media.

Finally we discuss the time behaviour of complete plug flows relating it to the microscopic dynamics of the particles. At variance with dilute systems, dense systems exhibit velocity fluctuations when driven into channels by a constant pressure difference. We find that there exists a threshold value of the flow rate below which oscillations in the velocity are absent and above which their frequency scales as a power law of the flow rate. Despite quantitative predictions on this issue that are still missing, we present a microscopic description of the phenomenon highlighting the interplay between the particles and the solvent.

Declaration

I do hereby declare that this thesis was composed entirely by myself and that the work described within is my own, except where explicitly stated otherwise.

Lucio Isa
October 2007

Acknowledgements

I have spent in Edinburgh the best time of my life.

This fantastic experience would not have been the same without all the people I have met and who have helped me and supported me during my PhD.

I would first like to thank Wilson. He has not only constantly encouraged me during these three years, but he has also transmitted to me his passion for getting to the core of scientific problems. I will cherish the memories of our long scientific discussions as the most exciting times of my PhD.

A big thanks goes to Rut, with whom I have worked day by day and with whom I have shared *"gioie e dolori"* of the VtEye. I really appreciate his indefatigable ability to find time for helping and discussing and his constant readiness for a good laugh to wash the daily grind away.

I would also like to thank Peter for his kindness and helpfulness in dealing with my studentship.

Despite his refusal to take me hillwalking with him (based on dubious grounds that I would be too fast!), I thank Andrew for making my particles and for being generally helpful and wise in the lab.

I sincerely thank Mike for showing constant interest in my project and for all the useful comments and discussions. I also truly appreciate Alexander's efforts to find a model for my experiments. Thanks to Nhan for the microfluidics collaboration, to Laurence and Tiffany (and Rut again!) for reading my thesis, to Mark Haw for introducing me to colloidal channel flows and to Khoa Pham for his help with rheology. Finally I'd like to thank Eric Weeks and George Petekidis for the work done together during their visits.

To my office mates, past and present (especially to Susie, Rowan, Danielle, Tom, "The Knee"-lofer and the lovely Miss BB Kate), to all the other students and friends I have met in Edinburgh: thanks for making these years an unforgettable time.

A special mention goes to the members of the Physics Squash team, the lunchtime-running people and the climbing monkeys in the `we-rock` list. Aye, we rock!

Un ringraziamento speciale va alla mia famiglia, ai miei genitori, ai miei fratelli ed ai miei nonni; anche se lontani, siete sempre vicini nei miei pensieri.

This work would have never seen the light of the day without Federica. Her simple presence makes my life better and gives me the tranquillity to face whatever challenge the day has to offer.

Thanks.

[...] one morning,
chancing to awaken very early,
he arose to make an excursion
to the top of Arthur's Seat,
to breathe the breeze of the dawning,
and see the sun arise
out of the eastern ocean.

"The private memoirs and confessions
of a justified sinner"

James Hogg, 1824

Contents

Abstract **i**

Declaration **iii**

Acknowledgements **v**

Contents **ix**

1 Introduction **1**
1.1 Why study the flow of complex fluids? 1
1.2 Thesis outline 3

2 Colloids **5**
2.1 Interactions between colloidal particles 6
2.1.1 van der Waals forces 6
2.2 Charge stabilization 7
2.3 Steric stabilization 8
2.4 DLVO potential 9
2.5 Hard-sphere phase diagram 9
2.5.1 Alterations to the phase diagram: charge and polydispersity . . . 13
2.6 Radial distribution function 14
2.7 A brief aside: thermal and a-thermal systems 16

3 Rheology of colloidal systems **19**
3.1 Stresses and strains 19
3.1.1 Equilibrium equations 26
3.2 Steady state rheology of dense systems 27
3.2.1 Low shear rates regime: yield stress and shear-thinning 28
3.2.2 High shear rates regime: shear-thickening and jamming 29
3.3 Channels flows: Velocity profiles 30
3.3.1 Non-Brownian suspensions 31
3.3.2 Polymers 34
3.3.3 Pasty systems 35
3.3.4 Dense dry granular flows 36
3.3.5 Analytical profiles for simple constitutive relations 38
3.4 Channel flows: oscillations and instabilities 47

4 Confocal microscopy and tracking of colloidal particles 51
4.1 Light scattering . . . 51
4.2 Optical microscopy . . . 52
4.2.1 Bright field microscopy . . . 53
4.2.2 Fluorescence microscopy . . . 58
4.3 Confocal microscopy . . . 60
4.3.1 Principles of confocal microscopy . . . 60
4.3.2 Resolution . . . 62
4.3.3 Image acquisition rate . . . 63
4.3.4 Multiphoton . . . 64
4.4 Particle identification and tracking . . . 65
4.4.1 Tracking the particles . . . 66
4.4.2 Advective motion removal . . . 68
4.4.3 Comments on tracking errors . . . 71

5 Materials and Methods 73
5.1 The system . . . 73
5.1.1 The particles and the solvents . . . 74
5.1.2 Sample preparation . . . 76
5.1.3 The particles in the different solvents . . . 79
5.1.4 Volume fraction . . . 84
5.2 Experimental set-up . . . 89
5.2.1 A typical experiment: sample cell preparation and flow . . . 89
5.2.2 The confocal microscope and the laser . . . 92
5.2.3 The pressure gauge and the acquisition software . . . 94
5.2.4 The glass capillaries . . . 94

6 Density and velocity profiles in the flow direction 97
6.1 Experimental results . . . 97
6.1.1 Transition . . . 103
6.2 Discussion . . . 106

7 Flow profiles 109
7.1 Velocity Profiles . . . 109
7.1.1 Boundary conditions effects . . . 112
7.1.2 Volume fraction effects . . . 115
7.1.3 Size effects . . . 118
7.1.4 z-dependence . . . 120
7.1.5 Two-dimensional flows . . . 122
7.2 A granular model for dense colloidal flows . . . 125
7.2.1 Motivation . . . 125
7.2.2 A model . . . 127
7.2.3 Model predictions and comparison with the data . . . 131
7.2.4 Differences between friction-dominated colloidal flow and dry granular flow . . . 137
7.2.5 z-dependence of b: a simple explanation . . . 140

7.2.6 A microscopic description . . . 142
7.2.7 Summary . . . 146
7.3 Concentration Profiles . . . 147
7.3.1 Discussion: particle migration and shear-induced density inhomogeneities . . . 148

8 Time domain **153**
8.1 Methods . . . 153
8.2 Velocity oscillations . . . 156
8.2.1 Results . . . 157
8.2.2 Discussion . . . 172

9 Conclusions **181**
9.1 Confocal microscopy and particle tracking . . . 181
9.2 Density gradients and shear profiles . . . 182
9.3 Flow profiles: data and quantitative analysis . . . 182
9.4 Time behaviour: velocity oscillations and a microscopic description . . . 185

10 Outlook and future work **187**
10.1 Sedimentation . . . 187
10.2 Additional work on channel flows . . . 188
10.3 Colloids vs Grains . . . 190

A Image filtering and particle location **191**
A.1 Image filtering . . . 191
A.2 Finding the particle centres . . . 193

B Pressure recovery in capillary flows **199**

List of figures **205**

List of tables **215**

Bibliography **217**

Publications **227**

Chapter 1

Introduction

Everything flows. The ancient Greek philosopher Heraclitus of Ephesus (ca. $535 - 475$ BC) constructed around this assumption a philosophical system based on the presence of continuous change in a reality determined and driven by the interaction of opposite forces. His ideas have permeated many fields of the modern body of knowledge from Philosophy to Social Sciences. The very same concept can also be extended to the realms of Physics and Engineering; following the application of an external *force* or *stress*, materials respond by *flowing* or by *being deformed*. The study of the flow and deformation of materials, or *rheology*, has become a fundamental part of Materials Science and as a tribute to Heraclitus' ideas, $\pi\alpha\nu\tau\alpha\ \rho\varepsilon\iota$ (everything flows) has become the motto of the Society of Rheology.

1.1 Why study the flow of complex fluids?

Engineers have been performing deformation tests in order to determine the resistance and failure of materials since the dawn of modern design of buildings and machines. With the increase in the general knowledge of Materials Physics, understanding the rheological properties of materials has also become an interesting challenge for the physicist. Complex fluids, soft systems and granular media offer the appealing opportunity of combining a vast practical interest from the engineering community with the study of model systems of fundamental physical relevance. Soft systems are ubiquitous in nature and in industrial processes and include uncountable materials such as polymers, emulsions (droplets of a fluid dispersed into another immiscible fluid), suspensions of solid particles in a fluid and systems of biological interest. Understanding the rheological behaviour of complex fluids starting from their constituents poses deep fundamental challenges and also has large scale practical applications, a few relevant examples of which are given below.

Silos and hoppers are the industrial pieces of equipment which register the highest number of failures every year. Perfectly sound silos unexpectedly collapse especially during filling operations with grains, calling for a better understating of stress distributions of granular media under flow [1].

Polymers are frequently shaped by extrusion. This process consists in forcing a polymer melt through a geometrical constriction of a desired shape (die). The flow of the melt in the die has a crucial impact onto the quality of the final extruded product. Flow instabilities can lead to non-uniform flow rates and variable texture and structure of the polymer [2].

Similar problems are encountered in blood flows. Our blood goes continuously in and out of blood vessels of different sizes. In some pathologies (e.g. stenosis) the vascular diameter is drastically reduced forcing the blood to flow into a narrowing [3]. When the presence of "particles" (blood cells) is taken into account, the scenario acquires more complexity, and the precise vessel geometry as well as the particle properties (e.g. deformability) play crucial roles [4]. Rheological studies on blood flows can help characterize and eventually fight those pathologies.

Another example where the rheological properties of the system play an important role concerns the use of emulsions for drug delivery [5, 6]; the drug is incorporated into the emulsion droplets and administered to the patient. Controlled, monodisperse emulsions are needed for an effective treatment; they can be for instance obtained by shear [7] and therefore the rheological properties become of extreme relevance for the production of well characterized systems.

Finally pastes are widely used in many industrial processes including cosmetics, pharmaceutical and food industry. Many pills are produced by extruding, shaping and drying pastes containing the active principles and the binding agents. Flow instabilities during extrusion can lead to a non-uniform distribution of the components of the paste resulting in an uncontrolled composition of the final product [8]. Moreover the processing and transport of concentrates through tubes is a basic part of food production; with the processing of tomato concentrate in the USA having been valued at $ 719 million for 2005 (USDA-NASS Agricultural Statistics) [9], understanding, control and optimization of the rheology of dense systems finds a wide range of applications.

On the other hand, soft systems have served as an important benchmark for Equilibrium and Non-Equilibrium Statistical Mechanics theories. Very recent developments have started to deal with driving the system out of equilibrium by applying external fields. Understanding the response of the systems to the external perturbation in terms of interactions between the components is an open and very interesting question.

In particular, much effort has been directed to the study of the response to shear. Experimental complex fluid rheology typically starts in a rheometer, in which stresses

and strains are applied and measured in well-defined, 'rheometric' geometries ('cone-plate', etc.). Translating rheometer data to more complex flows is non-trivial, but well developed in polymers (see, e.g., [10]). The understanding of colloidal flows lags considerably behind and despite their equal practical importance [11, 12], studies on model systems have been carried out only recently [13]. Compared to polymers, colloids pose some unique challenges. Concentrated suspensions ('pastes') are generally non-ergodic (or 'glassy'), so that *any* flow involves non-linearities (e.g. yielding [14, 15] or shear thickening [16, 17]). Moreover, specific geometries in applications may involve dimensions comparable to single particles and lead to confinement effects, such as in micro-fluidics [18]. The most quantitative theory for quiescent colloidal glasses, mode coupling theory, has only recently been extended to deal with simple shear [19].

1.2 Thesis outline

Having introduced the importance of investigating the flow of soft systems, we present here an outline of this thesis which deals with the experimental study of the flow of dense suspensions of colloidal particles into micro-scale capillaries.

Chapter 2 gives an introduction to colloidal systems discussing the interaction between particles and focussing on the phase behaviour of collections of hard spheres. The concept of radial distribution function as a means of describing the structure of a material is presented together with a brief aside on the length and time scales which distinguish colloidal systems from non-colloidal ones.

In Chapter 3 we introduce the basic elements of rheology, defining stresses and deformations and discussing their relation for a series of examples. We examine the specific rheological behaviour of hard-spheres systems, presenting the characteristic traits and reviewing some of the existing literature on the subject. We then move on to a review of the literature on channel flows for a variety of dense systems, firstly concentrating on the measured velocity profiles and then focussing on the time behaviour. Quantitative arguments describing the shape of the velocity profiles are presented and their applicability and limitations are discussed.

Chapter 4 introduces and discusses the details of the experimental techniques used in this thesis: confocal microscopy and particle tracking. We first present a brief review of conventional optical microscopy which prepares the way for the subsequent detailed discussion of confocal microscopy. We conclude the chapter providing a description of the procedures used to track colloidal particles from confocal images, presenting new work on the optimization of these techniques for systems in strongly non-uniform shear flows.

Chapter 5 discusses the details of the specific materials and methods used in this

thesis. We first give a detailed description of the colloidal particles, characterizing their behaviour in different solvents and describing the procedures used to perform density and index matching. The different procedures to determine the suspensions' volume fraction are then discussed, highlighting pros and cons. Finally we move to the description of the experimental set up and present a typical experimental run.

In Chapter 6 we give a global introduction of the channel flows of dense colloidal suspensions highlighting and discussing the presence of non-uniform concentration profiles along the channels and their link with the local velocity profiles.

Chapter 7 focusses on the discussion of the velocity profiles in micrometer-sized channels as a function of a variety of parameters such as channel size and particle volume fraction. We discuss the deviations form the behaviour expected from bulk rheology and propose the extension of a model initially conceived for dry granular flows. We highlight the similarities and differences with granular systems and present a microscopic description of the phenomena. Finally the presence of non-uniform concentration profiles across the channel is discussed in relation to the available literature on colloidal systems.

Chapter 8 discusses the time behaviour of our dense flows. In analogy with the existing literature on dry grains and pastes and in contrast to the behaviour of simple fluids, dense suspensions exhibit velocity fluctuations when driven into narrow channels by constant pressure differences. We present our data which relate the local velocity with the frequency of the oscillations and provide a microscopical description of the phenomenon.

Chapter 9 concludes and summarizes the main findings of this thesis and Chapter 10 describes a series of opportunities for interesting future work on similar systems.

Two appendices complete this thesis. The first one (Appendix A) contains background information on standard image-filtering techniques and algorithms for locating particle centres, while the second one (Appendix B) reports the derivation of the expression for the pressure variations during channel flows like the ones studied in this work.

Chapter 2

Colloids

Colloidal systems are constituted by objects suspended in a fluid. The defining character of a colloidal particle is its size which must lie between 1 nm and 1 μm. This size ranges between the microscopic one typical of atoms and simple molecules and the macroscopic one characteristic of objects observable by naked eye. Objects living in this *mesoscopic* (intermediate) world are big enough to consider the atoms and molecules of the suspending fluid as a continuum but small enough that the force due to gravity is small compared to the interactions with the solvent. On such length scales Brownian motion plays a fundamental role: particles are jiggled around randomly by collisions with the molecules of the suspending fluid and this determines the way they move in solution [20].

As a consequence colloids behave as '*big atoms*' [21, 22]; through the interactions among particles and with the suspending medium, colloids are able to reproduce atomic or molecular phenomena, proposing themselves then as ideal candidates for model systems. Examples of such possibilities are numerous; perhaps the most famous one is the identity between the barometric distribution in an ideal gas and the sedimentation profile of a colloidal suspension discovered by Perrin in 1910 during some experiments aimed to confirm the molecular nature of matter and to measure Avogadro's number [23]. More recent work has explored interfacial phenomena between a liquid and its vapour via a colloidal model system [24]. Finally, most important for us, is the role played by colloids in shedding light on the phase behaviour of simple substances, in particular on the dynamics of crystallization and glass formation [25, 26].

After describing the interactions between colloidal particles we shall discuss the phase behaviour of hard-spheres systems and introduce the radial distribution function as a means of characterizing the structure of a colloidal suspension.

2.1 Interactions between colloidal particles

The word colloid comes from the Greek $\kappa o\lambda\lambda\alpha$ meaning glue; this nomenclature reflects the tendency of colloidal systems to irreversibly aggregate and it was considered as fundamental characteristic by the first chemists working in the field. In order to exploit colloids as model systems and study the dynamics of single particles we need to *prevent* aggregation. The tendency of aggregating is due to the presence of an attractive force (van der Waals) which can be be effectively screened by inducing steric or Coulombic repulsion.

2.1.1 van der Waals forces

van der Waals forces originate from the interactions between the fluctuating electron distributions of atoms and molecules and are therefore present for any object. These forces, also known as dispersion or London forces, are due to the charge polarization induced in a molecule (colloid) by the fluctuations in the charge distribution in a neighbouring molecule (colloid) and therefore also affect electrically neutral objects.

For atomic systems the attraction goes as $\sim r^{-6}$ where r is the distance between the two atoms. For spherical colloids an analogous expression can be obtained by integrating over all atomic pair contributions; the resulting van der Waals interaction pair potential is:

$$U_{\mathrm{vdW}}(r) = -\frac{A}{12}\left[\frac{4R^2}{r^2-4R^2} + \frac{4R^2}{r^2} + 2\ln\left(1-\frac{4R^2}{r^2}\right)\right], \tag{2.1}$$

where r is the distance between the centres of the two particles, R is their radius and A is the so-called Hamaker constant [27]. The value of the Hamaker constant depends on the properties of the particles and the solvent, and in particular on their polarizabilities; if the suspended particles and the suspending medium have the same polarizability then $A = 0$. It is therefore possible to minimize van der Waals attraction by refractive index-matching the solvent with the particles. We recall though that the polarizability is frequency-dependent and therefore by index-matching within a given frequency range (usually in the visible) we do not fully suppress dispersion forces.

In the limit of large distances between the colloids we get

$$\lim_{r\to\infty} U_{\mathrm{vdW}}(r) = -\frac{16}{9}A\left(\frac{R}{r}\right)^6$$

which displays the $\sim r^{-6}$ behaviour, as expected. The other limit case is when the two

particles come vary close together and the interaction potential becomes

$$\lim_{r \to 2R} U_{\mathrm{vdW}}(r) = -\frac{A}{12}\left(\frac{R}{r-2R}\right)$$

which exhibits a divergence approaching contact ($r = 2R$). Therefore we note that if the particles come close together their attraction grows as the inverse of their separation distance and it becomes rapidly larger than the thermal energy $k_{\mathrm{B}}T$ leading to irreversible aggregation. In order to prevent such aggregation, the particles need to be stabilized and prevented from coming into extremely close contact. This is generally achieved in two ways: charge and steric stabilization.

2.2 Charge stabilization

In some cases, colloidal particles have ionisable groups on their surface which dissociate when the particles are suspended in polar solvents. The dissociated ions partially diffuse away in solution due to Brownian motion but tend to remain in the particle's vicinity due to Coulomb attraction. The particle, now charged and thus named *macro-ion*, is surrounded by a cloud of the dissociated ions and of any other electrolyte present in solution (see Figure 2.1). The ion cloud is frequently known as the *double layer* and as two particles come close together the two double layers overlap yielding a repulsive electrostatic force which prevents van der Waals aggregation.

The charge distribution in the double layer is given by the balance between the diffusion of the counter-ions and their Coulombic attraction with the macro-ion. The resulting potential $U_{\mathrm{C}}(r)$ can be obtained by solving the Poisson-Boltzmann equation (or usually its linearized version, the Debye-Hückel equation):

$$U_{\mathrm{C}}(r) = \frac{(Qe)^2}{4\pi\epsilon\epsilon_0 r}\frac{\exp[-(r-2R)/\lambda_{\mathrm{DH}}]}{(1+R/\lambda_{\mathrm{DH}})^2}, \tag{2.2}$$

where Q is the number charge per particle, e is the electron charge, ϵ and ϵ_0 are respectively the vacuum's permittivity and the solvent's dielectric constant and λ_{DH} is the Debye-Hückel length. λ_{DH} is also known as the screening length because it provides a measure of the distance over which the electrostatic repulsion decays and represents therefore the size of the double layer:

$$\lambda_{\mathrm{DH}} = \left(\frac{\epsilon\epsilon_0 k_{\mathrm{B}}T}{e^2\sum_i z_i^2 n_i}\right)^{\frac{1}{2}}, \tag{2.3}$$

where k_{B} is the Boltzmann constant, T is the system's temperature, z_i is the valence of the i-type of counter-ion and n_i is the corresponding number density; the sum is carried

out over all the species of counter-ions in solution [27]. We note that by increasing the concentration of electrolytes in solution (e.g. by adding salt) the screening length becomes smaller; the addition of salt to charged colloidal suspensions is a common way of reducing the range of Coulombic repulsion and it is frequently used to approximate the hard-spheres limit in charged, polymer-coated colloids.

2.3 Steric stabilization

Another way of preventing aggregation is accomplished by coating the surface of the particles with a layer of polymers. In the case of the particles used in this thesis, the polymers have one end irreversibly attached (chemically-grafted) onto the particles's surface (see Figure 2.1) and are therefore in contact with the solvent. The temperature of the solvent, together with the chemical properties, determines its "goodness" for the polymers; there exists a temperature (T_θ, theta temperature) for which is equally favourable for the polymers to coil around themselves or to stretch out. For an effective steric stabilization the system must therefore be above T_θ and favour the full expansions of the polymer chains in solution. When two particles come close together the two polymer layers begin to overlap; the overlap frustrates the possible configuration which the single chains can assume under Brownian motion and therefore reduces the entropy of the system leading to an increase in the free energy and so to a repulsive potential U_{HS}. If the thickness δ of the polymer layer is larger then the range of van der Waals' attraction, then the particles are fully stabilized. Below T_θ the polymers chains "prefer each other's company" to the solvent and effectively attract each other nullifying steric stabilization. The details on the particular system used in this work will be give in Chapter 5.

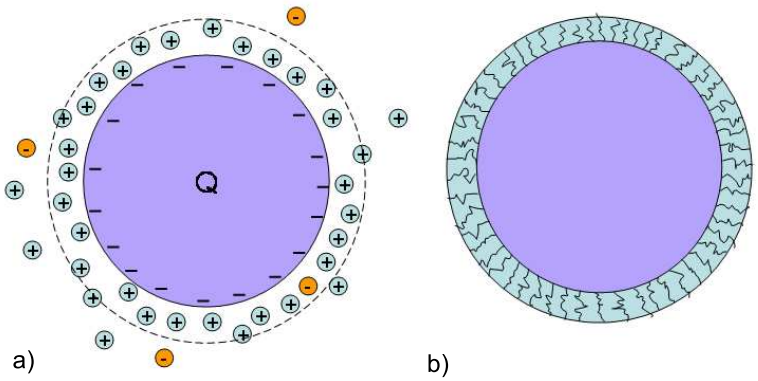

Figure 2.1: a) Schematic representation of a charge-stabilized colloid highlighting the presence of the double layer. b) Schematic representation of a sterically-stabilized colloid highlighting the presence of the polymer layer.

2.4 DLVO potential

Adding up all the contributions discussed in the previous sections we obtain the full interaction potential between colloids in suspension, known by the name of DLVO potential, from the names Derjaguin-Landau-Verwey-Overbeek:

$$U_{\mathrm{DLVO}}(r) = U_{\mathrm{vdW}}(r) + U_{\mathrm{C}}(r) + U_{\mathrm{HS}}(r). \tag{2.4}$$

The DLVO potential seems to describe well many experimental data but holds only if a series of assumptions are made, for instance assuming bulk properties of the solvent all the way to the interface and considering van der Waals forces and repulsion from the double layer as additive, ignoring possible correlation between the two. An interesting comment on the validity of the DLVO potential accompanied by an historical perspective can be found in [28], while a discussion of its application and limitations for the case of charged colloids and colloid-polymer mixtures is contained in [29].

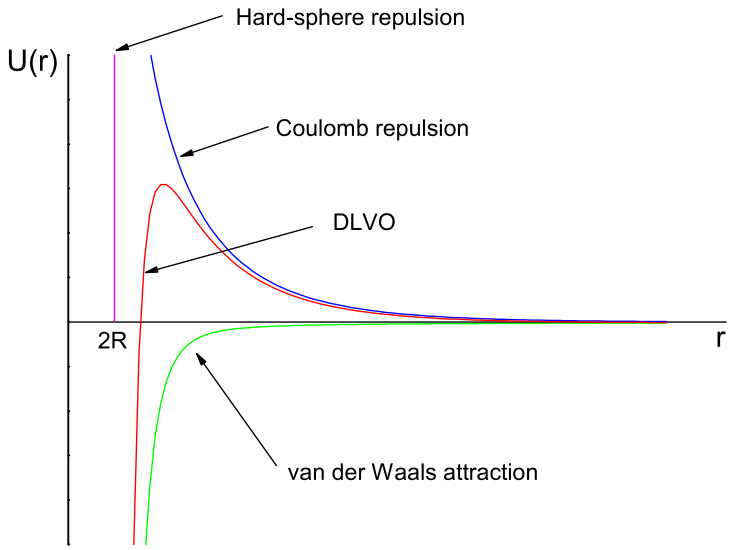

Figure 2.2: Illustration of the DLVO potential and all its components.

2.5 Hard-sphere phase diagram

Ideal hard spheres are the simplest objects which can constitute a model colloidal suspension. They are all identical, infinitely rigid spherical particles which interact elastically only at contact; their rigidity prevents any overlap or deformation and

their interaction potential is therefore a delta function of the interparticle separation, centred around $2R$, where R is the particles' radius (see Figure 2.5). As a consequence, only entropic effects are relevant in determining the phase behaviour of the system; temperature only scales the free energy (F) and therefore is irrelevant in minimizing F. The only parameter which affects the possible configurations and therefore entropy is then the number density ρ, defined as the number of particles N in a given volume V, or equivalently the volume fraction Φ

$$\Phi = \frac{4}{3}\pi R^3 \frac{N}{V}, \tag{2.5}$$

representing the fraction of volume occupied by particles.

The phase diagram of ideal hard-spheres has been calculated by numerical simulations [30, 31] (see Figure 2.3). Below a volume fraction of $\Phi_{\mathrm{F}} = 0.494$, the thermodynamically stable phase is a fluid of colloidal particles. No long-range order is present in the system and the particles are able to explore the full available space by undergoing diffusive motion (*ergodic system*).

For values of Φ between 0.494 and 0.545, the equilibrium state is a coexistence of a fluid phase and a crystalline phase. The ratio of the two phases is related to the volume fraction by the lever rule; this fact can be exploited to calibrate the volume fraction of any suspension in the coexistence region and will be described in detail in Chapter 5.

At $\Phi_{\mathrm{C}} = 0.545$ all the suspension is crystalline and according to equilibrium thermodynamics, the system remains crystalline up to the maximum crystalline close packing fraction of $\Phi_{\mathrm{CP}} = 0.74$.

However, experiments from Pusey and van Megen [25] showed that model suspensions of sterically-stabilized colloidal hard-spheres failed to crystallize for volume fractions $\Phi \gtrsim \Phi_{\mathrm{G}} = 0.58$, remaining "stuck" in a non-equilibrium phase known as the *colloidal glass*. The failure to reach the equilibrium crystalline phase is due to crowding effects; as the volume fraction of the system increases, particles are more and more caged by their neighbours. Structural rearrangements which relax the system towards the equilibrium structure involve more and more cooperative motion of the particles and their neighbours; the dynamics are therefore slowed down to the point at which the particles are 'permanently' caged by their neighbours and the structure of the suspension is frozen. Each particle is confined in the cage of its neighbours and prevented from exploring the whole available space: the system is now *non-ergodic*. For more than twenty years colloidal hard-spheres systems have been proved to be an interesting benchmark for the study of the dynamics of the glass transition [25], but up to now the actual presence of a glass transition at 58% volume fraction is still debated [32, 33].

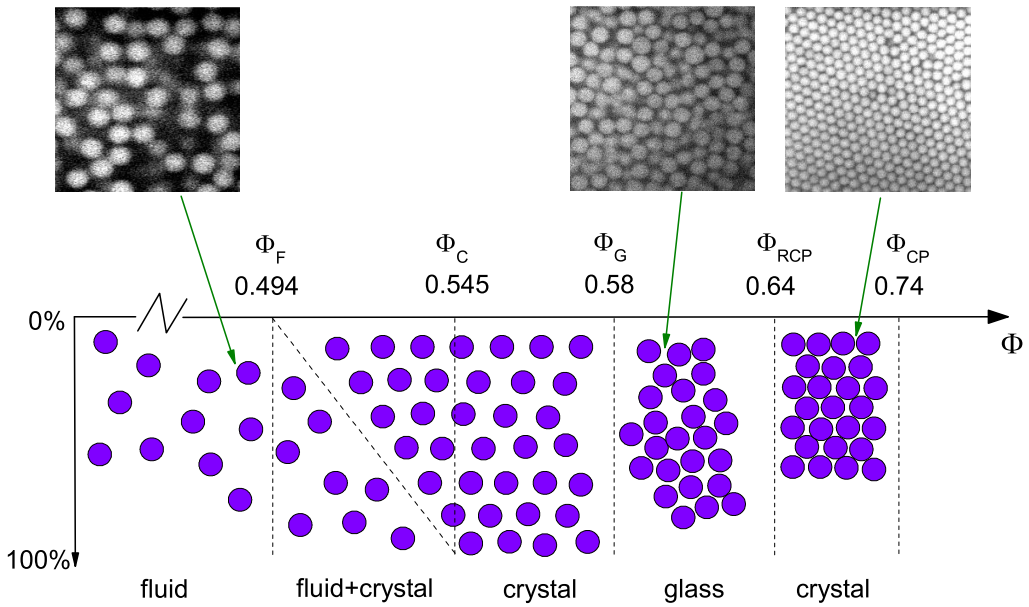

Figure 2.3: Phase diagram for ideal hard-spheres suspensions. Below a volume fraction of $\Phi_F = 0.494$ the stable phase is a liquid. For volume fractions between 0.494 and 0.545, a coexistence between liquid and crystalline domains is found, while for $\Phi > \Phi_C = 0.545$ the equilibrium phase is a crystalline solid. However for systems denser than $\Phi_G = 0.58$ the system fails to crystallize and is frozen in a disordered, glassy state. The maximum disordered packing fraction $\Phi_{RCP} = 0.64$ and the maximum crystalline close packing fraction $\Phi_{CP} = 0.74$ are also reported. The top part of the figure shows confocal images of colloidal fluid, glassy and crystalline close-packed phases.

In the glassy state, particles are arranged in a structure analogous to the one of a dense liquid and therefore no long-range order is present in the system. The seminal work of Bernal and co-workers showed that the maximum packing fraction of a disordered arrangement of identical hard-spheres is $\Phi_{RCP} \simeq 0.64$ [34, 35, 36]. This point takes the name of *random close packing* (RCP) and it corresponds to the highest possible volume fraction that can be obtained in a colloidal glass of monodisperse hard spheres.

In a hard-spheres system the phase behaviour is solely driven by entropy. The mechanism behind the liquid-solid phase transition can then be explained in the following way. Referring to Figure 2.4, which shows a simple example with 2D hard discs, we note that at the same volume (area) fraction, a disordered (a) and an ordered (b) phase are possible. The entropy of the system arises both from a configurational and a free volume term. The liquid state has a high configurational entropy and a low free volume one because the motion of each particle is restricted by the presence of the neighbouring particles; in the crystalline state instead, the configurational term is

small, but each particle has got a larger free volume. When the free volume entropy gain overcomes the configurational entropy loss the system is driven to a phase transition. At RCP the free volume entropy contribution drops to zero as there is no more free volume available and the structure is completely frozen (Bernal glass). We also observe that the maximum crystalline packing has a larger volume fraction than RCP, pointing out the importance of free volume in maximising the system's entropy.

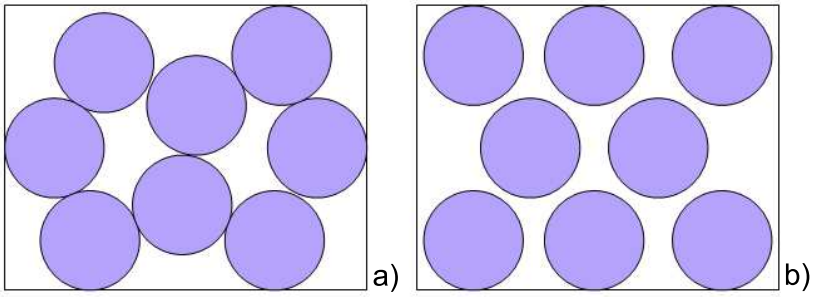

Figure 2.4: Schematic representation of an entropy driven phase transition in two-dimensional discs. In going from a disordered state (a) to an ordered one (b), the system loses configurational but gains free volume entropy; if the gain overcomes the loss, then the system is driven into a crystalline state.

Finally we comment on how accurately hard-spheres interaction can be reproduced experimentally. We have discussed in the previous sections that particles are stabilized against aggregation, either by charge or steric stabilization. Figure 2.5, shows schematically the repulsive part of the interaction potentials for ideal hard-spheres and for the stabilized particles. We observe that sterically stabilized colloids approximate better the hard-spheres potentials, given the short range of the interaction; we recall in fact that sterically-stabilized particles interact only when the two polymer layers of thickness δ grafted onto their surfaces start to overlap. In the case of charge-stabilized system, Coulombic repulsion has a much longer range and therefore the interaction potential turns out to be much softer; this can be partially corrected by screening the particles' charge with the addition of salt to the solution. A common situation is also the one of charged, sterically-stabilized particles (like the ones used in this thesis); in this case if the Debye-Hückel screening length is reduced below δ by the addition of an appropriate salt, then a harder potential arising from the sterical stabilization only can be recovered. The effective hardness of the interaction can be assessed by looking at the ratio $\frac{\Phi_C - \Phi_F}{\Phi_F}$ which for ideal hard spheres is 0.1032 [25].

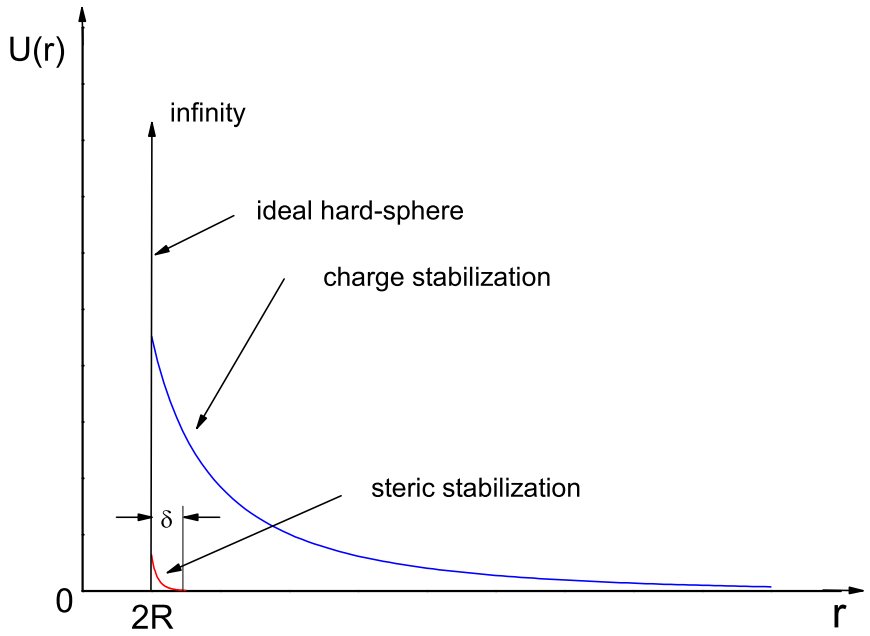

Figure 2.5: Schematic representation of the repulsive part of the interaction potentials for ideal hard spheres, sterically-stabilized and charge-stabilized colloids. The thickness δ of the polymer layer is highlighted.

2.5.1 Alterations to the phase diagram: charge and polydispersity

The hard-spheres phase diagram can be modified if the interactions between the particles deviate from the ideal case. In particular, given the practical importance, it is relevant to study the effects of charge and of particles' polydispersity. A detailed description is beyond the scope of this thesis and we comment only on some qualitative but important issues.

It has been observed that the presence of charges shifts the liquid-solid phase boundary and the value of Φ_G towards lower values. In one of the first experimental studies, a liquid-solid phase boundary was found for values as low $\Phi = 0.06$ and the glass transition occurred below 20% volume fraction [37]. We can qualitatively account for these facts by recalling that the presence of a charged double layer effectively increases the "effective size" of the particles; due to the long-range Coulombic repulsion, a particle will in fact start to feel the presence of another particle at a distance much larger than its diameter. By screening the charge, the size of the double layer can be reduced to the point that the effective size is very close to the actual particle size and the hard-sphere behaviour is almost fully recovered. This procedure is actually followed in laboratory practice to check the efficacy of the charge screening; salt is added to the suspension until the solid-liquid phase boundary matches with the hard-spheres one. We shall

discuss later in this thesis the consequences of this practice when it comes to study the behaviour of extremely dense suspensions ($\Phi \simeq \Phi_{\mathrm{RCP}}$).

Polydispersity also affects the phase behaviour of hard-spheres suspensions. Any assembly of colloidal particles comes with a size distribution, even the ones most carefully synthesized in a laboratory, with the only exceptions being biological objects such as proteins and viruses. The polydispersity is defined as the ratio between the standard deviation and the mean of the size distribution

$$\sigma \equiv \frac{\sqrt{\langle R^2 \rangle - \langle R \rangle^2}}{\langle R \rangle}, \tag{2.6}$$

where $\langle R \rangle$ is the mean particle size. The effects of polydispersity on the phase diagram of colloidal hard-spheres have been carefully investigated in the PhD work of D. J. Fairhurst [38]. He found that crystallization is suppressed for polydispersities larger than a critical value ($\sigma \gtrsim 0.12$); the presence of a size distribution distorts the crystalline lattice to the point where no more crystalline domains are recognizable. For polydispersities lower than 6% the behaviour is similar to the one of monodisperse systems, while for intermediate ranges, the dynamics of crystallization is considerably slower. The polydispersity of a suspension can be determined by light scattering [39] but it is practically impossible to accurately measure it by confocal microscopy. Due to the fact that our suspensions rapidly crystallize we know from previous experience that their polydispersity is $\lesssim 6\%$.

2.6 Radial distribution function

Perhaps the most common way of describing the structure of packing of spheres is the *radial distribution function*, known also as pair distribution function or $g(r)$. Given an assembly of N particles whose coordinates are known, the radial distribution function tells us what is the probability $P(r)$ of finding another particle at a distance between r and $r + dr$ from any randomly-chosen particle. For an isotropic system:

$$P(r)4\pi r^2 dr = \frac{\rho}{N} g(r) 4\pi r^2 dr, \tag{2.7}$$

where ρ is the average number density.

If the positions of the particles are completely uncorrelated, like in an ideal gas, than the probability is independent of r; if the system is arranged into a crystalline lattice, then the probability will be peaked at the lattice spacings. For liquids or amorphous systems like glasses, there is no long-range order and therefore $g(r)$ will decay to the ideal gas profile at large distances, but the presence of short-range order will transpire

through the presence of peaks at small distances. Figure 2.6, shows an example of how to build two-dimensional radial distribution functions from an amorphous assembly of discs. The colour coding relates the particles in the image on the left to the $g(r)$ on the right. The particles have been coloured according to the centre-centre separation with the black one; the probability of finding another particle at distances smaller than twice the particle radius from the centre of the black one is zero due to the excluded volume. We then observe a peak at $r = 2R$ corresponding to direct contact between the black particle and its nearest neighbours, other peaks are found for the second, the third and the fourth nearest neighbours, but they are progressively lower and broader implying a larger distribution of distances. The structure of the suspension is lost after 3-4 particle diameters from the initial particles. By repeating this procedure for every particle in the image, we then construct the system's radial distribution function. More formally, $g(r)$ is obtained by performing the summation:

$$\rho g(r) = \frac{1}{N} \sum_{i=1}^{N} \sum_{j \neq i, j=1}^{N} \delta[r - r_{ij}], \tag{2.8}$$

where δ is the Dirac delta function and r_{ij} is the distance between particles i and j [1].

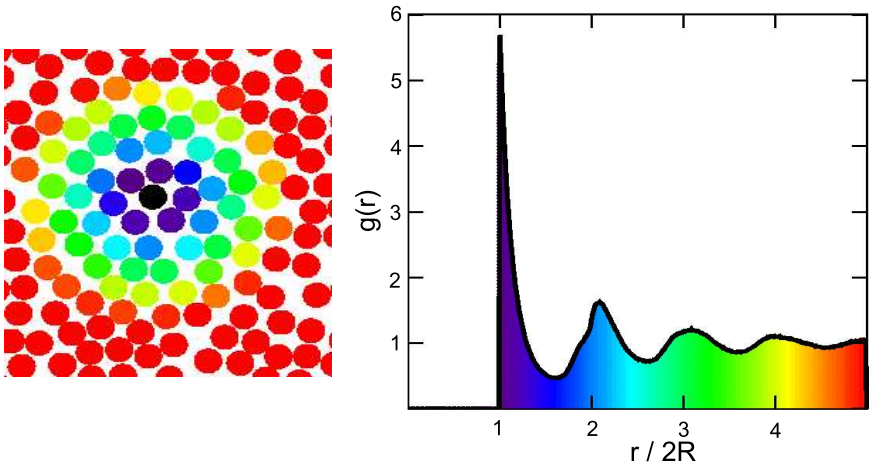

Figure 2.6: Illustration of the procedure for calculating the radial distribution function (right) of an amorphous assembly of discs (left); the colour coding of the discs is relative to the distance from the centre of the black one. Figure taken from Eric Weeks' web page: *http://www.physics.emory.edu/ weeks/idl/gofr.html*

In the case of ideal spheres, $g(r)$ is sharply truncated at $r = 2R$; for data taken from real confocal images, due to inaccuracies in locating the particles' centres and due to polydispersity, a low r tail is always present. Moreover the position of the first peak of

[1] Both Equation 2.7 and 2.8 can be easily extended to a non-isotropic case by substituting r with $\vec{r}$.

the radial distribution function gives a precise indication on the hard-spheres character of the interaction. For the case of ideal hard spheres, the position of the first peak of $g(r)$ is independent of the suspension's volume fraction; two particles feel each other only when they come in contact, regardless of the presence of other particles. If the colloids are charged, they will be pushed away from each other at distances larger than their diameter and therefore the first peak of $g(r)$ will be at a distance $r > 2R$; when the volume fraction is increased, particles are pushed closer together and therefore the distance between nearest neighbours will decrease, yielding a shift in the first peak of $g(r)$ towards smaller r [40, 41]. This method will be used in Chapter 5 to discuss the presence of residual charges in our samples.

Finally the radial distribution function can be used to deduce important thermodynamics properties of the system as the pressure and the isothermal compressibility [39].

2.7 A brief aside: thermal and a-thermal systems

In the next Chapter we will discuss the flow behaviour of dense colloidal suspensions frequently comparing it to the one of granular systems. Nowadays a vast literature is present on the statics and the dynamics of granular media and therefore is a titanic task to attempt an exhaustive description of the involved phenomena. Here, only the elements relevant to our discussion will be presented. We believe that this is a good place for a series of considerations on the nature of the differences between colloidal and granular systems, focussing on the different time and length scales which play a role in the game, in particular in relation to flow.

Colloids and granular systems respectively fall in the categories of *thermal* and *a-thermal* systems. With this nomenclature we indicate those systems for which thermal fluctuations and therefore Brownian motion are relevant or not. We previously introduced colloidal systems, as those for which gravity does not play a dominant role; a more precise definition can be extracted from the results of Perrin's experiments on the sedimentation profiles of colloidal suspensions.

A quiescent dilute colloidal suspension under gravity acquires a density profile $\Phi(z)$ analogous to the barometric profile of an ideal gas:

$$\Phi(z) = \Phi(0)\exp(-z/\xi_g). \tag{2.9}$$

ξ_g is the gravitational length and it is equal to $\xi_g = (k_\mathrm{B}T)/(mg)$, with k_B the Boltzmann constant, T the system's temperature, m the particle's buoyant mass and g gravitational acceleration.

If we substitute values for a 10 nm radius silica particle in water, we obtain a

gravitational length of the order $\approx 10^{-2}$ m, much larger than the particle size; if we perform the same estimate but using a 100 μm silica sphere, we get $\xi_g \approx 10^{-11}$ m, which is obviously much smaller than the particle size. We can then define as colloids or thermal systems those objects for which the gravitational length is larger then their size; in thermal systems Brownian motion is the relevant mechanism which determines the suspension's dynamics. If ξ_g is smaller than the object size, then Brownian motion is not sufficient to keep the particles in solution and they all sediment; the system is a-thermal and dominated by external fields. Numerous studies have been performed in the two regimes, but little is known on the behaviour of intermediate, or *weakly Brownian*, systems. Particles in the micrometre range, especially in nearly density-matching, solvents still exhibit Brownian characteristics but have very slow dynamics due to their large size. A recent attempt to review and classify the rheological behaviour of systems ranging form purely Brownian to completely a-thermal, has been presented by Coussot and Ancey [42], but remains an isolated case.

The dynamics of a colloidal particle in a dilute solution is determined by diffusion. The characteristic time scale is the so called Brownian or diffusion time, defined as the time that a particle takes to diffuse over a distance equal to its radius and is

$$\tau_B = \frac{R^2}{6D_0}, \tag{2.10}$$

where $D_0 = \dfrac{k_\mathrm{B}T}{6\pi\eta R}$ is the diffusion coefficient of a single particle of radius R in a solvent of viscosity η at temperature T and it is given by the Stokes-Einstein relation [39].

For our 10 nm silica particle in water $\tau_B \approx 10^{-6}$ s, while for the particles used in this thesis (1.3 μm radius PMMA in decalin) the Brownian time is ≈ 4.4 s. Given the scaling of τ_B with R^3, the diffusive dynamics of the particles become rapidly slower for larger particles allowing for detailed real-time observation, for instance with a confocal microscope.

For systems with large τ_B, the role played by Brownian motion in events happening on shorter time scales becomes less important. An example of extreme relevance for this thesis is the case of shear or flow-driven events. If we imagine the simplest case of applying a uniform, unidirectional shear field to a colloidal suspensions, two time scales are present in the problem: the diffusion time and the time scale set by the flow equal to the inverse of the applied shear rate $\dot{\gamma}$.

The Pèclet number, defined as the ratio of the two time scales

$$Pe = \tau_B\dot{\gamma}, \tag{2.11}$$

gives an indication of the relative importance of each mechanism. For $Pe \ll 1$ Brownian

motion dominates the dynamics of the suspension, while for $Pe \gg 1$ the system behaves analogously to an a-thermal system and therefore the dynamics is set solely by the flow. Note that for a truly a-thermal system $Pe = \infty$ due to the absence of any diffusive motion. The transition regime $Pe \simeq 1$ is complicated, and therefore not much studied, due to the interplay of flow and Brownian motion but nonetheless intriguingly interesting.

So far we only considered dilute suspensions; we have reported earlier the phase diagram of hard-spheres systems and pointed out the presence of a dynamical arrest at $\Phi \simeq 0.58$. As the system approaches the glass transition, two separate time scales emerge: τ_β and τ_α. The latter represents the time needed for one particle to break the cage of its neighbours and diffuse, the former in-cage Brownian rattling; τ_α diverges approaching Φ_G while the β-relaxation time τ_β remains finite [43]. When dealing with glassy systems the α-relaxation time plays a crucial role in determining the dynamical response; recent work by Besseling [44] and co-authors, studied the effect of shear on the cage-breaking dynamics in colloidal glasses, finding a power law dependence $\tau_\alpha^{-1} \propto \dot{\gamma}^{0.8}$.

Summarizing, we have set out some of the length and time scales which discriminate thermal (colloids) from a-thermal (e.g. granular media) systems. We have also seen that external fields (e.g. flow) can strongly affect the local dynamics. These concepts will prove useful in the discussion contained in the following chapter.

Before concluding we make a last caveat on the nomenclature we shall use in the rest of this thesis in relation to granular systems. There is some potential confusion on how suspensions of non-Brownian objects are called. Some authors refer to grains in a solvent (buoyancy-matched or not) as *wet granular materials* [45, 46] while many others call with the same name assemblies of humid grains with liquid bridges between them [47, 48]. The mechanical properties of these two systems are radically different, in particular the behaviour of the former is much more similar to the one of dry grains than the one of the latter. We will frequently compare our system to dry grains and suspension of non-Brownian particles and will leave the "wet granular name" to humid systems with liquid bridging.

Chapter 3

Rheology of colloidal systems

This chapter is aimed at giving a general introduction to basic rheological concepts and then applying them to the rheology of dense colloidal suspensions, together with presenting a review of the previous literature on the subject focussing in particular on dense channel flows.

The first section introduces the notions of stresses and strains together with some examples of mechanical responses of simple systems. The second one reviews the rheological behaviour of concentrated colloids highlighting the key characteristics which will be needed for the rest of the discussion. We then focus our attention on channel flows, firstly discussing the shape of the velocity profiles in relation to the existing literature and then in the light of simple analytical models. Finally we comment on the presence of temporal oscillations and fluctuations in the velocity of dense systems flowing into two and three-dimensional channels.

3.1 Stresses and strains

We all know that by wearing a pair of snowshoes we can happily cruise on fresh snow, while without them we are very likely to sink in at every step. This (almost) everyday experience tells us that considering solely the weight of an object may not be sufficient to accurately describe many mechanical problems. With or without the snowshoes our weight is pretty much the same, what changes is the area on which such weight is distributed; the relevant quantity is not the exerted force but *the force per unit area, or stress*. Stresses can be decomposed between the ones acting along a direction normal (*normal stresses*) or parallel (*tangential or shear stresses*) to a surface.

Figure 3.1 shows the stresses acting on a cube of side L of a continuous medium; each face of the cube can be subject to three different stress components, a normal one τ_{ii} and two tangential ones τ_{ij}, where the subscripts i, j indicate the x, y and z

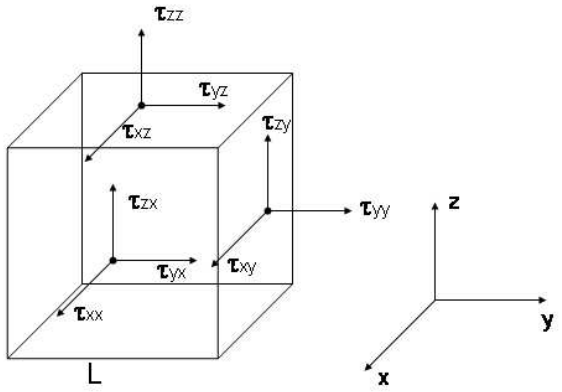

Figure 3.1: Stress components acting on the faces of a cube of side L. The stresses are decomposed in the normal and tangential components with respect to each face. The vectors on three out of six faces have been omitted for clarity.

directions. All the stress components can then be collected in a *stress tensor* $\underline{\underline{\tau}}$ [1]

$$\underline{\underline{\tau}} = \begin{pmatrix} \tau_{xx} & \tau_{xy} & \tau_{xz} \\ \tau_{yx} & \tau_{yy} & \tau_{yz} \\ \tau_{zx} & \tau_{zy} & \tau_{zz} \end{pmatrix} \tag{3.1}$$

We can show with an easy argument that the stress tensor has to be symmetric. Consider for instance the pair of shear components τ_{xy} and τ_{yx}; they exert a torque T on the cube equal to $(\tau_{xy} - \tau_{yx})L^2L$. The moment of inertia of the cube scales with the mass ($\propto L^3$) times a distance squared, so $I \propto L^5$. If we imagine now to shrink the cube ($L \to 0$), the angular acceleration corresponding to the torque $\ddot{\omega} = T/I \propto (\tau_{xy} - \tau_{yx})L^{-2}$ and therefore diverging to infinity if $\tau_{xy} \neq \tau_{yx}$ [2].

Pressure is defined as the mean value of the normal stresses:

$$p \equiv -(\tau_{xx} + \tau_{yy} + \tau_{zz})/3. \tag{3.2}$$

In the case of quiescent liquids the normal stresses are all equal and the pressure is simply the hydrostatic pressure; we shall see in the next sections that normal

[1] Stresses in the literature are either indicated by τ or σ. Sometimes in the engineering literature, normal stresses are called σ and shear ones are called τ. In the rest of this thesis we shall always indicate the stresses as τ.

[2] This argument is valid for continuous matter, i.e. above the level where single-molecule effects become dominant.

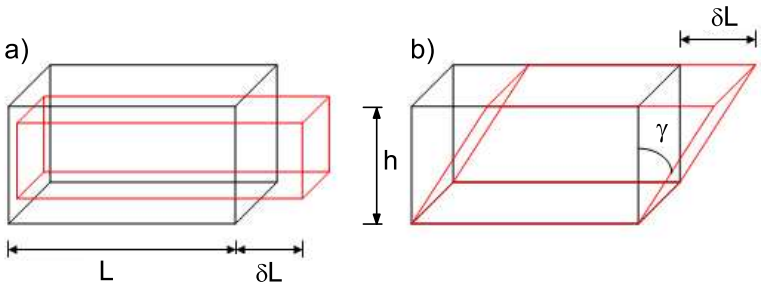

Figure 3.2: Illustration of elongation (a) and shear (b) deformations.

stress differences can instead arise during flow and constitute important signals for the mechanical response of the system.

Let us now consider the *deformations or strains* following the application of a stress. The way a body is deformed under the application of a stress depends on the nature of the body itself; solids and liquids for instance respond to shear in a radically different manner. The following definitions of elongational and shear deformations hold in general, regardless of the system's properties, but their link with the applied stress will be different.

Imagine first to have a solid bar of length L; if the bar is subjected to a tensile (compressive) stress, then it will be stretched (compressed) along the direction of the applied force (Figure 3.2 (a)). We can quantify the deformation δL by introducing a quantity, the axial elongation or strain ε:

$$\varepsilon = \frac{\delta L}{L}. \tag{3.3}$$

We can also think of another category of deformations following the application of shear (Figure 3.2 (b)); if we take the same bar and displace the top surface by δL keeping the bottom one fixed, we can quantify the deformation by considering the angle γ induced by the shear as:

$$\tan(\gamma) = \frac{\delta L}{h}, \tag{3.4}$$

where h is the height of the bar; for small deformations $\tan(\gamma) \simeq \gamma$.

More generally the local shear deformation $\gamma(h)$ can be defined as $[L(h+\delta h) - L(h)]/\delta h$, where $[L(h+\delta h) - L(h)]$ is the shear displacement between positions h and $h+\delta h$, with δh a small distance in the direction normal to the shear.

Analogously to what we introduced for the stress, axial and shear strains can also be incorporated into a strain tensor:

$$\underline{\underline{\varepsilon}} = \begin{pmatrix} \varepsilon_{xx} & \varepsilon_{xy} & \varepsilon_{xz} \\ \varepsilon_{yx} & \varepsilon_{yy} & \varepsilon_{yz} \\ \varepsilon_{zx} & \varepsilon_{zy} & \varepsilon_{zz} \end{pmatrix} \tag{3.5}$$

which has the same symmetry properties of the stress tensor. In the rest of the discussion the shear components of the strain tensor will be indicated with γ instead of ε_{ij}.

Any relation which connects the applied stress to the resulting deformation is called a rheological or *constitutive equation*. Different models, and therefore different constitutive relations, describe the rheological behaviour of different continuum media such as solids, liquids and complex fluids. The efforts of the rheological community, especially from an engineering point of view, are generally devoted to finding a suitable constitutive relation which allows them to make predictions on the characteristic flow or deformation behaviour of a given system.

Let us first consider a solid body subjected to an uniaxial tensile stress as the one in Figure 3.2 (a). As the bar stretches in the direction of the applied stress, it shrinks in the other two directions to conserve the volume; shear is absent and the only non-zero component of the stress tensor is τ_{xx}. The corresponding non-zero deformations are:

$$\varepsilon_{xx} = \frac{\tau_{xx}}{E} \qquad \text{and} \qquad \varepsilon_{yy} = \varepsilon_{zz} = -\nu\frac{\tau_{xx}}{E}, \tag{3.6}$$

where E is the Young's modulus and represents the objects elongation in the direction of the applied stress per unit stress and ν is the Poisson's ratio and represents the deformation in the direction perpendicular to the stretching per unit elongation; we note the minus sign in front of ν as the object contracts in y and z when stretched along x and vice versa.

Similarly for an elastic body subject to simple shear in the x direction, as reported in Figure 3.2 (b), we obtain that:

$$\gamma = \frac{\tau_{xy}}{G}, \tag{3.7}$$

where G is called the shear modulus. Systems for which the deformation is proportional to the applied stress are called *linear elastic solids*. Real systems are more likely to have an elastic response which depends on the applied stress (non-linear elastic solids), but for sufficiently small values of τ a linear elastic regime can usually be found. Real systems are also able to elastically sustain only finite stresses; if the

applied stress exceeds a certain value, named the *yield stress* τ_{yield}, the deformations become permanent or *plastic* and the system is said to be *elastoplastic*. Below the τ_{yield}, the system behaves as a linear or non-linear elastic solid, but above it small stress increments lead to exceedingly large deformations. Figure 3.3 illustrates some stress-strain relations for solid bodies; the graph refers either to axial or shear deformations, where the slope of the curve is the elastic or the shear modulus respectively.

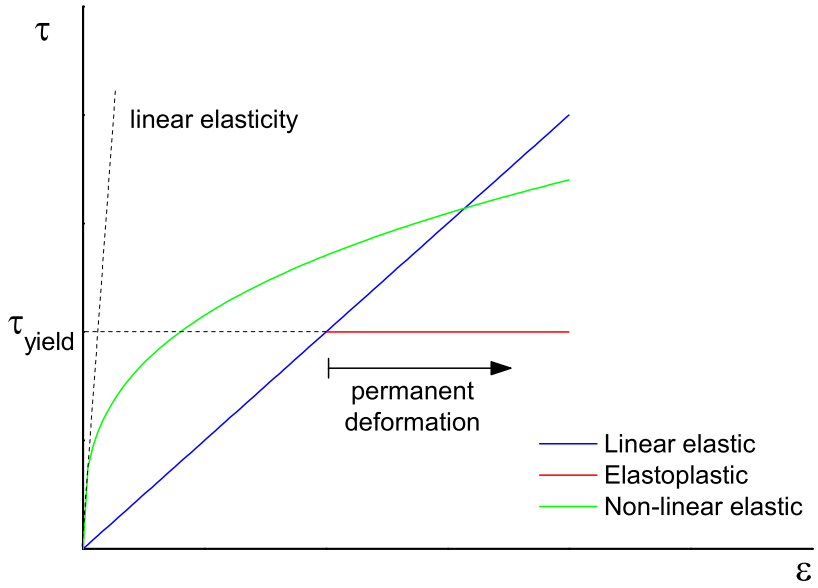

Figure 3.3: Schematic stress-strain relations for different kinds of solid bodies.

At variance with solids, ideal liquids have zero shear and elastic moduli and therefore do not oppose any resistance to the application of a shear and axial stress; a liquid responds to stress by *flowing*. What characterizes a liquid is the link between the applied stress and the rate at which the corresponding deformation occurs $\underline{\underline{\dot{\varepsilon}}} \equiv \dot{\varepsilon}_{ij}$. Similarly to what is reported above for the strain, the non-diagonal components of the strain rate tensor are called $\dot{\gamma}$.

A simple example is constituted by the planar shear geometry reported in Figure 3.4. A fluid is inserted between two parallel infinite slabs; the top one is moved with a constant speed V_x while the bottom one is held fixed. In the simplest case the velocity of the fluid has to be equal to the velocity of the two plates at the contact points (no-slip condition) and varies linearly between them. The rate of shear deformation is defined as follows:

$$\dot{\gamma} = \frac{d\gamma}{dt} = \frac{d}{dt}\left(\frac{dx}{dy}\right) = \frac{d}{dy}\left(\frac{dx}{dt}\right) = \frac{dV_x(y)}{dy}, \tag{3.8}$$

which corresponds to the following non-zero components of the stress and strain rates tensors:

$$\dot{\varepsilon_{xy}} = \dot{\gamma} = \frac{\tau_{xy}}{\eta}, \tag{3.9}$$

where η is called the fluid *viscosity*. A fluid for which shear stress and shear rate are proportional is called an ideal or *Newtonian fluid*. Many real fluids are well described by Equation 3.9 for a vast range of applied rates or stresses, but other, more complex systems, like the ones studied in this thesis, can strongly deviate from the ideal Newtonian behaviour.

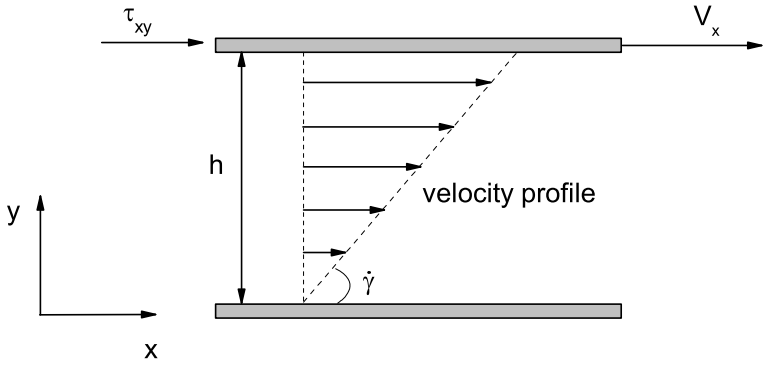

Figure 3.4: Example of planar shear between two infinite parallel plates. The upper plate is dragged with constant speed V_x and the bottom one is kept fixed; the velocity of the fluid varies linearly from 0 to V_x.

For Newtonian fluids, the viscosity is independent of the applied stress, while system for which this statement is not valid are called *non-Newtonian*; fluids for which the apparent viscosity decreases with increasing shear rate are called *shear-thinning fluids*, while system for which the viscosity increases with applied rate are called *shear-thickening fluids*. For the former it becomes increasingly easier to shear them as they are sheared faster, while for the latter a progressively larger effort is needed in order to achieve larger rates. Shear-thinning fluids generally show linear responses in the regimes of small and large applied stresses and therefore we can define η_0 and η_∞ as the zero-rate and the infinite-rate viscosities. Some materials also exhibit the presence of a *yield stress*; in analogy with the definition reported for solid systems, the yield stress for a fluid system is defined as the stress below which no flow takes place. For stresses above the yield stress, the system can, for instance, flow as a Newtonian fluid or as a power-law fluid, for which the stress scales as a power n of the shear rate. We can explicitly write some relevant constitutive equations in terms of the shear stress τ

and the shear rate $\dot{\gamma}$ as

$$\tau = \tau_{\text{yield}} + \eta\dot{\gamma} \qquad \text{Bingham Fluid (BF)} \tag{3.10}$$

$$\sqrt{\tau} = \sqrt{\tau_{\text{yield}}} + \sqrt{k_C\dot{\gamma}} \qquad \text{Casson Fluid (CF)} \tag{3.11}$$

$$\tau = \tau_{\text{yield}} + k_H\dot{\gamma}^n \qquad \text{Herschel} - \text{Bulkley Fluid (HBF)} \tag{3.12}$$

η, k_C and k_H represent the Bingham, Casson and Herschel-Bulkley viscosity parameters. Figure 3.5 illustrates the stress-strain rate relations here described.

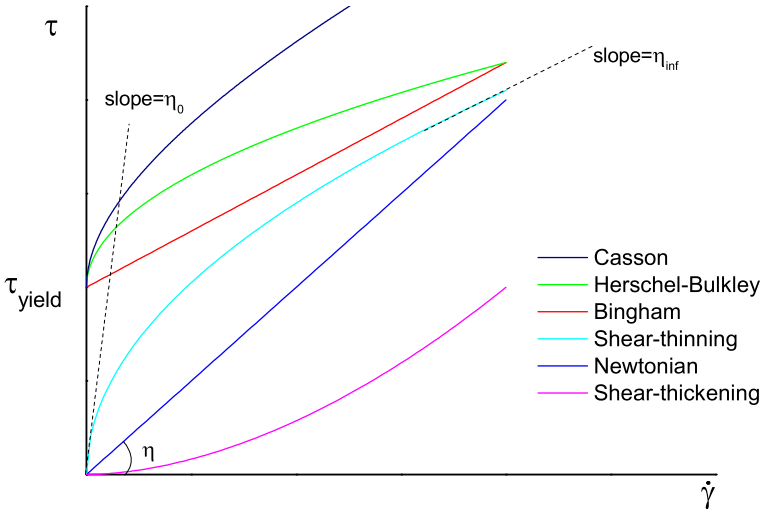

Figure 3.5: Illustration of constitutive relations for Newtonian and non-Newtonian fluids. The presence of a yield stress is highlighted where necessary. The curves are named in the legend from top to bottom.

Summarizing, ideal solids give elastic responses to shear stress whilst ideal liquids show purely viscous behaviour; most real complex systems are neither one or the other, but generally respond as a combination of the two and are therefore called *viscoelastic systems*. The linear mechanical response of these systems can be decomposed into an elastic and a viscous contribution which generally depend on the frequency ω at which the stress is applied

$$\tau(\omega) = [G'(\omega) + iG''(\omega)]\gamma(\omega), \tag{3.13}$$

where $G'(\omega)$ is the elastic or storage modulus and $G''(\omega)$ is the viscous or loss modulus. G' and G'' can be measured by applying an oscillatory stress to the system and measuring the mechanical response; the viscous response is multiplied by the imaginary unit i as for an ideal liquid shear stress and shear strain are out of phase by 90 degrees. A detailed discussion on these issues is beyond the scope of this thesis and further details can be found in [49].

In the following sections we will refer only to steady state rheological properties ignoring the time evolution of the mechanical responses. The conventional way of characterizing the steady state flow response of a viscoelastic system is via the so-called steady state flow curve. A steady state flow curve basically maps the constitutive relation by applying a given stress and measuring the corresponding shear rate or vice versa in a well defined or *rheometric geometry*. This operation is performed in a *rheometer* and common rheometric geometries are parallel plates, concentric cylinders (Couette cell) and cone-plate. Each point on the flow curve is measured until steady state is achieved by checking that the measured rate or stress is stationary within a given time window. Once equilibrium is reached for a given applied stress/rate, another point is collected at a different stress/rate and this operation is repeated scanning the desired stress/rate range.

In the next section we shall introduce and describe the main features of the flow curves of dense colloidal suspensions, highlighting and discussing their main features. Before this we make a brief aside on the equations which determine the mechanical equilibrium of a continuum under the application of a given stress field. These equations will be used later in the chapter to determine for instance the steady state velocity profiles in a channel.

3.1.1 Equilibrium equations

We have defined stresses and deformations for continuous media and also introduced constitutive relations which link one to the other. Based on these elements we can then look for the equations which determine their evolution.

In the case of an elastic solid we can write down the equation for mechanical equilibrium. Given an object of volume V enclosed by a surface S subject to a force per unit volume $\vec{f}$ and to a stress field $\underline{\underline{\tau}}$, the total force $\vec{F}$ acting on it is

$$\vec{F} = \int_V \vec{f} dV + \int_S \underline{\underline{\tau}} \cdot \vec{n} dS = \int_V [\vec{f} + \nabla \cdot \underline{\underline{\tau}}] dV, \tag{3.14}$$

where $\vec{n}$ is the unit vector normal to the surface S and where the surface integral has been made into a volume integral by using Gauss' theorem. In mechanical equilibrium the total force acting on the body has to be zero $\vec{F} = 0$; moreover this condition has to be valid for each part of the object and so equation Equation 3.14 has to be equal to zero for any volume V and therefore

$$\vec{f} + \nabla \cdot \underline{\underline{\tau}} = 0, \tag{3.15}$$

called the Cauchy equilibrium equation.

Similarly applying Newton's law to an element of fluid of density ρ subject to a volume force $\vec{f}$ and a force per unit area $\underline{\underline{\tau}}$, we obtain that the rate of change of linear momentum $\int_V \rho\vec{v}dV$ is equal to

$$\frac{d}{dt}\int_V \rho\vec{v}dV = \int_V \vec{f}dV + \int_S \underline{\underline{\tau}}\cdot\vec{n}dS = \int_V [\vec{f} + \nabla\cdot\underline{\underline{\tau}}]dV, \tag{3.16}$$

where $\vec{v}$ is the velocity field resulting from the application of the volume and surface forces. Since V is an arbitrary volume, the equation is satisfied only if

$$\rho\frac{d\vec{v}}{dt} = \vec{f} + \nabla\cdot\underline{\underline{\tau}}. \tag{3.17}$$

In steady state $\frac{d\vec{v}}{dt} = 0$ and therefore the steady state equation of motion for a fluid is

$$\vec{f} + \nabla\cdot\underline{\underline{\tau}} = 0, \tag{3.18}$$

identical to Equation 3.15.

These derivations tell us an important point. The equations which determine the steady state/equilibrium of a continuum are identical regardless of the nature of the medium; the nature of the medium enters via the constitutive relations and determines the deformation/flow fields associated with the equilibrium stress distribution. This concept will be used later in determining the velocity profiles of a Newtonian fluid and will serve as the basis of the subsequent discussion on dense channel flows.

3.2 Steady state rheology of dense systems

In this section we discuss the rheological behaviour of dense colloidal suspensions commenting on the features which characterize the flow curves and in particular focussing on hard-spheres systems. The aim is not to review the vast existing literature on the subject, but to introduce the fundamental elements necessary for the rest of this thesis. We can broadly divide the flow curves in two regimes in relation to the system's behaviour at low and high shear rates (or Péclet numbers). We recall from previous discussions that Brownian hard-spheres suspensions undergo a glass transition at a volume fraction $\Phi_G \simeq 0.58$; the rheological behaviour at low shear rates radically changes for $\Phi \geq \Phi_G$ with the appearance of a yield stress. At high rates, dense systems ($\Phi \gtrsim 0.5$) exhibit non-linear flows with shear-thickening responses and stress-induced jamming.

3.2.1 Low shear rates regime: yield stress and shear-thinning

Experimental studies have now established the behaviour of fairly dilute Brownian hard-sphere suspensions, which for volume fractions below 0.4 simply behave like Newtonian fluids (see Figure 3.6). When Φ is increased, the scenario changes to a shear-thinning one: a first, low-rate Newtonian region is observed in which the Brownian motion of the particles is able to relax the disturbances induced by the shear ($Pe \ll 1$). The solution viscosity η_0 measured in this first Newtonian regime can be significantly larger than the one of the pure solvent. At higher rates, Brownian motion is not sufficiently fast to restore the perturbation of the micro-structure of the suspension and the system shear thins ($Pe \gtrsim 1$). The viscosity of the suspension decreases with applied rate until a second Newtonian region of viscosity η_∞ is reached where the flow is dominated by hydrodynamic interactions between the colloids [50] ($Pe \gg 1$, see Figure 3.5).

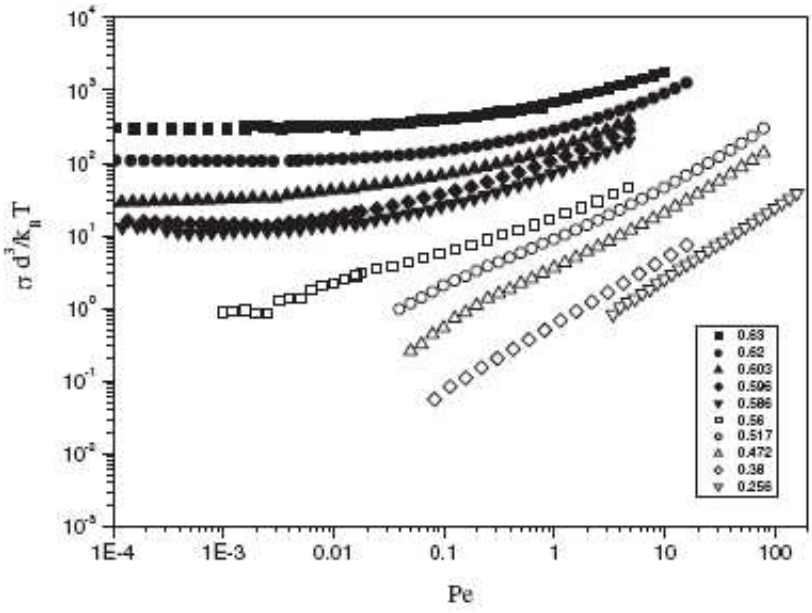

Figure 3.6: Flow curves for PMMA hard-spheres suspensions of diameter D in the glass regime (full symbols) and at concentrated liquid suspensions (open symbols). The normalized stress, $\sigma D^3/k_B T$, is reported as a function of the Péclet number (normalized shear rate). Figure from [14]

When further increasing the volume fraction above Φ_G, the behaviour is radically different with the appearance of a yield stress. Experimental measurements [14] as well as numerical and theoretical approaches [51, 50, 52], predict a transition between shear-thinning fluid flow and solid yielding, with a finite yield stress at (and beyond) the glass point. In particular Petekidis et al. measured the flow curves for PMMA hard-spheres in terms of a-dimensionalised stresses and rates allowing us to map our data onto their

measurements (see Figure 3.6); for volume fractions above Φ_G, the system behaves as an Herschel-Bulkley fluid. It is important to note that the experiments were carried out by decreasing the applied rate form $Pe \gg 1$ down to $Pe \to 0$ and therefore measured a *dynamic yield stress*; proceeding in the other direction gave unreproducible results.

3.2.2 High shear rates regime: shear-thickening and jamming

In the limit of high shear rates, the behaviour of the suspensions also strongly depends on concentration. Dilute systems show the occurrence at high rates of a Newtonian region as commented above, while more concentrated systems undergo shear-thickening. The viscosity increases with increased applied stress as a result of micro-structural changes due to the inability of particles to overlap when they are forced together by the shear field. According to the type, the size and the concentration of the suspended particles as well as the flow geometry, the system can experience either a smooth viscosity increase (continuous shear-thickening) or a sudden jump, frequently associated with strong stress fluctuations (discontinuous shear-thickening) and eventually a viscosity divergence or solidification under flow (stress-induced jamming). Examples taken from measurements performed by the author of this thesis on PMMA suspensions are reported in Figure 3.7. At present there is no general consensus on the role played by the hard-sphere glass transition on the occurrence of jamming and shear-thickening and the matter constitutes the object of interesting debate [53, 54].

Continuous shear-thickening for Brownian particulate systems has been extensively reported in experiments [16, 55, 56, 57] as well as in simulations. Simulation studies have interpreted the occurrence of shear thickening within two different frameworks and an ultimately accepted answer to the problem is still missing. The group of Hoffman [58] attributes the viscosity increase to an order-disorder transition. At low rates the flow of the particles is organized in layers sliding past each other; at higher rates, collisions between particles in adjacent layers end up destroying the ordered flow structure and cause a viscosity increase. The other, more accepted, school of thought follows the seminal simulation work of Bossis and Brady [59] who predicted that shear thickening is due to the formation of particle aggregates held together by lubrication forces (hydroclusters). The idea of the creation of particle networks has been developed also by Melrose and co-workers in shear thickening systems [60] and Cates and co-workers for stress or flow-induced jamming [61]. Of particular interest is the concept of developing "force chains", networks of particles able to sustain a finite load in opposition to the imposed flow; depending on the situation, stress fluctuations [57] and even permanent solidification [62] can take place as a consequence of the presence of

such stress-bearing structures. Finally extensions to theoretical models dealing with the dynamics of dense quiescent systems have been successfully applied to the case of shear-thickening and shear-induced jamming suspensions, delineating a series of interesting scenarios and dynamical properties [53, 63].

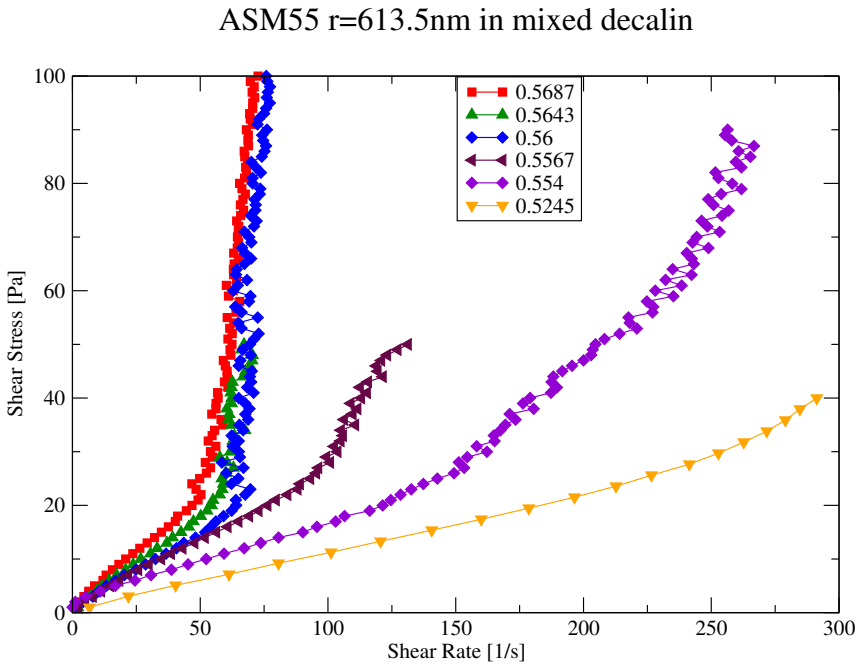

Figure 3.7: Flow curves in the high rate regime for concentrated PMMA suspensions; the volume fractions are reported in the legend. The transition from continuous to discontinuous shear-thickening and jamming is visible as the volume fraction of the suspension increases. The measurements were performed in a cone-plate rheometer by the author of this thesis.

3.3 Channels flows: Velocity profiles

Rheometric geometries like cone-plate, plate-plate or concentric cylinders (Couette) offer simple stress or shear rate distributions and therefore are preferred for characterizing the rheological responses of substances and for obtaining constitutive relations; practical applications on the other hand often involve more complicated flow geometries. Channel flows constitute an exception: the simplicity of the geometry is appealing from the fundamental perspective as well as being very commonly found in industrial processing. It also makes direct contact with microfluidic applications.

In this section we review the velocity profiles of a variety of dense systems flowing into two and three-dimensional channels. Examples for dense suspensions of non-Brownian particles, polymer blends and dry granular media are presented together

with some additional examples of pasty systems of practical relevance but far from being physical model systems. The central point of the discussion will be the deviation of these profiles from the ideal behaviour of a Newtonian fluid. Moreover these systems all present a common feature: in the centre of the channel there exists a zone where shear is suppressed or greatly reduced and correspondingly most of the shear is localized in lateral bands or zones close to the channel's walls. The reason for such seemingly universal velocity profiles can be found in the rheological properties of the flowing media and will be discussed in the following paragraphs.

This section is structured as follows. In a first part we review examples of velocity profiles for different flowing media while in a second one we focus on the calculation of the flow profiles in two-dimensional channels. Results are initially derived for Newtonian fluids and then extended to the case of shear-thinning and yield stress fluids. Finally we comment on the reasons behind the failure of these simple models in accurately describing most of the results presented in this thesis.

3.3.1 Non-Brownian suspensions

Numerous experimental, numerical and theoretical studies have been performed to address the problem of the channel flow of suspensions of non-Brownian objects including hard particles and deformable droplets, where the former constitute a core component of many industrial systems and the latter can also be used as a model system for blood flows. Very little investigation has been carried out on the colloidal counterpart despite equal practical relevance in the processing of many systems including micro-emulsions and Brownian particulate systems.

In 1970 Cox and Mason [64] published a review on particulate channel flows reporting the experimental evidence of a blunting in the velocity profiles of suspensions of neutrally buoyant, non-Brownian particles with volume fractions larger than 20%; the reported velocity profiles in circular pipes deviate from the expected pressure-driven, Newtonian, parabolic ones and consist of lateral sheared zones and a central, almost unsheared band. Moreover the shape of the velocity profile is independent of the applied pressure gradient and each profile can be normalized on a single master curve (see Figure 3.8).

Analogous velocity profiles have since then been observed in a number of studies on non-Brownian suspensions; we report some of the fundamental ones which we divide according to the visualization technique used.

A first group of studies focussed on investigating the flow in rectangular channels by using Laser Doppler Velocimetry (LDV) [65] and lead to consistent findings on a number of different systems. Koh et al. [66] reported the blunting of velocity profiles in

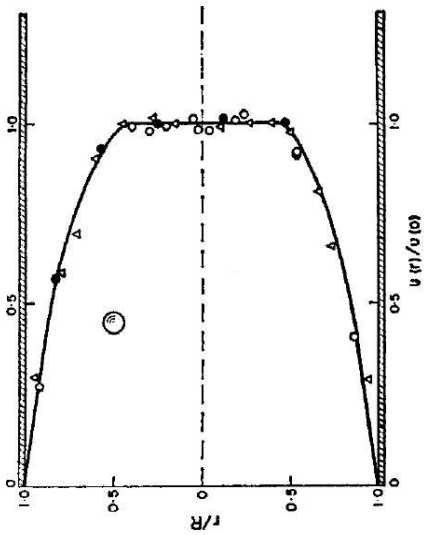

Figure 3.8: Experimental velocity profiles normalized by the centreline velocity across a cylindrical tube of radius R for a non-Brownian suspension with $\Phi = 0.34$. The different symbols refer to different flow rates; all the curves collapse on one single master curve. Figure from [64].

buoyancy-matched suspensions of polystyrene spheres (diameter of 28 μm) of volume fractions $0.20 \leq \Phi \leq 0.30$; samples with $\Phi = 0.10$ showed parabolic profiles. Similar results were obtained by Averbakh et al. [67, 68] who investigated the deviations of velocity profiles from the Newtonian ones for suspensions of poly-methyl-methacrylate (PMMA) of 85 μm diameter both in the long and in the short direction of the rectangular cross section for volume fractions up to 0.5. Finally, Lyon and Leal [69] performed accurate measurements of the flows of suspensions of PMMA spheres (70 and 95 μm diameter) with $\Phi \leq 0.45$ investigating the scaling of the profiles with flow rates and particle to channel size ratios. They found that the shape of the velocity profiles is independent of the flow rate and shows only a very weak dependence on the channel size as previously observed in numerical simulations [70].

A second line of research employed Nuclear Magnetic Resonance Imaging [71] as the means for visualizing the flow in cylindrical tubes, yielding results similar to those reported above. Sinton and Chow [72] showed blunted velocity profiles for suspensions of 130 μm diameter PMMA spheres up to $\Phi = 0.45$ and also performed bulk rheological measurements showing pronounced shear-thinning at the highest volume fractions. Hampton et al. [73] reported similar velocity profiles for much larger suspended PMMA particles (650 μm and ≈ 3 mm diameter) and for volume fractions up to 0.52.

Together with these experimental studies, numerical simulations of two-dimensional channels flows which include hydrodynamic interactions between the particles are also

present in the literature, mainly carried out in the group of Brady. An initial study by Nott and Brady [70] investigated the effects of particle concentration, interparticle repulsive interactions and system size on the velocity profiles in pressure-driven flows of neutrally buoyant particles. The authors found good agreement with the profiles observed experimentally for volume fraction up to 0.5 and also investigated the presence of velocity fluctuations discussing a model which accounted for the observed profiles. Another study by the same group (Morris and Brady [74]) reported similar results for non-neutrally buoyant particles, studying the effects of gravity on horizontal pressure-driven flows up to $\Phi = 0.6$. Both these studies showed velocity profiles consisting of lateral sheared zones and of a low-shear central region.

Another phenomenon is associated with the flows described above: the presence of a non-uniform shear profile induces particle migration which leads to the creation of a non-uniform concentration profile across the channel. The consequences of particle migration where first reported in Couette flows [75]: the viscosity of the sheared suspensions was found to decrease with increasing shearing time. This effect was later explained by Leighton and Acrivos [76] as due to the migration of particles from the high shear rate region to the low shear rate region in the Couette cell, resulting in the building up of a low viscosity band close to the rotating cylinder. Analogous effects were later reported also in the channel flow experiments and simulations mentioned above. When flowing along a channel the particles migrate away from the walls, where the shear rates are higher, and accumulate in the centre where the rates are lower, influencing the velocity profiles.

Leighton and Acrivos [76] and Nott and Brady [70] proposed two different modelling approaches analysing the microscopic origins of the migration of non-Brownian particles; a detailed discussion is beyond the scope of this section and the interested reader can find all the necessary information in the cited references. Subia et al. [77] proposed instead a simpler approach which does not include a microscopic description but which uses the presence of a non-uniform particle distribution in order to account for the observed macroscopic velocity profiles. The authors suggested a generalized Newtonian constitutive equation including a volume fraction dependent viscosity and calculated the velocity profiles via such a continuum approach. More recent simulation work by Miller and Morris [78] also investigated the build-up of a concentration gradient along the flow direction and the influence that this has on the velocity profiles at different positions. Similar experiments were earlier reported in [73].

Finally we remark upon the point observed by Nott and Brady on the influence of repulsive forces between the particles on the build-up of the non-uniform velocity and concentration gradients. The authors found that, in the presence of a short range repulsion, the volume fraction in the centre of the channel was larger than that with

pure hard-spheres interactions. In the absence of repulsion, particle come into very close contact and create clusters held together by lubrication forces which hinder additional migration. We found similar results in the study of the sedimentation of our colloidal particles in the presence or in the absence of surface charges (see Chapter 5).

As previously mentioned, only very few studies on Brownian systems are available in the literature. Buyevitch and Kapbsov [79] proposed a model which describes particle migration and velocity profiles of neutrally-buoyant Brownian suspensions in different flow geometries, comparing their results with experimental findings in Couette and channel flows for non-Brownian systems. More recent experimental and modelling work has been carried out by the group of Weeks. In an earlier paper [80] they used confocal microscopy to report the first detailed experimental study on velocity profiles and particle migration for colloidal suspension of neutrally-buoyant PMMA particles (2.2 μm diameter) in rectangular (2D-like) channels with 50 μm thickness. The measured concentration profiles agreed with the theory and the velocity profiles showed only negligible deviations from the parabolic Newtonian ones for values of Φ up to 0.34. Later studies [81] focussed on the longitudinal build-up of the concentration gradients and found blunting of the velocity profiles for 0.4 volume fraction suspensions.

There also exists a vast literature concerning the channel flows of deformable droplets; this subject constitutes a very interesting one due to the possibility of modelling blood stream flows but drifts beyond the present discussion. We just report that for high densities of droplets, blunted velocity profiles have been observed both experimentally [82] and numerically [83].

3.3.2 Polymers

Polymeric materials play a vast role in industrial production and therefore the understanding of their mechanical and flow properties has attracted numerous efforts from the scientific community. In particular many polymer melts are shaped by forcing them through an aperture (die) of a desired shape (extrusion process). The flow along the die has a fundamental impact on the outcome of the final product [2, 84, 85] and therefore numerous studies have been devoted to its understanding. Theoretical and modelling approaches have been able to predict macroscopic deformations and flows starting from microscopic models at the polymer level and moreover to successfully extend rheometer data to more complex geometries such as the ones involved in extrusion [10, 86]. Thanks to the advances in imaging techniques, in the last decade experiments have also been able to directly measure the flow fields in extrusion channels and relate them to the properties of the resulting extrudate. Laser Doppler Velocimetry studies on polyethylene melts have shown that the velocity profiles exhibit lateral zones

where most of the shear is localized and a central almost unsheared plug [87, 88].

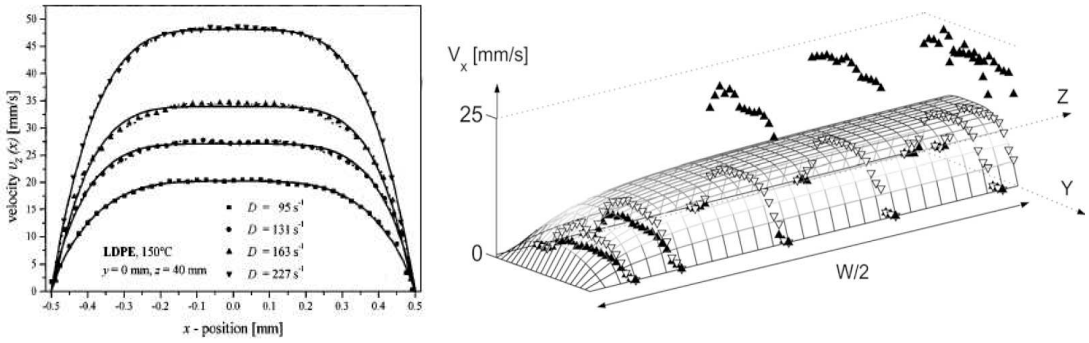

Figure 3.9: Examples of velocity profiles for polyethylene melts in rectangular slits. Left: transverse velocity profiles in a rectangular slit for different applied rates; figure from [87]. Right: three-dimensional reconstruction of the velocity profile in a rectangular slit (open inverted triangles, the full symbols refers to a situation with large wall slip); figure from [88].

3.3.3 Pasty systems

Pastes are defined as fluid systems with a high content of solid particles or droplets of a second liquid phase and are frequently encountered in food, pharmaceutical and ceramics industry to name a few. Pipe-line flow behaviour affects the mixing and transport of food products [89, 9] as well as the rheology of particulates determine the final properties of ceramics [11]. Understanding flow and particle distributions plays also a crucial role in processing of pastes of pharmaceutical interest [8]. Pasty systems in general exhibit velocity profiles analogous to the ones previously described, with lateral sheared zones and central almost unsheared bands (Figure 3.10).

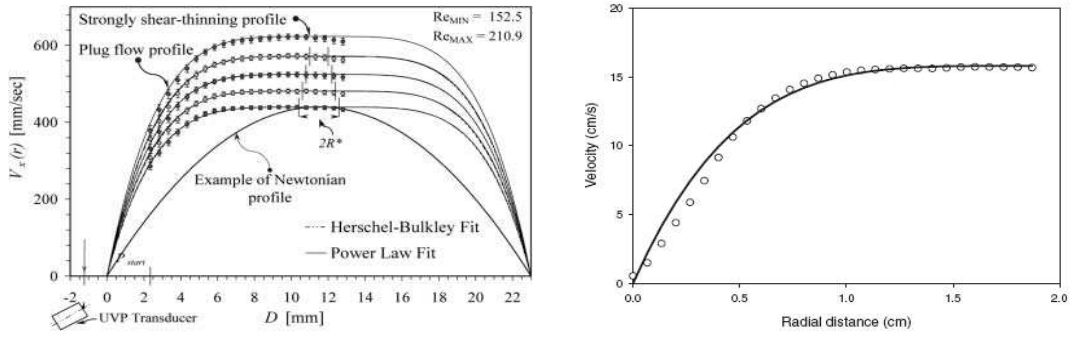

Figure 3.10: Examples of velocity profiles for 40% starch suspensions in silicon oil (left) and tomato concentrate (right). Figures from [89] and [9] respectively.

3.3.4 Dense dry granular flows

Granular media are frequently encountered in many industrial applications and natural processes and have the peculiar property of behaving as a solid, liquid or gas according to the conditions; sand piles can sustain finite loads as solids do, sugar flows out of a bowl like a liquid and corn grains can behave very much like gases when strongly agitated on a sieve. This versatility gives rise to peculiar properties which have strongly attracted the attention of scientists in recent times. In particular we are interested in commenting on the nature of granular flows [90].

At low densities and high applied rates the dynamics of the medium are dominated by the inelastic collisions between the grains; each grain only interacts with the other grains via nearly instantaneous collisions and the mean free path between two collisions is larger than the grain size. These systems are found to behave as 'granular gases' and kinetic theories based on analogies with atomic gases have been proposed [91]. On the other hand, slower and denser flows show rather different features. Each grain interacts with many neighbouring grains at the same time and the interactions are long lasting compared to the time scales of the flow; many different approaches have been proposed to describe this flow regime [92], including extensions of kinetic theories [93] and ideas stemming from self-activated processes [94], but the subject is still a matter of debate. We will focus on the dense regime which presents strong analogies with our dense colloidal flows.

Flows in different geometries of direct practical relevance, including vertical-chute or channel flows, inclined planes, heap flows and rotating drums have been studied as well as simpler rheometric geometries as planar shear, annular shear and Couette flows; we focus here on channel flows, but references to literature on other geometries can be found in [95]. Channel flows, especially vertical channel flows, have been extensively studied to model silo flows; the first experimental papers date back to the end of the 70s and have multiplied since then.

Savage [96] investigated the flow of millimetre-sized polystyrene beads in inclined and vertical cylindrical channels finding velocity profiles consisting of a central plug and lateral shear zones of roughly ten particle diameters; moreover the velocity profiles could be scaled by the applied flow rate. Natarajan et al. [97] observed the flow of millimetre-sized glass beads in a 1 m vertical channel with rectangular cross section. They measured the velocity profiles by recording the motion of dyed tracer particles for different flow rates and they varied the boundary conditions from rough to smooth walls. Again, the flow profiles were constituted of 4-5 particles diameters wide lateral sheared zones and a central unsheared plug and could be rescaled by the centreline velocity. Moreover they observed a transition from such blunted velocity profiles to

complete plugs sliding along the channel's walls by eliminating boundary roughness.

Pouliquen and Gutfriand [98] reported the measurements of velocity profiles in a purely two-dimensional vertical channel with rough walls by using a mixture of 3 and 2 mm diameter aluminium cylinders. They measured the width of the lateral sheared zones as a function of channel size, finding only a very weak dependence that they interpreted as a size independence (see Figure 3.11). In order to describe the origin of the shear zones, the authors proposed, also accompanied by numerical simulations [99], a model based on the presence of stress fluctuations which we shall explore in more details in Chapter 7. Simulations by Denniston and Li [100] also reported analogous velocity profiles in chute flows of hard-spheres granular media, highlighting the presence of velocity fluctuations. Tsai et al. [101] measured the time evolution and the velocity profiles of the flow of millimetre-sized steel beads in an inclined two-dimensional channel by tracking the motion of each individual particle and therefore gaining also quantitative information on the microscopic dynamics. They observed profiles consisting of a central plug and lateral shear zones of about 3 particle diameters for 12 particle diameters wide channels, while for 6 particles wide channels, the shear extended all the way to the centreline. Finally a recent review [95] collected most of the experimental material on channel flows of dry grains; all the velocity profiles consist of lateral sheared zones and of a central unsheared plug. The size of the plug is of the order of a few particles diameters and depends weakly on the channel size. Moreover the profiles maintain the same shape and can be rescaled by normalizing with the centreline velocity. Finally the size of the shear zones strongly depends on the walls roughness, with larger zones induced by rougher walls.

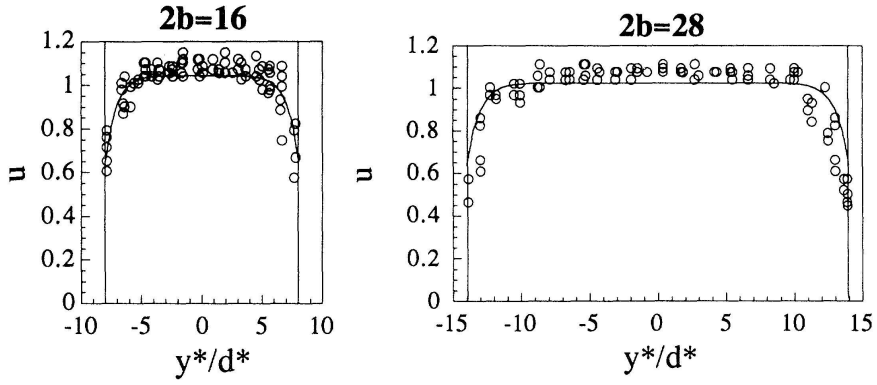

Figure 3.11: Examples of velocity profiles of dry grains flowing into two-dimensional vertical channels with roughened walls with widths of 16 (left) and 28 (right) particle diameters d. Note that the size of the lateral shear bands is of roughly 5 particle diameters irrespective of channel width. Figures from [98].

3.3.5 Analytical profiles for simple constitutive relations

In the following paragraphs we derive analytical expressions for the velocity profiles in two-dimensional channels for a series constitutive relations, starting from Newtonian fluids and then generalizing the approach for power-law and viscoelastic systems. The derivations are based on solving the equations for the equilibrium stress distribution and relating them to the corresponding flow field via the specific constitutive equations. A final paragraph comments on the applicability of these solutions to the systems described above and ones used in this thesis.

Newtonian flows

Recalling Equation 3.17 we have that Newton's law applied to a fluid element gives

$$\rho \frac{d\vec{v}}{dt} = \vec{f} + \nabla \cdot \underline{\underline{\tau}}. \tag{3.19}$$

If we consider a simple two-dimensional flow between two infinite parallel slabs separated by a distance $2a$ (see Figure 3.12), then the velocity $\vec{V}$ only has one component along parallel to the slabs and shear only takes place in the direction perpendicular to flow. If x is the flow direction then $\vec{V} = (V_x, 0, 0)$ and the only non-zero components of the stress tensor are τ_{xx} and τ_{xy} with y the direction perpendicular to flow. Therefore the equation of motion for a fluid between two parallel plates is:

$$\rho \frac{dV_x}{dt} = f_x + \frac{\partial \tau_{xx}}{\partial x} + \frac{\partial \tau_{xy}}{\partial y}, \tag{3.20}$$

where f_x is the component of the volume force along the flow direction. In the case of steady state ($\frac{dV_x}{dt} = 0$) flows and in the absence of an external force this equation is reduced to:

$$\frac{\partial \tau_{xx}}{\partial x} + \frac{\partial \tau_{xy}}{\partial y} = 0, \tag{3.21}$$

which represents for instance the case of pressure-driven flows in horizontal channels (no gravity) with $\tau_{xx} = -p(x)$ the driving pressure. If $\partial \tau_{xx}/\partial x$ is constant and equal to the pressure gradient $-\nabla p$ (the minus sign accounts for the fact that flow proceeds from high to low pressure) then Equation 3.21 becomes

$$\frac{\partial \tau_{xy}}{\partial y} = -\nabla p \quad \Longrightarrow \quad \tau_{xy}(y) = -\nabla p \, y + const. \tag{3.22}$$

For symmetry reasons $\tau_{xy}(y) = -\tau_{xy}(-y)$ and therefore $const = 0$.

In order to link the stress distribution to the flow profile we need now to specify the constitutive relation for the flowing medium; if we assume a Newtonian fluid of

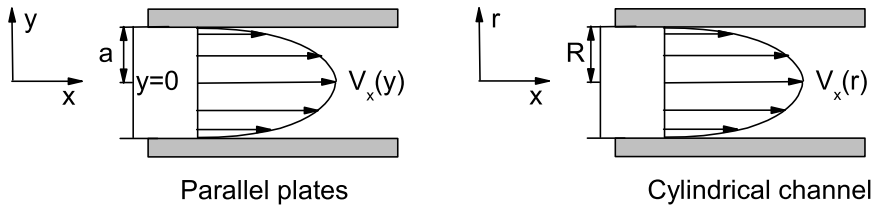

Figure 3.12: Schematics of two-dimensional Newtonian flows between two parallel plates and in a cylindrical channel.

viscosity η, we recall from Equation 3.9 that

$$\dot{\gamma} = \frac{\partial V_x}{\partial y} = \frac{\tau_{xy}}{\eta} \tag{3.23}$$

and therefore by substituting from Equation 3.22 and integrating we obtain:

$$V_x(y) = -\frac{\nabla p}{2\eta} y^2 + k, \tag{3.24}$$

where k is an integration constant. In order to calculate the value of k we need to specify the boundary conditions for Equation 3.24. Newtonian fluids undergo the so-called *no slip boundary condition* which states that at a solid-fluid interface, the velocity of the of the fluid has to be equal to the velocity of the solid . This condition is not always valid for non-Newtonian systems [102, 103] and it has been recently proven to have limited validity also in the case of Newtonian fluids [104, 105]. For the moment we will assume no-slip at the boundary and comment on the presence of slip for our experiments in Chapter 7. Since the parallel slabs are fixed, the boundary condition becomes

$$V_a(y) = -\frac{\nabla p}{2\eta} a^2 + k = 0 \quad \Longrightarrow \quad k = \frac{\nabla p}{2\eta} a^2, \tag{3.25}$$

and therefore

$$V_x(y) = \frac{\nabla p}{2\eta}(a^2 - y^2), \tag{3.26}$$

which finally gives the analytical form of the velocity profile. For two-dimensional flows, the stress varies linearly from zero in the channel's centre to a maximum at the wall, while the flow velocity grows quadratically with the distance from the channel walls and reaches a maximum in the middle (see Figure 3.12).

An analogous expression is obtained for Newtonian fluids in horizontal cylindrical channels by solving Equation 3.17 in the cylindrical (r, θ, x) coordinates. In the absence of any θ dependence, the equation is reduced to

$$\frac{\partial \tau_{xx}}{\partial x} + \frac{1}{r}\frac{\partial (r\,\tau_{xr})}{\partial r} = 0, \tag{3.27}$$

which can be then integrated to give

$$\tau_{xr}(r) = -\nabla p\, r/2 + const; \quad \tau_{xr}(0) = 0 \implies const = 0. \tag{3.28}$$

By applying the non-slip boundary condition for $r = R$, with R the channel radius, and by recalling the constitutive relation for a Newtonian fluid (Equation 3.9), we finally obtain

$$V_x(r) = \frac{\nabla p}{4\eta}(R^2 - r^2). \tag{3.29}$$

This profile takes the name of Hagen-Poiseuille profile and historical details can be found in [106](see Figure 3.12)

This approach can be extended to the case of fully three-dimensional problems like the case of flows in channels with cross sections of various shapes. For a list of analytical solutions in useful geometries refer to [107]. We reproduce here the one for a channel with a square cross section of side $2a$ which will be relevant for our discussion.

$$\begin{aligned} V_x(y,z) = \quad & \frac{-16a^2\nabla p}{\eta\pi^3} \sum_{k=1,3,5\ldots}^{\infty} (-1)^{(k-1)/2} \times \\ & \times \left[1 - \frac{\cosh(k\pi z/2a)}{\cosh(k\pi/2)}\right] \frac{\cos(k\pi y/2a)}{k^3}. \end{aligned} \tag{3.30}$$

Shear-thinning power law fluid flows

Equations 3.28 and 3.29 can be generalized from the case of a Newtonian fluid to any power law fluid with exponent n and gives [108]

$$V_x(r) = \left(\frac{\nabla p}{2k}\right)^{1/n} \left(\frac{n}{n+1}\right) \left[R^{(n+1)/n} - r^{(n+1)/n}\right], \tag{3.31}$$

where k is the viscosity parameter.

Figure 3.13 show some examples for different values of $n \leq 1$; $n = 1$ is the Newtonian case. Such shape of the velocity profile is a consequence of the shear-thinning character of the fluid; as we approach the channel walls the local shear stress increases and thus the local viscosity decreases making it increasingly easier for the system to flow. The curvature of the velocity profile scales inversely with the local viscosity and as a consequence we observe a velocity profile composed of lateral, low viscosity zones where most of the shear takes place and a central, almost unsheared part.

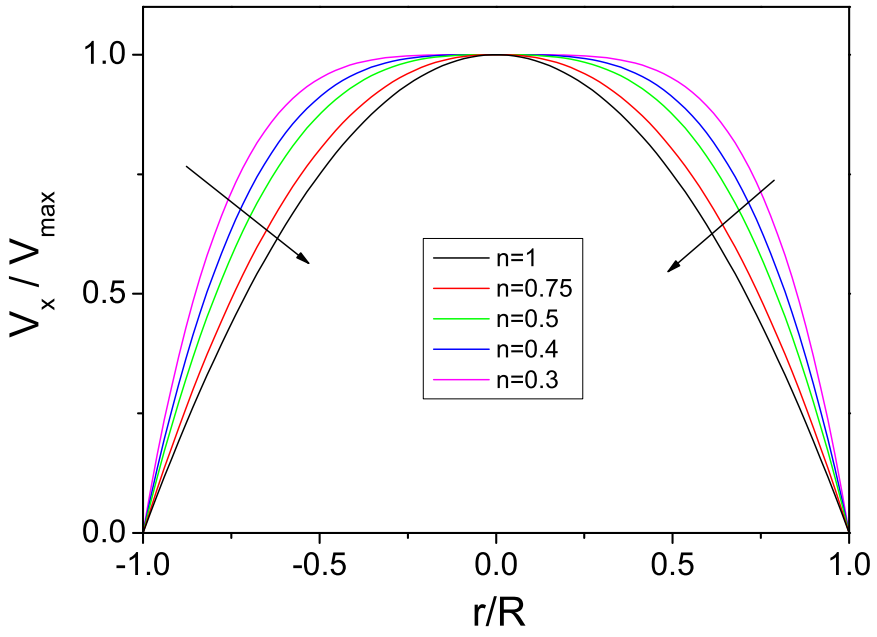

Figure 3.13: Examples of velocity profiles for shear-thinning power law fluids in a cylindrical channel for different exponents $n \leq 1$. $n = 1$ corresponds to the Hagen-Poiseuille parabolic profile for a Newtonian liquid. The arrows point in the direction of increasing n.

Yield stress fluid flows

We can extend the results just obtained for Newtonian and power law fluids to the case of yield stress fluids. Numerical studies have been performed for different systems and flow geometries [109, 110]. We limit ourselves to two-dimensional flows starting with the simpler case of Bingham fluids and then extending the argument to the case of Herschel-Bulkley systems. Let us consider the simple case of 2D flows in cylindrical channels. Equation 3.28 tells us that the stress is zero in the centre of the channel and grows linearly towards the channel's walls; the corresponding velocity profile for a Newtonian fluid is parabolic with a maximum in the channel centre. If the fluid has a finite yield stress, then flow is not allowed where $\tau_{xr}(r) < \tau_{\text{yield}}$ and therefore an unsheared plug appears in the channel centre; the boundary of the plug is determined by loci of solutions of the equation $\tau_{xr}(r) = \tau_{\text{yield}}$. If the applied stress is increased, the position at which it meets the yield stress changes and so does the width of the plug (see Figure 3.14).

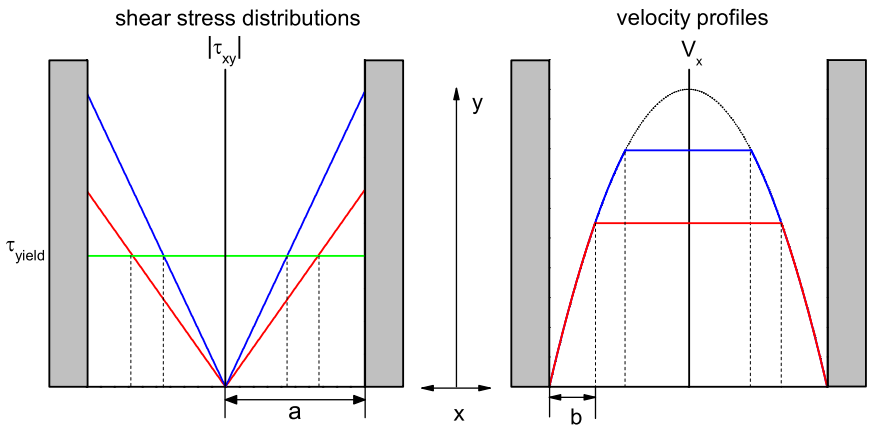

Figure 3.14: Schematics of 2D Bingham flows. Left: stress distributions for two different applied stresses. No flow is allowed for $\tau_{xy} < \tau_{\text{yield}}$ and therefore the points where the applied stress meets the yield stress determine the size of the unsheared plug. Right: corresponding velocity profiles normalized by the Newtonian profile in the absence of a yield stress (dashed line). The different width of the lateral shear zones b is highlighted; the unsheared plug has a half-width $a - b$.

For a cylindrical channel this can be easily calculated by taking Equation 3.28 and substituting the constitutive equation for a Bingham yield stress fluid (Equation 3.10)

$$\tau_{xr}(r) = \tau_{\text{yield}} - \nabla p\, r/2 \quad \Longrightarrow \quad \frac{\partial V_x(r)}{\partial r} = \frac{\tau_{\text{yield}}}{\eta} - \frac{\nabla p\, r}{2\eta}. \tag{3.32}$$

By integration [108] with no-slip boundary conditions we obtain

$$V_x(r) = \frac{\nabla p\, R^2}{4\eta}\left[1 - \left(\frac{r}{R}\right)^2 - \frac{2R_0}{R}\left(1 - \frac{R_0}{R}\right)\right], \tag{3.33}$$

for $|r| \geq R_0$, where $R_0 = (2\tau_{\text{yield}})/\nabla p$ is the distance from the centre for which $\tau_{xr}(r) = \tau_{\text{yield}}$. For values $|r| \leq R_0$ the fluid flows as an unsheared plug of velocity $V_{\text{plug}} = \nabla p\,(R - R_0)^2/(4\eta)$. Figure 3.15 reports some velocity profiles calculated from Equation 3.33 for different values of R_0/R.

An analogous reasoning can be carried out for an Herschel-Bulkley fluid and the resulting velocity profile for the sheared part of the fluid is [108]:

$$V_x(r) = \frac{2}{\nabla p\,(1 + 1/n) k_H^{1/n}}\left[(\tau_w - \tau_{\text{yield}})^{1+1/n} - \left(\frac{\nabla p\, r}{2} - \tau_{\text{yield}}\right)^{1+1/n}\right], \tag{3.34}$$

where τ_w is the maximum stress at the wall, n is the exponent of the HB power law and k_H is the Herschel-Bulkley viscosity parameter. Figure 3.16 shows some velocity profiles calculated from Equation 3.34 for different values of $\tau_{\text{yield}}/\tau_w$ and for different values of $n < 1$.

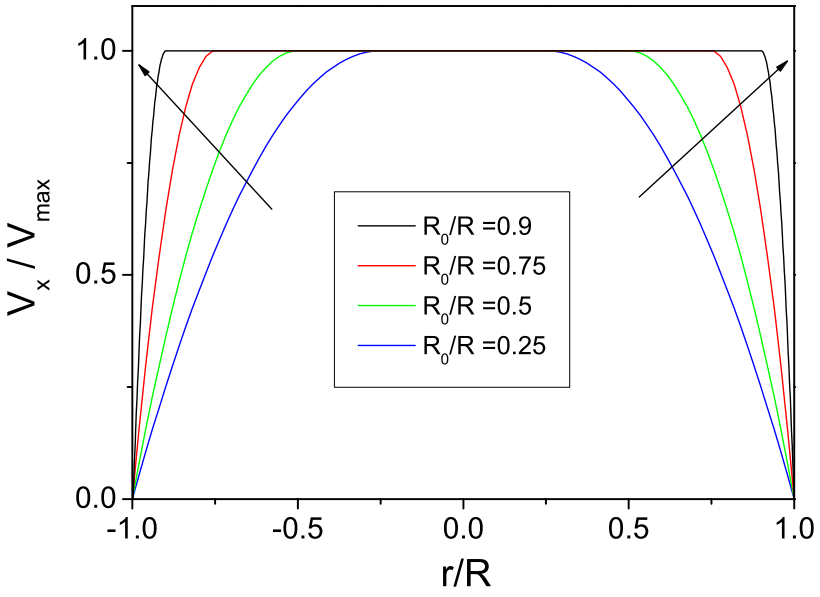

Figure 3.15: Examples of velocity profiles calculated for a Bingham fluid in a cylindrical channel. Note that the width of the plug depends on the value of R_0; for a constant yield stress, the width of the plug then depends on the applied pressure gradient ∇p. The arrows point towards increasing R_0/R.

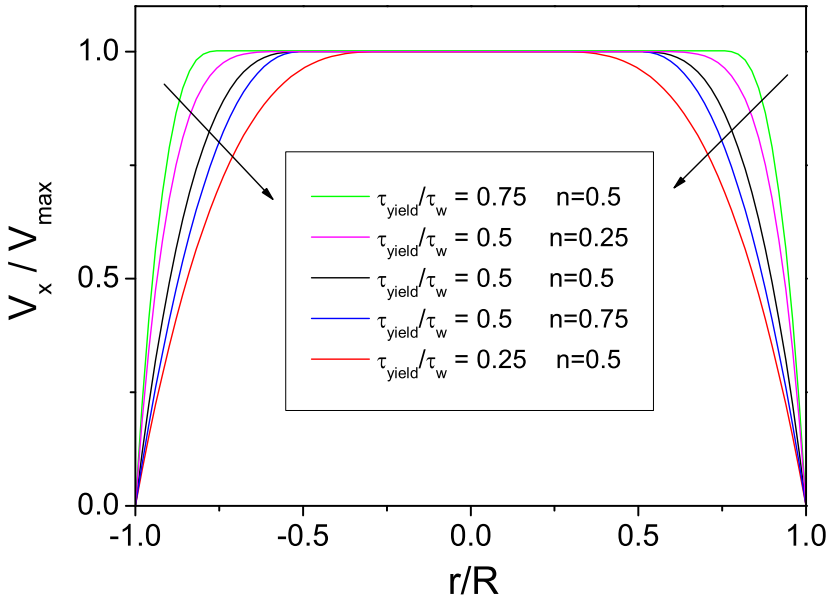

Figure 3.16: Examples of velocity profiles calculated for an Herschel-Bulkley fluid in a cylindrical channel. Note that the width of the plug depends on the ratio $\tau_{\text{yield}}/\tau_w$ and on the HB exponent n; for a constant yield stress and for a given n (both properties of the material), the width of the plug then depends on the maximum applied stress τ_w. The arrows refer to the curves in the legend from top to bottom.

This same reasoning can be applied to any channel geometry and any constitutive relation. The parameter which determines the width of the plug is the Oldroyd number, defined as the ratio of the yield stress to the viscous stress

$$Od = \frac{\tau_{\text{yield}}}{a\nabla p}, \tag{3.35}$$

where a is a typical length scale of the channel, e.g. the radius in a cylindrical channel or half the side length for a square channel.

By using the definition of the Oldroyd number we can then rewrite Equation 3.34 in an a-dimensionalised form

$$\tilde{V}_x(\tilde{r}) = \left[\left(\frac{1}{2\,Od} - 1\right)^{\frac{n+1}{n}} - \left(\frac{\tilde{r}}{2\,Od} - 1\right)^{\frac{n+1}{n}}\right], \tag{3.36}$$

where $\tilde{r} = r/R$ and $\tilde{V}_x(\tilde{r}) = V_x(\tilde{r})/V^{max}$ with $V^{max} = \dfrac{2\,n\,\tau_{yield}^{(\frac{n+1}{n})}}{(n+1)\,k_H^{1/n}\,\nabla p}$.

It is a crucial point for our argument that we are able to estimate the Oldroyd numbers for our flows. Two quantities are needed: the yield stress τ_{yield} and the applied pressure gradient ∇p.

Starting form the latter, there is a trivial way to obtain ∇p. We shall see in Chapter 5 that we externally apply a *pressure difference* to drive the flow; therefore we can calculate the pressure gradient by dividing the pressure difference by the the length over which such pressure difference exists. The typical applied pressure differences are in the range of 10 to 100 torr, corresponding to 10^3 to 10^4 Pa while the typical lengths are of the order of centimetres, giving pressure gradients between 10^5 and 10^6 Pa/m. This estimate is based on the assumption that the flow is uniform; we shall see in the results chapters that the actual flows are very far from being uniform. Not only velocity oscillations are present for constant pressure differences, but also the flow profiles and the density of the suspension vary along the flow direction and therefore the *local* pressure gradients can be very different from the ones calculated above.

Another, more local, approach uses the values of the measured velocities to get ∇p; in order to link the two we need a constitutive relation. We have seen in Figure 3.6 that a dense colloidal suspension above $\Phi \simeq 0.58$ shows an Herschel-Bulkley (HB) behaviour at low applied rates in a bulk rheological measurement and we therefore decide to proceed with this. Generalizing for an HB fluid the Newtonian relation between velocity and pressure gradient we obtain:

$$\text{Newtonian}: \ \frac{u}{a} = \frac{a\nabla p}{\eta} \quad \Longrightarrow \quad \text{Power law (HB)}: \ \left(\frac{u}{a}\right)^n = \frac{a\nabla p}{k_H}, \tag{3.37}$$

where u is the characteristic flow velocity, η is the Newtonian viscosity and n and k_H are the HB exponent and viscosity parameter respectively.

Petekidis and co-workers [14] measured a set of flow curves (reported in Figure 3.6) that, when appropriately a-dimensionalised, are universal for colloidal hard-spheres and can therefore be used to obtain the values of rheological quantities, such as n, k_H and the yield stress, for other systems. We tested the scaling of the flow curves and Figure 3.17 reports the most relevant example for our discussion. We report here the data for the 63% volume fraction suspension taken from [14] and a flow curve measured by us in the same conditions for a suspension of particles identical to ones used in this thesis but of a smaller size ($D = 280$nm, from light scattering). The scaling of the curves is remarkable and we can then extract the parameters we need by fitting the data of Petekidis with an Herschel-Bulkley relation. In a-dimensional units we obtain $\tilde{\tau}_{\text{yield}} = 274 \pm 10$, $n = 0.5 \pm 0.017$ and $\tilde{k}_H = 464 \pm 17$ which correspond to a yield stress of 0.063 ± 0.002 Pa and to a viscosity parameter of 19.45 ± 1.41 Pa s$^{0.5}$ once the following normalizations are made:

$$\tilde{\tau}_{\text{yield}} = \tau_{\text{yield}} \frac{D^3}{k_{\text{B}} T}, \tag{3.38}$$

$$\tilde{k}_H = \frac{8^n \, k_H^{(1-n)} D^{3(1-n)}}{\pi^n \, (k_{\text{B}} T)^{(1-n)}}. \tag{3.39}$$

Using these values, in the typical experimental velocity range ($5\ \mu\text{m/s} < u < 100\ \mu\text{m/s}$), we can estimate from Equation 3.37, that $3.48 \pm 0.025 \times 10^5$ Pa/m $< \nabla p <$ $1.556 \pm 0.025 \times 10^6$ Pa/m. These values are consistent with the rough estimates for uniform flows reported above.

Finally we can calculate the values of the Oldroyd numbers for our $50 \times 50 \mu$m square channels obtaining $1.6 \times 10^{-3} \pm 1 \times 10^{-4} < Od < 7.2 \times 10^{-3} \pm 7 \times 10^{-4}$.

Huilgol and You [111] have obtained numerical results which give the width of the plug as a function of the Oldroyd number for square and cylindrical channels for a variety of constitutive equations (Figure 3.18). The figure shows that our values of Od correspond to an almost fully yielded system with practically no central plug; *later we shall see that this is not what we observe in our data*. We will return on this point in Chapter 7 and we will comment on differences between the expected behaviour for an HB fluid and our experimental observations; additional comments are also found in the following section.

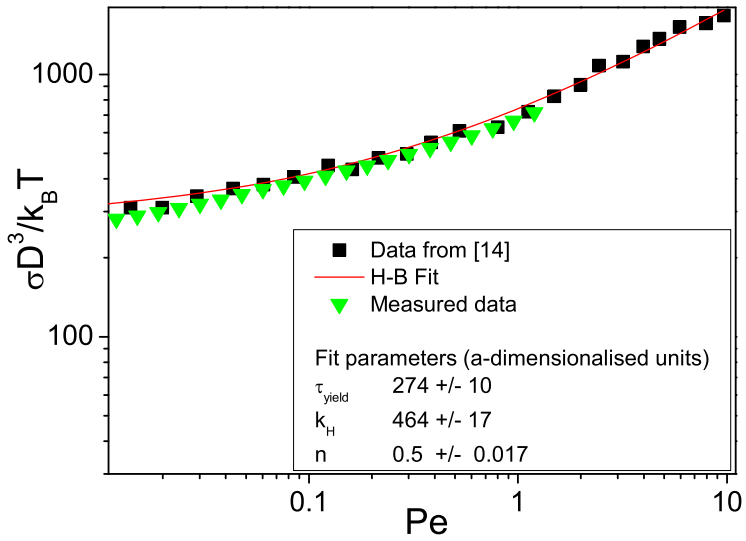

Figure 3.17: Flow curves in a-dimensionalised units for a hard-spheres suspension measured by Petekidis [14] (squares) and for a suspension of particles identical to ones used in this thesis but of a smaller size ($D = 280$nm, from light scattering) measured by us in the same conditions (triangles). Both suspensions have a volume fraction of 0.63. The full line is a HB fit to the data from [14] and the fit parameters are reported in th legend in a-dimensionalised units.

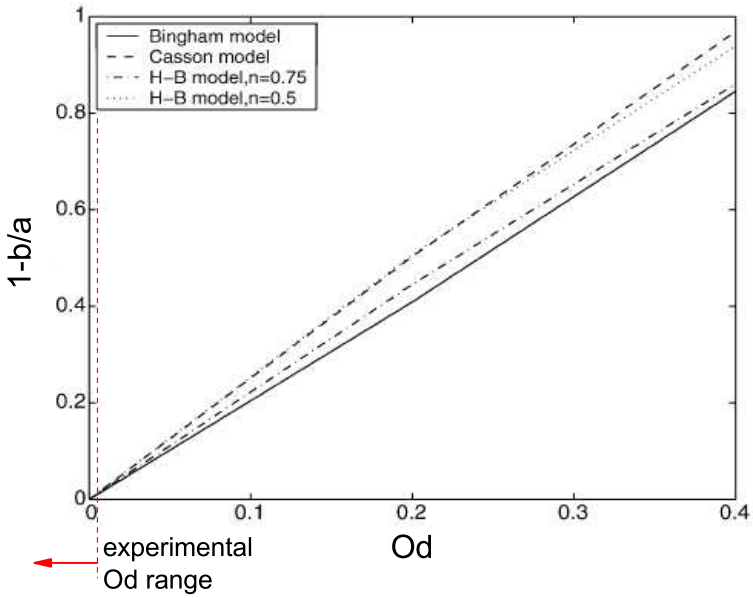

Figure 3.18: Normalized half-width of the central plug in terms of the extension of the lateral shear zones b as a function of the Oldroyd number Od for channels with square cross section and for different constitutive relations. The values of Od in our experiments are to the left of the vertical dashed line, corresponding to a plug of negligible width. Figure from [111].

Comments

We can compare the velocity profiles calculated above with the results reported in the previous review. We have seen that profiles consisting of lateral sheared zones and a central band where shear is absent or greatly reduced can be obtained for a number of different constitutive relations involving the presence of shear-thinning, of a yield stress or a combination of the two.

Starting with purely shear-thinning system, we note that the velocity profiles given by Equation 3.31 scale with the applied pressure gradient and therefore with the overall flow rate; the shape of the velocity profiles is conserved and they all collapse on a single curve when normalized by the centreline velocity. As consequence of this, if we define the shear zones as those parts in the profile where the velocity is below a given fraction of the centre velocity, then their width is independent of the applied rate. This situation applies well to such shear thinning fluids as particulate suspensions, polymer blends and non-viscoelastic pastes.

The scenario changes if the flowing medium has a yield stress. In this case we have seen that the shape of the velocity profiles is determined by the ratio between the maximum applied shear stress and the system's yield stress. No flow is allowed if the local stress is below the yield stress; conventional rheology of viscoelastic systems gives a constant value for the yield stress and therefore the size of the lateral shear zones and consequently the shape of the velocity profiles will depend on the applied rate. Such a situation applies for instance to colloidal gels [112] and viscoelastic pastes.

Granular media cannot be described by either scheme; they have a yield stress but their velocity profiles are independent (or only very weakly dependent) of the applied rates. Similar considerations apply also to our dense colloidal systems and we shall return on this issue in Chapter 7 where we present the data in detail and discuss a modelling approach.

3.4 Channel flows: oscillations and instabilities

Dense systems have non-linear responses to external perturbations. We have already seen in Section 3.2.2 that in the presence of stress-induced jamming, dense suspensions of colloidal particles exhibit strong viscosity fluctuations. The presence of time-dependent responses is indeed a feature common to many dense flows. In particular we report here a list of experimental and simulation studies which observed the occurrence of velocity fluctuations in channel flows driven by constant forces. We first review the case of dense dry granular flows and then move to pasty suspensions and polymers. Finally we mention the very limited literature dealing with model colloidal suspensions.

Temporal oscillations in dry granular flows have long been known with hourglasses being certainly the most famous example. Despite their long history, the mechanism behind hourglasses' regular 'ticking' has only recently been explained [113, 114]. Grains flowing into the constriction jam into each other creating a dome-like structure which temporarily stops the flow; the counter propagating flow of the interstitial air disrupts the structure and allows the flow to restart. Within a rather narrow range of grain to aperture size ratios this mechanism repeats with a very well defined frequency. The creation and relaxation of stress-bearing structures or force chains is a common denominator in oscillations and fluctuations in the time behaviour of granular channel flows.

Raafat et al. [115] studied the flow of 200 μm diameter glass beads freely falling into vertical channels reporting the presence of density waves; the grains were flowing through a sequence of regularly spaced, high density clogs and low density, fast flowing regions. A later study from the same group [116] reported additional flow regimes including dense intermittent flows dominated by stick-slip motion with density modulations of much smaller magnitude. The authors also studied the effects of environmental humidity on the frequency of the oscillations. Low humidity eliminates static charges originating from interparticle friction while high humidity can cause capillary bridges between the grains and therefore induce strong binding forces; humidity control was therefore found to be a crucial factor in determining the flow properties. Similar studies were also performed by Bertho et al. [117] who additionally measured pressure signals as well as flow rates and local densities during flow. They observed a back-propagating stoppage front moving with a speed larger than the average flow speed and related both to small changes in the local packing fraction and to large pressure variations. The authors also proposed a simple model which described their observations. Luding et al. [118] performed numerical simulations and were able to relate the macroscopic clogging events to the microscopic dynamics of the single grains, following the formation of stress bearing structure and the subsequent counter propagation of density and pressure waves. More recent experimental studies were also able to follow single grains dynamics and relate them to the macroscopic flow. Tsai et al. [101] studied the two-dimensional flow of millimetre-sized steel balls reporting the presence of various flow regimes determined by the channel to particle size ratios and by the flow rates, highlighting again the presence of dense intermittent flows. The authors also pointed out the crucial role of side wall roughness in triggering the occurrence of local jams responsible for presence of velocity oscillations and density waves. Horluck et al.[119, 120, 121] also followed the dynamics of millimetre-sized brass balls flowing into inclined, small-angle funnels focussing on the presence of density and velocity shock waves originating from jamming points along the channel and subsequently back-

propagating towards the inlet. The roles of side wall roughness and grain polydispersity were also investigated.

The engineering community has also been actively studying the occurrence of oscillations in the channel flow of dense particulate systems and polymers due to the analogy with extrusion procedures. Yaras et al. [122] studied the instabilities during the pressure-driven capillary flow of two concentrated suspensions (65.6 and 76.5% volume fraction) of non-Brownian polydisperse particles. By measuring the time evolution of the force needed to drive the flow at a constant rate, they observed time-periodic oscillations whose frequency and amplitude depended on the capillary diameter and the volumetric flow rate. An increase in the applied rate and in the initial volume fraction as well as a narrowing of the capillary led to higher frequencies and larger oscillation amplitudes. Similar results were obtained by Suwardie et al. [123] with suspensions of ceramic particles in polymeric binders reporting fluctuations in the force driving the extruding ram. Lukner and Bonnecaze [124] also studied the piston-driven flow of highly concentrated suspensions glass or PMMA millimetre-sized spheres (55% to 59% by volume solids) as a function of piston speed, liquid viscosity, particle material, and particle size. By means of imaging they we able to relate the oscillations in the piston force to stick-slip motion of the suspensions.

Stick-slip instabilities and velocity oscillations have also been the extrusion of high-density polymers. Robert et al. [125] studied the extrusion of high-density polyethylenes (HDPE) through a rectangular transparent slit die. At low flow rates they observed stable flows while at higher rates a stickslip instability appeared.

We have already mentioned that despite their practical importance, a very limited literature on model colloidal systems is present. A recent exception has been the work of Haw [13] who studied by optical microscopy the flow of model hard-sphere colloidal suspensions at high volume fractions driven through a constriction by a pressure gradient. Above a particle-size dependent threshold volume fraction, direct microscopic observations demonstrated the presence of velocity fluctuations caused by jamming and unjamming during flow. Larger particles and denser systems showed a higher tendency to undergo discontinuous flows. Preliminary studies by Isa et al. [126] also showed that for a given volume fraction there exists a threshold flow rate above which the afore-mentioned jamming events have the effect of slowing down the overall flow; below the threshold the flow rate increases with applied pressure gradient, while above it increasing the driving force has the effect of slowing down the flow.

Chapter 4

Confocal microscopy and tracking of colloidal particles

In this chapter we discuss the main experimental technique used in this thesis, confocal microscopy, and we also present the details of the procedure used to gain particle tracks from confocal images. Before this though, we briefly discuss light scattering as a more traditional means of investigating structural and dynamical properties of colloidal systems, highlighting the advantages and limitations which favour the use of confocal microscopy instead. Following this, we examine the principles of microscopy and image formation setting the steps of the path from conventional optical microscopy to more advanced confocal techniques. We then present a discussion on the principles of confocal microscopy and on a series of practical and technical issues. This is followed by a detailed description of the methods used to locate and track particles via the analysis of confocal images, focussing in particular on recent advances which allow us to follow particles in strongly non-uniform flow fields.

4.1 Light scattering

Light scattering has been for many years a main technique used to investigate the properties of colloidal systems. A detailed description of the principles of scattering is beyond the scope of this thesis and we will mention here only the fundamental concepts in relation to the properties of colloidal systems. For background on scattering in general refer to [127] while for more details on dynamic light scattering [128] can be consulted. An excellent description on scattering applications to Soft Matter can be found in [39].

A scattering experiment exploits the interaction between an incident beam of radiation or particles and a medium to obtain information on the properties of the

medium itself. The two main techniques applied to the study of colloidal suspensions are static and dynamic scattering.

Static light scattering allows us to obtain information on the shape of the scattering particles and the structure in which they are arranged by probing the spatial correlation of particle density fluctuations or, more in general, of refractive index modulations [39]. The temporal evolution of density (or refractive index) fluctuations can instead be measured by dynamic light scattering (DLS) and is related to the dynamics of the suspended particles [39]. DLS is an appropriate technique to detect the occurrence of dynamical arrest as in the presence of colloidal gelation [129] or of a glass transition [130, 43].

Developments of traditional DLS, such as two-colour light scattering (TCLS) [131, 132, 133] and diffusing-wave spectroscopy (DWS) [134], have been devised in recent years in order to measure the properties of very dense and turbid systems, yielding some of the most important results in the field of colloidal glasses [135, 136].

The spatial resolution of light scattering is related to the accessible values of the scattering vector; for visible light and water based suspensions the limit is of ~ 300 nm. In order to resolve structures with smaller features other types of radiation are needed, such as X-ray or neutrons, which can bring the resolution down to the nanometre range. The temporal resolution of the technique is determined by the instrumental resolution; present day equipment makes possible to resolve events in the microseconds range.

Light scattering measurements are obtained by averaging very large ensembles of particles and therefore yield very accurate information on the bulk properties of the systems but because of this, they also fail to describe events localized in space and time.

A recent development of DWS, called time-resolved correlation, has been devised to describe phenomena with temporally heterogeneous dynamics, such structural rearrangements in colloidal gels [137]. An even more recent refinement of this technique makes it also possible to select the length scales of the rearrangements [138].

4.2 Optical microscopy

In this section we trace the steps that lead from a conventional optical microscope to a confocal microscope. We initially present the basic mechanisms of image formation and briefly discuss issues on magnification and resolution together with comments on the workings and operation of a conventional optical microscope. We shall then give a brief description of the principles of fluorescence microscopy. We also highlight along the way the limitations of these techniques which opened the way for the introduction of confocal microscopy. Mathematical details on image formation and optical microscopy

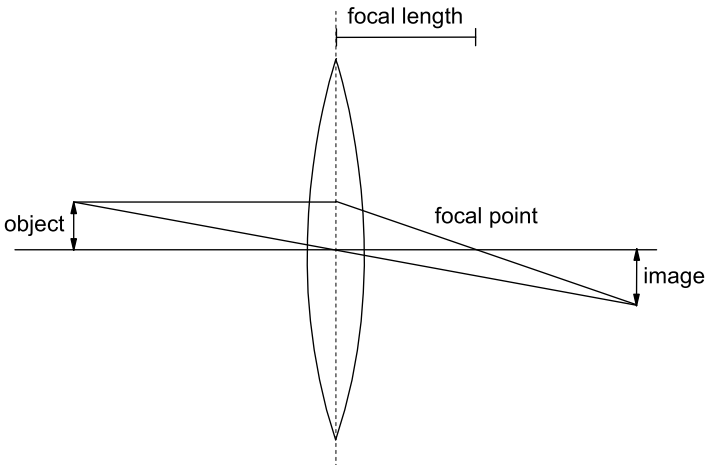

Figure 4.1: Image magnification by a single converging lens.

can be found in [139, 140] while for an introduction which is more qualitative, but very rich in practical and technical details, one can consult [141]. Finally a detailed description of conventional (non-confocal) optical microscopy applied to the study of colloids is given in [142].

4.2.1 Bright field microscopy

Vision is the process by which the eye lens forms an image on the retina. As powerful and flexible as our eyes are, human vision has a limited resolution; the smallest object than can be seen by naked eye is of the order of 10 μm [1] and so, in order to resolve the details of smaller features, we need a magnifying system. The simplest system we can devise is given by a single lens (see Figure 4.1) by which we can achieve magnification up to ten times. In order to obtain larger magnifications we need a compound system of lenses: a microscope.

Figure 4.2 reports a diagram of an infinite tube compound microscope. The fundamental components of such a system are: the objective, the tube lens and the eyepiece. The objective produces a magnified image at an infinite distance. The tube lens focuses the parallel rays coming from the objective producing a magnified image onto the eyepiece plane (intermediate image). Finally the eyepiece further magnifies the image that is then observed, directly or via a digital camera (charge coupled device or CCD), by the user. The role played by the tube lens is to decouple the eyepiece and the objective. In fact, in the absence of the tube lens, both the position of the objective and of the eyepiece need to be adjusted when changing the focus; thanks to the tube lens, the axial position of the objective becomes relatively unimportant and focussing

[1] As seen by the author of this thesis!

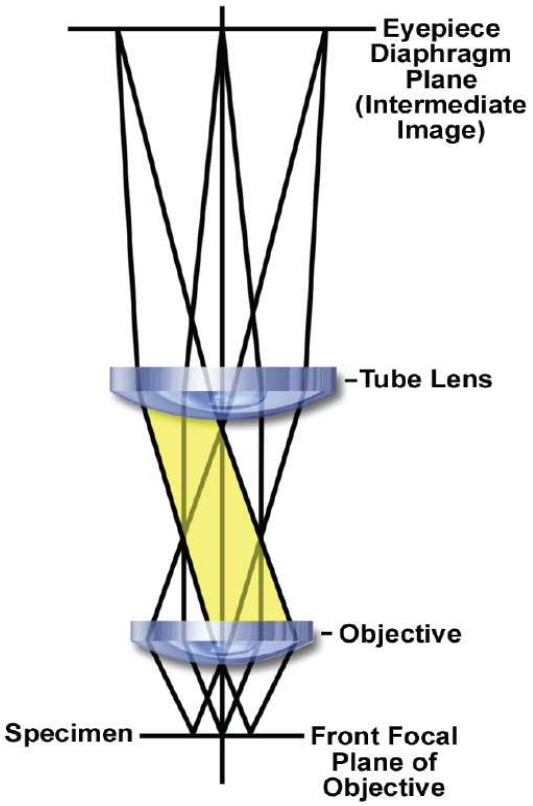

Figure 4.2: Diagram of an infinite tube length compound microscope. Image from [141].

can be accomplished by moving the objective only.

The total magnification of the system is the product of the magnifications of the objective, the tube lens and the eyepiece. Each magnification is defined as the ratio of image to object size at a given distance (see Figure 4.1) and standards are present for single lenses and objectives [141, 143].

The magnification is not the parameter which finally determines the ability to observe features of a certain size. In fact to do so, we need to *resolve* the features. The resolving power r of a microscope is given by the minimum distance between two objects which are seen as separate. The main factors which determine r are light diffraction and refraction.

Figure 4.3 (top) shows a diagram of the light going from the specimen to the objective. If only air is present between the cover glass and the objective, the travelling light experiences a difference in refractive index n and it is therefore deflected; since $n_{\text{air}} < n_{\text{glass}}$, according to Snell's law, the exit angle will be larger and therefore only a fraction of the light will be collected by the objective. If we now insert between the

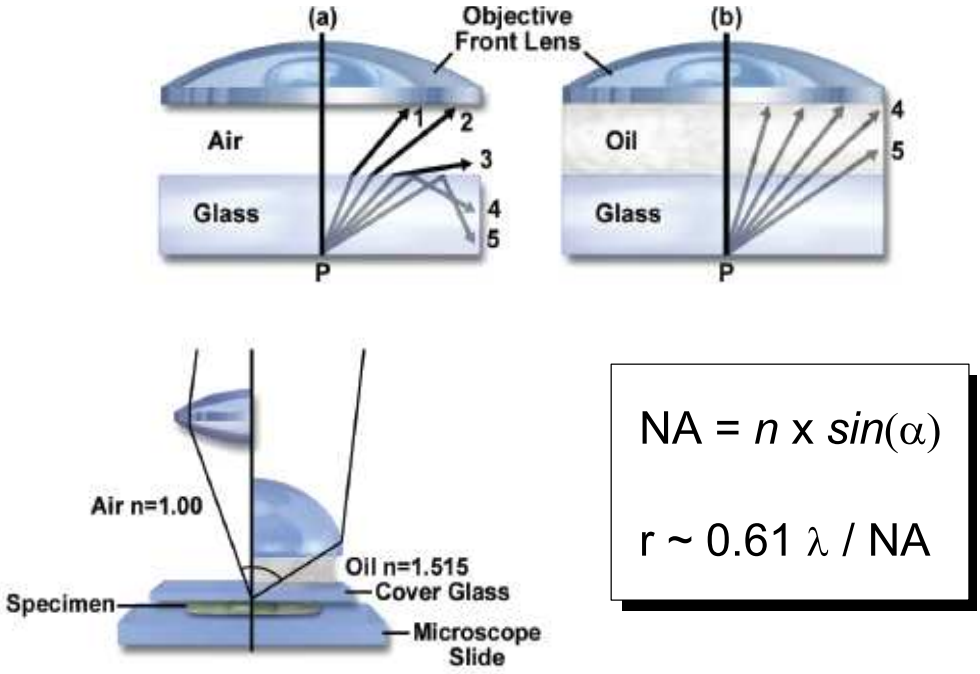

Figure 4.3: Effect of immersion oil on the numerical aperture (NA) of the objective and thus on the resolving power r. α is the angle between the cone of light and the optical axis. Image from [141].

cover slide and the objective some immersion oil which matches the refractive index of the glass ($n_{\text{oil}} \simeq 1.515$), we observe that refraction is eliminated and a larger cone of light can be collected by the objective. We define the numerical aperture (NA) as:

$$\text{NA} = n \times \sin(\alpha),$$

where n is the refractive index of the medium between the cover glass and the objective and α is the angle of the cone of light with the optical axis. We then note that by using immersion oil we can achieve larger numerical apertures.

The resolution of any optical instrument is also limited by diffraction. We know that a point-like object imaged through a circular aperture produces a diffraction pattern known as *point spread function* [144]; its projection on the focal plane of a lens is known as the *Airy pattern* and is reported in Figure 4.4 (a) an (b). Two objects close to each other will produce an intensity distribution given by the superposition of the two point spread functions and we are able to resolve them on the image plane if their diffraction patterns are sufficiently far apart.

This is known as the *Rayleigh criterion* and it states that two objects can be resolved if the maximum of the Airy pattern of one object falls at a distance equal or larger to

the position of the first minimum in the Airy pattern of the other object (see Figure 4.4 (c) and (d)). For lateral resolution this yields [139, 145]:

$$r = \frac{0.616\lambda}{\mathrm{NA}},$$

where λ is the wavelength of the incoherent illuminating light. This translates into limits of 200 nm for most commercially available optical microscopes.

A similar expression can be found for the axial resolution [140]; various authors have come up with slightly different criteria, but all of the form:

$$r_{\mathrm{axial}} \propto \frac{n\lambda}{\mathrm{NA}^2}.$$

The axial resolution is lower (typically 500 nm) due to the shape of the point spread function [146, 145].

We observe then that the resolving power can be improved by using objectives with larger numerical apertures and by using light of shorter wavelength. We shall see that both axial and lateral resolutions can be improved by using a laser scanning confocal microscope.

Köhler illumination

There exists an optimal configuration of a microscope called Köhler illumination. This set up guarantees sharp images and uniform illumination of the specimen even if the light source is not homogeneous. Figure 4.5 shows a diagram of the illuminating and the imaging rays in Köhler illumination.

Starting from the illuminating rays, we observe that the condenser directs a uniform patch of light onto the specimen; this light is then focussed onto the back (rear) focal plane of the objective and, passing through the eyepiece, is subsequently refocussed on a lens (camera or eye lens) which gives an even illumination on the observation plane (retina or film plane).

Let us consider now the the image-forming light path. The illumination of the specimen is uniform and the light coming from the sample is focussed on the front focal plane of the microscope objective which then produces an intermediate image onto the eyepiece plane (see Figure 4.2). Finally the eyepiece and the camera (eye) lens produce a focussed image of the specimen onto the observation plane. A description of the practical procedure to follow in order to correctly ensure Köhler illumination can be found for instance in [142].

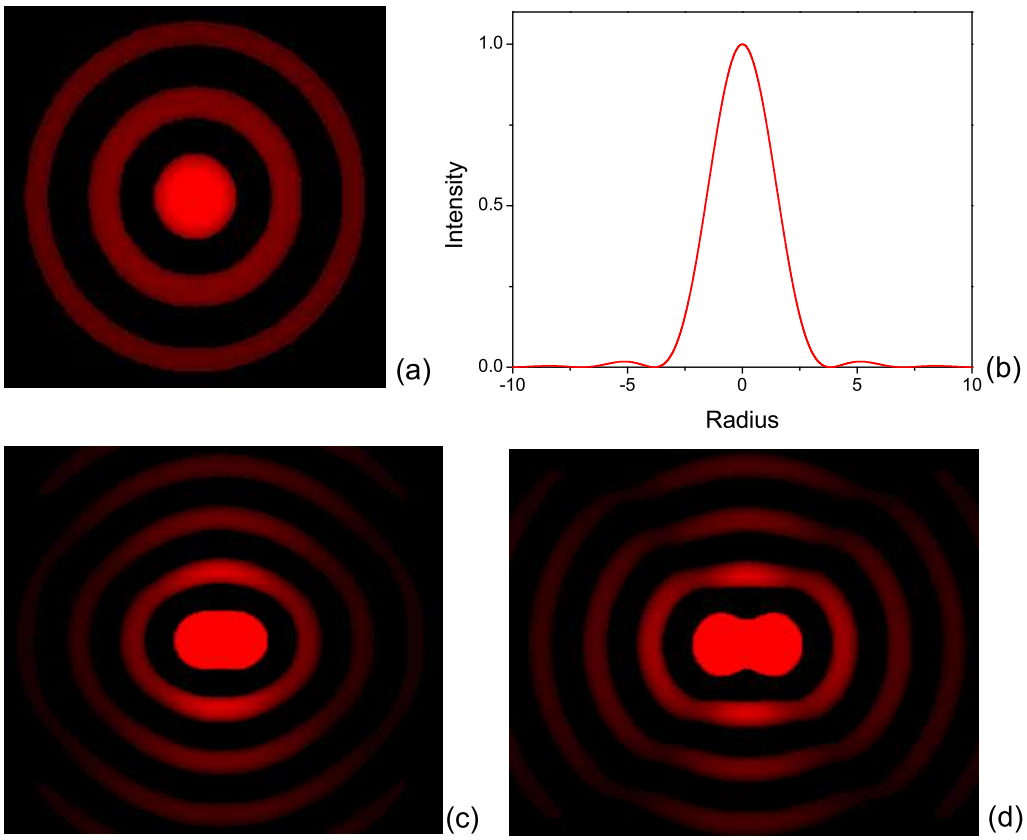

Figure 4.4: (a) Airy pattern for a single point. (b) Normalized intensity of the Airy pattern on across a diametrical section in the focal plane. Diffraction patterns of two objects not fulfilling the Rayleigh criterion (c) and of two objects which do (d). The brightness of the secondary rings has been artificially increased to make them more clearly visible

Comments

Summarizing, we have briefly discussed the basic elements of conventional optical microscopy highlighting the limits in the resolving power. By the use of large numerical aperture, oil immersion objectives and by ensuring Köhler illumination, optical microscopy can produce images able to resolve sub-micron features. A main drawback of the technique though is the limited thickness of the observable volume due to the presence of noise induced by stray and background light. The specimen is uniformly illuminated and therefore a large background illumination is collected. Moreover the system is not able to discriminate effectively the light coming from out of focus planes. When working with dense colloidal suspensions the light scattered by the particles surrounding the imaged volume also enters the objective contributing to the noise in the image. This can be limited by index-matching the suspension but this

operation has the drawback of strongly reducing the contrast in the image and more sophisticated microscopy techniques are needed [142].

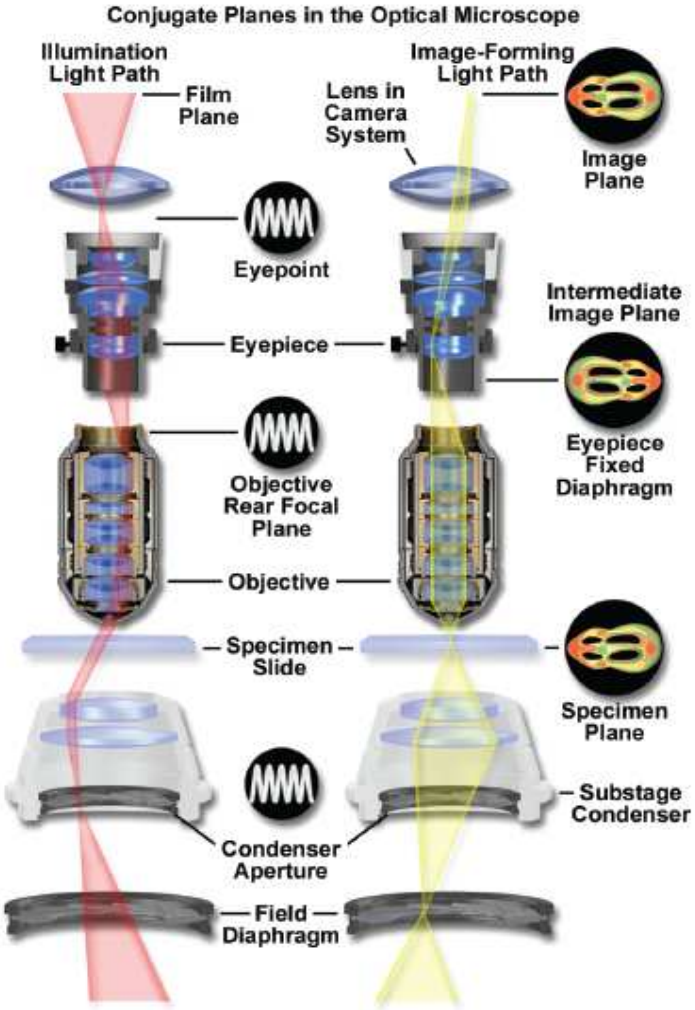

Figure 4.5: Ray diagram of the Köhler illumination set up. Image from [141]

4.2.2 Fluorescence microscopy

The problem of background illumination can be resolved with the use of *fluorescence microscopy*.

The specimen is tagged with a fluorophore, a molecule which absorbs radiation at a given wavelength, becomes excited and after losing some energy non-radiatively, emits light at a longer wavelength. By filtering out the unwanted excitation light, only the emitted fluorescent radiation is captured.

Figure 4.6 shows a diagram of a conventional fluorescence microscope. The light

coming from the illuminating source is shone on a dichromatic or 'dichroic' mirror which has the property of transmitting light above a certain wavelength and reflecting it below. The dichroic mirror in the microscope is selected to transmit the fluorescent light emitted by the specimen but to reflect the illuminating light. The light source can either be monochromatic or not and be successively filtered by an excitation filter which selects only light of the frequency needed to excite the fluorophores. Once the light hits the sample, the fluorescent molecules absorb it and emit at a lower frequency. The emitted fluorescent light is focussed by the objective in an analogous fashion to a conventional microscope, it is transmitted through the dichroic mirror and finally imaged onto the image plane.

Despite eliminating background illumination, a conventional fluorescence microscope collects the fluorescent light coming from all the illuminated volume in the specimen within the objective's numerical aperture. This includes stray light from out of focus planes which decreases the signal to noise ratio; in order to reject out of focus light a confocal set up is needed as described in the next section.

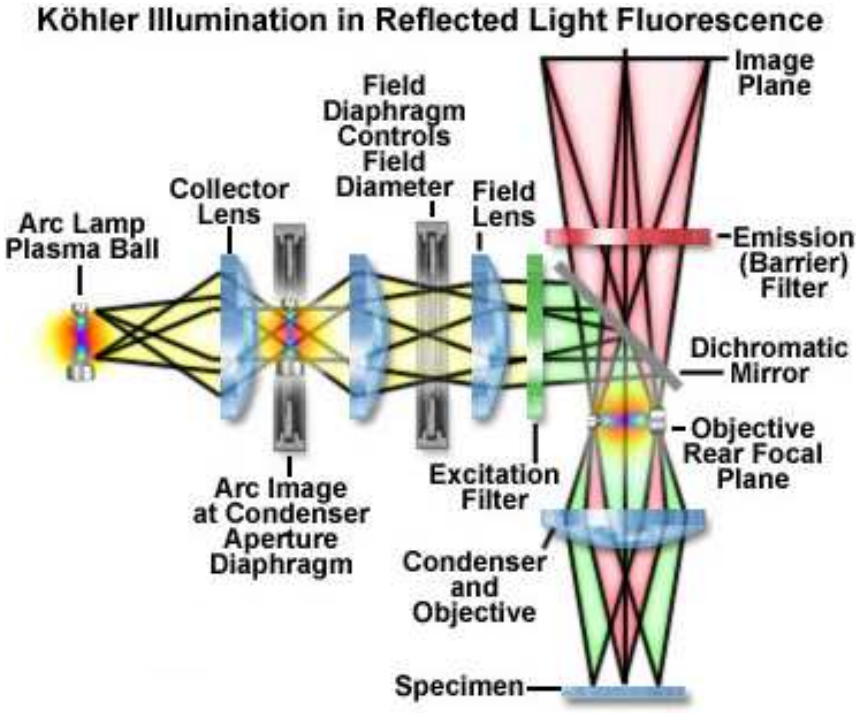

Figure 4.6: Diagram of a conventional fluorescence microscope. Image from [147]

4.3 Confocal microscopy

This section gives an overview of the basic principles of confocal microscopy together with a discussion on resolution and image acquisition rates in relation to colloidal science. Finally we present a brief comment on recent advances (multi-photon microscopy).

Confocal microscopy has now become a well–established method of studying the dynamical and structural properties of colloidal systems. The key advance consists in the possibility of imaging deep in the sample and, through image analysis procedures described in the next section, of obtaining the coordinates of the particle centres in each image and then tracking them frame by frame. Compared to light scattering techniques, local information is available, making confocal microscopy suitable for studying heterogeneous processes. Compared to the conventional optical and fluorescence counterparts, a confocal microscope has a better resolution but moreover has an optical sectioning capability; only light coming from a given focal plane is collected at any one time, making confocal microscopy an excellent technique to scan deep into the specimen and reconstruct three-dimensional images. Recent advances made it even possible to 'lock' the image onto a given feature and thus follow its three-dimensional motion and growth [148].

For a mathematical description of confocal imaging refer to [144] while for references on the principles and on the applications consult [149]. Additionally, a very comprehensive introduction to confocal microscopy which contains a large number of very useful technical and practical details can be found in [145, 147]. Finally we recommend an excellent recent review on the application of confocal microscopy to colloidal science which offers a variety of interesting discussion points [150] and that will be used as a base for the following discussion together with [151].

4.3.1 Principles of confocal microscopy

The birth of confocal microscopy originates from the desire to reduce the amount of scattered light coming from portions in the imaged sample which are not of interest.

The solution to this problem was devised in the 50s by Minsky [152] while working on imaging of samples of biological interest. He built an instrument where light was only shone on a small spot of the sample and the signal was collected by a detector sitting behind a screen with a pinhole (point-like detector). By moving the sample under the point illumination, he was able to reconstruct a full image of the specimen. By placing a screen with a pinhole in front of the detector, it was possible to discriminate the light coming from out of focus planes. His instrument was patented in 1955, but only a few decades later confocal microscopy became a widely used experimental technique,

thanks to the advances in the computing power necessary to elaborate and process the images.

Since the original, the design has improved and Figure 4.7 shows a schematic diagram of the workings of a modern laser scanning confocal microscope (LSCM). Laser light (light blue line) is shone on a dichroic mirror which reflects it along the optical path. The incident beam is then scanned across the sample by a pair of mirrors, passes through the microscope objective and excites the fluorescent specimen. The emitted fluorescent light (green line) returns along the same optical path but passes through the dichroic mirror and before reaching the photomultiplier tube is filtered by a pinhole. By construction, the aperture in front of the detector sits on the conjugate focal plane (hence the name confocal) of the illuminated spot in the sample. Figure 4.8 shows the mechanism by virtue of which out of focus rays are rejected. We can observe in the ray diagram that only light coming from the focus of the objective is successfully refocussed through the pinhole and therefore detected, while light coming from planes at different depths is only marginally transmitted through the aperture. It is this ability of the instrument to discard background light known as *optical sectioning* which makes it extremely convenient to scan dense systems and obtain sharp images.

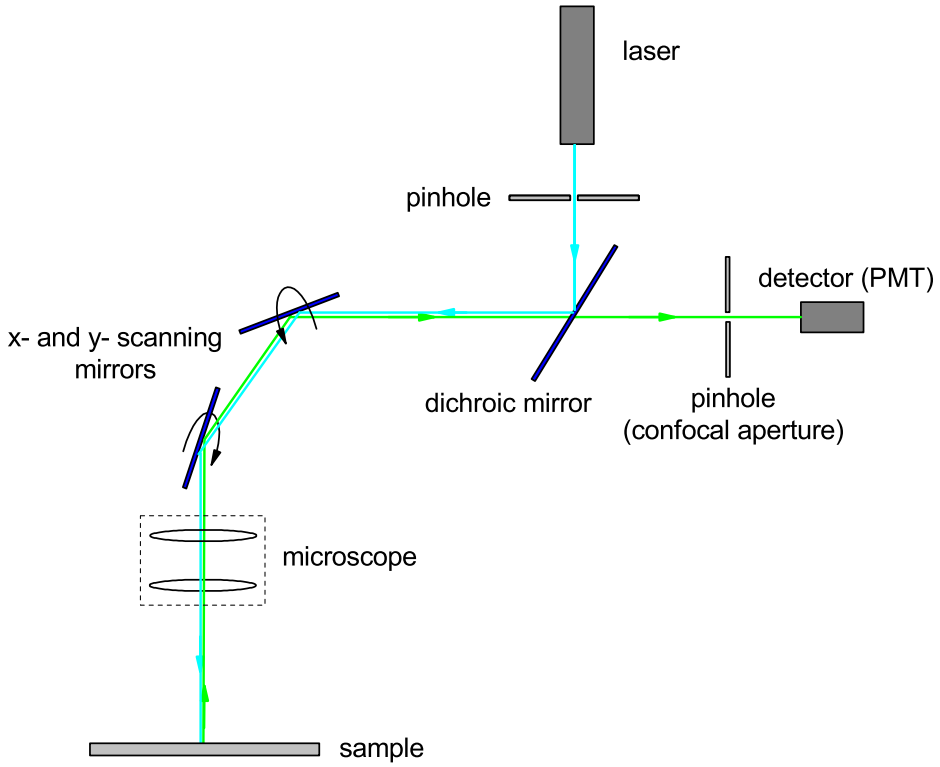

Figure 4.7: Diagram of a laser scanning confocal microscope highlighting the main components. The illuminating (light blue) and emitted (green) beams are displayed.

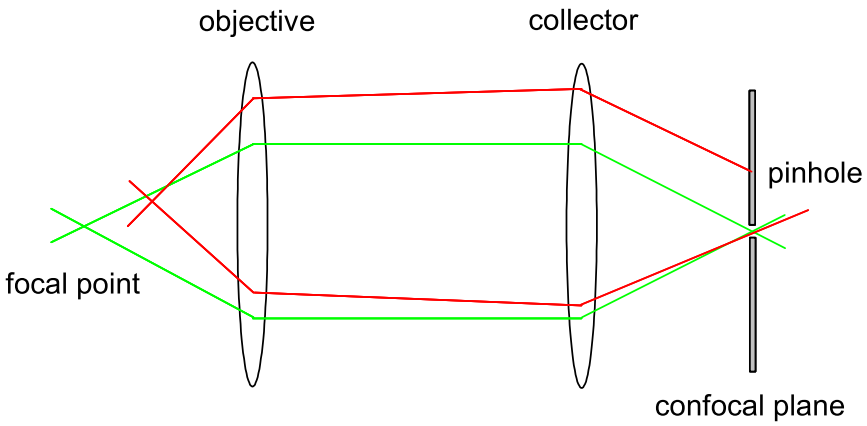

Figure 4.8: Schematics of the principle of out-of-focus light rejection. Only the light coming from the objective focus (green) is successfully passed through the pinhole aperture in front of the detector, while rays coming from other planes are screened (red).

4.3.2 Resolution

It can be shown that for a LSCM the resolution can be improved beyond the value discussed earlier for a conventional optical microscope. We observe from Figure 4.8 that the image on the confocal plane is obtained by exploiting the resolving power of both the objective and the collector. The point spread function on the confocal plane is therefore the product of the point spread functions of each lens, which, in the configuration reported in Figure 4.7, are identical. For a complete explanation and mathematical details please refer to [146, 149], we point out here that the lateral and axial extent of the point spread function are reduced by about 30% [145] [2].

We recall though that confocal microscopy gives higher quality images mainly not for its better resolution but rather for its optical sectioning capability.

In practice, the size of the confocal pinhole is matched to the size of the Airy disc in the confocal plane; a smaller aperture will reduce the transmitted intensity leading to a loss of information and larger pinholes will allow greater amounts of out-of-focus light to be detected. A detailed description of the optimal pinhole size which maximizes the intensity and minimizes the noise to signal ratio can be found in [147].

We then recall that our images are digitized and composed by $n \times m$ pixels; since the resolution of the instrument is governed by its optical properties and by diffraction,

[2] The single lens point spread function is $\propto \left(\frac{J_1(r)}{r}\right)^2$ where J_1 is a first order Bessel function of the first kind and r is the radial coordinate on the confocal plane. As a result of the confocal configuration the point spread function is squared and becomes therefore sharper.

it is pointless to sample the image with a spatial frequency higher than the spatial resolution. The magnification and the image size can be adjusted to optimize image sampling.

Finally we remark on the difference between resolution and accuracy in determining the position of features in the image. We shall describe in Appendix A algorithms which allow us to locate the centre of an object in a confocal image with an accuracy larger than the spatial resolution of the microscope.

4.3.3 Image acquisition rate

The main instrumental limit for a LSCM is the rate at which images can be acquired. The laser beam is scanned across the specimen by two scanning mirrors. The actual process of scanning proceeds as follows: one mirror positions the beam at a given x (or y) and then the other one scans the beam along the line, after completing the line scan, the first mirror displaces the beam and the second one scans a second line. The process carries on until the whole field of view has been scanned and then it starts again. The number of complete scans in the unit time is called the *frame rate*. The frame rate depends on the image size and on the method used for moving the scanning mirrors. The basic construction employs galvanometers whose operation frequency is limited to a few kilohertz. It is easy to see that to scan an image of 512×512 pixels with a rate comparable to video rate (30 Hz) requires a scanning frequency of $30{\times}512 \times 512 \approx 8$MHz, much lager than the capability of galvanometers.

Different solutions have been devised to solve this problem and we name three of them here: acousto-optic deflectors (AODs), spinning (Nipkow) discs and scanning arrays.

AODs are crystals which act as diffraction gratings. By sending a standing sound wave at radio-frequency across the crystal we change the local index of refraction creating a grating which deflects laser beams passing through the crystal. By changing the frequency of the sound wave we change the diffraction angle and we are therefore able to perform extremely rapid scans. The main problem associated with AODs is that the diffraction grating deflects light of different wavelengths by different angles and therefore obstructs the fluorescent light travelling back along the optical path. This inconvenience is partly resolved by combining one AOD with one galvanometer. The galvanometer positions the beam on a line which is then rapidly scanned by the AOD. Instead of a pinhole, the light is detected through a slit. This reduces the effectiveness in rejecting out-of-focus light and slightly distorts the image. This practical solution is the one used in the confocal microscope used in this thesis, a Visitech VtEye. We measured that the y pixel size is 5 to 10% larger than the x one (see Chapter 5), but

nonetheless the system is able to give good quality images and reach frame rates larger than 100 s^{-1} for images of 512 $\times$ 512 pixels.

Another technique which improves the scanning speed even further is the use of a spinning (Nipkow) disc [149]. This solution operates by shining laser light through an array of pinholes printed onto a spinning disc and thus achieving the scanning of the sample during the disc's revolution. To increase the scanning speed and reduce the size of the discs, the pinholes are arranged in such a way that laser light passes through several of them at the same time. Spinning discs can achieve full scanning of the field of view by fractions of a revolution and therefore yield frame rates of hundreds of Hz. Disadvantages of this method lie in the fact that the pinhole spacing on the disc is calibrated only for $\times$ 100 oil immersion objectives and that the light goes through many pinholes at the same time increasing the background intensity and giving lower quality images.

Another very recent solution consists in scanning the sample with a two-dimensional array of pinholes instead of a single one achieving a much higher speed. An expanded laser beam passes through a mask of pinholes, and the resulting array of beam spots is scanned across the image using galvanometers. This method ensures high frame rates but has the disadvantage of requiring high laser powers in order to guarantee a sufficient illuminating intensity. Alignment and synchronization of the collection (de-scanning) of the fluorescent light also present technical challenges.

The minimum necessary acquisition rate is set by the motion of the colloidal particles. The Brownian time for a colloid of diameter $\bar{D} = 500$ nm is ≈ 70 ms (see Chapter 2). In order to accurately track the particle during its diffusive motion we need an acquisition rate larger than $1/0.07$ s ≈ 15 Hz which is easily obtained by our set up. In the presence of shear, particles may undergo larger displacements; higher frame rates are required together with more sophisticated image analysis procedures to successfully track the colloids.

4.3.4 Multiphoton

A recent development of confocal microscopy is that of multi-photon microscopy [153]. This technique employs the fluorescence coming from processes of absorbing two or more photons in a single event. The probability of these processes is very low and therefore they take place only where the intensity of the laser beam is sufficiently high. Using ultra-short pulses of strongly collimated high power lasers, the intensity is high enough to give a sufficient probability of absorbing more than one photon only in the proximity of the beam waist. This fact removes the need of a pinhole in front of the detector to ensure optical sectioning as the emitted fluorescent light comes only from

the focussed beam spot. Multi-photon microscopy is widely used in imaging biological systems as the time exposure to laser light is limited and therefore less damage is caused to the specimen; for a review refer to [154].

4.4 Particle identification and tracking

This section presents a detailed description of the procedure used to track fluorescent particles in sequences of confocal images. The procedure can be divided into three basics steps. Firstly the raw images are processed to suppress noise and to enhance the contrast between the features and the background. Secondly the centre of each feature is located (pre-tracking) and finally the coordinates of particle centres are merged into their trajectories which will be used for further analysis. The details of image processing and pre-tracking are given in Appendix A, while we focus here only on the last step. In the case of suspensions subjected to strong shear or flow fields, an additional step is required before tracking. The advective motion needs to be removed in order to make particle tracking possible in a comoving frame. We discuss here the details of an advection removal algorithm able to deal with non-uniform shear flows which we devised in collaboration with Eric Weeks [126]. Finally we comment on the errors arising from particle tracking.

The procedure used for finding and tracking the particles in our confocal images is based on the initial work of Crocker and Grier [155] and on successive refinements by Weeks. The following discussion is based upon the work of these authors. Three main assumptions are needed. The features must appear as bright objects on a dark background and we assume that they are spherical in shape and that the maximum in the brightness of a feature corresponds to its centre.

The concepts at the basis of the features location are still applicable to objects which do not meet these requirements but the practical algorithm for locating them will be different.

All the data in this thesis, unless specified differently, refer to *the location and tracking of particles in two-dimensional slices of three-dimensional samples*. The concepts and methods described here for the 2D case can be extended to the 3D case. For a detailed treatment of three-dimensional data refer to [146].

We recall that the images we discuss here refer to colloidal suspensions flowing into glass capillaries. The magnification and the size of the field of view have been calibrated to image the full cross section of the channel. The presence of particles in the image is therefore limited in the transverse (y) direction by the size of the channel and in the flow direction (x) by the size of the image itself. This statement does not affect the locating algorithm but we shall see that the experiment geometry plays an important

role in the motion removal procedure.

All the software used to analyse and process the data and the images has been written in the IDL language.

4.4.1 Tracking the particles

Once the coordinates of the centres have been found in each frame, we need a procedure to merge them into trajectories describing the particle motion in the xy image plane. This procedure goes under the name of *tracking* and involves labelling each particle with an identification tag and looking for particles in the following frame that can be assigned the same tag.

Colloidal particles are indistinguishable and we can only be reasonably confident that the identification works correctly if the average displacement of the particles between two successive frames is sufficiently small. In practice the assumption which makes the procedure work for dense systems is that the frame by frame displacements are less than a particle diameter. A first requirement is thus to use a sufficiently high frame rate in the image acquisition so that the frame by frame displacements are below the limit stated above. We shall see in the next section that by performing additional image analysis we are indeed also able to track particles which move more than their diameter between two successive frames.

The algorithm devised by Crocker and Grier to track the particles is motivated by the dynamics of non-interacting colloidal systems. Given the position of a particle in a frame and all the possible new positions within a certain range in the following frame, the algorithm considers all possible identifications of the old position with the new ones, and chooses that identification which results in the minimal squared displacement.

As a consequence of Brownian dynamics the probability that a colloidal particle diffuses a distance Δr in the plane over the time τ is

$$P(\Delta r \mid \tau) \propto \exp\left(-\frac{\Delta r^2}{4D\tau}\right),$$

where D is the free diffusion constant of the particle.

For an assembly of N non-interacting colloids the probability is the product of the single particle distributions:

$$P(\Delta r_i \mid \tau) \propto \exp\left(-\sum_{i=1}^{N} \frac{\Delta r_i^2}{4D\tau}\right),$$

and the most likely particle identification is the one which minimizes the total mean

squared displacement $\sum_{i=1}^{N} \Delta r_i^2$. Introducing a tracking range we limit the combinatorics to all those displacements for which Δr_i is smaller than the tracking range.

The procedure just described was tested by Crocker and Grier [155] on self-diffusion of dilute colloidal suspensions and has since been proved successful in a variety of studies of quiescent colloidal systems; for an extensive list of references refer again to [150]. Only recently the interest in colloidal science has moved towards driven systems, where the colloids are subjected to the drive from an external field. In particular we are interested in the application of confocal microscopy to the study of colloidal systems under shear. Results on confocal imaging in a counter-rotating cone-plate rheometer [156], in a parallel plates shear cell [44] and in capillary flow [157] have recently been published.

Shear or flow can increase the particle displacements between two subsequent frames above the tracking range and therefore lead to problems in correctly identifying the particles. For our experiments in particular, given the geometry and the flow field, the particles undergo much larger displacements in the flow direction x than in the transverse one y.

Tracking the particles in our flow field presents non-trivial challenges; Figure 4.9 shows an example of this.

Part (a) shows a histogram of the frame by frame displacements in the x (flow) and y (transverse) direction for a typical flow experiment. We notice that the y histogram decays nicely within the tracking boundaries (i.e. the identified y displacements are limited and inside the tracking range) but the one in the x direction is ill behaved. Due to the flow, the particles are moving too far to be tracked successfully and many of them move out of the tracking range. The y displacement histogram is therefore also not to be trusted; many of the transverse displacements are obtained from incorrect identification although the overall distribution appears reasonable. In order to perform the tracking effectively, we need to find a way to remove the advective motion and follow the particles in a co–moving frame, so that also the x displacements are limited.

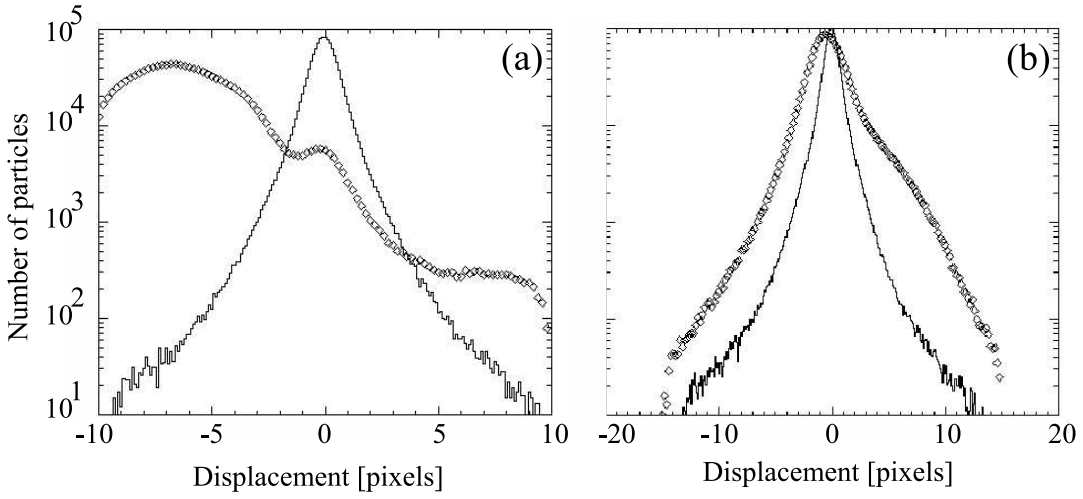

Figure 4.9: Histograms of x ($\Diamond$) and y (–) displacements after 8000 frames for a typical experiment in the laboratory reference frame before (a) and in the the co–moving reference frame after (b) the advection removal procedure. The y displacements are always smaller as the flow is along x. The histograms show the number of particles which centre moves a certain number of pixels within two consecutive frames.

4.4.2 Advective motion removal

The procedure that we developed is based on the correlation between two consecutive images. Let $I_1(x, y)$ and $I_2(x, y)$ be the intensity patterns at position (x, y) in the first and the second image. Image 2 is shifted back by a certain number of pixels $(\Delta x, \Delta y)$ and the correlation coefficient

$$c = \frac{cov[I_1(x,y)I_2(x-\Delta x, y-\Delta y)]}{\sqrt{var[I_1(x,y)]var[I_2(x,y)]}} \tag{4.1}$$

is computed for each shift within a desired range and this procedure is repeated for different $(\Delta x, \Delta y)$, until c is maximized (Figure 4.10) [3]. The values of the frame by frame shifts $(\Delta x(t), \Delta y(t))$ are then subtracted from the particles coordinates in order to have them in a time dependent co–moving reference frame.

The geometry of our experiments has further consequences for the implementation

[3]The covariance of two digital images I_1 and I_2 made of N pixels is defined as $cov = \frac{1}{N-1}\sum_{i=1}^{N}(I_1^i - \langle I_1\rangle)(I_2^i - \langle I_2\rangle)$, where I_1^i and I_2^i are the intensities of the i-th pixel in each image and $\langle I_1\rangle$ and $\langle I_2\rangle$ are the respective average intensities. Analogously the variance of a single image I is $var = \frac{1}{N-1}\sum_{i=1}^{N}(I^i - \langle I\rangle)^2$.

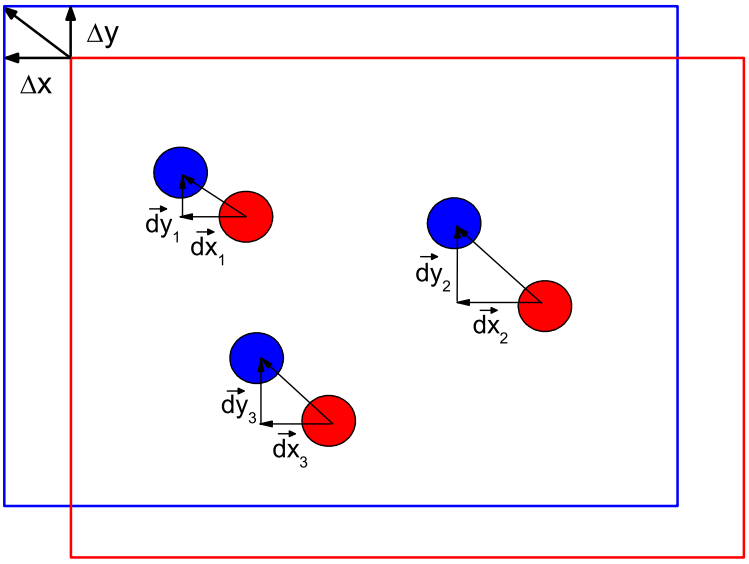

Figure 4.10: View of the shifting/correlation procedure. Each particle is displaced by a given (dx_i, dy_i) between frame 1 and frame 2. The whole image is shifted by a $(\Delta x, \Delta y)$ which maximizes the correlation between the two successive images.

of this method. Firstly, the flow is exclusively in the x direction, so only horizontal shifts are considered. Secondly, the procedure cannot be performed straight away on the whole images because the flow velocity varies with y, i.e. the flow profile is not uniform and so maximizing the correlation only relates to an average motion. However, this problem can be overcome if we examine the positions of the particles inside the capillary as obtained by the pre–tracking. We will note from Figure A.3 that the particles are arranged in remarkably well–defined horizontal layers. The presence of layering makes the image correlation much easier despite the y–dependent flow profile. The images can now be divided into y–bins corresponding to layers and the correlation procedure can be run separately on each of them (Figure 4.11); within each layer the value of c is averaged over x and y. Once all the values of the displacements for the different y–bins have been obtained, they are merged together to create a velocity profile to be subtracted from the particle coordinates to have them in a y–dependent co–moving frame of reference. This image correlation procedure is however not able to eliminate completely the advective motion, especially in the central part of the capillary where the layering is not as defined as at the edges. A second advection removal is therefore necessary, but because now the main non–uniformity has already been cancelled, removing an averaged flow proves to be effective enough. By tracking the particles after the non–uniform advection removal we can compute the average of the frame by frame displacements. Subtracting this from the previously corrected coordinates we obtain thus a new set of values in a

truly co–moving reference frame. Figure 4.9 (b) shows the histograms of the x and y displacements in the co–moving reference frame obtained when performing the tracking after the two–steps advection removal procedure described above. We now notice that the x histogram falls well within the tracking range. Finally, adding the total motion back to the coordinates allows us to move back to the laboratory frame of reference and to study the flow following each particle's trajectory.

The method was tested on $\simeq 30\%$ volume fraction suspensions in two-dimensional channels yielding the expected parabolic flow profiles (refer to Section 7.1.5 and to [126]). With this procedure we have been able to successfully track particles in flows with velocity as high as 250μm/s corresponding to frame by frame displacements larger that the average particle diameter.

The non-uniform advection removal can also be extended to three-dimensional simple shear flows; images of xy slices at different depths z are correlated to obtain a z-dependent advection profile to be subtracted from the particle coordinates. The shifts at the different depths can be interpolated to remove successfully the advective motion of particles whose centres lie between the imaged xy planes [44].

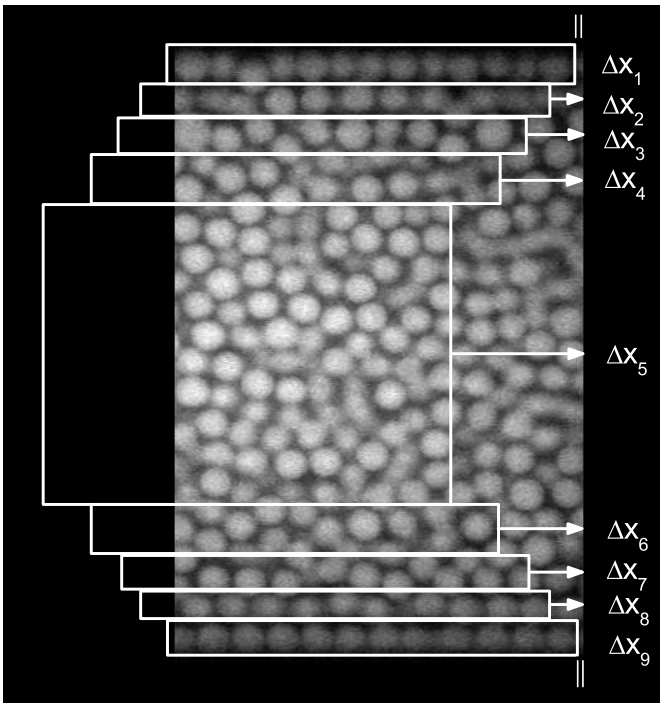

Figure 4.11: View of the non–uniform advection removal procedure. The images are divided in y–bins corresponding to particle layers and the shift/correlation procedure is run separately on each of them producing an array of displacements Δx_i to be subtracted to the particle coordinates.

4.4.3 Comments on tracking errors

Particle location and tracking with the procedure discussed above is a rather well-established task and, as recalled previously, has lead to notable advances in the understanding of colloidal science. Moreover advective motion removal algorithms make it possible to extend conventional tracking to shear and flow experiments where the simple, traditional approach failed.

Despite the robustness of the algorithm we will show that the centroiding procedure intrinsically carries errors when applied to the analysis of dense systems. In the case where extraordinarily detailed information on the particle locations is needed, these errors can become crucial. Matthew Jenkins [146] has thoroughly investigated the inaccuracies introduced by the centroiding procedure and has devised a more accurate way of locating the particle centres. His algorithm is based on mapping the intensity profiles of the particles with the "model" intensity distribution of a colloidal particle. This approach has proved effective in further refining the pre-tracking but is computationally expensive and time consuming. Based on the following reasoning, we believe that the errors introduced by the centroiding procedure do not strongly affect our analysis.

Firstly, a refinement to the centroiding procedure becomes necessary if it is needed to resolve the motion of particles with an accuracy much better than the pixel digitization of the image; this can, for instance, be the case with the analysis of the distributions of particle displacements in a strongly jammed system where the average motion of each particle is extremely small. This is not the case for our experiments, where we instead have the opposite problem: particles tend to move too much between frames. In the cases where the average particle motion between successive frames is well below one pixel, we calculate the displacements using a larger time interval so that the relative error becomes smaller. Moreover the bridging between neighbouring particles, described in Appendix A, happens with no preferential direction on an xy plane; we calculate the velocity in different regions of the channel by averaging the displacements of all the particles in that region and therefore we tend to average out the errors induced by the erroneous location of the single particles. Finally, we recall that we work with two-dimensional slices of three-dimensional systems, therefore the size of the imaged objects depends on where the image plane cuts across them and so the mapping of each feature with the model intensity distribution will have to take that into account. The refined algorithm was conceived to work with three-dimensional images.

Additional sources of errors can arise from the presence of flow. Xu et al. [158] have analysed in detail the errors coming from digital image analysis of the shear flow of dry grains and the effects they have on the measured velocity of the particles. The points

relevant to our experiments involve the errors caused by finite size of the pixels, the inability of tracking fast moving objects and the occurrence of interparticle collisions between frames. In our previous discussion we have already addressed the first two, while the third remains an intrinsic problem. The only solution to this which does not involve the use of very sophisticated algorithms which interpolate the speed of every particle between two successive frame to check for the likelihood of collisions, is increasing the frame rate. We shall see in Chapter 7 that we are able to fully reconstruct the motion of the particles in our experiments and detect the presence of collisions; moreover we shall also see that interparticle contacts will play a major role in determining the dynamics of the flow.

Chapter 5

Materials and Methods

In the previous chapters we have introduced the fundamentals of colloidal systems and of their flow behaviour. We have also discussed the principles of confocal microscopy and of particle tracking as means of obtaining quantitative information of the structure and the dynamics of colloids. In this chapter we focus on the specific systems, the experimental set ups and the methods used to obtain the results presented in this thesis.

We initially characterize the colloidal particles used and then discuss the preparation of samples. Details on the procedures followed to obtain index and buoyancy matching are presented and we also stress the different behaviour of the system in different solvents comparing with the theoretical hard-spheres system. We then move to the description of the methods used for calculating the volume fraction of the suspensions discussing the pros and cons of each one. We finally present the experimental set up giving an account of a typical experimental run together with an accurate description of the different components.

5.1 The system

The colloidal systems used in this work are all composed by suspensions of nearly monodisperse poly-methyl-methacrylate (PMMA) spheres sterically-stabilized by the grafting of a layer of short polymer chains onto their surface. We mentioned in Chapter 2 that, in a good solvent, the polymer chains stretch out and stabilize the colloids against aggregation; the colloidal particles effectively interact as hard spheres. Depending on the solvent, the PMMA particles can also acquire charges which soften the interaction potential; the charges can be screened by adding a salt to the suspension re-establishing hard-spheres repulsion.

5.1.1 The particles and the solvents

The particles used in this work have been prepared in Edinburgh (School of Physics) by Dr. Andrew B. Schofield. They consist of poly–methyl–methacrylate (PMMA) spheres (the batch we used in this thesis is named ASM 286 [1]) sterically-stabilized by chemically-grafting poly–12–hydroxy stearic acid (PHSA) onto their surface (see Figure 5.1 for a schematic representation). The particles are also dyed with a fluorophore (NBD, 4 chloro–7 nitrobenz–2 oxa 1,3 diazole) which absorbs radiation at 488 nm and emits fluorescent light at 525 nm.

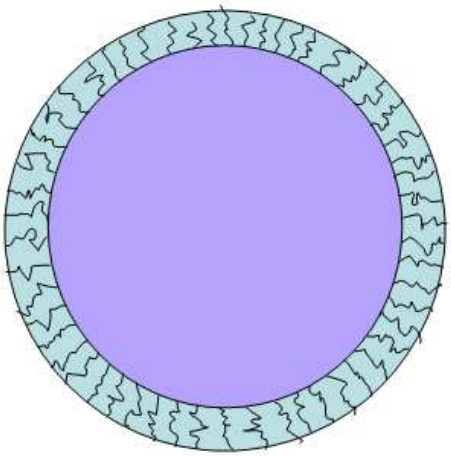

Figure 5.1: Schematic representation of a sterically-stabilized colloid highlighting the presence of the polymer layer.

The colloids were prepared following a procedure based on the original recipe reported in [159] where information on the synthesis of the PMMA spheres and of the PHSA are described together with an account of the sterical stabilization.

Fluorescent dyes or fluorophores must be incorporated in the particles to perform confocal microscopy. The procedure followed by Dr. Andrew B. Schofield is based on [160] where a small percentage of the initial methyl–methacrylate monomers is substituted by the NBD dye; during the polymerization process which leads to the formation of the PMMA spheres, the NBD molecules are chemically bonded to the particles. Fluorescent PMMA produced according to this procedure maintains the hard-sphere character of the interactions also when different types of fluorophores are used [161]. On the contrary, other methods which for instance incorporate the dye

[1]The author of this thesis, with his head full of classical studies, initially thought that the nomenclature ASM stood for *Andrew Schofield Made it* in analogy with the signature often found on many ancient Roman artefacts *Titius Caius Fecit* indicating the name of the author (Titius Caius being the Latin equivalent of John Smith) who made them (fecit). Only later he had to face the prosaic reality that ASM meant *Andrew Schofield Methacrylate*!

at a later stage in pre-formed particles [162], have been shown to induce charges and therefore introduce a softer repulsion and may also lead to dye leakage over time.

The choice of the solvent plays an important role in determining the interparticle interactions and can be chosen to ensure that the particles interact as hard spheres. Thus the solvent has to be a poor solvent for PMMA, in order to limit the swelling of the particles, but is required to be a good solvent for the PHSA so that the polymer chains stretch out. If two particles come in close contacts, the repulsive energy given by the superposition of the two polymer layers rapidly increases with decreasing distance [163].

The particles are initially prepared in dodecane. This solvent ensures hard-sphere interactions [164] but is not suitable for microscopy or light scattering observations given the large refractive index mismatch with PMMA ($n_{\text{dodecane}} \simeq 1.42$, $n_{\text{PMMA}} \simeq 1.5$) which makes the suspensions look too turbid. An alternative solvent which maintains hard-spheres interactions is decahydronaphtalene (decalin) [164]; decalin exists in two different chemical structures: *cis*– and *trans*–decalin. The pure structures and a mixture of the two are available commercially (Sigma–Aldrich). Decalin has a higher refractive index ($n_{\text{decalin}} \simeq 1.48$) but not sufficiently to give a complete index-matching. *cis*–decalin is frequently used in light scattering experiments [130, 135] while either decalin [165] or dodecane [14] can be used for rheological measurements. Given the relatively large amounts of samples used in this thesis and the high cost of pure *cis*–decalin, we used *mixed*–decalin instead.

In order to perform optical measurements (e.g. microscopy) the index-matching with decalin may not be sufficient; this can be substantially improved by mixing decalin with tetrahydronaphtalene (tetralin) ($n_{\text{tetralin}} \simeq 1.54$). Particles in decalin-tetralin mixtures interact as hard-spheres [166] but have been found to swell over long periods of time. Additionally, the index-matching changes with swelling and needs to be periodically adjusted. Also, tetralin and decalin evaporate with different rates and therefore the composition of the suspension slowly changes with time. Finally tetralin photo-degrades over months.

The bulk density of PMMA ($\rho_{\text{PMMA}} = 1.188\text{g/cm}^3$) is larger than the density of both mixed-decalin and tetralin and therefore particles suspended in these solvents sediment. The actual density of the PMMA particles can vary from batch to batch but we will assume in the rests of the discussion that is not too different from the bulk value.

We can quickly estimate the effects of sedimentation for our particles by calculating the gravitational force F_{g} acting on a single particle given by the buoyant mass (m_{b}) times gravitational acceleration (g).

$$F_{\mathrm{g}} = m_{\mathrm{b}} g = (\rho_{\mathrm{p}} - \rho_{\mathrm{s}}) \frac{\pi \bar{D}^3}{6} g, \tag{5.1}$$

where $(\rho_{\mathrm{p}} - \rho_{\mathrm{s}})$ is the difference between the density of the particle and the solvent and $\bar{D}$ is the particle diameter. A particle falling in a fluid also experiences viscous drag. In the limit of dilute systems (which ours are not but we assume this for simplicity) the viscous drag F_{v} is

$$F_{\mathrm{v}} = 3\pi\eta\bar{D}v_{\mathrm{s}}, \tag{5.2}$$

where η is the solvent's dynamic viscosity and v_{s} is the sedimentation velocity. By equating 5.1 to 5.2 we obtain:

$$v_{\mathrm{s}} = \frac{(\rho_{\mathrm{p}} - \rho_{\mathrm{s}})\bar{D}^2 g}{18\eta}. \tag{5.3}$$

Substituting the values for our PMMA particles and mixed-decalin ($\bar{D} = 2.6\mu$m and $\eta \simeq 0.002$ Pa s) we obtain a sedimentation velocity of $\approx 0.5\mu$m/s, meaning that a particle sediments over a distance equal to its diameter in 5 s. The effect plays therefore an important role but can be strongly reduced by density-matching the suspension.

In order to density-match the suspension, mixed-decalin needs to be mixed with a solvent of density higher than the one of PMMA; the choice is to use cyclo–heptyl–bromide (CHB). CHB also has a refractive index closer to PMMA so by performing the density-matching we are also partially index-matching the solution.

A summary of the properties of the solvents described above can be found in Table 5.1.

5.1.2 Sample preparation

As previously mentioned, the particles are suspended in dodecane after the synthesis. In order to prepare suspensions of given volume fractions for our confocal microscopy experiments we need to proceed through a few preparation steps.

Solvent washing

As mentioned earlier, dodecane has much lower refractive index and density than PMMA and therefore we need to transfer the particles into another more suitable solvent: decalin. This task is accomplished by repeatedly "washing" the suspension in decalin. Thanks to the density difference, particles can be separated by centrifugation. By centrifuging a vial containing the suspension at 3000 rpm for a few hours, we obtain a dense sediment surmounted by clear solvent (supernatant) which we pour away and

replace with mixed–decalin. By repeating this procedure we reduce the amount of dodecane with every wash. A satisfactory degree of purification is achieved with seven to ten washes. The purity of the final suspension can be checked by measuring the refractive index of the supernatant and by comparing it with the one of pure mixed-decalin. The accuracy of the refractometer allows us to declare the washing completed when the refractive index is within 0.1% of n_{decalin}.

Solvent	Refractive index n at 20°	Density ρ[g/cm^3] at 25°
PMMA	$\simeq 1.50$	1.188
cis–decalin	1.4800	0.897
trans–decalin	1.469	0.870
mixed–decalin	1.4725	0.881
Tetralin	1.5410	0.973
CHB	1.5050	1.289
Dodecane	1.4220	0.750

Table 5.1: Physical properties of interest of PMMA and the solvents used.

Index matching

The index-matching is achieved by adding small amounts of tetralin to the suspension until it becomes highly transparent. For the case of the particles ASM 286 used in this thesis we measured a refractive index at room temperature of the index-matched suspension of $n_{\text{susp}} = 1.5015 \pm 0.0005$.

We can easily calculate the volume fraction of tetralin Φ_{tetr} in the index-matched system by recalling that the refractive index of the suspension n_{susp} is

$$n_{\text{susp}} = n_{\text{tetr}}\Phi_{\text{tetr}} + n_{\text{dec}}(1 - \Phi_{\text{tetr}}), \tag{5.4}$$

and therefore

$$\Phi_{\text{tetr}} = \frac{n_{\text{susp}} - n_{\text{dec}}}{n_{\text{tetr}} - n_{\text{dec}}} = 0.43 \tag{5.5}$$

which corresponds to a 0.455 mass fraction.

Buoyancy matching

In order to avoid sedimentation during the experiments we need to achieve density-matching (or buoyancy-matching) between the particles and the solvent. We will see in Chapter 7 that the model we use to describe our data also neglects the presence of gravity.

The buoyancy-matching is achieved adding cyclo–heptyl–bromide (CHB) to the mixed-decalin according to the indications found in the literature [167]. The use of other solvents as cyclo–hexyl–bromide leads to analogous results [168].

The buoyancy-matching is very sensitive to temperature changes; the thermal expansivity of the solvent is about ten times larger than the one of PMMA and therefore a decalin-CHB mixture of a given composition will appropriately match the density of the particles only in a very narrow temperature range [169]. Previous work on similar systems [29] reported a mass ratio of 4:1 between CHB and mixed-decalin to achieve buoyancy-matching. By taking this composition as a starting point for our suspension, we found the exact buoyancy-matching point by successively centrifuging at 6000 rpm at 20°C in a temperature controlled centrifuge; if after a few hours the particles had sedimented to the bottom of the vial, we added some extra CHB, if they were sitting at the top of the vial (creaming), it meant that the density of the solvent was too high and so more decalin was required. By adding small amounts of either CHB or decalin according to the need, we were able to tune the density of the solvent so that after spinning the suspension at 20°C at 6000 rpm overnight we did not see any appreciable sedimentation or creaming.

We kept track of the added amounts of the two solvents and obtained for our suspension a final mass ratio of CHB to decalin of 3.24 which amounts to mass fraction of 76.4% and 23.6% for CHB and mixed-decalin respectively. This numbers are also consistent with the ones reported in other studies [170]. We also double-checked the values obtained by weighing the different solvent top ups by measuring the refractive index of the final, buoyancy-matched suspension $n_{\mathrm{susp}} = 1.494$. Analogous considerations to Equation 5.4 yielded a volume fraction of CHB of 68.3% corresponding to a mass fraction of 76.9%, extremely close to the number reported above.

It has been reported in the literature [167] that the addition of CHB to a hard-spheres suspension induces a positive charge in the particles resulting in a softer interaction potentials. It is possible to screen such charge by adding a suitable amount of salt (see Chapter 2). Following the procedure reported by Yethiraj and van Blaaderen, this can be achieved by using tetrabutylammonium chloride (TBAC,$(C_4H_9)_4NCl$, $M_W = 277.92$g/mol, Fluka). They reported that a concentration of 1 mg/ml of TBAC had been sufficient to screen the charges in their system enough to

reproduce the liquid-crystal phase boundary for hard-spheres interaction. The Debye screening length at such salt concentrations becomes comparable to the length of the stabilizing polymer layer ($\approx$ 10 nm) eliminating long-range Coulombic repulsion. The effectiveness of the screening has been proved by other studies on similar systems using the same concentration of TBAC [29, 146]. Despite this, the outcome of the charge screening seems to be strongly system-dependent; recent studies in the group of van Blaaderen have also shown that by adding the same amount of TBAC, other suspensions exhibited a negative charge instead [171] with a batch-dependent charge inversion point. The specific effect of CHB and of the screening salt on our system will be reported in the next section. The appearance of surface charges on PMMA spheres either induced by solvent or dyes and their screening, has proved to be an effective way of tuning interparticles potentials and it has lead to interesting results relative for instance to the formation of colloidal crystals of oppositely charged particles [170, 172]. Another factor which can finally influence the presence of charges in density-matched suspensions is the degradation of CHB by light [173]. To minimize these effects the samples were stored in the dark at 4°C.

5.1.3 The particles in the different solvents

We chose to test the behaviour of our PMMA particles in three different solvents: an index-matching decalin-tetralin mixture and CHB-decalin mixtures with and without the screening salt TBAC.

In order to perform this analysis we measured the 3D radial distribution functions ($g(r)$) of the particles suspended in the solvents for different values of the suspensions' volume fractions. Recalling the discussion of $g(r)$ reported in Chapter 2), we remind the reader that, in the case of pure hard-spheres interactions, the position of the first peak of $g(r)$ is volume fraction independent and it accounts for the interparticle separation at contact and it can therefore be used as measure of the particle size. A change in the position of the first peak of the radial distribution function shows the presence of soft, long-range repulsion which modifies the "effective" particle size. For charged systems, the position of the first peak of $g(r)$ increases with decreasing Φ. At low volume fractions Coulombic repulsion inhibits colloids from coming close to each other resulting in an effectively larger particle size; when the colloids are "squeezed together" at higher densities, repulsion is limited by the locally available space, resulting in a smaller effective size. At random closed packing particles are in direct contact and the interparticle separation reaches a minimum independent of the presence of charge.

We performed the measurements in the following way. Fairly dilute suspensions were prepared in a custom-made sample cell consisting of a glass vial whose bottom

was previously chopped and then attached onto a square 22×22 mm microscope slide (Figure 5.2). The vial was glued onto the microslide by using UV-curing glue (Norland Optical Adesive) and exposing the glassware to UV light for at least an hour. The sample cell was successively mounted onto a wooden base and inserted into a moulded polystyrene foam holder. The whole object was then inserted into a metal centrifuge tube and the sample was centrifuged at 2000 rpm for several hours. The close fitting of the wooden base and the foam padding ensured that the sample cell was protected during centrifugation. Since the centrifugation was performed at a temperature higher than the density-matching one, the particles sedimented. The construction of the sample cell made possible to perform confocal microscopy measurements directly after centrifugation, without the need of transferring the sample to another cell and thus disturbing it. This allowed us to collect confocal images of the undisturbed sediment (after pouring the supernatant away) and so to measure the radial distribution function of a random-closed-packed system (see Chapter 2). In this configuration the particles are "squeezed" as tightly as possible and therefore we expect the first peak of $g(r)$ to give an accurate measure of the interparticle separation irrespective of the interparticle interactions. Successively adding solvent, we diluted the suspensions in the same sample cells and performed the confocal imaging again.

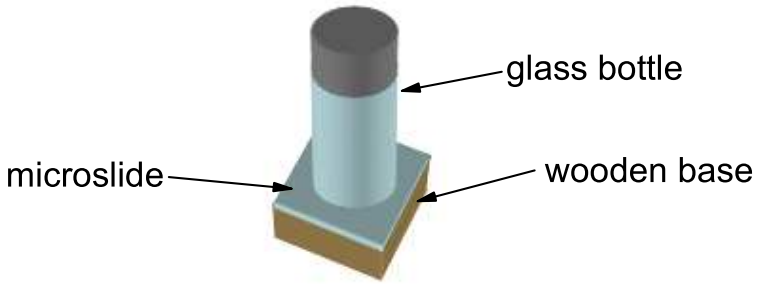

Figure 5.2: Sample cell. Once the centrifugation is completed, the wooden base is removed and the cell is directly placed onto the confocal microscope stage where the suspension is imaged from below.

Stacks of 101 images of 256×256 pixels (57×61μm, see Section 5.2.2 for details) were collected at a frequency of 90 frames per second, scanning the system in steps of 300 nm. 20 stacks were recorded in one location (10 scanning upwards and 10 scanning downwards) and the operation was repeated for five different locations in the sample to obtain good averages. The image stacks were collected at least 20μm deep in the sample in order to avoid effects induced by the proximity of the microscope slide (we shall see in the results chapters that the presence of a flat surface induces layering in the particles and therefore affects the measure of the local radial distribution function).

The confocal images were processed according to the procedure described in Appendix A and the particle centres were located. In order to achieve a higher accuracy the procedure devised by Jenkins [146] was used to additionally refine the particle coordinates. From the latter the three-dimensional radial distribution functions were constructed and are here reported in the following figures.

Figure 5.3 reports the radial distribution functions for three sediments, respectively in index-matching (decalin-tetralin) and density-matching (decalin-CHB) solvents in the presence or the absence of the screening salt (TBAC). We note that the three curves practically overlap regardless of the presence of surface charges. In particular the position of the first peak of $g(r)$ is almost identical in the three cases suggesting that the particles have come in contact and that the former is a good indication of the actual particle diameter. The slight differences can be addressed to small swelling in tetralin and to image quality issues. A higher quality $g(r)$ is obtained in the fully index-matched system (sharper and higher first peak), while the low r tails in the density-matched cases move the position of the first peak towards smaller values. From the figure a value of the average particle diameter $\bar{D} = 2.6 \pm 0.1 \mu$m has been extracted and will be used in the rest of this thesis.

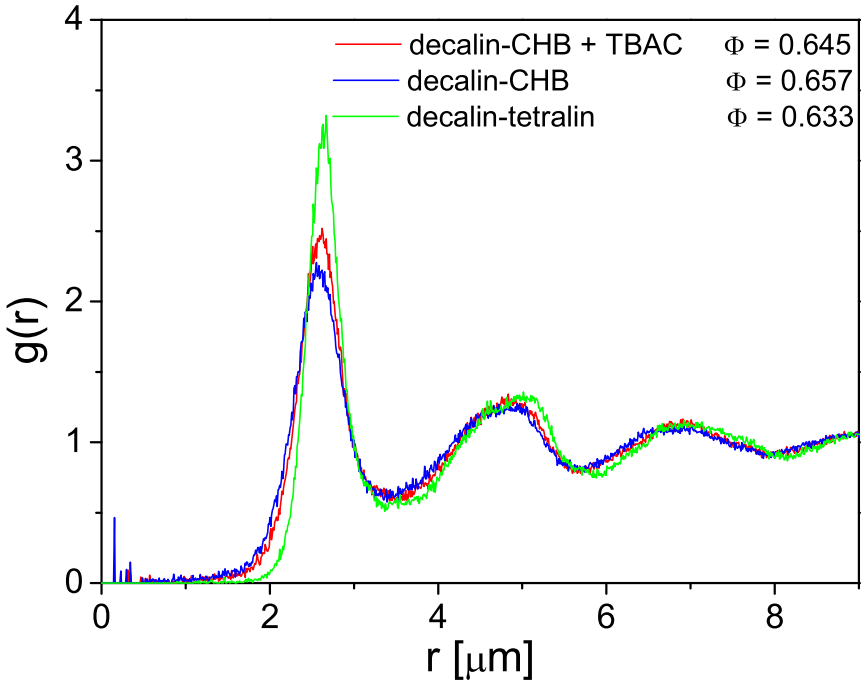

Figure 5.3: Radial distribution functions for sediments in index-matching (decalin-tetralin) and density-matching (decalin-CHB) solvents with or without the screening salt (TBAC). Note the different volume fractions.

In order to check if the charge has been effectively screened we also performed the measurement of $g(r)$ in the density-matched case with and without 1 mg/ml of TBAC. Contrary to what reported by other authors [167, 29] we see that *the charges have not been fully screened*. Figure 5.4 reports the radial distribution functions in the presence (top) and in the absence (bottom) of salt for three dilutions. We note that in both cases the position of the first peak of $g(r)$ moves as Φ changes showing the effects of long-range repulsion. The solid vertical lines mark the position of the first peak for the unscreened system; in the densest case (sediment), analogously to what reported above, the positions of the peak for the two cases coincide and are equal to the particle diameter. As the volume fraction is reduced the peaks move towards larger distances but the shift is more pronounced in the unscreened case; reducing Φ even further leaves the position of the first peak of the screened system's $g(r)$ unchanged, while in the unscreened case the curve keeps shifting to larger values. The variations with the behaviour previously reported can either be due to differences in the particles or in the method used to check the charge screening. A small residual charge in fact may not be detected by pinpointing the liquid-crystal phase boundary if the effective particle size is comparable to the interparticle distance at that given volume fraction.

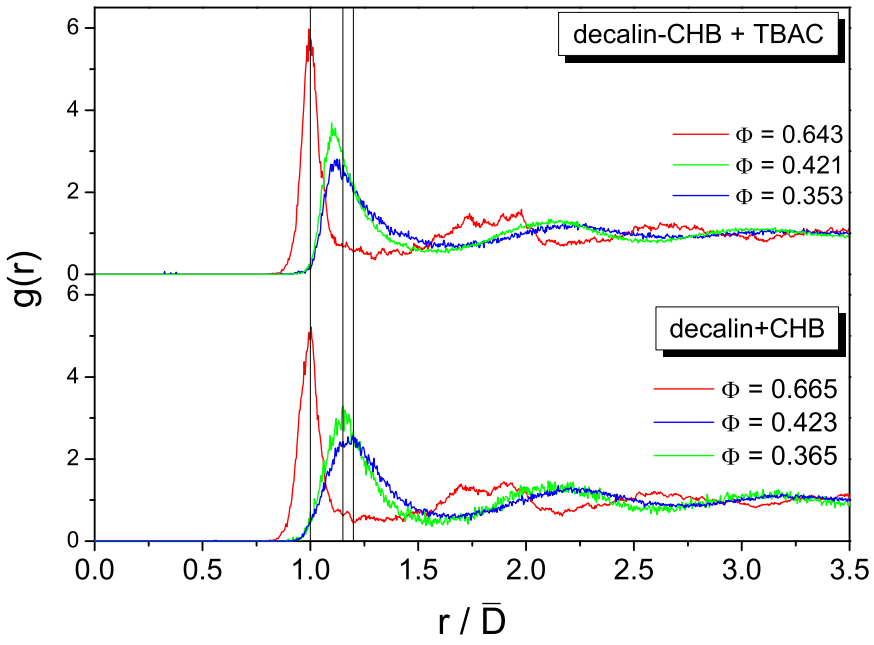

Figure 5.4: Radial distribution functions for suspensions of three volume fractions in the presence (top) and in the absence of screening salt TBAC (bottom). The vertical solid lines mark the positions of the first peak of $g(r)$ in the unscreened case.

Returning now to Figure 5.3, we can offer an interpretation on the reason behind the difference in the volume fractions of the three sediments. In the decalin-tetralin case the particles behave as hard spheres; as they come into contact sedimenting in the centrifuge, we expect them to *jam* against each other due to the surface roughness induced by the stabilizing polymer coating. In the density-matching solvent, particles are charged and therefore start to repel before coming into contact and so manage to "avoid each other" during sedimentation. As a result, sediments of charged systems are slightly more compacted than uncharged ones, where particles jams create a more holey structure. The trend for our suspensions proceeds in the right order with increasing volume fraction from the decalin-tetralin to the partially screened and to the fully unscreened density-matching system. In one of the first studies of colloidal systems by confocal microscopy, van Blaaderen and Wiltzius [174] reported a volume fraction of 0.64 for a sediment obtained by centrifuging suspensions of nearly monodisperse charge-stabilized silica particles. The particle charge was sufficiently screened to correctly find the hard-spheres liquid-solid phase boundaries but nonetheless "a double layer very small relative to the radius" was still present affecting particle contacts during sedimentation. Another study by Pusey and van Megen [25] found a volume fraction "close to the value expected for the random close-packed hard-sphere glass" in "nearly hard-sphere" sediments obtained by "low-speed centrifugation", remarking again the relevance of the roles played by the details of the interparticle interactions and of sample preparation. Finally we report the results of a simulation of pressure-driven flows of non-Brownian particles where the non-uniform shear profiles induce particle migration towards the channel centre [70]; the inclusion of short-range repulsive forces between the particles lead to the result that "the particle concentration at the centre is greater than when no interparticle force is present". In the absence of repulsive interactions "persistent particle clusters" are formed and impede "the extent of particle migration". In our case slightly larger volume fractions are found due to larger polydispersity and bigger inaccuracy in determining the particle radius.

In this thesis *we always use density-matched samples without the addition of the screening salt*. This choice was initially dictated by practicality given the relatively small quantity of ASM 286 particles. Once the TBAC is in solution it is not clear if and how it is possible to remove it while it can always be added at a later stage. For this reason we initially performed the measurements without its addition. Moreover, we discovered later that for our particles the addition of 1 mg/ml of TBAC did not actually fully eliminate charge effects. Given also that for the highest volume fraction, the suspensions with and without the screening salt show an identical radial distribution function and that the initial measurements we performed were indeed done on sediments, the attempt of screening the charge did not seem essential at the time

and we therefore opted for the simplest system. Later measurements at lower volume fractions were then done on the same system for consistency. An additional reassurance on the scarce influence of charge in our experiments comes from the analysis of the role played by volume fraction in ion dissociation (see Section 2.2). As the volume fraction of the suspension increases, the 'free volume' available for the dissociated ions is progressively reduced, making it increasingly less favourable for them to dissociate from the particle surfaces and therefore effectively reducing the charge; this confirms the negligible role played by the screening salt at the highest Φ [175]. Moreover, for $\Phi > 20\%$, the surface charge of the suspended particles depends weakly on volume fraction [175] and therefore we do not expect strong variations in the behaviour within our Φ range (0.43 to 0.635). A careful investigation of the role played by surface charge in our results is an interesting point for future work.

5.1.4 Volume fraction

We have seen in Chapter 2 that volume fraction is the fundamental parameter which regulates the behaviour of suspensions of hard spheres. It is therefore of great practical interest to determine Φ in the most accurate way possible. We discuss here the various approaches that can be used presenting their pros and cons and highlight the procedure that we followed in our experiments.

Phase diagram

A first way of approaching the problem of preparing suspensions of known volume fraction relies on the use of the phase diagram for hard spheres. As seen in Chapter 2, a suspension of colloidal hard spheres undergoes a liquid-solid transition at a volume fraction of 0.494. For values of Φ between 0.494 and 0.545, liquid and crystalline phases coexist and from their ratio it is possible to pinpoint the suspension's volume fraction using the lever rule. This operation is achieved in the lab as follows. The suspensions are centrifuged at 3000 rpm for a few hours in order to get a sediment at the bottom of the sample holder (this is performed at a temperature higher than the buoyancy-matching temperature for density-matched suspensions). Based on the hard spheres phase diagram, we assume that the sediment is at random-close-packing, which for a collection of monodisperse hard spheres is at a volume fraction of 0.64. By eliminating the supernatant we are left with a suspension of "known" volume fraction. The sediment is then diluted into the liquid-crystal coexistence region and transferred into a thin capillary. If the particles have a low polydispersity, they rapidly crystallize and, given that the crystals have a higher density then the liquid, they sediment to the bottom of the capillary. Once the suspensions reaches equilibrium we can calculate the actual

volume fraction using the lever rule by measuring the height of the sedimented crystals and of the liquid. By repeating this procedure for several initial volume fractions we obtain a calibration curve which relates the initial volume fraction of the prepared suspension to the actual volume fraction of the system. Experience shows that a precise mapping is obtained by assuming that the volume fraction of the sediment is slightly larger than 0.64 accounting for some polydispersity.

This method is in principle extremely accurate (apart from experimental errors in measuring the height of the crystalline and liquid phases in the capillary) but it presents some practical inconveniences. The first problem is that in the case of rather large particles as the ones used in this work, they sediment in decalin before they can crystallize making the whole procedure futile. Conversely, an accurate buoyancy-matching, also nullifies it; if the liquid and the particles have a very close density, there is no density difference between the crystal and the liquid and therefore the crystallites do not sediment making impossible to measure the relative extension of the two phases. A second inconvenience comes from the presence of charges on the particle surface which can significantly move the phase boundary compared to the hard-spheres case. In this case a priori accurate knowledge of the phase behaviour of the specific system is required to build an appropriate calibration curve. An additional issue comes from the use of a thin capillary. A thin holder is needed in order to be able to shine light through the suspension and detect the presence of crystals, but it also means that the we are not looking at a bulk sample any longer, but at a system with a high surface to volume ratio. We will show in the results chapters that the presence of a wall induces crystallization (crystals can indeed be seen growing from the capillary walls) and therefore a high surface to volume ratio can alter the fraction of crystalline phase relative to the bulk.

One of the advantages of confocal microscopy is that the volume fraction of the suspension can be directly measured, therefore knowing it with high precision *before* the experiment is not extremely relevant. In our experiments we then prepare the suspensions assuming that the sediment is at 64% and then measure the *actual* volume fraction of the prepared suspension in the microscope. Relying on assuming the sediment's volume fraction does not yield the absolute value of Φ but determines the relative volume fractions between the suspensions and the sediment. This is based on the assumption that the sediments always are at the same volume fraction. Previous work [146] has instead shown that the volume fraction of a sediment depends for instance on the preparation procedure, e.g. on the sedimentation speed. We have also shown in Section 2.6 that centrifuging particles suspended in different solvents gives rise to differences in the Φ of the respective sediments. Therefore we have always followed the practice of directly measuring the volume fraction of the suspension before the flow

experiments. We will shortly discuss the method used to determine volume fractions from confocal images, but before that we briefly comment on another procedure based on drying and weighing.

Drying

Another means to prepare suspensions of known volume fraction consists in first determining the mass fraction of the suspension by weighing a droplet before and after all the solvent has been eliminated by completely drying it; the ratio of the droplet's mass before and after the drying gives the mass fraction. This straightforward method presents some complication for sterically-stabilized particles; in fact we recall that the stabilization is achieved by grafting a layer of polymer hairs onto the particle surface. The polymer brush has a negligible contribution to the particle's mass, but contributes to the effective volume of the particle in solution and therefore affects the determination of the volume fraction. By determining the volume fraction by drying and weighing we neglect this contribution. The thickness of the polymer layer in the solvent is of the order of 10–20 nm and therefore contributes to the 2–4% of the particle's volume for a 1.3 μm radius particle. Other authors [166, 29] have obtained conversion factors between the volume fractions obtained by drying and the actual volume fractions of the suspensions by calibrating the former against the phase diagram of hard-spheres. The reported conversion factors are

$$\Phi = 1.04 \text{ to } 1.06\Phi_w,$$

where Φ_w is the volume fraction determined by drying and weighing.

Experimental errors in weighing the suspensions lead to inaccuracy in the volume fraction determination, but can be reduced by repeating the measurements on a large number of droplets. In addition to this also a *systematic* error is introduced by assuming the length and density of the polymer layer when converting the mass fractions into volume fractions. This implies that some uncertainty arises (estimated in [29] to be 5%) in determining the absolute value of Φ but that the relative volume fractions can be trusted with a much larger accuracy.

Voronoi volume

Confocal microscopy offers an easy way to measure the volume fraction of suspensions of fluorescent particles. We recall that Φ is determined by the number of particles in the unit volume and therefore by counting the fluorescent colloids in the imaged volume V, we have direct access to the volume fraction:

$$\Phi = \frac{4}{3}\pi \left(\frac{\bar{D}}{2}\right)^3 \frac{N}{V}, \tag{5.6}$$

where $\bar{D}$ is the average particle's diameter and N is the number of particles in the imaged volume. This method gives an excellent estimate of the average volume fraction provided that all the particles in the volume are correctly identified; the location of the features can be optimized by tuning the pretracking parameters (see Appendix A) but in practice there is no way to determine if particles have been missed in the count.

A way to avoid this inconvenience is to determine the *local volume fraction around each particle* and calculate the bulk Φ by averaging the local ones. Provided that the sample is spatially homogeneous this method gives a very accurate measure. If one particle has been missed in the count, the local volume available to its neighbours will be anomalously large; we can then eliminate the bias induced by the missing particles by discarding those local volumes larger than a threshold value. Similarly, particles close to the edges of the image will also give errors in determining the local volumes and will be discarded as well.

An effective way of determining the local volume available to the particles is obtained via a procedure called the Voronoi construction. The Voronoi construction is a way of dividing the space around a assembly of points into a set of convex polygons (or polyhedra in more than two dimensions) which fill up all the available space (tessellation). An example of how to construct the Voronoi partition in two dimensions is reported in Figure 5.5. Starting from a set of points randomly distributed in space (green dots) we first construct the so called Delaunay triangulation (light blue lines) by joining each point with its nearest neighbours and obtaining a series of triangles which tessellate the space. We then trace the perpendicular bisectors of each of the segments in the Delaunay triangulation and extend them until they intersect. The points of intersection are the vertices of the Voronoi diagram (red dots) and the bisectors themselves (red lines) constitute the sides of convex polygons which in turns also tessellate the plane: the Voronoi cells. We observe in the figure that only one point (particle) is included in each Voronoi cell and the area of each cell represents the space available to each point. We also notice that some of the cells are bounded (thicker lines) and others are not; particles close to the edges of the images are not fully surrounded by neighbours and therefore the triangulation does not close around them yielding unbounded Voronoi cells. We can also observe that some of the bounded cells have a larger area (e.g. the last bounded cell on the right of Figure 5.5). This can be a consequence, as mentioned earlier, of the absence of neighbours in a given direction due to proximity to the image edges or due to a missed particle. The construction presented here can be easily extended in three (or more) dimensions. For mathematical

and computational details on Delaunay triangulations and Voronoi constructions refer to [176].

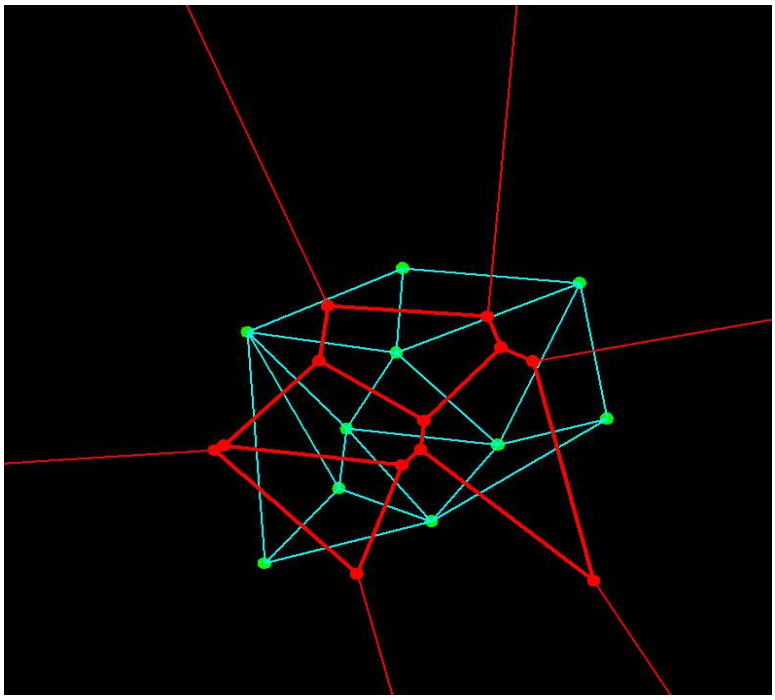

Figure 5.5: Example of Delaunay triangulation and Voronoi diagram. The green dots (●) are the positions of the centres of the particles and therefore also the vertices of the Delaunay triangulation (light blue). The red dots (●) are the vertices of the Voronoi cells. Thicker lines mark the bounded cells, while thinner ones delimit the unbounded ones.

In practice the construction of Delaunay triangulations and Voronoi diagrams is preformed by an IDL routine (used in producing the example figure) which returns the vertices of the Voronoi cells; once the vertices are known each cell can be decomposed in set of triangles (tetrahedra) and the area (volume) is calculated by adding up the area (volume) of all the triangles (tetrahedra) in the cell. We then obtain a distribution of the Voronoi volumes and we discard those contributions given by unbounded cells, particles close to the images' edges and missed particles.

This method yields very accurate measurements on the local volume available to the single particles but in order to determine the volume fraction we have to rely on the knowledge of the particle radius. We recall that we determined this quantity from the position of the first peak of $g(r)$ in the sediment; this value is subject to inaccuracy and will induce a systematic error in the volume fraction. We can estimate a relative error $\delta\bar{D}/\bar{D} \simeq 2\%$ and therefore a relative error in the volume fraction of $\delta\Phi/\Phi \sim 3\delta\bar{D}/\bar{D} \simeq 6\%$, remembering that $\Phi \propto \bar{D}^3$. This seems a rather large error but this

method gives extremely accurate relative volume fractions and therefore all the values can be easily rescaled if more accurate measures of the particle radius are available. The method also gives results in accordance with other analogous characterizations of similar systems [146, 44].

5.2 Experimental set-up

A schematic view of the experimental apparatus is shown in Figure 5.9. We report the details of its various components and of the calibration procedures. We initially describe the preparation of the sample cell and give an account of a typical experimental run; we then present some technical specifications of the confocal microscope and the laser. Details on the pressure sensor and on the acquisition of the pressure signal followed by a description of the glass capillaries conclude this section.

5.2.1 A typical experiment: sample cell preparation and flow

Figure 5.6 gives a schematic representation of a sample cell for flow experiments. The cell is assembled as follows: a glass capillary is initially glued onto a microscope coverslide with UV curing glue (Norland Optical Adesive) by exposing it to UV light for a few minutes; the glass capillary is generally longer than the standard microscope slides (50 $\times$ 22 mm) and therefore more than one slide is needed. The capillary is arranged so that one end pokes out of the glass substrate and will later be connected to a PVC tubing. Once the glass channel is attached to the coverslide(s), a glass vial (1.5 cm diameter) whose bottom was previously removed is glued onto the capillary and the coverslide(s) with UV curing glue (2 hours exposure) so that it includes the extremity of the capillary which is not protruding from the coverslide. The right part of the figure shows a schematic top view. Finally a thicker glass slide is glued on top of the uncovered part of the capillary to give more solidity to the whole construction, a PVC tube (1mm internal diameter) is connected to the free end of the capillary and the connection is sealed with epoxy glue. After all the connections and bonds are checked, the sample cell is ready to be positioned onto the microscope stage and used for the measurements. The bottom of the cell is in direct contact with the microscope objective via the immersion oil and the sample is therefore imaged from below.

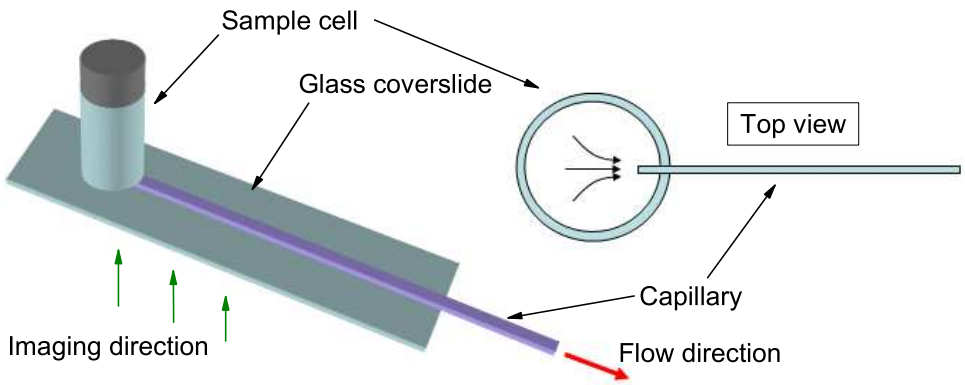

Figure 5.6: Schematic drawing and top view of the sample cell. The capillary, either with a square or rectangular cross section, is not drawn in scale. The construction on the left is placed on the microscope stage plate and the flow is imaged form below with the confocal microscope.

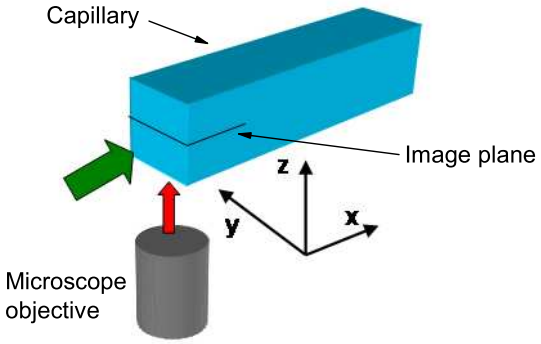

Figure 5.7: Schematic view of the experimental geometry. The glass coverslide, the sample cell and the microscope stage plate have been omitted from the drawing for clarity. The flow (green arrow) is imaged from below and two-dimensional xy slices are collected at a depth z. The the microscope objective can be translated by a piezoelectric motor, allowing the user to collect images at various depths. The microscope stage can also be translated relative to the microscope objective making it possible to collect images at different positions along the channel.

Figure 5.7 gives a schematic representation of the imaging geometry; for simplicity the bottom coverslide, the bottle and the microscope stage plate have been omitted from the drawing. The flow proceeds along the channel in the x direction; by adjusting the size of the confocal image we are able to simultaneously image the full transverse y cross section of the capillary. Two-dimensional xy slices are acquired at a depth z; by displacing the microscope objective with a piezoelectric motor, images at various depths can be collected and used for three-dimensional reconstructions. Finally a modified microscope stage plate is used; instead of the conventional circular aperture, a long rectangular slot allows us to translate the microscope objective along the x direction

and collect images at different positions along the channel (see Figure 5.8) .

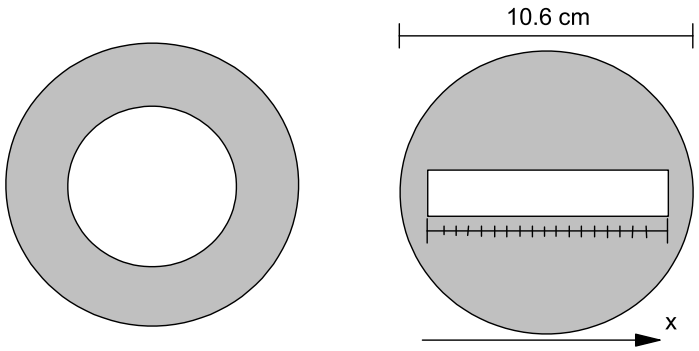

Figure 5.8: Drawings of microscope stage plates. On the left a conventional design with a circular aperture while on the right a modified one with a rectangular slot. The graded scale allows to keep track of the displacements.

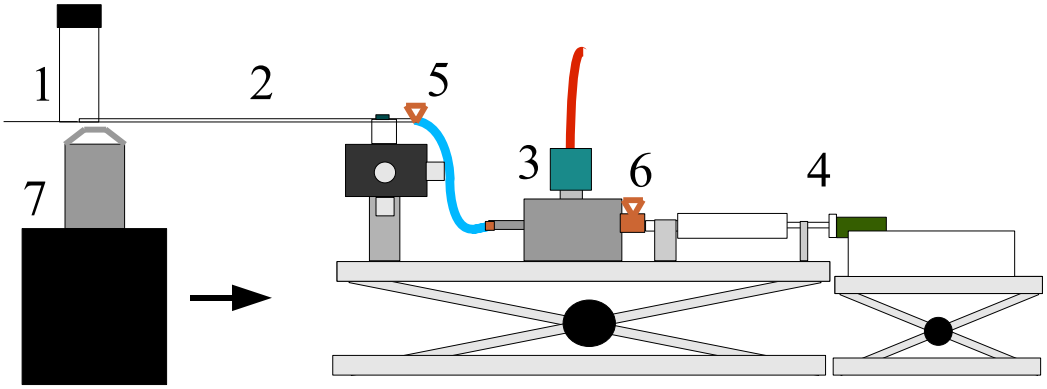

Figure 5.9: Experimental set-up. 1) Sample cell. 2) Capillary. 3) Pressure gauge. 4) Syringe and syringe motor. 5) and 6) Valves. 7) Microscope objective. The arrow highlights the relative displacement between the microscope objective and the capillary which allows the user to image different locations along the channel. The sample cell is resting on the microscope stage (not in the drawing).

A typical experimental run proceeds in the following way (refer to Figure 5.9 and Figure 5.10). The suspension to be sucked into the capillary (2), is first loaded into the sample cell (1) while the first valve (5) is closed; at this stage the capillary is full of air. By displacing the plunger of a syringe with a motor (4), the pressure of the air downstream from the valve (5) is reduced from atmospheric to P_0, building up an initial driving pressure $\Delta P_0 = P_{atm} - P_0$. The value of the downstream pressure is measured with a pressure gauge (3) (MKS Series 902 Piezo Transducer) through the acquisition of a voltage signal with an I/O card (NI PCI–6014) interfaced with a custom–written Labview program. At this stage the second valve (6) is closed to exclude the syringe volume from the measurement; the measuring volume V_0 is thus given by the sum of

the volumes of the pressure gauge, the tubing from (3) to (5) and of the capillary (2). When the first valve (5) is opened again, the suspension starts flowing into the glass capillary (2) and the pressure $P(t)$, in a measuring volume $V(t)$, is recorded at a sampling rate of 1000 Hz. Simultaneously the flow is imaged via the confocal scanner (Visitech VtEye) and a Nikon Eclipse TE300 inverted microscope.

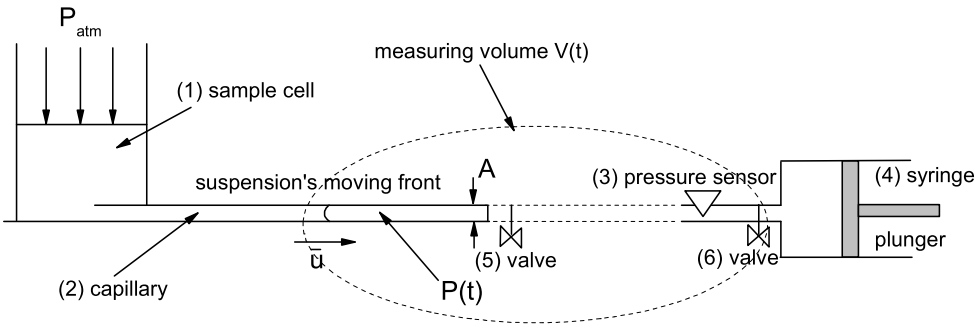

Figure 5.10: Schematic representation of the flow set-up. The front of the flowing suspension is highlighted.

During the flow the syringe plunger is kept at a fixed position. This means that as the suspension fills the channel the initial pressure difference is relaxed; in the case of our set-up the pressure variations during the flow are negligible compared to ΔP_0. In fact it can be shown that for a Newtonian fluid (details in Appendix B):

$$\frac{P(t)}{P_0} = \frac{P_{atm}}{P_0 + (P_{atm} - P_0)\exp(-t/t_0)}, \tag{5.7}$$

with t_0 a typical time scale for the pressure signal recovery. We can estimate that for micron-sized capillaries t_0 is of the order of 10^7s (see Appendix B) and so $P(t)/P(0) \simeq 1$ within our experimental window, meaning that the pressure difference acting onto the flowing suspension is constant during our experiments. Non-Newtonian fluids will lead to more complex expressions, but the key-point in this discussion will remain unchanged: the relaxation of the pressure difference is related to the variations of the measuring volume, since the volume of the capillary is only very small fraction of the total, volume changes due to the flow do not affect the pressure difference. We can then conclude that our flows are *driven by a constant pressure difference.*

5.2.2 The confocal microscope and the laser

The confocal microscope we used for our experiments is a Visitech VtEye, mounted onto an inverted optical microscope (Nikon Eclipse TE300). Such a combined instrument allows us to use bright field microscopy to locate the areas of interest in the sample

before switching to confocal imaging. The VtEye is able to give extremely high acquisitions frame rates; according to the manufacturer's specifications, frame rates up to 115 frames per second for 512×512 pixels images can be achieved. The typical image size we used in our experiments is of 256×320 pixels at a frame rate of 107 frames per second which allowed us to accurately track particles for flow speeds up to $\approx 250\mu$m/s. This high acquisition speed is obtained by a scanning system consisting of a galvanometric mirror and an acousto-optic deflector; the pinhole is substituted by a slit whose aperture can be adjusted to optimize the image quality (see Chapter 4 for details). The specified frame rate is actually fluctuating in time due to small inaccuracies in the scanning system. The software which operates the confocal offers the possibility of recording a list of the exact times at which each image is collected; by looking at the variations in the time lags between two successive images we estimate an inaccuracy of 2% in the frame rate.

The confocal is powered by a solid-state, diode-pumped, frequency-doubled laser which emits light at 488 nm (Coherent Sapphire 488–20 Optically Pumped Semiconductor Laser). A control unit allows the user to regulate the output power and a maximum of 20 mW can be achieved. Given the high fluorescence yield of the NBD fluorophore, a very low power is sufficient to give bright images; low laser powers are also preferred in order to limit photobleaching, the loss of fluorescence over time due to continuous exposure to the exciting frequency. Since the laser is not very stable at the lowest output powers, an additional control over the emitted power is achieved by connecting two crossed polarizers onto the laser head; by aligning the first one with the polarization direction of the laser light, and by rotating the second one, the intensity of the light passing through can be tuned from zero to the maximum. It is therefore preferred to operate the laser at intermediate powers and adjust the emitted intensity by using the crossed polarizers. The crossed polarizers are then connected to an optical fibre via an adjustable mounting; once the best alignment between the laser and the fibre has been achieved, the former is connected to the confocal head. An additional set of adjusting screws allows the user to perform a very fine final alignment of the optical fibre with the confocal head, maximizing thus the illuminating intensity and achieving the most uniform illumination possible.

Once the digital images are recorded, pixels need to be converted into real distances. This is accomplished by imaging some calibration standards and translate the pixels readings into micrometers readings. We used a Richardson test slide as our calibration standard. Figure 5.11 shows an example of an image of the test slide for a particular calibration. We note that there is an asymmetry in the size of x and y pixels due to image distortion. Moreover we noticed that the calibration changes over time and needs to be periodically updated.

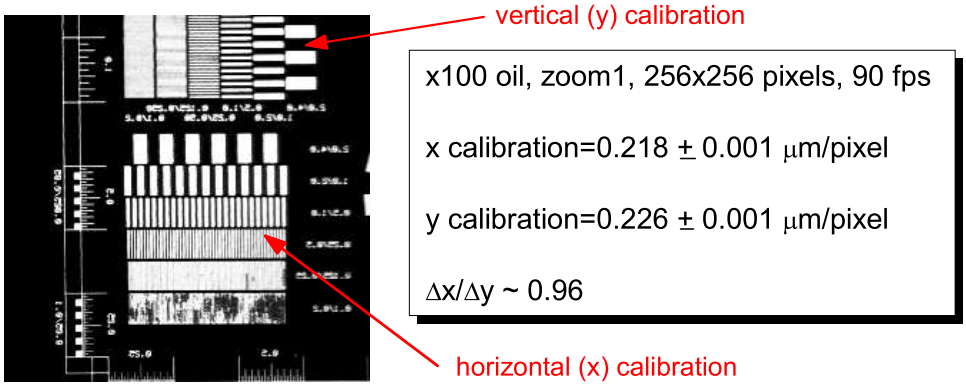

Figure 5.11: Confocal image of the Richardson test slide used for calibrating the pixel size. The spacing between the vertical (horizontal) bars is of 2.0, 1.0, 0.5, 0.25, 0.125 and 0.1 μm from top to bottom respectively. Only the first three sets of scale bars are used for the calibration. The x pixel size is ≈ 4 % smaller than the y one.

5.2.3 The pressure gauge and the acquisition software

The pressure gauge used in our set up is the MKS Series 902 Piezo Transducer. It consists of a series of piezo-resistive elements connected to a stainless steel diaphragm. One side of the diaphragm is in contact with a sealed chamber at vacuum (pressure < 10 mtorr) and the other one with the external environment; once the environmental pressure changes, the diaphragm is deformed and therefore compresses or stretches the piezo-resistive elements changing their electric resistance. A voltage reading across the resistances gives a direct measurement of the deformation and therefore of the pressure change relative to vacuum. The sensor has an accuracy of 1.0% of the reading and a 50 ms response time. The analogue voltage output ranging from 0 to 5 V is read into a PC with an I/O card (NI PCI–6014) connected to the pressure gauge and interfaced with a custom-written Labview program. The software converts the voltage reading into a pressure reading recording atmospheric pressure, the initial pressure difference and the full pressure signal as a function of time.

5.2.4 The glass capillaries

The flow channels used in this work are all borosilicate glass capillaries from Vitrocom. The manufactures provide either rectangular channels of dimensions $20 \times 200\mu$m, $30 \times 300\mu$m, $40 \times 400\mu$m, etc., or square channels of cross sections $50 \times 50\mu$m, $80 \times 80\mu$m, $100 \times 100\mu$m and larger. Square channels with smaller cross sections would have been extremely interesting for our studies, but the manufacturer claims that 40–50 μm is the limit for non-cylindrical capillaries; for smaller sizes, surface tension in the molten

glass rounds the channels off during fabrication. The length of the capillaries used in this work is 10 cm.

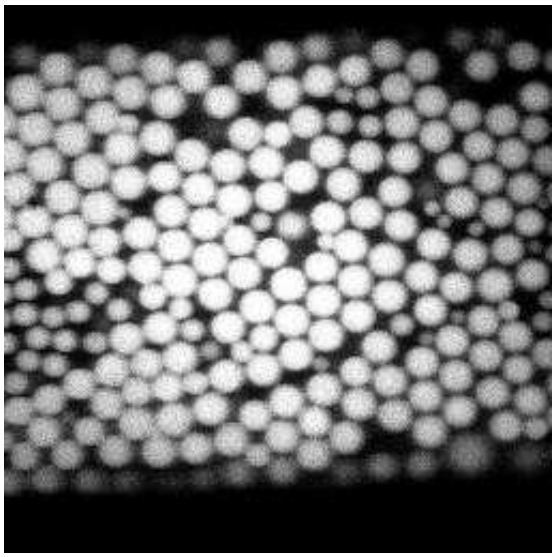

Figure 5.12: Confocal image of the first layer of particles in a coated $50 \times 50\mu$m glass capillary. The larger particles are the coating ones while the smaller ones are suspended and flowing.

The capillaries can either be used untreated and therefore be smooth on the particle level or have their inner walls coated with a disordered layer of PMMA particles to ensure boundary roughness. Figure 5.12 shows a confocal image of the bottom wall of a $50 \times 50\mu$m glass capillary coated with particles with a average diameter $D_{\text{coat}}^{-} = 2.8\mu$m. The larger coating particles are visible together with the smaller flowing ones. The coating is obtained by filling the capillary with a 15–20% suspension of the larger particles and by drying in a vacuum oven at 110-120 °C. Once the capillary is filled with the dilute suspension one end is sealed to ensure that the drying only proceeds in one direction and, as the suspension dries, the particles are left on the inner walls of the channel. It has been proven by practice that by having the capillary tilted by an angle of roughly 30 degrees in the oven and by leaving the sealed end at the top, the drying front moving upwards competes with particle sedimentation optimizing the coating. Once all the solvent has evaporated, given that the temperature at which the oven is kept is larger than the melting temperature of PMMA, the particles partly melt and attach to the glass walls. When the suspension dries, particles tend to accumulate at the edge of the drying front as observed for coffee stains [177]. Before performing the flow measurements we scan the whole length of the capillary with an optical microscope and cut the channel excluding those parts where the drying has accumulated an anomalous amount of coating particles.

Chapter 6

Density and velocity profiles in the flow direction

From this chapter, we begin to describe the results of our experiments. We shall present in detail the properties of pressure-driven flows of dense colloidal suspensions into microchannels in relation to a series of external control parameters.

In the next two chapters we shall thoroughly analyse the details of the velocity profiles and of the flow time dependence, but before that, we are first presenting in this chapter an overview of the results. The following discussion is focussed on characterizing the flow at different positions along the channel, giving thus the possibility of commenting on the properties of our system in the flow direction. The main result is the presence of a non-uniform concentration profile along the flow direction and its link with the local velocity profiles in the transverse direction. We shall see that the local shear profiles are hinged upon the local volume fraction of the suspension and that their properties also vary along the channel. We shall also comment on the time evolution of the flows and on the origins of the non-uniformities mentioned above.

6.1 Experimental results

We have previously reviewed (Chapter 3) a series of experiments reporting data on non-uniform distributions of Brownian and non-Brownian particles in a number of shear flows including channel flows, extrusion flows and squeeze flows. Despite the deviations due to the differences in the systems and the geometries used, there seems to be a common denominator in the results. Considering the suspension as a two-component system, one component being the suspended particles and the other one being the solvent, a difference in the flow between the two can lead to change in the concentration

of the suspension. In particular, for the case of channel or squeeze flows [178], as a result of this difference, the suspension "after" the flow has taken place (e.g. at the outlet of a channel or of an extrusion die) has a lower volume fraction than the initial suspension. Referring for instance to the work of Haw [13], whose system was the closest to ours, it was found that after driving concentrated colloidal suspensions into millimetre-sized capillaries, the final volume fraction of the suspension could be as much as 5-6% lower than the initial one. This effect depended on the initial volume fraction and on the particle size increasing for denser systems and larger particles.

In all the works reported previously the particle distributions were obtained and deduced from bulk measurements, typically involving weighing the suspension before and after the flow. With our set up we are instead able to characterize the *local* particle distribution, link it with the local shear or velocity profile and follow the two in time.

Let us first describe the density profiles along the flow direction. We report here only the relevant experimental details, for a more complete description refer to Chapter 5. In Figure 6.1 we report the average number of particles per frame as a function of the position at which the images have been taken relative to the inlet of the capillary; the channel has a square cross section of side $2a = 50\mu$m and the inner walls are untreated and therefore smooth on the particle level. The values reported have been obtained by averaging 1000 $38 \times 62\mu$m images (therefore containing the whole width of the channel) collected at a depth of 17μm from the bottom surface of the capillary. The frame-rate was of 107 Hz, so each point took approximately 10 seconds. Both the upper and the lower part of the figure refer to pressure-driven flows of a suspension of PMMA hard spheres of diameter $\bar{D} = 2.6 \pm 0.1\mu$m with an initial volume fraction $\Phi \gtrsim 0.635$.

For a dilute suspension we expect to find a uniform concentration along the flow direction. By looking at the figure we can immediately notice that this is not true for a dense suspension.

Focussing initially on the upper part of the figure, we observe that the volume fraction Φ [1] is roughly constant from 1 to 2.5 cm from the inlet and it then decreases approaching the front of the flowing suspension. To gain more insight on the local properties we can then relate the density profile to the corresponding sequence of velocity profiles reported in Figure 6.2. We can mainly distinguish between two cases: one where the flow speed is uniform across the whole section of the capillary and another one where it is not. We shall refer to the latter as *shear flow*, while we shall call the former *complete plug flow*. This distinction will prove crucial in the rest of this discussion and we shall thoroughly explore the details of each case focussing in particular on the transition between the sheared and the un-sheared regions.

[1] We shall use from now on the words volume fraction, concentration and number of particles per frame as synonyms even though we are counting particles on a 2D slice of a three-dimensional system.

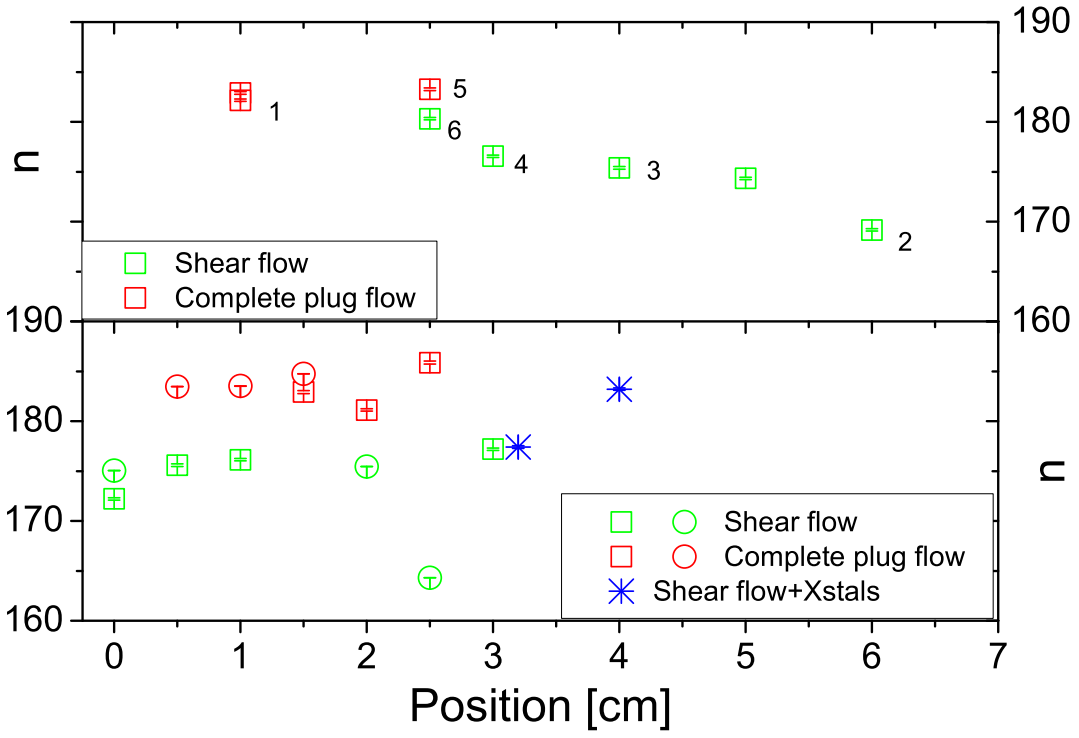

Figure 6.1: Average number of particles per frame as a function of the distance from the capillary inlet (0 cm). Red symbols refer to complete plug flow, green ones to the shear case and the blue stars to the presence of crystals. The averages have been performed on 1000 images (collected at 17μm from the bottom surface of the capillary) and the error bars are the standard deviations divided by the square root of the number of frames. The top and the bottom part refer to two different experiments and the latter contains two separate runs. All the measurements were performed in smooth square capillaries (width $2a = 50\mu$m) and the initial volume fraction was $\Phi \gtrsim 0.635$ in all the cases. Top: initial driving pressure $\Delta P_0 = 70$ torr. The data points were collected in the order of the numbers in the figure. Bottom: first run (circles): $\Delta P_0 = 40$ torr, second run (squares and stars): $\Delta P_0 = 40$ torr. The data points (both runs) were collected moving away from the inlet in steps of 0.5 cm.

The data points in the upper part of Figure 6.1 were collected as follows. We initially recorded the images at 1 cm from the inlet observing complete plug flow with the suspension slipping uniformly along the channel (data point 1). We then moved the microscope objective 5 cm downstream (2), almost at the front of the flowing suspension; the density measured here was considerably lower than the one at the previous position. A dramatic difference in the flow profile is also visible. At (2) the flow profile was very close to the dilute, Poiseuille one (see Figure 6.2) and the particles at the edges were attached to the channel's walls. The local density had dropped to the point where the ideal flow profile was almost restored, as measured for lower volume

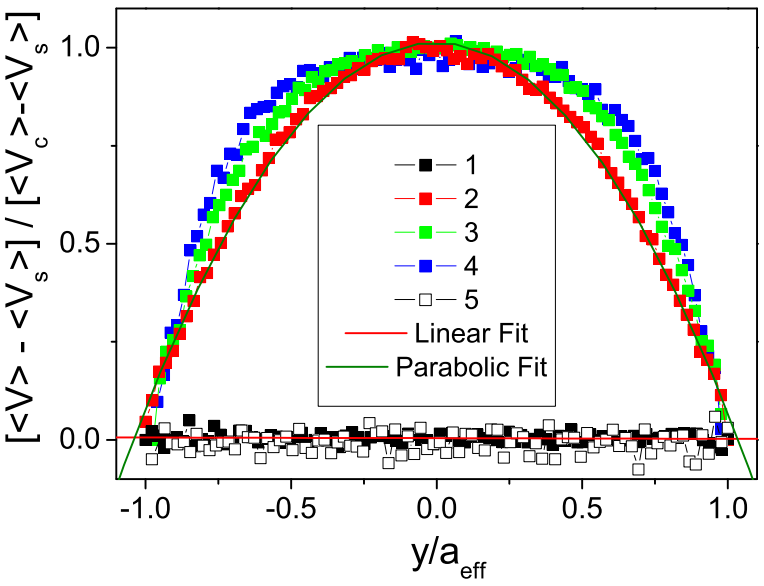

Figure 6.2: Velocity profiles relative to the measurements reported in Figure 6.1(top, the numbers in the legend correspond to the order in which the data have been taken). We report here the scaled velocity profiles $[\langle V\rangle - \langle V_{\rm s}\rangle]/[\langle V_{\rm c}\rangle - \langle V_{\rm s}\rangle]$ where $\langle V_{\rm c}\rangle$ is the velocity in the centre of the channel and $\langle V_{\rm s}\rangle$ is the velocity of the suspension at the wall or *slip velocity*. The data are obtained by averaging on 1000 frames and are plotted as a function of $y/a_{\rm eff}$ where in this case the effective channel half-size $a_{\rm eff} = a - \bar{D}/2$. The full lines are fits; a constant line for the complete plug (1) and a parabola for the most dilute case (2). The exact ideal profile in a square channel will be reported in Chapter 7 but at the depth where the images were collected ($z = 17\mu$m) it deviates very slightly from a parabola. All complete plug flows show up as flat lines around 0 since $\langle V\rangle = \langle V_{\rm s}\rangle$ everywhere.

fraction suspensions [80, 126].

We then moved back towards the inlet of the capillary in steps of 1 cm; the average number of particles per frame kept increasing and shear was still present. As the volume fraction increased, the velocity profiles also changed; the particles at the edges had now a small, non–zero slip velocity and the flow profiles deviated from the ideal one. In particular we notice that a central low shear region, whose extension related to Φ (curves(3) and (4)), appeared. This type of velocity profile is commonly found in dense flows and several examples have been reported in the literature for granular systems, polymers and concentrated suspensions [125, 88, 95, 157] to name a few. The shape of the velocity profiles and its dependence on many parameters, as for instance volume fraction, will be the subject of Chapter 7; for the present purposes it is sufficient to highlight the fact that as the system gets denser, the velocity profiles deviate from the ideal one and consist of a nearly unsheared central plug and two lateral shear zones

whose amplitude decreases with increasing Φ. At point (5) we hit again the complete plug flow region; the density of the suspension jumped back up to the initial levels and the velocity profile returned uniform. Point (6) (just 40μm downstream of (5)) marked the transition between complete plug and shear flow. We notice that a lower volume fraction was measured for the shear flow. This is a crucial point we shall go back to in the following discussion; *in order to allow for shear, the system has to lower its volume fraction* [179].

We finally moved back to the initial position and observed that the suspension was still flowing as a complete plug. At the end of the experiment, the complete plug region expanded, extending upstream of this point almost up to the inlet of the capillary, where it was formed after just a few particles diameters.

By looking at this data set we can already highlight the presence of several striking features. Firstly we notice that the concentration of a dense suspension flowing along a micro-channel is not constant, but the suspension gets more and more diluted as we move away from the inlet; this is consistent with the non-uniform distribution effects mentioned earlier. Moreover there is a strong link between the local volume fraction and the presence or absence of shear in the flow. Finally we have also started to appreciate that the density profile along the flow direction is also time dependent and we shall comment on the nature of its evolution in the following sections.

Let us now look at the lower part of Figure 6.1, where a second similar experiment is reported but where data were also collected at smaller distances from the capillary inlet. The graph reports two successive longitudinal scans of the channel; the flow was stopped for several minutes to save the data between the two runs. Starting from the circles (first run) we observe that the density profile is not only non-uniform, but also *non-monotonic*. In fact we note that the point immediately after the channel entrance has a lower volume fraction than the successive ones; after the initial increase the volume fraction reaches a plateau to decrease again further downstream. The colour coding tells us that shear is present close to the capillary inlet, then we find complete plug flow in the region of the density plateau, and finally we observe again a significant dilution towards the front of the flowing suspension. The scan was performed moving away form the inlet of the capillary in steps of 0.5 cm. We stopped the flow and, after waiting for several minutes, we restarted it and performed a second sequence (squares) starting again from the channel entrance and scanning in 0.5 cm steps. We observe that the suspension now fills a larger portion of the capillary and that the same kind of density profile is recovered, but now the initial sheared region has expanded and the complete plug has migrated further downstream. After the complete plug, the volume fraction starts to decrease again and shear takes place. At variance with what was reported above, though, even further downstream we observe for this experiment the presence of

a large crystallized region where, due to the more effective packing, the concentration rises again. The presence of crystalline patches can be seen as a consequence of the dilution of the suspension and of the experimental history. Due to the stopping of the flow after the first sequence, the particles to had enough time to rearrange into crystals given that, in the region downstream of the complete plug, the volume fraction was low enough for crystallization to happen (see Chapter 2); moreover a crystalline packing is a more favourable one for flow where layers of particles can easily slide past each other and therefore an ordered structure was furthermore enhanced by the flow. Shear-induced crystallization has been reported for high strain oscillatory shear in similar colloidal systems [180, 181]; in our experiment typical strains often exceed several particle diameters within one field of view and flow induced crystallization is not infrequent.

In addition to what was extracted from the upper part of the figure, the data just discussed continue to stress the presence of a non-uniform, non-monotonic density profile along the flow direction. Furthermore they highlight again the presence of a time evolution in the density profiles themselves. We have already stated that each flow is strongly history dependent, but we can nonetheless point out the presence of three distinct regions: an initial region, close to the inlet of the capillary where shear is present but where the volume fraction is high enough to yield significant variations from the ideal velocity profiles, a second region where complete plug flow is observed and where the density reaches a maximum and is fairly insensitive to position and a final sheared region where the suspension undergoes a progressive dilution down to significantly lower values of Φ. As these two examples already pointed out, the complete plug can for instance migrate downstream and/or propagate backwards towards the entrance of the channel depending on the history of the experiment; in the next sections we will discuss both mechanisms. Before moving to the detailed discussion on the complete plug formation and time evolution, it is worth emphasizing that the aforementioned regions are macroscopic (cm) compared to the particle size (μm). Recalling that the typical size along the flow direction of our field of view is of the order of tens of microns and that the density gradients discussed above take place on the length scales of centimetres (thousands of particles), we are unable to detect any density variation in single images. The only case when this is possible is in the case of a sharp transition between shear and complete plug flows, where the density jumps up when shear ceases.

6.1.1 Transition

While the temporal dynamics of the complete plug region will be discussed in detail in Chapter 8, we examine here the mechanisms leading the time evolution of the density profile in relation to the shear/complete plug interface.

We have already reported the presence of a rather sharp transition between the sheared region and the complete plug flow region. Figure 6.3 depicts such transition zone.

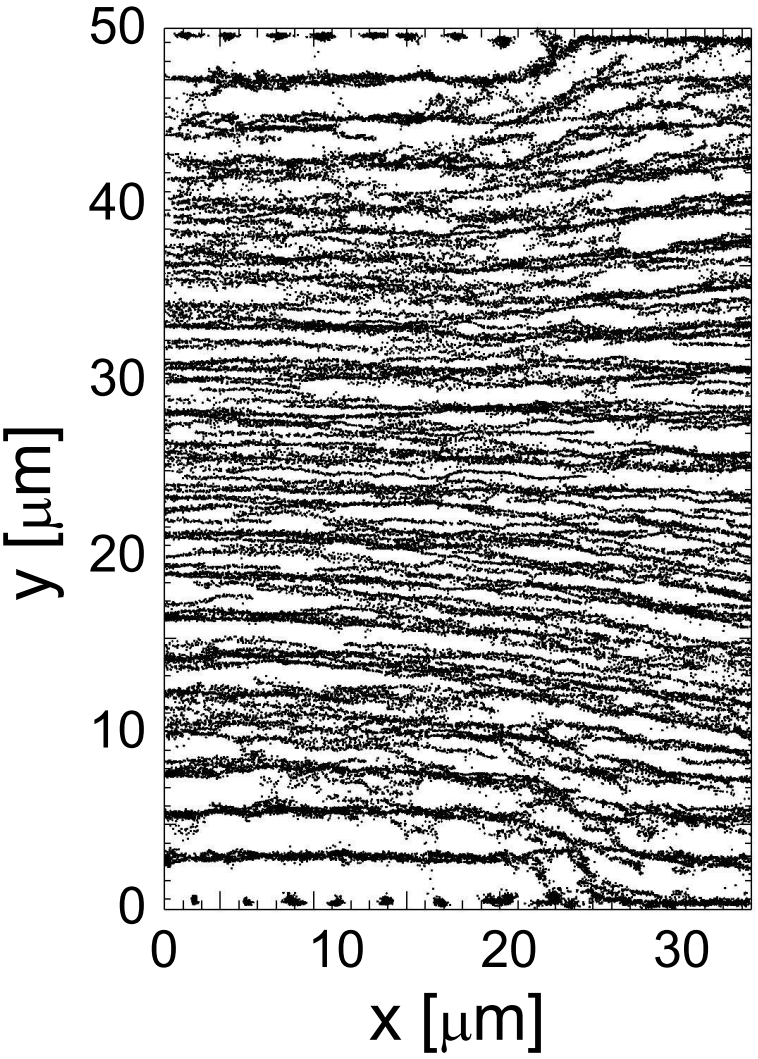

Figure 6.3: Superposition of particles positions during flow (50 images). In the left part of the image the particles are undergoing shear flow and wall slip is absent (smooth, 50 $\times 50\mu$m square channel). On the right the transition to complete plug flow is visible; note that the full plug "kicks particles off" the walls as it proceeds. The flow direction is from right to left and $\Delta P_0 = 40$ torr.

In the graph we plot the positions of the particle centres in 50 successive frames; if a particles moves, we see a trace corresponding to its trajectory. We can observe two distinct regions. On the left of the image we find shear flow whose velocity profile has been described earlier; we also remark that the particles closest to the walls are not moving. On the right instead we see that also the particles at the walls have non-zero velocity and analysing the particle displacements we discover that their velocity is uniform across the channel; therefore this part of the figure displays complete plug flow. Finally we notice the presence of a transition between the two zones where the particles attached to the walls are "kicked off' by the incoming plug; in the transition zone large transverse components of the velocity are present.

The forward propagation of the complete plug can also be analysed adding more quantitative details.

Figure 6.4 reports the difference in velocity between adjacent layers of particles close to one of the inner walls of the capillary as a function of time. Initially a non-zero relative velocity difference is present, implying a non-uniform velocity profile; we notice furthermore the fact that the velocity difference between layer 1 (closest to the wall) and 2 is larger than the one between layer 2 and 3 showing that the shear profile is also non-uniform and that shear is reduced towards the channel's centre. For later times we observe that the relative velocity difference vanishes indicating that the speed has become uniform across the channel and so meaning that the suspension is now flowing as a complete plug. At intermediate times we see a reduction of the velocity differences as the complete plug moves downstream and progressively fills the field of view.

On the same graph we also report the number of particles per frame as a function of time. We notice that the density of the suspension in the field of view increases steadily in time until it reaches a plateau at a value roughly 5 % larger that the initial one. We can easily relate the change in particle density to the change in the flow; as time progresses the complete plug moves downstream, progressively filling up the entire field of view. The fluctuations in the number of particles per frame are due to different factors. The image quality fluctuates in time introducing errors in the tracking procedure. Additionally, the local structure of the suspension that comes into the field of view changes with time leading to different particle counts. Finally we recall that we are counting 3D objects out of two-dimensional slices, therefore particles that are just above or below the imaged plane can come in and out and additionally contribute to the noise in the particle count.

We also mentioned earlier that the complete plug region is not only moving downstream but that it is also expanding backwards towards the inlet of the channel. Data analogous to the ones reported in Figure 6.4 can be shown, but we report here another way of looking at the transition between complete plug and shear flow.

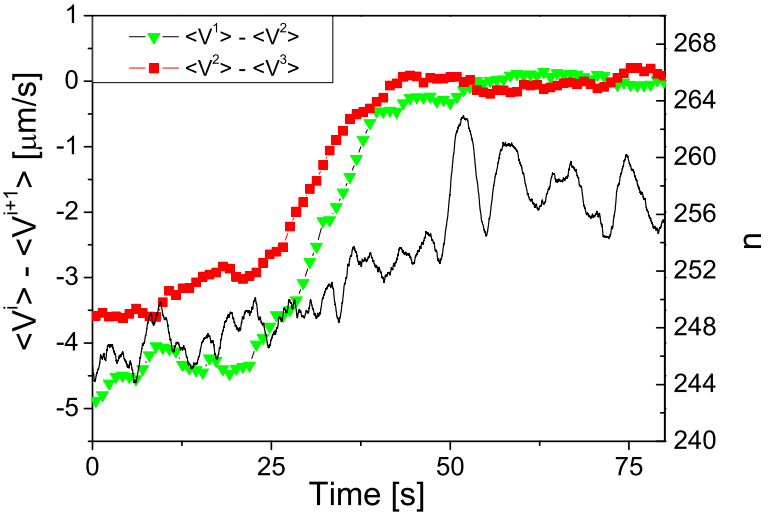

Figure 6.4: Average velocity difference for three external layers of particles inside the capillary as a function of time (squares). On the right axis: average number of particles per frame(n) as a function of time (full line).

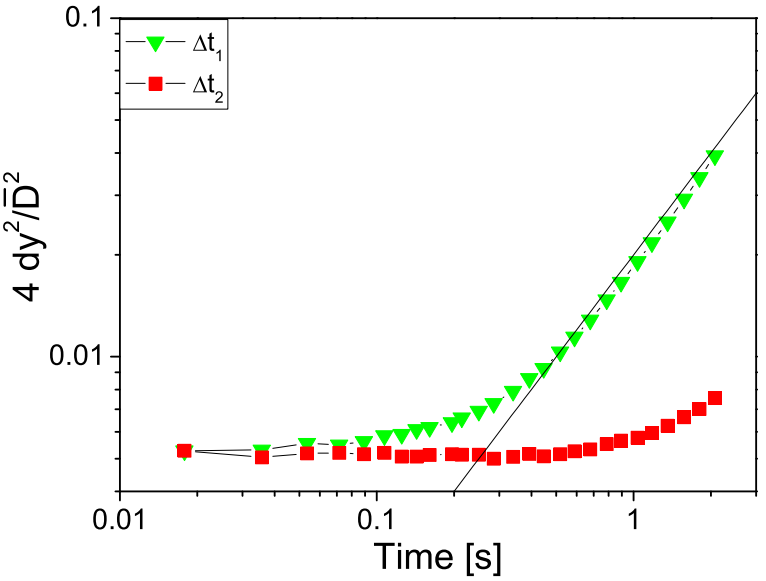

Figure 6.5: Normalized mean square displacements in the transverse direction as function of time. The green curve is relative to a sheared suspension (Δt_1) and the red one to complete plug flow in the same position at later times (Δt_2). The straight line has a slope of 1.

Figure 6.5 is showing the mean square displacements (msd) in the transverse direction normalized by the particle radius as a function of time for two portions of the flow of 1000 frames each. As we stayed at a fixed position we observed how the local properties

of the suspension change with time. The green curve represents the normalized msd in the presence of shear. The red curve shows the same quantity at the same position after $\approx$ 30 s when the complete plug has expanded backwards and filled the field of view. We can observe for the latter case how the particles are more confined by their neighbours and how diffusive motion is practically absent in the time window.

6.2 Discussion

Summarizing, we can say that we observed the presence of a non-uniform density profile along the flow direction and we also related the local volume fraction with the local velocity profiles highlighting the presence or the absence of shear. But what is the origin of the non-uniformity in the concentration along the channel? In what follows we shall present a qualitative explanation of the origin of such phenomenon discussing the mechanisms of plug formation and the effects of wall roughness.

As already mentioned at the beginning of this chapter, returning to the two-component-system picture, non-uniform particle distribution effects can be ascribed to the presence of relative velocity differences between particles and solvent.

At high volume fractions, the motion of every particle is strongly coupled to the motion of its neighbours while such effect is absent for the solvent whose molecules are several orders of magnitude smaller than the colloids and can therefore "move freely". In the presence of a confinement the motion of the colloids undergoes also geometrical restrictions. Interactions between the suspended particles and with the geometry boundaries, impede the flow of the former resulting in a net solvent flow responsible for the overall volume fraction reduction reported in the literature [13]. The scenario can range from a zero velocity difference when colloids and solvent are moving with the same speed, to a maximum where the particles are permanently jammed and the solvent is flowing through the porous matrix constituted by the particles themselves. In the latter case there is a complete *permeation* of the solvent and any situation in between leads to a partial effect.

In the specific geometry of our experiments, the origin of the relative velocity differences can be ascribed to the presence of the following factors: confinement, high volume fraction and shear.

As found by Osborne Reynolds [179], when a densely-packed system of grains is sheared under a constant external load (i.e. pressure), it needs to locally increase its volume, or *dilate*, in order to allow the shear; more space is needed to overcome the geometrical restrictions imposed by the presence of the surrounding particles. In the presence of a free interface, particles will protrude as when we walk on wet sand.

Our situation is different: we work under conditions of constant volume, i.e. in the

presence of a confinement. In our case, shearing a densely-packed suspension cannot lead to dilatancy, but gives rise to *density inhomogeneities* instead. The system needs to *lower its volume fraction locally for shear to take place*, and therefore, as reported in the previous data analysis, the volume fraction of the complete plug is always higher than the one of any sheared region. As a consequence of this, since in our flows the shear profile is not uniform across the channel, density inhomogeneities will take place preferentially where shear is higher (close to the channel walls); this leads to the formation of a non-uniform density profile *across the channel* as will be described in more detail in Chapter 7.

In the presence of a confinement, shear can also lead to the formation of structures able to bear a stress as shown in the cartoon in Figure 6.6.

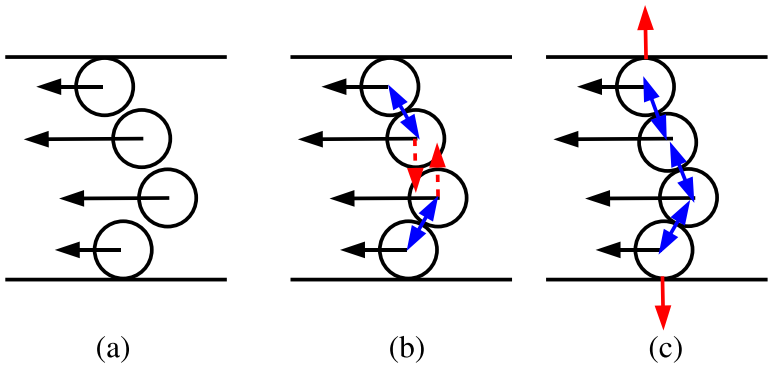

Figure 6.6: Cartoon of non-uniform in a confined geometry leading to the formation of particle contacts. The black arrows represent the flow (x) component of particle velocity and the red dashed ones the transverse (y) component. The blue arrows indicate particles contacts and the red ones the stress exerted onto the walls.

Part (a) sketches a situation in which particles are subjected to a non-uniform velocity field inside a confined geometry. When the faster particles come in contact with the slower ones (part (b)), they need to acquire a transverse velocity component (dotted lines) in order to overtake their slower neighbours. In the case of dense systems and high particle to confinement size ratios, such situations can lead to the formation of structures of jammed particles actively exerting transverse stresses onto the confinement (part (c)). The occurrence of particle networks in shear flows of dense systems has been reported in the literature [62] and we shall return to it in more detail during the discussion at the end of the following chapter.

We can speculate that the temporary occurrence of such networks is responsible for the slowing down of the flowing particles and therefore for the build up of the concentration gradients.

Imagine now to perform an experiment (i.e. using NMR imaging) where it would

be possible to step back and observe the flow at all positions along the channel as a function of time from the moment when the flow starts.

As the suspension enters the channel, the particles undergo shear, and, as just described, their interactions with the channel walls and with the other particles effectively slow their motion down, influencing thus also the speed of the particles which follow upstream. Since the actual velocity is lower than the "desired" one, particles accumulate in a slower, denser region and a velocity difference with the solvent appears. The density of such a region increases up to a maximum packing where any relative motion between the particles is practically absent. This is what we previously called a *complete plug*. In the presence of a small friction force with the walls, the plug can slide along the channel as a rigid body if such stress is exceeded. Downstream of the complete plug region, due to the velocity difference, a net flow of solvent is present (permeation) and therefore the suspension is diluted allowing shear to take place again. Thus, as time progresses, at large distances from the inlet we find a dilute, sheared region. Moving upstream towards the channel's inlet we then find a dense complete plug sliding forward and expanding upstream at the same time. According to the speed of the moving plug compared to the speed at which it builds up, another dilute, sheared region close to the entrance is present. We experimentally found this region to range from the order of centimetres to few particle diameters, depending on the time of observation and on the experimental history.

The interactions between particles and confinement play a crucial role in determining the fate of the particle contact networks described before. If only a small friction force between the particles and the confinement is present (i.e. smooth walls), the jammed particles can slide as a rigid body if such stress is overcome, but if the friction is much higher (i.e. rough walls) they can lead to permanent jamming. We shall return on this aspect in the discussion of Chapter 8.

Finally we comment on the presence of a minimum volume fraction for the *onset of dilatancy* in sheared granular media. Onoda and Liniger measured a threshold value of $\Phi = 0.555 \pm 0.005$ below which dilatancy was absent when shearing neutrally-buoyant suspensions of non-Brownian spheres [182]. They claimed this value to coincide with *random loose packing* (RLP) which represents "the loosest, random packing which is mechanically stable". The identity between the dilatancy onset and RLP is based on the argument that dilatancy, although dynamic, requires "at least intermittently, a rigid continuous network" able to transmit stresses through the system. They similarly suggested that dilatancy events can be at the origin of shear-thickening. We shall see in Chapter 7 that above a very similar volume fraction ($\simeq 0.56$), our systems acquire granular features, failing to be described by conventional colloid rheology and showing density inhomogeneities.

Chapter 7

Flow profiles

This chapter describes experiments on the flow of dense colloidal suspensions in microchannels, focussing in particular on the measurement of the velocity profiles in the direction transverse to the flow. Results for different volume fractions, boundary conditions, channel sizes and shape will be reported, highlighting along the way the differences and incongruities with the behaviour expected from bulk rheology and ideal fluids. After presenting the results, we shall interpret our data by extending and applying a model initially conceived for two-dimensional dry granular flows to three-dimensional flows of weakly Brownian suspensions. A theoretical description of the model will be given together with the results of its application to the experimental data. Finally a short description of the concentration profiles across the capillary will be given, followed by a discussion on the mechanisms at their origin.

7.1 Velocity Profiles

Analytical solutions to the flow of ideal Newtonian fluids have been found for a range of simple flow geometries ([107] and references therein) since the days of Hagen and Poiseuille [1] and thanks to the progress in computational power and techniques, solutions have also been extended to a number of situations of high practical relevance involving more elaborate geometries and more complex fluids [109, 110, 111]. We study here flows in channels with square cross sections which present notable experimental advantages (Chapter 5) and strong links with microfluidics applications [18]. An analytical solution for square channels can be calculated for an ideal Newtonian fluid (see equation 3.30) and it is reported again here in Figure 7.1. Results of numerical analysis for more complex systems (e.g. yield stress fluids) were also reported in Chapter 3.

The scenario changes when the flowing medium is a dense colloidal suspension.

[1] For an interesting review of the original experiments refer to [106] and references therein.

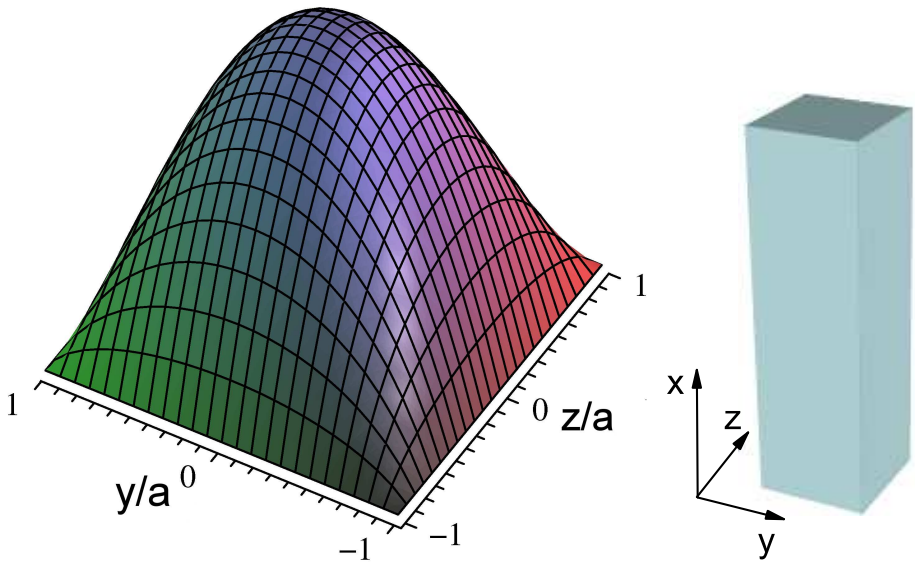

Figure 7.1: Velocity profile for a Newtonian fluid in a square channel of side a (drawn on the side).

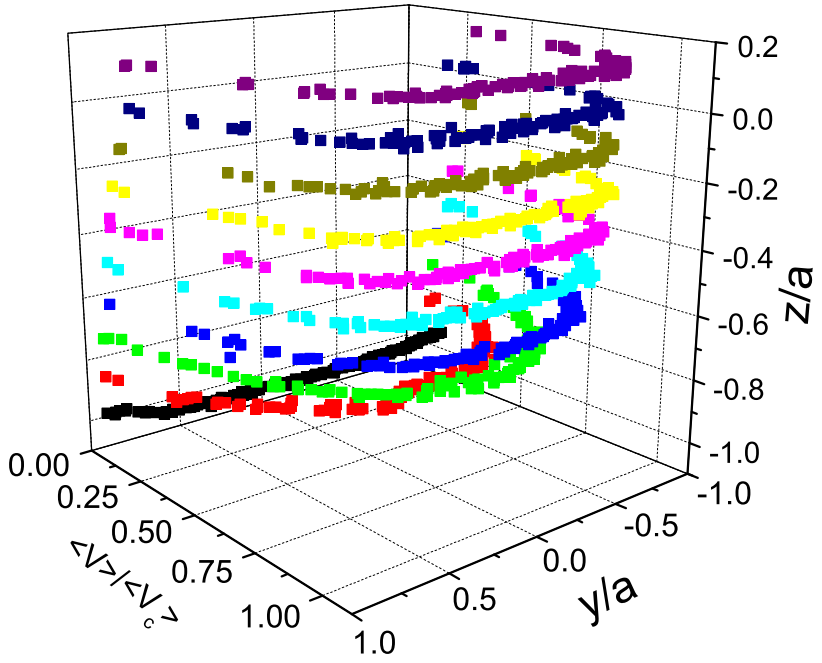

Figure 7.2: Velocity profiles in the lower half of a square capillary (width $2a = 50\mu$m) with smooth walls reconstructed in 3μm steps for PMMA particles with diameter $\bar{D} = 2.6 \pm 0.1\mu$m suspended in a buoyancy-matching solvent ($\Phi \gtrsim 0.635$). The average velocity $\langle V \rangle$ is in units of the average velocity of the central, unsheared 'plug', $\langle V_c \rangle = 20\mu\mathrm{m}s^{-1}$.

In the following sections we shall refer to samples of different volume fractions, but we initially report here in Figure 7.2 an example of a velocity profile for the densest suspension (sediment, $\Phi \gtrsim 63.5\%$, average diameter $\bar{D} = 2.6 \pm 0.1\mu$m, determined by confocal microscopy) flowing in a smooth-walled channel with a square cross section of 50μm (roughly 20 particle diameters). The flow (in the x direction) across the whole width ($y \leq \pm|a|$) of the channel was imaged and $44\mu\text{m} \times 58\mu\text{m}$ images were collected (107 frames per second) at depths $-a < z < +0.2a$ ($z = -a$ is the lower surface). From these images, we identified [155] and tracked particles [126]; from time-dependent coordinates, we calculated particle velocities and from those we extracted the flow profiles of the suspension obtaining thus the flow speed on xy planes at fixed values of z (see Chapter 4 for details on particle tracking). Finally, by merging these, we reconstructed three-dimensional velocity profiles.

After start-up transients, we found oscillations in the particle velocities with frequencies from 0.1 Hz (slow flow) to 1 Hz (fast flow). This feature, which we shall discuss in detail in Chapter 8, is ubiquitous in the pipe flow of pastes [13, 122]. In this chapter, we restrict ourselves to steady-state average velocity profiles, $\langle V \rangle$, obtained by averaging over 20 s (slow flow) to 10 s (fast flow), corresponding to ~ 2000 and to ~ 1000 frames, respectively. We imaged at $x \sim 0.5$ cm from the entrance to the capillary (corresponding to ~ 2000 particles), where entry effects have died out and the results show negligible x dependence.

At this high packing fraction the measured velocity profile (Figure 7.2) deviates strongly from the ideal case as already shown in the previous chapter. For $|z| \lesssim 0.6a$, each velocity profile consists of a shear zone close to the walls and a nearly unsheared central 'plug'. The unsheared plug shrinks at larger $|z|$. We also observe wall slip with velocity $\langle V_s \rangle$. As reported in Chapter 3, plug flow is a common feature in dense flows and a quantity of particular interest is the size of the plug, or conversely the size of the shear zones b. In terms of the difference between the averaged centre and wall speeds, $\Delta V = \langle V_\text{c} \rangle - \langle V_\text{s} \rangle$, we define b to be the distance from the wall where the flow speed is $\langle V_s \rangle + 0.95\Delta V$. This corresponds to the point where noise in the raw data becomes comparable to the curvature in the profiles. To obtain the value of b we fit the data to a polynomial[2] which faithfully reproduces the profile and calculate b by applying the criterion above to the fit curve. The values of b reported later in the text are always calculated via this method if not stated differently. Using different criteria to define the shear zones lead to qualitatively similar results.

[2]The fitting polynomial we used is of the kind $f(y) = a + by^2 + cy^4 + dy^6$. By using higher order polynomials no differences were found.

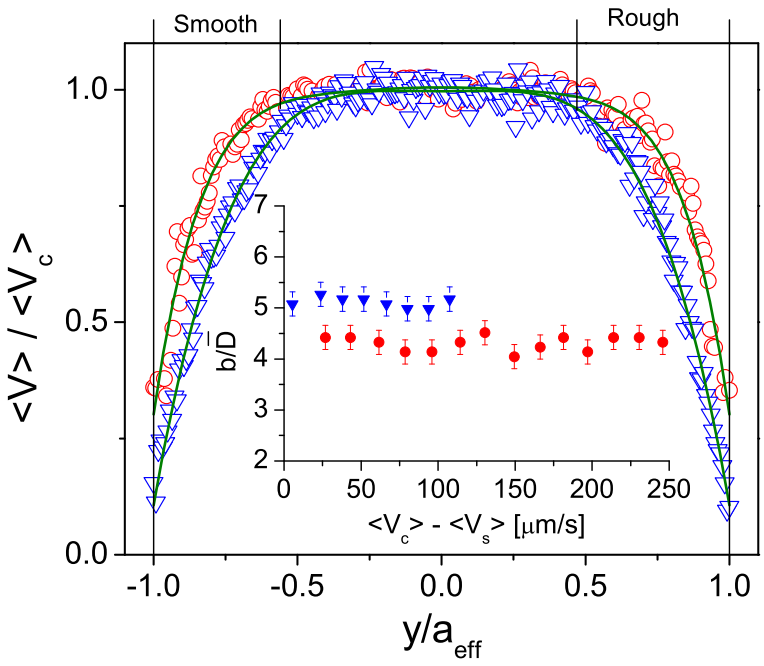

Figure 7.3: Examples of averaged velocity profiles as a function of y/a_{eff} for smooth (○) and rough (▽) walls at 17μm from the bottom wall of the capillary ($z/a_{\text{eff}} = -0.32$) for a sediment ($\Phi \gtrsim 0.635$) flowing in a channel with cross section of 50μm × 50μm. Full lines: polynomial fits; Vertical lines: extents of shear zones. Inset: width of shear zone in units of particle diameters as a function of ΔV; ▼ rough walls and ● smooth walls.

7.1.1 Boundary conditions effects

In Chapter 5 we saw how the inner surface of the channels can be coated to insure roughness on the particle level and we discuss here how the presence of rough boundaries affects the flow profiles.

Figure 7.3 shows two velocity profiles for smooth and rough boundary conditions in a 50μm × 50μm capillary for the densest suspension. All the data have been taken at a depth of $z/a_{\text{eff}} = -0.32$. The two profiles are qualitatively similar, but the latter displays smaller wall slip and larger shear zones. Note that for rough walls, we use an effective half width $a_{\text{eff}} = a - \bar{D}_{\text{coat}} - \bar{D}/2$ and for smooth walls $a_{\text{eff}} = a - \bar{D}/2$, where $\bar{D}_{\text{coat}}$ is the average diameter of the particles in the coating layer. The width of the shear zones as a function of the applied shear rate is reported in the inset. It can be noted how b is larger for rough walls and how it is *independent* of ΔV (which is a first order measure of the average shear rate) for both cases. This constitutes a crucially important finding and its implications will be thoroughly analysed in Section 7.2. More examples of velocity profiles are reported in Figure 7.4 and in Figure 7.5 for smooth and rough walls respectively.

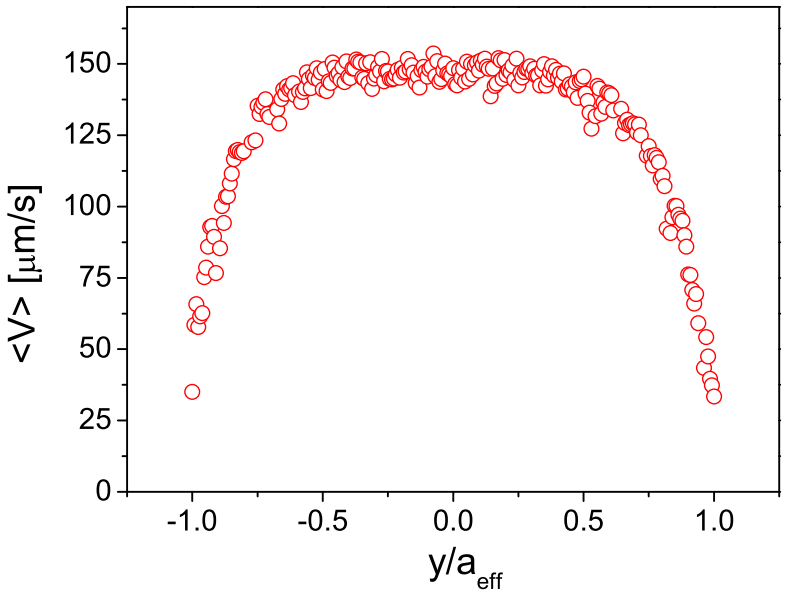

Figure 7.4: Averaged velocity profile as a function of y/a_{eff} for a $\Phi \gtrsim 0.635$ suspension in a $50\mu\text{m} \times 50\mu\text{m}$ square capillary with smooth walls at $z/a_{\text{eff}} = -0.32$. The average has been calculated on 1000 frames. The distribution of velocities in the plug region gives an indication of the error bars for the velocity values. ΔP_0 =10 torr.

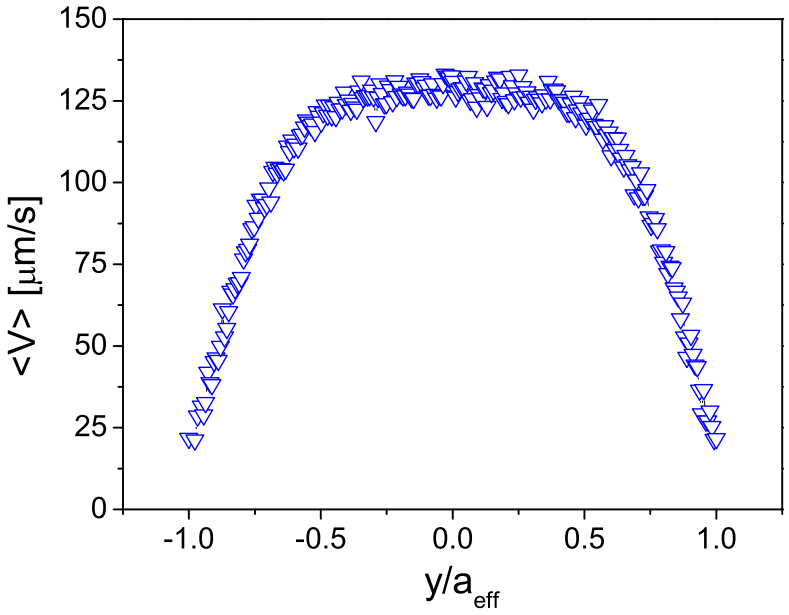

Figure 7.5: Averaged velocity profile as a function of y/a_{eff} for a $\Phi \gtrsim 0.635$ suspension in a $50\mu\text{m} \times 50\mu\text{m}$ square capillary with rough walls at $z/a_{\text{eff}} = -0.32$. The average has been calculated on 1000 frames. ΔP_0 =20 torr.

The dependence of the slip velocity $\langle V_s \rangle$ on the velocity of the plug $\langle V_c \rangle$ also shows interesting features. Starting from the rough walls case, we observe that $\langle V_s \rangle$ grows linearly with $\langle V_c \rangle$ for all velocities in the measured range (other data sets show the linearity in a clearer way but we chose to report the same set as in Figure 7.3 for continuity). Conversely, the smooth boundaries case presents different regimes; at low speed $\langle V_s \rangle$ is linear in $\langle V_c \rangle$ while at higher rates the slip velocity decreases and reaches a plateau. This feature can be attributed to the presence of stick–slip motions which will be discussed in Chapter 8. We also note again that the wall slip is more pronounced is the absence of rough boundaries.

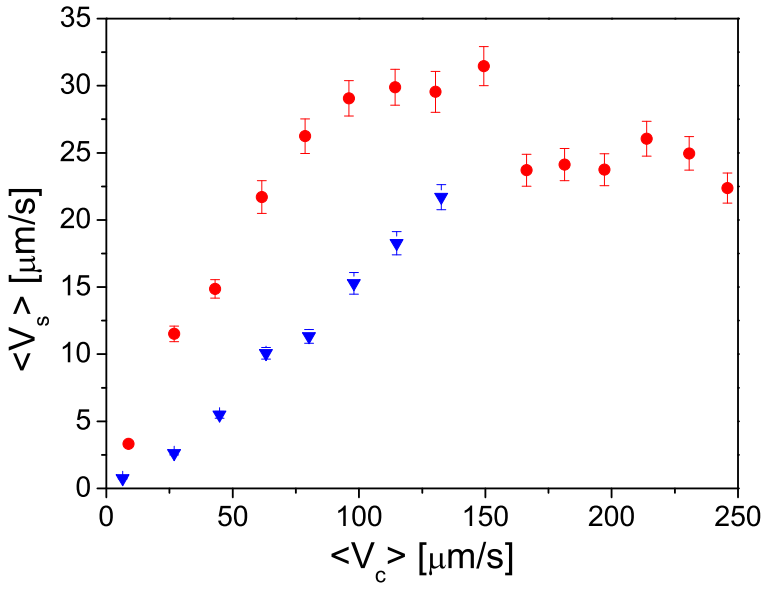

Figure 7.6: Wall slip velocity $\langle V_s \rangle$ as a function of the velocity of the plug $\langle V_c \rangle$ for rough (▼) and smooth walls (●). The points correspond to the data reported in the inset of Figure 7.3.

Finally, to further enforce the evidence of the effects of boundary roughness on wall slip and shear zones, we report in Figure 7.7 an example where only one of the two side walls of the channel was coated; we can thus observe the effects of boundary roughness simultaneously on the same profile. We again note how the presence of a smooth wall increases the value of $\langle V_s \rangle$ and how, in the presence of a rough boundary, shear penetrates more towards the centre of the geometry. The values of b for the two cases are consistent with what reported in the inset of Figure 7.3. Furthermore, as we will highlight again in Section 7.3, a smooth wall induces layering of particles close to the wall; such structuring is much less pronounced in the presence of a disordered coating layer.

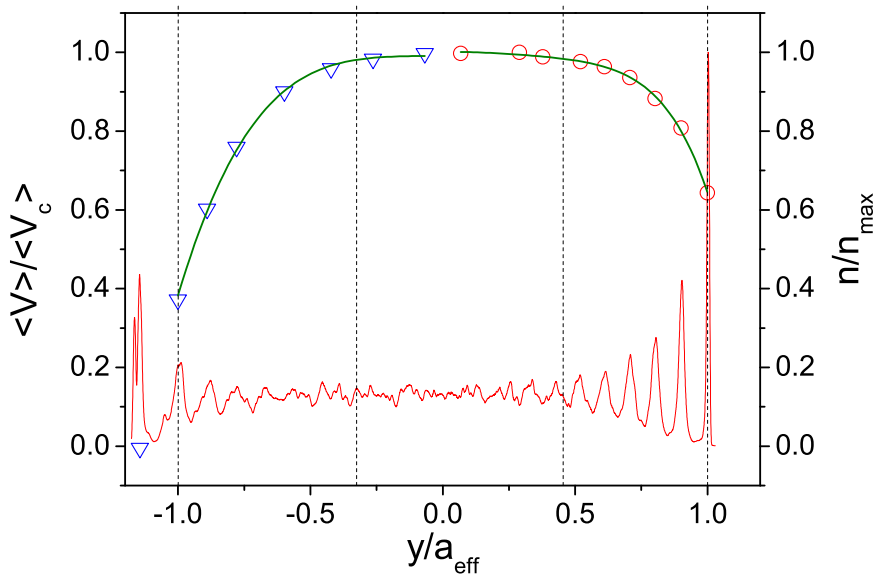

Figure 7.7: Averaged velocity profile as a function of y/a_{eff} for a channel where only one side walls (the left one) is coated (smooth side(○), rough side (▽)) at $z = 17\mu$m. Full lines: polynomial fits; dashed lines: extents of sheared zones. Note that the value of a_{eff} is different on the two sides of the channel. Red line: histogram of particle y positions normalized to its maximum value. The outermost histogram peak to the left corresponds to the coating layer and therefore the measured speed is zero.

7.1.2 Volume fraction effects

Let us now examine the effects that changing the volume fraction of the flowing suspension has on the velocity profiles. Suspensions of different Φ, ranging from sediments (63.5%) to notably more diluted ones (43%), were prepared. For details on the preparation of the suspensions refer to Chapter 5. We measured the transverse velocity profiles in at a depth of $z/a_{\text{eff}} = -0.32$ in a capillary with a cross section of $50\mu\text{m} \times 50\mu\text{m}$ and smooth walls. The results on the width of the shear zones relative to the effective channel width as a function of the applied rate (ΔV) are reported in Figure 7.8.

Two main facts are to be noted. First the value of b is independent of the applied rate for all the volume fractions investigated in the reported velocity regime. Secondly, in the limit of high volume fractions ($\Phi \gtrsim 0.58$), the value of b is also independent of Φ. Decreasing the volume fraction below 0.58, b starts to rise. The solid horizontal line marks the prediction for the loci of the 5% decay of the velocity for an ideal Newtonian liquid in a square channel. The dashed line highlights the same quantity for a shear-thinning power law fluid with exponent $n = 0.65$ in a two-dimensional channel. Such value of n was obtained by fitting the velocity profiles of suspensions with $\Phi = 0.43$,

using the expression from Equation 3.31 and leaving the shear-thinning exponent as a free parameter [3] (Figure 7.9). Both the lines are horizontal (constant b/a_{eff}) since Newtonian and shear-thinning profiles scale with the speed of any point (see Figure 3.13 and relative discussion).

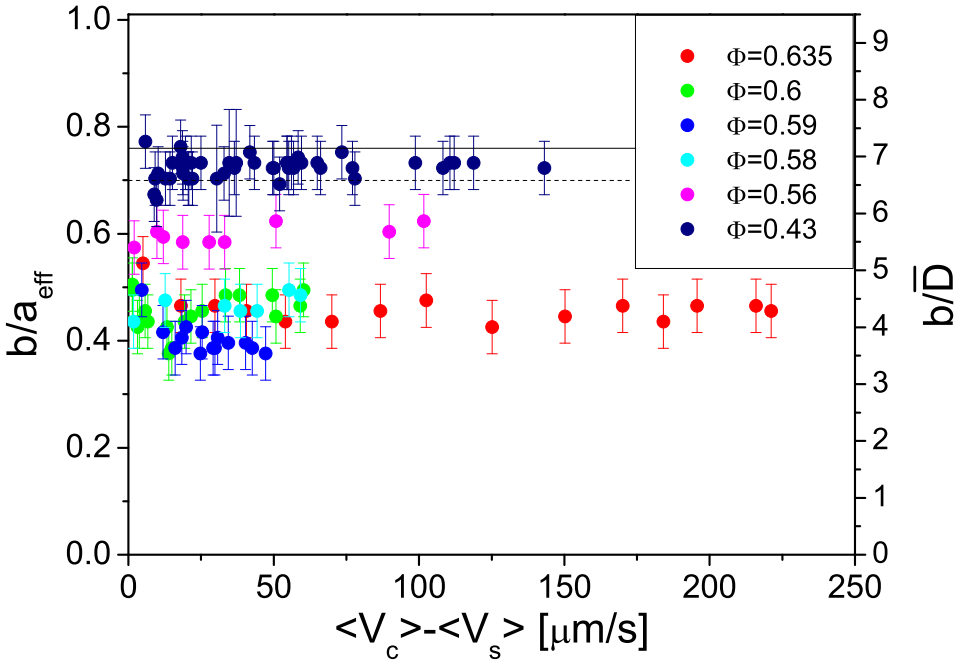

Figure 7.8: Values of the width of the shear zone b normalized to the effective channel size a_{eff} as a function of the applied rate ΔV for different values of the suspension volume fraction Φ. The solid and the dashed lines give the respective size of the shear zones for an ideal Newtonian liquid and for a shear-thinning power law fluid with $n = 0.65$ according to our criterion. The data refer to smooth-walled channels.

Fitting the velocity profiles of 0.56 volume fraction suspensions with a shear-thinning model gave exponents $n = 0.35 \pm 0.004$, well below the value of 0.5 measured for much denser suspensions ($\Phi = 0.63$ from Figure 3.6).

In the high volume fraction region ($\Phi \gtrsim 0.58$), we fitted the velocity profiles using the Herschel-Bulkley model reported below (Equation 3.36)[4]:

$$\tilde{V}_x(\tilde{y}) = \left[\left(\frac{1}{2\,Od} - 1 \right)^{\frac{n+1}{n}} - \left(\frac{\tilde{y}}{2\,Od} - 1 \right)^{\frac{n+1}{n}} \right], \tag{7.1}$$

where $\tilde{y} = y/a_{\text{eff}}$ and $\tilde{V}_x(\tilde{y}) = V_x(\tilde{y})/V^{max}$.

[3] The use of a simplified, two-dimensional profile does not give an exact value for n, but at the depth $z/a_{\text{eff}} = -0.32$ at which the flows were imaged, we expect only minor differences.

[4] This is also an approximated 2D expression.

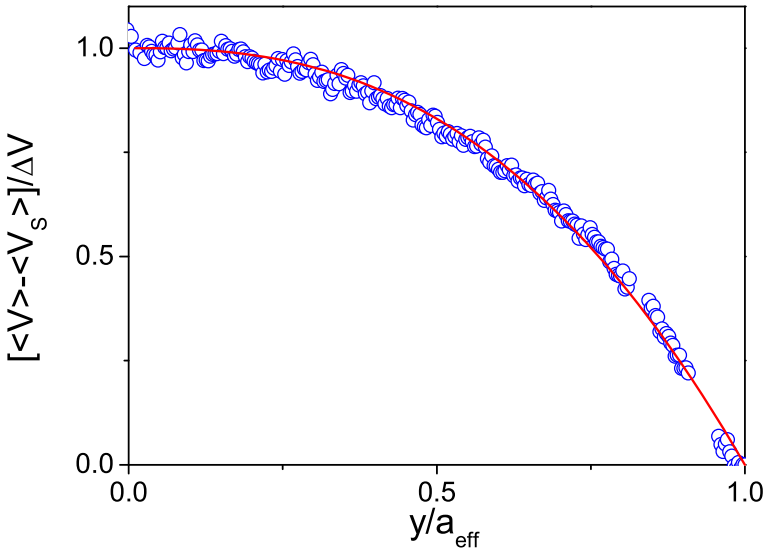

Figure 7.9: Normalized velocity profile for a 0.43 volume fraction suspension flowing into a 50μm $\times$ 50μm smooth capillary. The solid line is a fit where the shear-thinning power law exponent is left as a free parameter. A value of $n = 0.65 \pm 0.02$ is found.

We have two choices on how to perform the fit and they lead to contradictory results. We leave n as the only free parameter and we can either enter the value of the Oldroyd number we calculated in Section 3.3.5 ($Od \simeq 10^{-3}$) or we can determine it by measuring the width of the plug. In fact we recall from Equation 3.33 that the half-width of the plug is $a_{\text{eff}} - b = 2\tau_{\text{yield}}/\nabla p$ and, given that $Od = \tau_{\text{yield}}/(a_{\text{eff}}\nabla p)$, we obtain:

$$1 - \frac{b}{a_{\text{eff}}} = 2Od, \tag{7.2}$$

which expresses the normalized half-width of the plug in terms of the Oldroyd number. Taking the example reported in Figure 7.10 for a $\Phi = 0.635$ suspension, even if we use a more relaxed criterion to determine the width of the plug (2% decay of the normalized velocity rather than the usual 5%), we obtain an Oldroyd number of 0.22, which is two orders of magnitude larger the value expected from the conventional rheological description of our system; if we fit the velocity profile in the shear zone we obtain an HB exponent $n = 0.456 \pm 0.018$. When we instead perform the fit using $Od = 5 \times 10^{-3}$, we obtain $n = 0.214 \pm 0.017$ which is considerably smaller than the value of 0.5 measured in a bulk experiment [14].

We therefore point out that the conventional rheological description fails to account correctly for the flow behaviour of suspensions with volume fractions greater than $\simeq$ 0.56. We note that this value of Φ is very close to the one corresponding to the dilatancy

onset in sheared granular packings (0.555) [182] and, after discussing the origin of the shear zones in Section 7.2, we will be able to comment further on these observations. Finally, we additionally highlight that b/a_{eff} is constant for $0.58 \lesssim \Phi \lesssim 0.635$. Given that the quiescent glass transitions occurs at $\Phi \sim 0.58$ in these colloids, these data suggest a universal behaviour for all glassy samples.

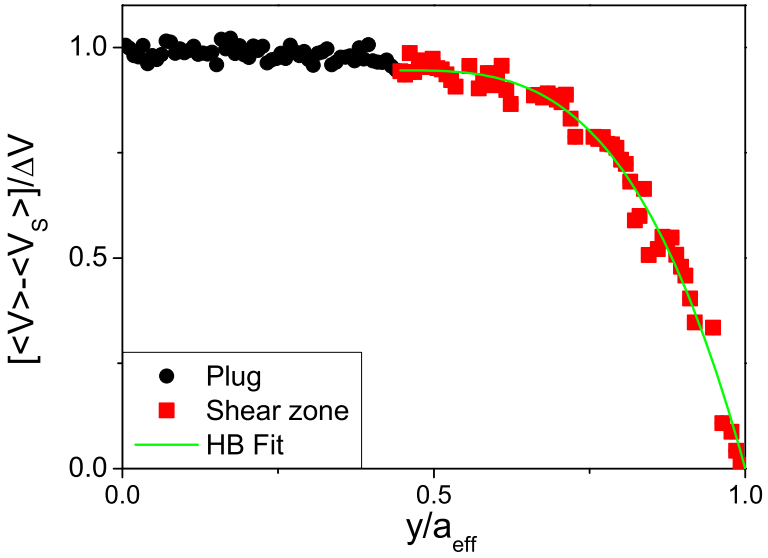

Figure 7.10: Normalized velocity profile for a 0.635 volume fraction suspension flowing into a 50μm $\times$ 50μm smooth capillary at $z/a_{\text{eff}} = -0.32$. The plug (bullets) and the shear zone (squares) are highlighted. The solid line is a HB fit to the profile in the shear zone performed using Equation 7.1, with $Od = 0.22$ and $n = 0.456 \pm 0.018$.

7.1.3 Size effects

Another important factor which determines the shape of the velocity profile is the width of the channel. The predictions for a Newtonian fluid give a fully independent profile once normalized to the channel width. Figure 7.11 (Top) shows b as a function of $\Delta V = \langle V_{\text{c}} \rangle - \langle V_{\text{s}} \rangle$ in units of particle diameters $\bar{D}$ for the flow of a sediment into three square cross-sectioned channels of different sizes with smooth boundary conditions obtained at $z/a_{\text{eff}} = -0.32$. The same relative depth ensures that the same stress level is maintained when looking at channels of different sizes. If we now plot the same quantity in terms of a_{eff} we observe how the data collapse on the same value; in other words the sheared portion of the system is linear with the channel size and the profiles can be rescaled by a_{eff}. This result presents a fundamental difference with the two-dimensional flow of dry granular grains as we shall see in Section 7.2. We can also observe again that b is independent of the applied rates in the investigated regime for

all channel widths.

Technical difficulties make it impossible to access velocity profiles at the correct relative depth (-0.32) for channels larger than 100 μm. When the channel size increases, the absolute depth at which the data need to be taken also increases getting to the point were it exceeds the working distance of the microscope objectives. Furthermore larger channels also come with thicker glass walls reducing thus the effective working distance. In order to image the whole cross section of the 80μm channel a $\times$60 objective was used instead of the usual $\times$100 (see Chapter 5). For the 100μm channels a $\times$40 objective was needed but, in order to get a high enough magnification to allow for accurate particle tracking, only a portion of the cross section was imaged. Furthermore a slower frame rate had to be used limiting the velocity range at which data could be collected.

Using smaller channels also presents technical problems. The manufacturer of the glass capillaries (Vitrocom) claims that the production of square channels of width lower than 40μm is unfeasible as surface tensions effect during the solidification of molten glass will round the capillary. In order to go to even smaller aspect ratios other techniques for producing the channels are needed. Discussion on this will be presented in the outlook of this thesis (Chapter 10).

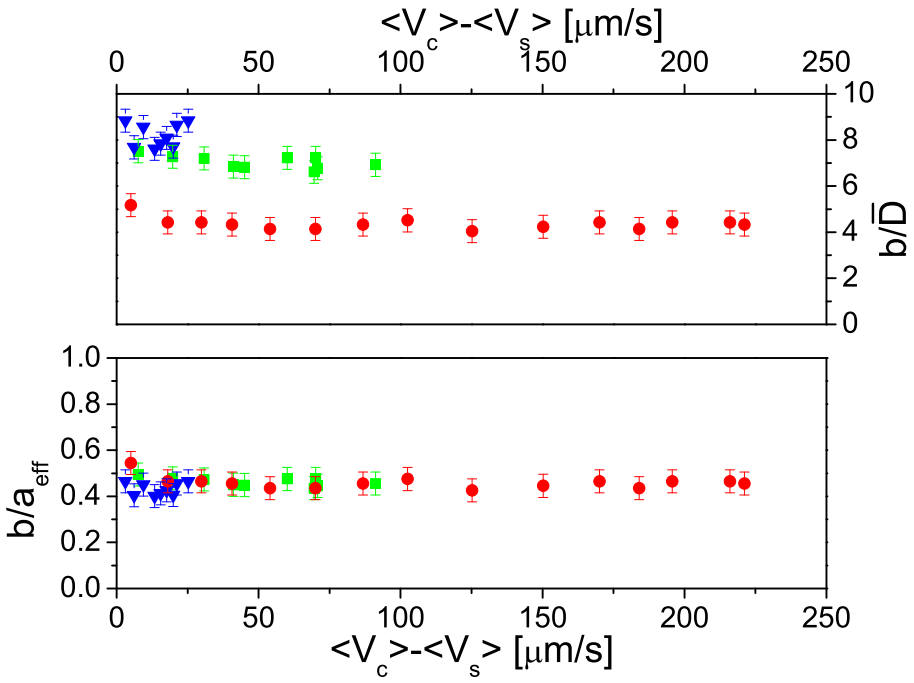

Figure 7.11: Top: size of the shear zone in units of particle diameters as a function of ΔV for sediments flowing into capillaries of 50μm $\times$ 50μm (●), 80μm $\times$ 80μm (■) and 100μm $\times$ 100μm (▼) cross sections respectively. Bottom: same data in units of relative effective channel width.

7.1.4 z-dependence

We now focus our attention on the z-dependence of the shear zones for different volume fractions, boundary conditions and channel sizes. We pointed out already while describing Figure 7.2 that the size of the plug varies with z and that it shrinks close to the walls. Figure 7.12 quantifies this for a series of suspensions of different volume fractions flowing into a smooth walls channel (cross section $50\mu\text{m} \times 50\mu\text{m}$).

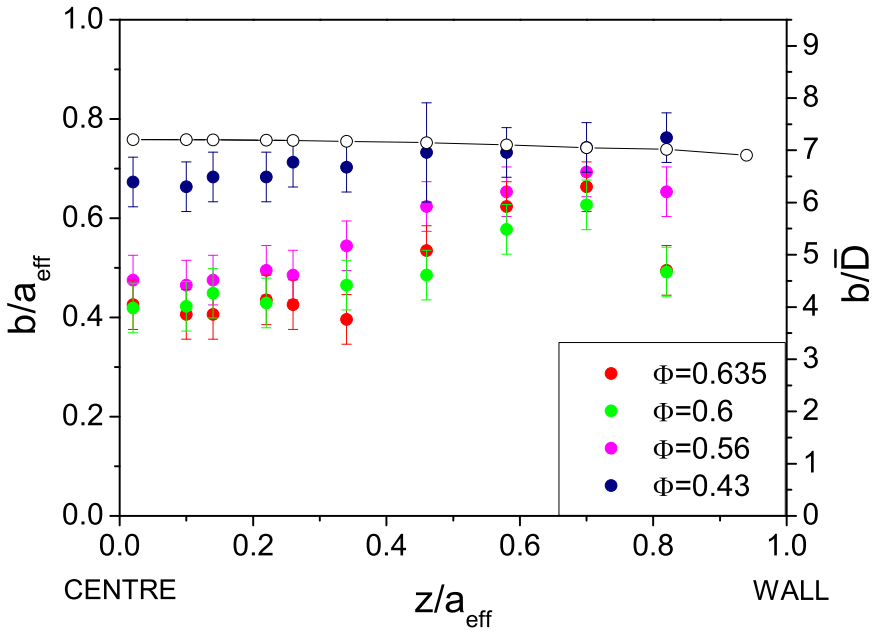

Figure 7.12: Size of the shear zone relative to the effective channel size as a function of z/a_{eff} for a series of suspensions of different volume fractions. The right axis reports the data in units of particle diameters. The horizontal line with the open symbols represents the size of the shear zone calculated with our criterion for a fully developed Newtonian flow.

We can note the following trend with volume fraction. In the high volume fraction regime ($0.58 \leq \Phi \leq 0.635$) the data practically overlap, consistently with the results of Figure 7.8; they show a rise in b in the first 2-3 layers of particles ($z/a_{\text{eff}} = 0.8$ to 0.7) and then the width of the sheared zone decreases ($z/a_{\text{eff}} = 0.7$ to 0.3) until it plateaus at the "plug size" in the centre ($z/a_{\text{eff}} = 0.3$ to 0). A more dilute sample ($\Phi \simeq 0.56$) basically shows the same trend, but with larger shear zones and a smaller initial rise. The lowest volume fraction sample shows a less pronounced z-dependence and the absence of the initial rise in b. The graph also shows the prediction for a Newtonian fluid in a square channel (solid line); the ideal values show a minor decrease close to the walls due to a "slight compression" in the flow profiles due to the proximity of the flat walls. A similar prediction is not analytically obtainable for a shear-thinning

power law fluid in this geometry, but for an exponent n close to 1, the predicted size of the shear zones will be similar but smaller than in the Newtonian case (see Figure 3.13). The data points for $\Phi = 0.43$ are accurately described by a shear-thinning exponent of 0.65 and therefore show a behaviour close to the expected one.

Figure 7.13 shows the effect of boundary conditions on the z-dependence of b for a sediment flowing in a 50μm $\times$ 50μm capillary. We observe how in the rough case the size of the shear zone monotonically decreases towards its plateau value in the centre, at variance with what observed for the smooth case. We can also note that the "plug size" in the centre is identical for smooth and rough walls in this case; this is due to the fact that in this particular experiment the coating particles were identical to the flowing ones. The consequences of this will be discussed in Section 7.2.

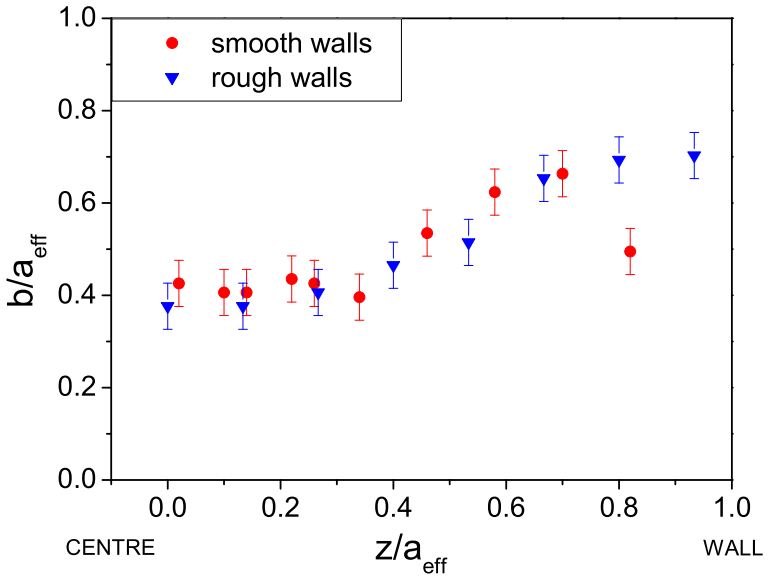

Figure 7.13: Size of the shear zone relative to the effective channel size as a function of z/a_{eff} for the flows of a sediment in channels with cross section of 50μm $\times$ 50μm for rough and smooth walls.

Finally we examine the effect of the channel size. As already shown from Figure 7.11, given the scaling of the velocity profiles with a_{eff} at a given value of z, we expect b also to scale with the effective width for every z. Figure 7.14 reports the data for a sediment flowing in 50μm $\times$ 50μm and 80μm $\times$ 80μm smooth capillaries. For the latter we obtained more data points since the z-binning was of 3μm in both cases; due to the limitations discussed above, it was impossible to image the 100μm channel deeper than $z/a_{\text{eff}} = -0.3$ and therefore no data are reported.

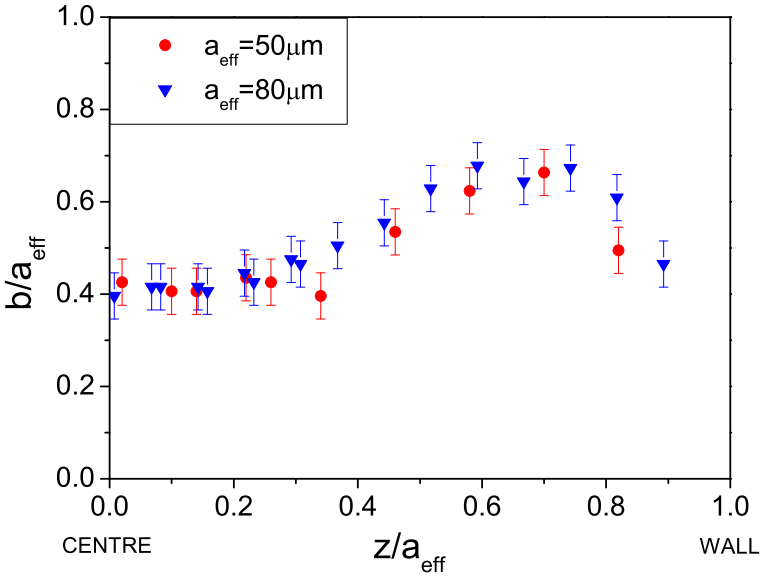

Figure 7.14: Size of the shear zone relative to the effective channel size as a function of z/a_{eff} for a sediment flowing into smooth channels with cross sections of $50\mu\text{m} \times 50\mu\text{m}$ and $80\mu\text{m} \times 80\mu\text{m}$, respectively.

7.1.5 Two-dimensional flows

Finally we examine the effects of channel shape on the flow. As described before, square cross-sectioned channels give a fully three-dimensional problem since the effects of the walls are equally "felt" throughout the whole section. Rectangular channels prove to be simpler to analyse. In fact, if the aspect ratio of the channel, defined as the ratio of the length of the two sides of the cross section, is large enough, the effects of walls decay rapidly in the long side direction (z). Sufficiently far from the shorter walls we recover a two-dimensional problem since the flow does not depend on z any more. Figure 7.15 shows the predicted velocity profile for a Newtonian fluid in a rectangular channel with aspect ratio of 10. Note that for $-8 < z/a < 8$ a "conventional" parabolic flow, analogous to the one in a 2D or cylindrical geometry, is recovered.

As a proof of this, we report in Figure 7.16 two examples of measured velocity profiles of a fairly dilute suspension ($\Phi \approx 30\%$) in a $40\mu\text{m}\times400\mu\text{m}$ channel with untreated walls. The solid lines are quadratic fits to the non-zero velocity data points; we can appreciate how the flow profiles are actually parabolic as reported in the literature for similar systems [80]. The points at $z/a_{\text{eff}} \simeq 1$ show the presence of particles attached to the walls which do not contribute to the flow. The PMMA particles naturally tend to stick to the glass walls and remain attached if the stress exerted by the other particles (strongly depending on volume fraction) and the fluid is not sufficient to detach them.

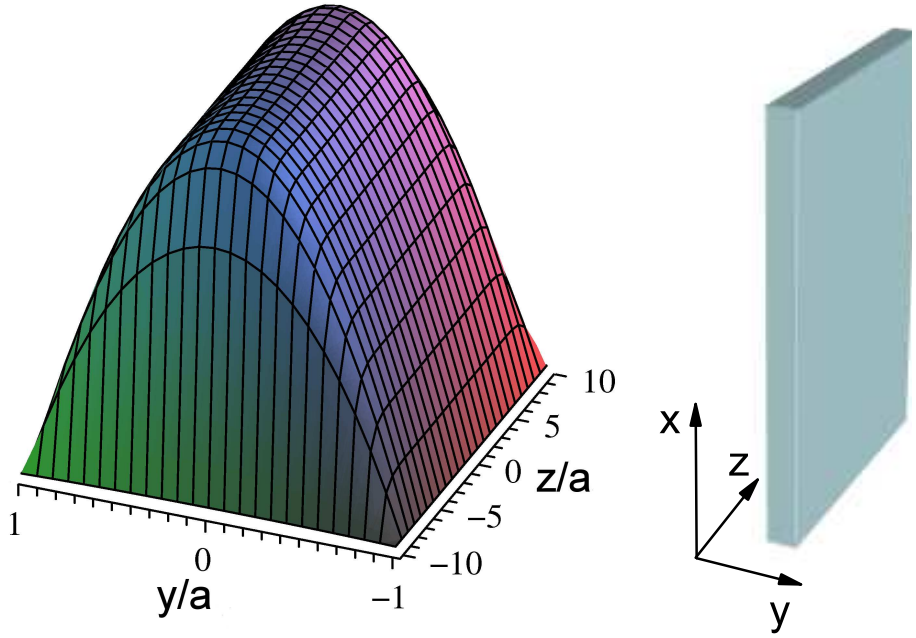

Figure 7.15: Velocity profile calculated for a Newtonian fluid in a rectangular channel with an aspect ratio of 10. Note that the profile in y rapidly becomes independent of z, giving a situation analogous to a 2-dimensional channel.

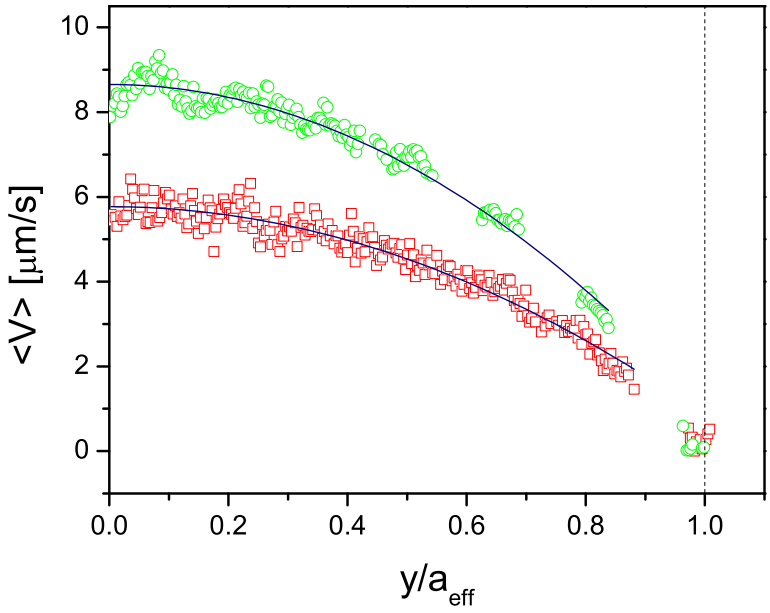

Figure 7.16: Examples of measured velocity profiles in a 40μm$\times 400\mu$m smooth wall channel for a $\Phi \approx 30\%$ ($a_{\text{eff}} = 40\mu$m). The solid lines are parabolic fits to the points corresponding to moving particles.

As shown previously for the square channel, we expect a deviation from the ideal dilute flow as the volume fraction of the flowing suspension is increased. Figure 7.17 reports an example of the flow of a sediment ($\Phi \gtrsim 0.635$) of the same PMMA particles in the same geometry as in Figure 7.16. We observe how the data points deviate from the ideal parabolic profile (blue solid line), showing a shear zone close to the walls and a central region where shear is reduced. Note also that the measured profile follows an exponential curve, as will be explained in Section 7.2. The dependence of the size of the shear zone on the overall flow rate follows the one reported above for square channels. $b/\bar{D}$ stays constant for all the shear rates applied (Inset to Figure 7.17). Additionally, the histogram of y particle positions, normalized to its maximum value, shows a high degree of layering close to the wall which then decays towards the centre of the channel.

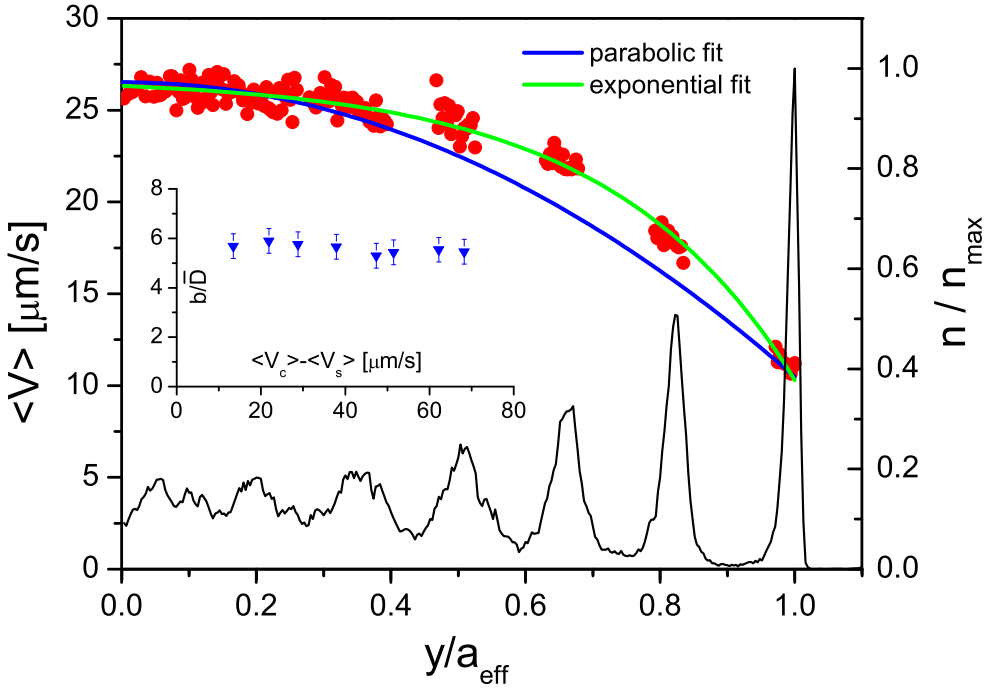

Figure 7.17: Example of measured velocity profile (•) in a 40μm$\times 400\mu$m smooth wall channels for a suspension with $\Phi \gtrsim 63.5\%$. The solid lines are fits to the data. The histogram of y particle positions, normalized to its maximum value, is also reported (right axis). Inset: value of the width of the shear zone b in units of particle diameters as a function of ΔV.

7.2 A granular model for dense colloidal flows

7.2.1 Motivation

In the previous sections we have presented a series of results which highlighted the differences between the ideal behaviour of a Newtonian fluid and the measured one of a dense suspension. Such a difference is, of course, expected. A dense suspension of colloidal particles is a non-Newtonian viscoelastic fluid (see Chapter 3).

Concentrated PMMA suspensions ($\phi > 0.58$) are generally believed to behave as glassy yield-stress fluids, known as Herschel-Bulkley (HB) fluids, with stress τ versus strain rate $\dot{\gamma}$ relation $\tau - \tau_{\text{yield}} \propto \dot{\gamma}^n$ with τ_{yield} the yield stress and $n \approx 0.5$ [14]. Plug flow is ubiquitous in all yield stress fluids, and has been extensively studied [111]. Thus, our observation of the presence of an unsheared plug in the flow profiles is, in itself, unsurprising. In conventional yield stress fluids though, as seen in Chapter 3, if the maximum applied shear stress in the channel exceeds τ_{yield}, we have plug flow with shear zones whose boundaries are given by $\tau = \tau_{\text{yield}}$; hence, the width of the shear zone, b, grows with the shear rate and eventually leaves a vanishingly small 'plug' [111].

As seen previously, the relevant parameter determining the extension of the plug is the ratio of yield to viscous stress, the Oldroyd number (Od) (see Figure 3.18). We can extract the rheological properties of our suspensions by rescaling the a-dimensional rheological curves in [14] and we can therefore predict how our system should behave as an HB fluid.

We estimate an upper limit of Od $\lesssim 7 \times 10^{-3}$ in our experiments (see Chapter 3); this limit is for the highest volume fraction case and the lowest applied rate. Less concentrated suspensions and higher applied rates will lead to even lower values of Od. From [111], this corresponds to a practically complete yielding throughout the channel at all values of ΔV. *This is not what we observe*; the description of our system as a conventional yield stress fluid fails to reproduce the experimental observations. Moreover, we have also mentioned earlier that conventional rheological models give erroneous results when applied to the description of the velocity profiles for suspensions with $\Phi \gtrsim 0.56$.

A clue to what may be happening in our experiments comes from observing that at the typical strain rates encountered in the shear zones, the Péclet number Pe $= \tau_B(\Delta V/a) \sim 50$. In this range of Pe, bulk rheology would lead us to expect severe shear thickening for all the volume fractions examined [16, 57]. Shear thickening in pastes is very far from fully understood on the microscopic level [61, 183], but we may speculate that for colloids stabilized by short grafted polymers, interparticle friction may become important as they jam against each other driven by shear as also suggested by [57].

Indeed, the measured transverse fluctuations of particle positions, for instance in the case of the densest suspension, clearly show the motion induced by them 'bumping' along neighbouring layers, Figure 7.18.

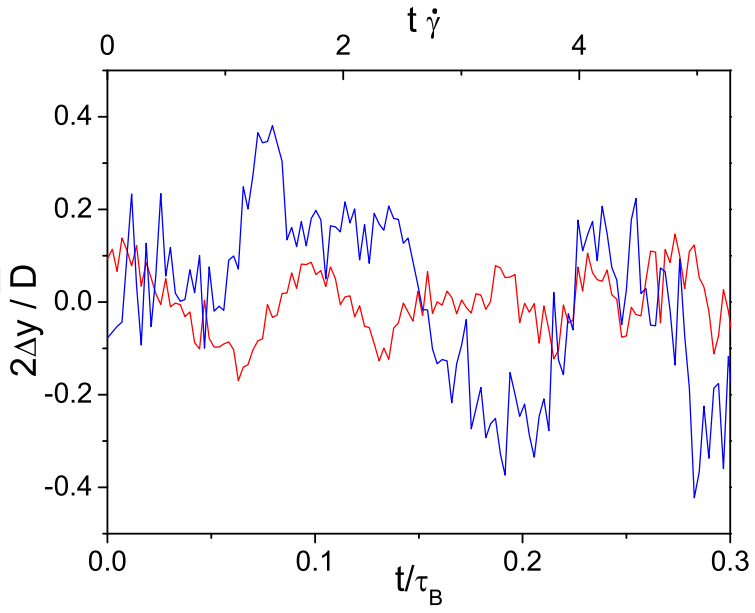

Figure 7.18: Normalized transverse fluctuations of particles in the shear zone for the smooth (–) and rough (–) boundary conditions, versus normalized time t/τ_B or *local* accumulated strain $t{\cdot}\partial\langle V(y)\rangle/\partial y = t{\cdot}\dot{\gamma}(y)$, top axis. The traces show larger fluctuations for rough walls.

A number of factors lead us thus to consider analogies with friction-dominated granular flows. Firstly both the shape of the velocity profiles and the width of the shear zone $b \sim 6\bar{D}$ ($\sim 5\bar{D}$ for smooth walls) are strongly reminiscent of observations in gravity-driven 'chute flow' of dry granular materials [98]. In particular, Pouliquen and Gutfraind observed $b \approx 6D$ in the two-dimensional flow of discs (diameter D) for channels of widths $10D \leq 2a \leq 44D$. They furthermore reported rate independence of the width of the shear zones with the applied rate as observed in our data. Other studies also show an analogous increase in the size of the shear zone by inducing boundary roughness in two-dimensional dry granular channels flows ([95] and references therein).

In addition to these similarities in the bulk flow profiles, the microscopic behaviour also presents common features. As just mentioned, the typical time scales induced by the flow are larger than the one set by Brownian motion (Pe > 1). Our suspension is therefore only weakly Brownian and we expect the particle dynamics to be flow dominated as in the case of fully a-thermal systems. Moreover the particle traces reported in Figure 7.18 show that the motion of particles in the shear zones is dictated

by interparticle contacts in analogy with dense granular flows.

It therefore appears justified to look for approaches conceived for dry granular flows and test if they can be extended to include the description of our results.

Given the strong similarity in the experimental results, we chose to follow the approach of Pouliquen and Gutfraind who developed a simple model to account for their observations in two-dimensional flows [94, 98, 99]. Below we extend their model to three dimensions, and show that it indeed predicts b independent of ΔV.

7.2.2 A model

The approach followed by Puoliquen and Gutfriand is based on the following consideration: a full microscopic description of the motion of every single grain is far too complicated and considering the system as a continuum fails to reproduce the physical results. The way around this comes in by using a continuum approach as a zero order approximation and by including the effects of the microscopic dynamics in the form of perturbations to the ideal continuum stress distribution. In particular given the granular nature of the system they make the assumption, then verified by simulations, that the stress is not distributed homogeneously through the system but that it only propagates when the grains are in direct contact with each other [62]. The stress is therefore fluctuating in space and time according to the local particle configuration; by using these elements they constructed a model which is able to predict the shape of velocity profiles of dry grains flowing into 2D channels.

Following [98] and recalling what was presented in Chapter 3, we start with the components of the stress tensor $\boldsymbol{\tau}$ in the fully-developed flow of a continuum medium in the x direction along a pipe, which satisfies

$$\frac{\partial \tau_{xx}}{\partial x} + \frac{\partial \tau_{xy}}{\partial y} + \frac{\partial \tau_{xz}}{\partial z} = 0\,, \tag{7.3}$$

$$\frac{\partial \tau_{yy}}{\partial y} = \frac{\partial \tau_{zz}}{\partial z} = 0\,, \tag{7.4}$$

with $\partial \tau_{xx}/\partial x = -\nabla p$. For a square pipe of side $2a$ [107]:

$$\begin{aligned} \tau_{xy}(z) = \; & \tau_0 \sum_{k=1,3,5\ldots}^{\infty} (-1)^{(k+1)/2} \times \\ & \times \left[1 - \frac{\cosh(k\pi z/2a)}{\cosh(k\pi/2)}\right] \frac{\sin(k\pi y/2a)}{k^2} \end{aligned} \tag{7.5}$$

where $\tau_0 = 8a\nabla p/\pi^2$. This constant sets the scale for the (z-dependent) maximum stress at the wall, $\tau_{\max}$ (see Figure 7.19).

In conventional yield stress fluid rheology, the yield stress $\tau_{\rm yield}$ is a constant. If $\tau_{\rm max}/\tau_{\rm yield} > 1$, we have plug flow with a shear zone whose boundaries are given by the solution of $\tau_{xy}(y,z) = \tau_{\rm yield}$ [111]. We use instead a Coulomb friction condition at the walls [5]:

$$\tau_{yy} = \mu_{\rm wall}^{-1}\tau_{\rm max} \ , \tag{7.6}$$

where $\mu_{\rm wall}$ is the friction coefficient between the suspension and the wall; this constant τ_{yy} satisfies Eqn. 7.4.

Everywhere inside the material, $\tau_{xy}/\tau_{yy} < \mu_{\rm wall}$, because $\tau_{xy} < \tau_{\rm max}$. But we expect $\mu_{\rm wall} \leq \mu_{\rm bulk}$, the friction coefficient inside the material, with '=' for a rough wall made of particles similar to those in the bulk, and '<' for smooth, glass walls. Thus, $\tau_{xy}/\tau_{yy} < \mu_{\rm bulk}$, or $\tau_{xy} < \mu_{\rm bulk}\tau_{yy} \equiv \tau_{\rm yield}$, so that the bulk never yields, and the whole material always slips as a plug. Note that

$$\tau_{\rm yield} = (\mu_{\rm bulk}/\mu_{\rm wall})\tau_{\rm max} \geq \tau_{\rm max} \ , \tag{7.7}$$

i.e. $\tau_{\rm yield}$ increases with $\tau_{\rm max}$ (and therefore ΔV). This reflects the rising normal stress τ_{yy}, Eq. 7.6, which increases the friction between particles and thus $\tau_{\rm yield}$.

We now assume that there exists stress fluctuations which, when added to the continuum τ_{xy}, Eq. 7.5, may take the local stress above $\tau_{\rm yield}$, Fig. 7.20. With [98, 94] we use a 'Boltzmann' ansatz for the yielding probability:

$$p_{\rm yield} \propto \exp\left[-\frac{\tau_{\rm yield}(z) - \mid \tau_{xy}(y,z) \mid}{\Delta\tau}\right] \ , \tag{7.8}$$

where $\Delta\tau \equiv \Delta\tau(z)$ is the amplitude of stress fluctuations, taken to be independent of y at any particular z. This idea stems from a wider range of phenomena which goes under the name of *self–activated processes*. The idea at the base of such activation processes in granular flows is that shear occurring at a certain point in the system triggers a stress fluctuation which is then able to bring shear about in another position in the system. The granular nature of the system implies that the stresses do not propagate homogeneously but along lines of contact between the grains (force chains). The stress distribution fluctuates according to the local particle arrangements and models [184] as well as experiments [185, 186, 187] have reported exponential force chains distributions or the presence of long exponential tails.

[5] A completely analogous discussion can be given for τ_{xz} and τ_{zz}, leading to a velocity profile $V(z)$.

The model is completed by the simplest possible ansatz relating shear rate to $p_{\rm yield}$: $\partial V(y,z)/\partial y \propto p_{\rm yield}$ [6]. At a fixed $z = z_0$, therefore, we have

$$\frac{\partial V(y,z_0)}{\partial y} = k_0 \times \exp\left[-\frac{\tau_{\rm yield}(z_0) - \mid \tau_{xy}(y,z_0) \mid}{\Delta\tau}\right] , \tag{7.9}$$

where k_0 is a proportionality constant.

It may be worth mentioning at this point that this approach is *not* self consistent. This means that once we calculated a shear profile from Equation 7.9, we are not able to go back and derive the corresponding stress distribution. In particular, the calculated shear profile *does not* yield back the continuum stress distribution we entered as an input. This apparent inconsistency is due to our lack of knowledge of a local (both in space and time) constitutive equation for the system. The basis of this model (and its simplicity) is indeed to ignore the local stress-strain rate relation and to include "our ignorance" into the parameter $\Delta\tau$. By doing this we pay the price of not being able to relate the shear rate profile to a stress profile, but we gain a simple effective description of an otherwise overwhelmingly complicated problem.

In order to perform the integration of Equation 7.9 analytically we fitted the continuum stress profile, Eqn. 7.5, with a quadratic approximation of the kind:

$$|\tau_{xy}(y,z_0)| = a(b+|y|)^2 - ab^2 \tag{7.10}$$

Such an expression ensures that:

$$\tau_{xy}(0^+,z_0) = \tau_{xy}(0^-,z_0) = 0 \quad \text{and} \quad \partial_y\tau_{xy}(0^+,z_0) = \partial_y\tau_{xy}(0^-,z_0).$$

Figure 7.19 shows the analytical form of τ_{xy}/τ_0 from Eq. 7.5 and the quadratic fit from Eq. 7.10 for the values of $z/a_{\rm eff}$ (reported on the right of the figure) at which the images in smooth channels are collected. We observe how the deviation from the quadratic fit occurs mostly close to the walls and how near the centre the stress distribution becomes almost z-independent. We recall that the data we referred to earlier in the text (Figures 7.3,7.8 and 7.11) were collected at a depth of $|z/a_{\rm eff}| = 0.32$; the stress distribution there is close to the one in the centre of the capillary and the quadratic fit reproduces it very well.

[6] The ansatz 7.8 was proposed in [98] to account for shear-zone behaviour next to walls, and is qualitatively incorrect for the centre of the pipe, where we must have $\partial u/\partial y = 0$. The gradient of the fitted profiles, Fig. 7.7, therefore do not vanish at $y = 0$. This effect was much less noticeable in [98] than in our case, because some of the channel widths in that work were much larger.

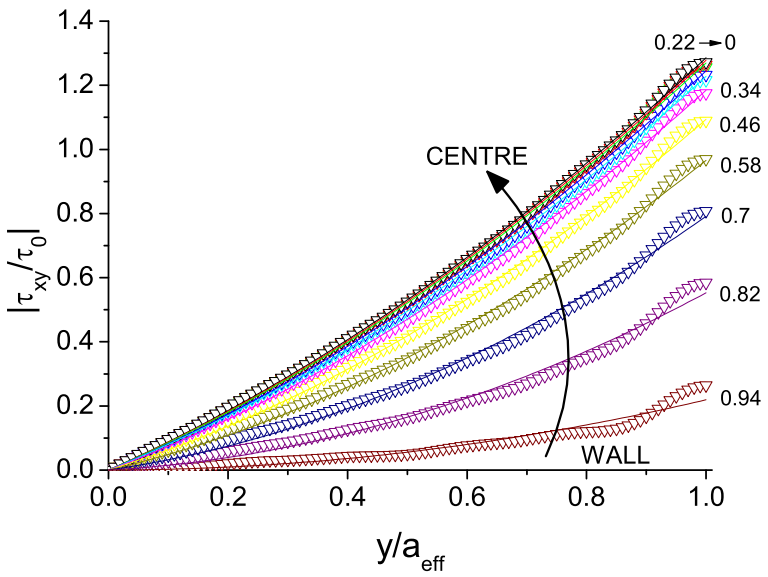

Figure 7.19: Analytical expressions ($\triangledown$) and quadratic fits (solid lines) for τ_{xy}/τ_0 in a square channel as a function of y/a_{eff} for different values of z/a_{eff}. The curved arrow points from the wall to the centre and the numbers on the right are the depths. Remember that $z/a_{\text{eff}} = 0$ is the centre.

If we now perform the integration of Eq. 7.9 we obtain:

$$V(y, z_0) = k_0 \int dy \, \exp\left[-\frac{\tau_{\text{yield}}(z_0) - \mid \tau_{xy}(y, z_0) \mid}{\Delta\tau}\right] + k_1 \, , \tag{7.11}$$

where k_1 is an integration constant.

Substituting the approximated expression for $\tau_{xy}(y, z_0)$ we get

$$V(y, z_0) \simeq k_0 \int dy \, \exp\left[-\frac{\tau_{\text{yield}}(z_0) - (a(b + |y|)^2 - ab^2)}{\Delta\tau}\right] + k_1 \, , \tag{7.12}$$

which gives for positive y

$$\begin{aligned} V(y, z_0) &\simeq k_0 \frac{\sqrt{\pi\Delta\tau}\, i \, \exp\left[-\frac{\tau_{\text{yield}}(z_0) - ab^2}{\Delta\tau}\right]}{\sqrt{|a|}} \operatorname{erf}\left[\frac{\sqrt{|a|}}{\sqrt{\Delta\tau}}\, i\,(y + b)\right] + k_1 \\ &= \tilde{k}_0 \operatorname{erf}\left[\frac{\sqrt{|a|}}{\sqrt{\Delta\tau}}\, i\,(y + b)\right] + k_1 \, , \end{aligned} \tag{7.13}$$

where $\tilde{k}_0$ is a new proportionality constant.

7.2.3 Model predictions and comparison with the data

We fitted the velocity profiles with the expression from Equation 7.13 (see Figure 7.21) and obtained the values of stress fluctuation amplitudes normalized to the wall stress, $\Delta\tau^* = \Delta\tau/\tau_{\max}$, at $|z/a_{\text{eff}}| = 0.32 = 17\mu$m for both smooth and rough walls which are plotted against ΔV in Figure 7.20. As $\tau_{\max}$ increases with the flow speed, $\Delta\tau$ increases proportionately so that $\Delta\tau^*$ remains constant. This finding taken together with Equation 7.5 and 7.7 means that the argument in the exponential in Equation 7.8 is independent of $\tau_{\max}$, giving rise to the constancy in b, Fig. 7.7.

The fact that $\Delta\tau$ scales as the wall stress $\tau_{\max}$ suggests that the stress fluctuations are controlled by what happens at the boundaries. Two-dimensional simulations of dry granular materials certainly relate stress fluctuations to inhomogeneities in the friction-dominated force chains originating from contacts at the walls [99]. In our case, we find (in mid channel) that $\Delta\tau^*$ for rough walls is somewhat larger than for smooth walls, Fig. 7.20; this difference is directly correlated with the observed difference in b, Fig. 7.7. The presence of such a difference, and its sign, is unsurprising. Flow next to a smooth wall is less 'bumpy' and therefore can be expected to generate a lower level of stress fluctuations which propagate then through the system. Such finding is consistent with what observed for dry granular flows.

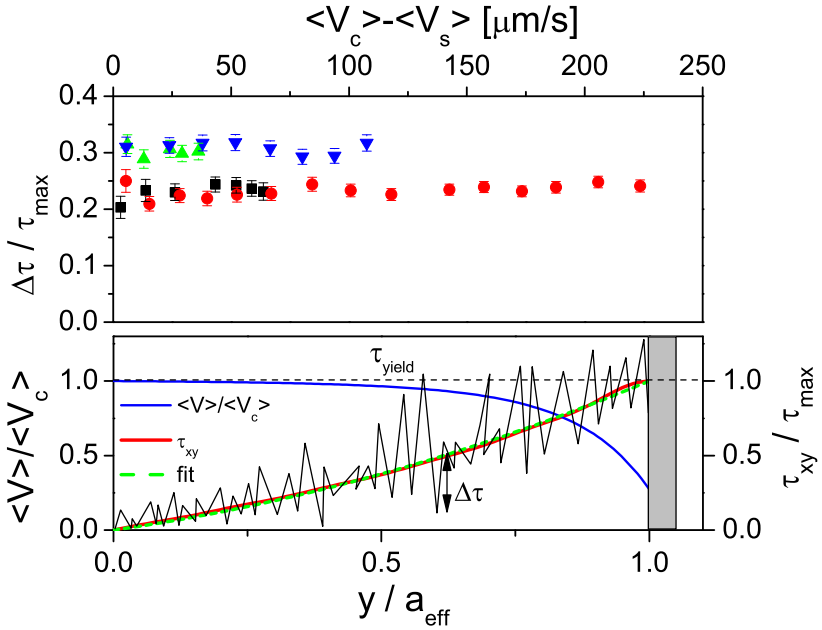

Figure 7.20: (Top) Fitted fluctuating stress amplitude $\Delta\tau$ in units of $\tau_{\max}$ as a function of the 'net shear', ΔV; ■ and ● two runs for smooth walls, ▲ and ▼ two runs for rough walls. (Bottom) Schematic of the fluctuating shear stress superimposed on the continuum τ_{xy}. The dashed line shows the quadratic fit used for the integration of equation 7.11. In the zone where the fluctuating stress overcomes τ_{yield}, flow results.

Figure 7.21 is analogous to Figure 7.3 but now the solid lines are fits obtained from Equation 7.13. In the inset we report the size of the shear zones b as a function of ΔV calculated on the new fits; this yields substantially an analogous result to the data obtained with the polynomial fitting, the only difference being slightly higher values of b due to a more pronounced curvature in the centre of the channel.

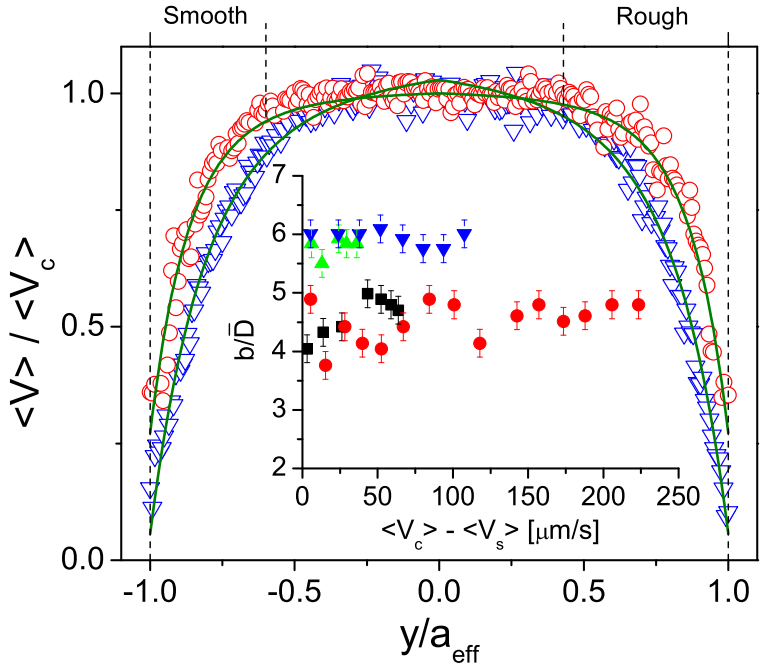

Figure 7.21: Examples of averaged velocity profiles as a function of y/a_{eff} for smooth (○) and rough (▽) walls at $z = 17\mu$m ($z/a_{\text{eff}} = -0.32$) for a sediment flowing in a channel with cross section of $50\mu\text{m} \times 50\mu\text{m}$. Full lines: fits obtained from equation 7.13; Vertical dashed lines: extents of shear zones. Inset: width of shear zone in units of particle diameters as a function of ΔV. ■ and ● two runs for smooth walls, ▲ and ▼ two runs for rough walls.

The scaling of $\Delta\tau$ with the wall stress has a stronger effect than just the constancy of b; in fact $\Delta\tau$ effectively sets the shape of the velocity profile. In other words as a consequence of the results of the analysis above, the flow profiles for the two boundary conditions should collapse onto two master curves when appropriately rescaled. Figure 7.22 shows exactly this. For clarity reasons the fitted profiles are plotted here instead of the raw data, but the presence of two master curves is evident.

We have therefore demonstrated that extending the original Pouliquen and Gutfriand's model to our geometry predicts indeed a velocity independent shear zone. Starting from what is discussed above, we can then comment on the other issues that have arisen during the previous data presentation.

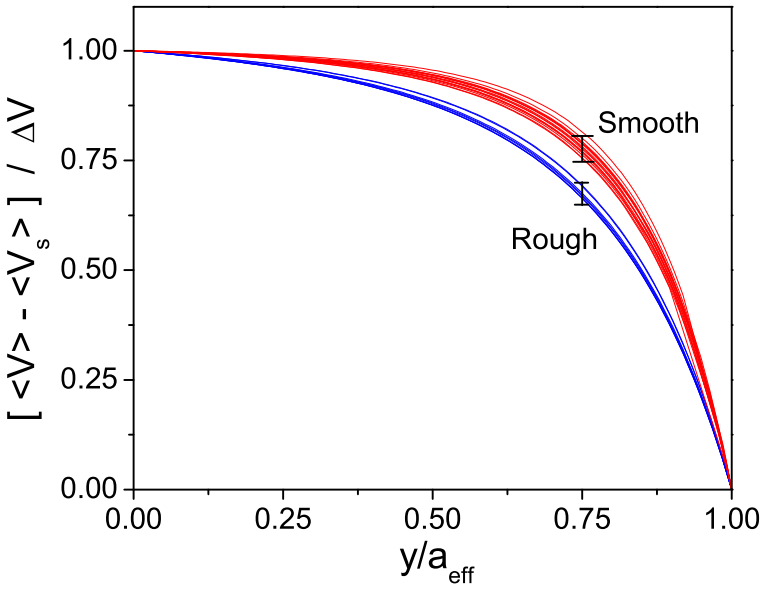

Figure 7.22: Normalized velocity profiles at $z = 17\mu$m as a function of y/a_{eff}. We use the fitting profiles from Eq. 7.13 instead of the raw data for clarity; the typical spread of the measured profiles in each case is indicated by the error bar ($\pm 2\sigma$).

The approach presented here can be also successfully applied to other flow geometries. In particular we will briefly describe the case of 2D-like flows and the case of Couette geometry.

The former constitutes the original geometry for which Pouliquen and Gutfriand initially developed the model and it also applies to the case of channels with rectangular cross sections and large aspect ratios. Recapping the results described in Chapter 3, we recall that in a 2D channel the shear stress varies linearly from 0 in the centre to its maximum at the wall. If we are sufficiently far from the bottom of the channel, this situation also applies to rectangular channels. Using this, Eq. 7.11 can be analytically integrated and leads to

$$\begin{aligned} V(y) &= k_0 \int dy \, \exp\left[-\frac{\tau_{\text{yield}} - |y|)}{\Delta\tau}\right] + k_1 \\ &= \tilde{k}_0 \, \exp\left[-\frac{\tau_{\text{yield}} - |y|)}{\Delta\tau}\right] + k_1 \, , \end{aligned} \tag{7.14}$$

which gives the exponential profile used to fit the data in Figure 7.17.

Let us now examine the results of this analysis applied to a Couette geometry. The motivation of this further extension relates to the work of of Huang et al. [45] who studied the Couette flow of dense non-Brownian suspensions. They report deviations from ideal continuum velocity profiles and find that an un-sheared portion of the system

is present at the outer cylinder. Moreover, they observe a rate dependence of the size of the un-sheared part at low rates which then becomes rate independent at high rates, when basically the (non-uniform) shear extends throughout all the gap. When rescaling the measured velocity profiles by $(R - R_i)/d_c(V_i)$, where R is the radial coordinate, R_i is the radius of the inner cylinder and d_c is the extent of sheared material function of the speed of the inner cylinder (V_i), they all collapse on a single master curve.

The measured velocity profiles seem to follow an exponential curve as found in previous works for dry granular material [188, 189]. In particular Losert et al. [189] describe their profiles by using a continuum model where the presence of density gradients and the effect of local velocity fluctuations affect the local viscosity and lead to velocities exponentially decaying from the inner cylinder.

We want to show that the simple model presented above is also able to qualitatively reproduce the velocity profiles in Couette geometries. Given the continuum stress distribution in a Couette cell, Eq. 7.11 can be integrated analytically. The shear stress $\tau(R) = \tau_i R_i^2/R^2$ and therefore

$$\begin{aligned} V(R) &= k_0 \int dR \exp\left[-\frac{\tau_{\text{yield}} - \tau_i R_i^2/R^2}{\Delta\tau}\right] + k_1 \\ &= \tilde{k}_0 \left[R \exp\left(\frac{R_i^2 \tau_i}{\Delta\tau R^2}\right) + i\sqrt{\frac{\pi\tau_i R_i^2}{\Delta\tau}}\text{erf}\left(\frac{i}{R}\sqrt{\frac{\tau_i R_i^2}{\Delta\tau}}\right)\right] + k_1 \,. \end{aligned} \quad (7.15)$$

Figure 7.23 gives an example of what was just discussed. The inset to the figure reports the original data from [45] while the main body takes one of the data curves and shows the different fits: the ideal Newtonian behaviour, the exponential profile and the one obtained from Equation 7.15.

The model proposed here presents itself as a simple approach to examine dense frictional flows in a range of experimental geometries, basically characterizing them in terms of only one parameter, the amplitude of stress fluctuations $\Delta\tau$.

This model lays its basis on the presence of stress–propagating, frictional contacts between the particles and we expect such events to take place only if the volume fraction of the suspension is sufficiently high. One of the advantages of working with suspensions as opposed to dry grains, is that the concentration of the system can be easily tuned, allowing us to explore the effects that changing the volume fraction has on the flow. As the volume fraction of the suspension is lowered we expect the velocity profile to get closer and closer to the shear-thinning one (or to the Newtonian one for really dilute systems) for which, with our criterion, the "shear zone" has also constant width. Figure 7.8 shows that the size of the shear zone b is constant for all the applied rates for all the volume fractions investigated and it also reports the size of b for a shear-thinning

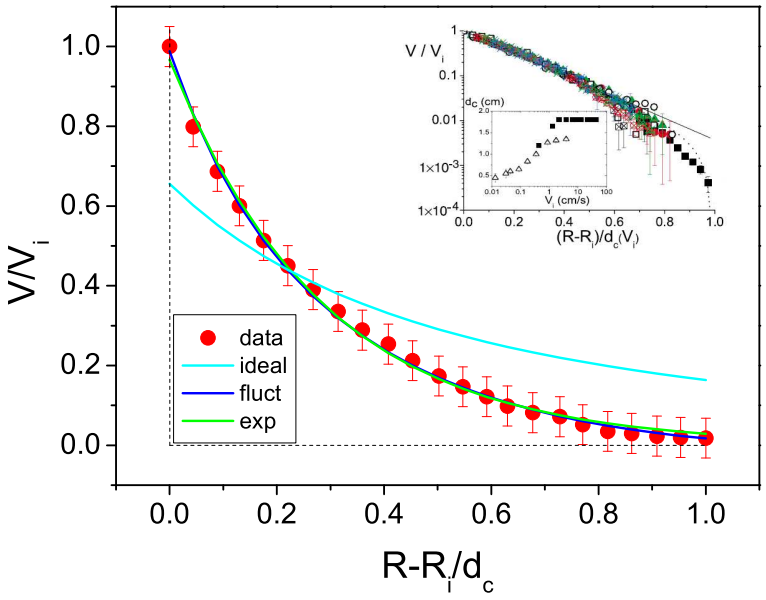

Figure 7.23: Inset: data from [45] giving the velocity profiles as a function of the normalized radial distance ($(R - R_i)/d_c(V_i)$), with R_i inner cylinder radius and d_c extent of sheared material) in a Couette experiment. The sheared system is a dense suspension of non-Brownian particles. The solid line is an exponential and the dotted one a power law fit. Body: • data points from the inset corresponding to ▲. The solid lines are fits to the data with the Newtonian profile (ideal), an exponential profile (exp) and a profile calculated from Eq. 7.15 (fluct).

and a Newtonian fluid calculated according to our criterion (dashed and solid lines). For all the volume fractions but $\Phi = 0.43$, the measured values are well below the Newtonian case and the constancy of the shear zone can be fully addressed to contact dynamics. The 43% suspension shows a behaviour in accordance to the one predicted for a shear-thinning fluid with exponent $n = 0.65$.

Such a conclusion is also supported by the existing literature on the bulk rheology of hard sphere suspensions. As previously mentioned, typical Péclet numbers for our systems are of the order of 10 to 100; rheology experiments on analogous systems (PMMA hard spheres) with cone and plate rheometers showed the onset of shear-thickening in this Pe range for volume fractions above 50% [16]. In particular a recent investigation [57] showed that for volume fractions down to 43%, rough silica particles showed, not only shear-thickening, but also *dilatancy*. This system constitutes a good analogy to ours since the silica particle roughness measured by atomic force microscopy is comparable (a few nm) to the one arising from the presence of the polymer hairs on the surface of the PMMA particles. We identify dilatancy as a sign of the presence of direct or lubricated particle contacts and therefore we believe that in our experiments

the hypothesis of friction or contact dominated flow is valid. We also recall the discussion at the end of Chapter 6, where we introduced the concept of dilatancy onset for sheared granular packings [182] and the equivalence with the occurrence of shear-induced density inhomogeneities in confined systems. By comparing the value of the volume fraction for the dilatancy onset in granular systems ($\Phi = 0.555$) with the one for which a conventional rheological approach fails to reproduce our experimental data ($\Phi \simeq 0.56$), we have additional grounds to believe that interparticle contacts dominate the flow behaviour in the high volume fraction regime.

Lowering the volume fraction brings the system to a more dilute regime, for instance analogous to the one studied by Frank and co-workers [80], where we expect contact dynamics to play an irrelevant role. We also expect that for sufficiently small applied rates, the flow will stop being contact dominated and that it will recover its "colloidal" nature. This transition to non–contact dominated flows is strongly related to the shear-thickening/dilatancy transition and therefore dependent on the volume fraction and the Péclet number. The most immediate way of checking the presence of the transition is to look at slower flows and furthermore, since we expect to observe the transition at higher rates (Pe) for lower volume fractions, this should be easier for more dilute suspensions. This was the initial motivation for checking the volume fraction dependence but as observed from the data we were not able to reach that regime even for the 56% suspension. Looking at really slow flows has a series of practical difficulties which made those experiments infeasible. The other obvious way to reduce the Péclet number is to use smaller particles; this also presents technical difficulties, because in order to keep the same particle to channel ratio, the cross section of the capillary would need to be scaled by the same amount, running into the problems described earlier.

Concluding these remarks, we can summarize by observing that for all the experiments we carried out except the lowest volume fraction, the flow proved to be contact-dominated, justifying the use of the model. In terms of the results of the application of the model, the reported trend of b as a function of volume fraction is mirrored by a corresponding trend of $\Delta\tau$; in other words the amplitude of the fluctuations seems to be a decreasing function of the volume fraction, reaching a constant value at $\Phi \gtrsim 0.58$, Figure 7.24.

Finally we comment on the nomenclature we used in the discussion above. We have implicitly and somehow loosely identified the concepts of friction and contact. There is no Coulomb friction in the absence of contact, but stress propagation networks can also occur for frictionless grains [190]. We believe therefore that the approach described above applies more generally to the case of systems where stresses propagate inhomogeneously, regardless of the nature of the interparticle contacts; the details of the interactions will determine the specific character of the flows.

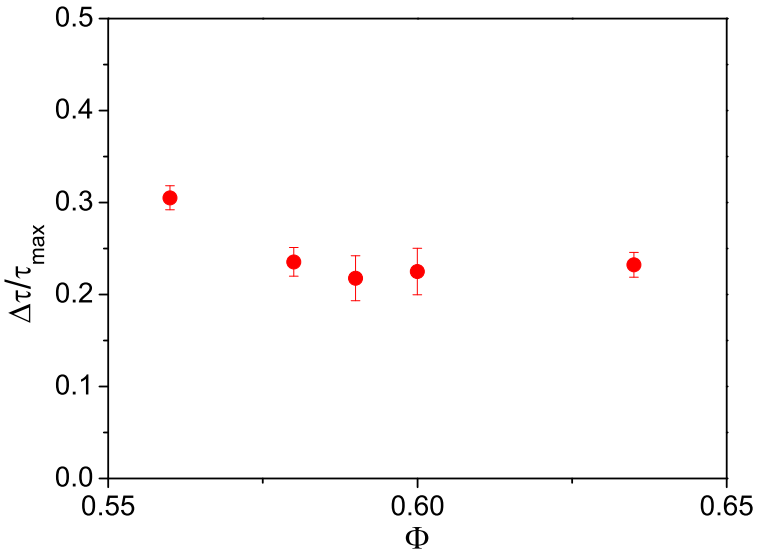

Figure 7.24: Mean value of stress fluctuations in units of the stress at walls as a function of the volume fraction of the flowing suspension.

7.2.4 Differences between friction-dominated colloidal flow and dry granular flow

Up to this point, the results obtained by applying the model to our suspension basically lead to findings analogous to what we obtained for the dry granular media; the lack of rate dependence and the width of the shear zones of the order of few particles are typical signatures of frictional dry granular flows. Despite this, when we analyse the results for b as a function of channel width, differences emerge. The literature for dry granular media shows that the size of the shear zones depends weakly on channel width [95, 98], increasing slightly for larger channels. Our experimental results show a different trend, exhibiting linear growth of b versus a. This trend is not an artefact of the analysis procedure, but comes straight from the raw data. Figure 7.25 shows b as a function of channel size for our experiments, for the data present in [98] and for more refined modelling approach in [94]. The difference is evident. We have now to ask ourselves what is the reason of such difference.

We firstly highlight the presence of some variations between our modelling approach and the original one. In their original paper, Pouliquen and Gutfriand wrote Equation 7.3 and 7.4 by a-dimensionalising the stresses by a fixed quantity, namely the stress acting on a single particle and as a result of this their expressions for the stresses are channel size dependent. Furthermore their analysis proceeded backwards; they selected the value of $\Delta\tau$ for all the velocity profiles by fitting *one* velocity profile for a channel of a given width and used such value to produce curves for the other channel widths.

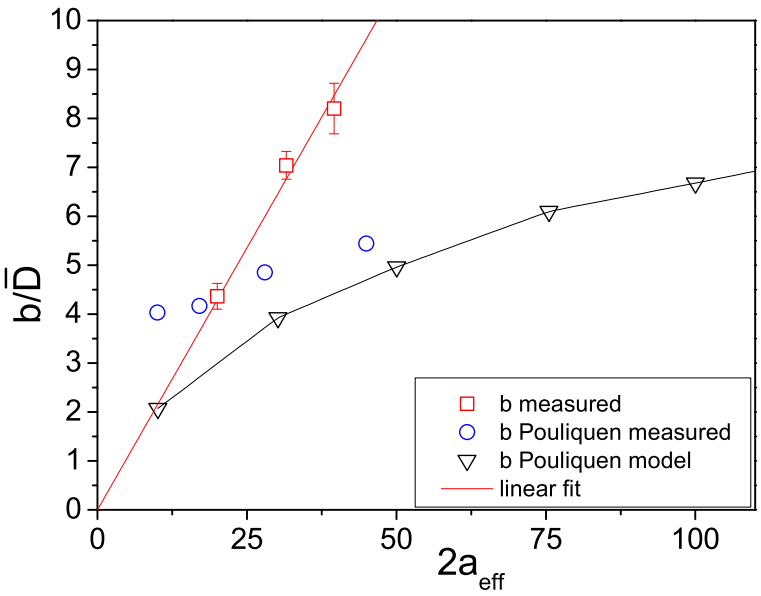

Figure 7.25: Size of shear zones b in units of particle diameters as a function of channel size for our data, for the data measured by Pouliquen [98] and from the modelling in [94].

By this procedure, they externally fixed the amount of fluctuations in the system and therefore selected the shape of the velocity profiles. Such procedure worked in their case because b (which is a proxy for $\Delta\tau$) was already known to be roughly constant from the analysis of the raw velocity profiles.

Our approach is instead different. Equation 7.3 and 7.4 are written in terms of y/a_{eff} (or z/a_{eff}) and in units of the maximum continuum stress at the wall τ_{max}; by doing this the continuum stress distribution is now independent of both applied stress and channel width. Applying the same normalization on the *measured* velocity profiles for different channel sizes, one observes that they collapse onto one single master curve given the same volume fraction and boundary conditions. We can therefore confirm a posteriori that the scaling we made was indeed correctly representing the physics of our problem.

After having clarified the variations in the approach to the model, we can comment on the nature of the difference in the results. We remind the reader that for our colloidal systems *the calculated amplitude of the fluctuations $\Delta\tau$, and therefore b, scales with the applied stress*, which is proportional to the applied driving force (pressure gradient or gravity) and to channel width. This does not apply to dry grains where, we repeat, b depends only weakly on channel size and thus depends on the applied stress. But where does this intrinsic difference come from? While we are not in possession of a

definitive answer to this question, we can still speculate starting from the following considerations.

The structure and the dynamics of dry granular media are only dictated by the contacts between the grains and by the local structure. The presence of interparticle contacts is *independent of the state of flow* of the material; contacts and force networks are present also in the quiescent state [186]. Moreover dense granular flows are *quasistatic*, meaning that the only important factor is the deformation the system experiences and not the path (or the rate) followed [98]. A continuous deformation or a series of steps are equivalent.

The situation for a suspension is different. We are in the presence of direct or lubricated contacts *only by virtue of the applied shear*. In the quiescent state contact networks are absent and the frictional regime is thus expected to take place only in the presence of shear thickening and dilatant flows.

What we remarked above determines the crucial point of the distinction between grains and colloids: the presence and the amplitude of the stress fluctuations $\Delta\tau$ for the dry granular case are fixed by the interparticle friction and by the local structure, for colloidal suspensions they exist only as a direct consequence of the applied shear. This implies that for dense, quasistatic granular flows $\Delta\tau$ is *independent* of the applied stress and equivalently of channel width. For colloidal suspensions this implies instead that $\Delta\tau$ *scales* with the applied stress and therefore with channel size. The description up to Equation 7.8 is identical for both cases, but the nature of $\Delta\tau$ is different.

Moreover, for dry frictional grains, there exists a static yield stress, consequence of the structure and of the interparticle contacts. For glassy colloidal suspensions there also exists an apparent zero rate yield stress but its nature is of a completely different origin (see Chapter 2) and we have seen how it is not relevant for the description of our rapid flows (failure of H-B modelling). One can mistake the rate independence of our experiments for quasistatic flows but the two are intrinsically distinct. If given enough time, for instance, shear-induced stress-bearing structures or density inhomogeneities will eventually relax due to Brownian motion; it is not equivalent for a suspension to undergo fast shear or being subjected to a sequence of small strain steps between which the system is left to equilibrate.

We furthermore note that for granular flows, b is not truly constant but depends weakly on channel width; increasing the distance between the two solid walls of the channel leaves the interparticle interactions unchanged but can allow for longer range particle rearrangements. We expect then to have complete size independence in the limit of very large channels [94].

Finally Figure 7.14 tells us that the values of b scale with channel size for every z.

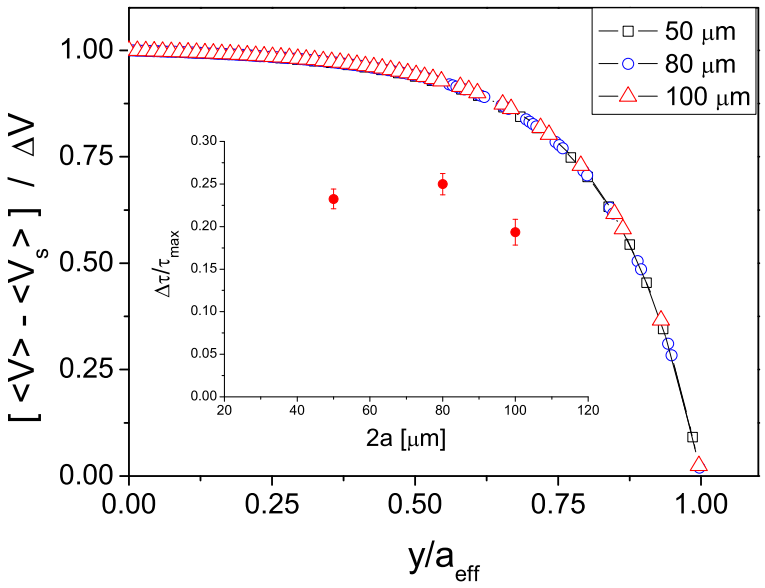

Figure 7.26: Example of normalized velocity profiles (polynomial fits) for the three channels sizes. Inset: $\Delta\tau/\tau_{\max}$ as a function of channel size.

7.2.5 z-dependence of b: a simple explanation

We turn now to investigate the role played by volume fraction and boundary conditions on the z-dependence of the width of the shear zones. We comment on the latter first. Looking at Figure 7.13 we observe that b increases monotonically towards the walls for a rough channel. The increase can be explained in the following way: let us consider a particle in the first layer close to the bottom and to one lateral wall (see Figure 7.27); by virtue of flowing onto the three-dimensionally rough bottom surface, the particle acquires a "bumpy" motion not only transversally (i.e. in the z direction) but also parallel to the wall (in the y direction). The contribution to the fluctuations in the particle's y positions coming from the lateral walls remains the same at every depth, while the one coming from the bottom (and the top walls) decays as we move deeper into the channel until it becomes z-independent and the size of the plug remains constant[7]. The origin of the fluctuations lies in the relative motions between the particle layers; in the case of rough walls these are transmitted by the motion of the first layer onto the coating layer and decay towards the centre as just described. The situation for smooth walls is slightly more complicated; the first layer of particles is sliding smoothly onto the inner glass surface and it is the relative motion between the first and the upper layers which will induce the fluctuations. At high packing fractions, the first layer of particles is generally arranged in a tightly packed crystalline fashion and therefore the

[7] A completely analogous description is valid for the y-dependence of z fluctuations.

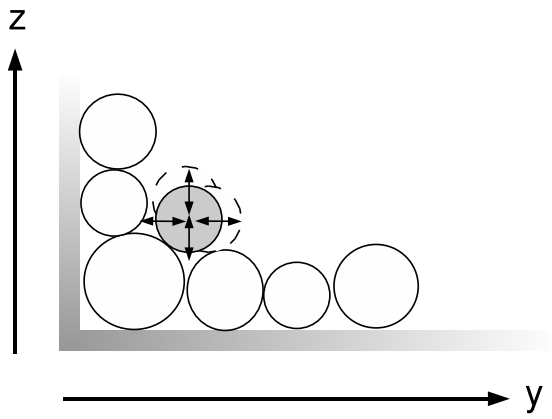

Figure 7.27: Sketch of the "bumpy" motion of a particle (in grey) flowing in the proximity of rough walls. The particles attached on the bottom wall induce fluctuations in both y and z positions.

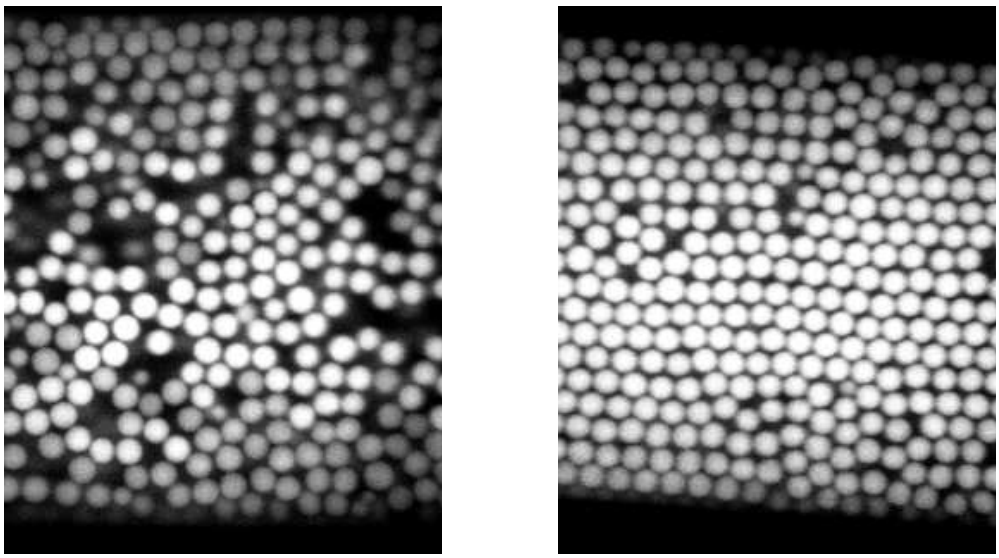

Figure 7.28: Confocal images of the first layer of particles in a 50μm $\times$ 50μm smooth channel; $\Phi \simeq 0.43$ (left) and $\Phi \gtrsim 0.635$ (right).

subsequent surface roughness is lower than of a disordered counterpart; after the first layer, the crystalline arrangement within the layer is quickly lost in favour of a more disordered one. This fact is responsible for the initial rise in b as a function of z for smooth-walled channels; the motion of the second layer of particles onto the ordered first one induces less fluctuations then the relative motion between the third and the second one, and then the mechanism described above for the rough walls is responsible for the decrease in b towards the centre (Figure 7.28). Finally we observe how the values of b in the centre are identical in this case; as already said earlier, for these measurements the coating particles were identical to the flowing ones and therefore the boundaries induced fluctuations of the same amplitude. We can then describe the results in Figure 7.12 within the same framework. In particular, when the volume

fraction is lowered, the first layer of particles presents a more disordered structure (and therefore the initial rise is reduced) moving the observed z-dependence of b towards a monotonic one analogous to the rough walls case. As Φ is reduced the width of the shear zone increases and it is less sensitive of the depth.

7.2.6 A microscopic description

The modelling approach we followed relies on the presence of fluctuations in the stress distribution which originate from the 'granularity' of the suspension; the stress distribution is not uniform but depends on the local particle contacts and arrangement. Numerical simulations [184] and experiments [185, 186, 187] for dry granular systems show non-uniform stress networks and presence of force chains. Such stress measurements are not accessible via our experimental technique but we can otherwise analyse position (or velocity) fluctuations. In order to relate stress and strain we need a local constitutive relation, which again is not available experimentally, but we can still expect to gather information about $\Delta\tau$ by looking at the velocity fluctuations. In the following figures we will analyse the behaviour of particles in the comoving frame of reference both for smooth and rough channels and map the observations relative to the velocity fluctuations onto corresponding considerations relative to the stress propagation and fluctuations.

Figure 7.29 and 7.30 show the normalized distributions of the absolute values of the transverse component of the velocity $V_{\mathrm{y}}^{\mathrm{cm}}$ calculated in the comoving frame of reference for different time intervals of varying average flow speed (ΔV) for smooth and rough-walled channels respectively. The values of $V_{\mathrm{y}}^{\mathrm{cm}}$ have been calculated on the total particle y displacements over five frames [8]. In both graphs we observe that the width of the distribution increases as ΔV does. We can think of these distributions as related to the distribution of stress. The y-motion of particles is regulated by them bumping into neighbouring particles (see Figure 7.18) and higher local shear makes such bumps more likely to happen; transverse motion and particle contacts give rise to local structure fluctuations and stress fluctuations.

The shape of the velocity distributions seems to be composed by a Gaussian part at low $\langle V \rangle$ and exponential tails at higher speed. This distribution has been observed also in simulations by Jens Harting and Hans Herrmann [191].

[8] Frame by frame and two frames by two frames displacements gave rise to more noisy data, while evaluating on more frames did not lead to any significant difference.

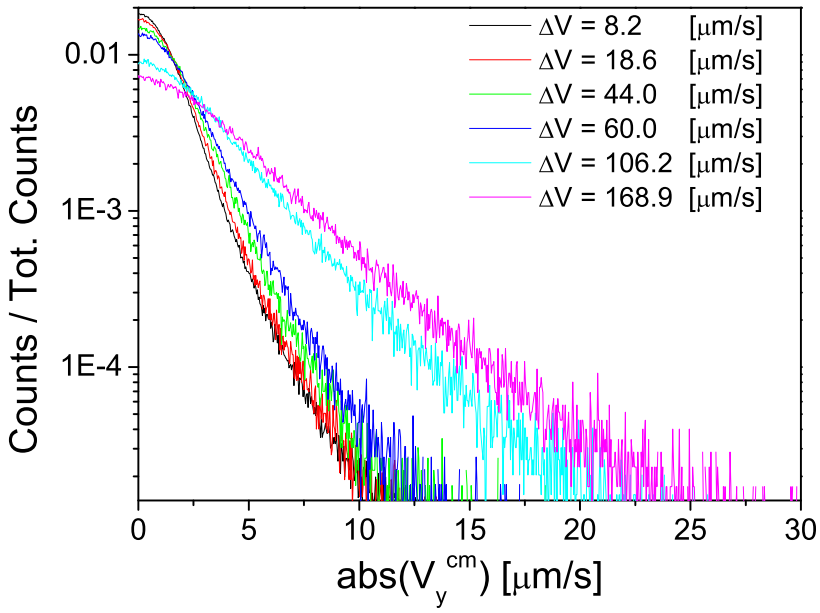

Figure 7.29: Normalized distribution of the absolute values of the transverse component of the velocity V_y^{cm} of all the particles in the field of view calculated in the comoving frame for different the average flow velocities reported in the legend at $z/a_{eff} = -0.32$. The data refer to smooth channels.

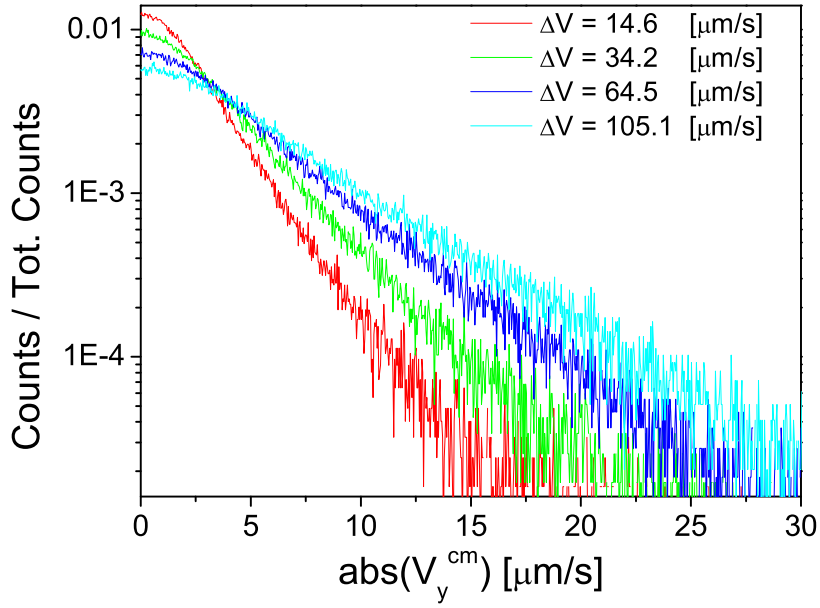

Figure 7.30: Normalized distribution of the absolute values of the transverse component of the velocity V_y^{cm} of all the particles in the field of view calculated in the comoving frame for different the average flow velocities reported in the legend at $z/a_{eff} = -0.32$. The data refer to rough channels.

We also recall that the values of $\Delta\tau$ we obtained from our measurements were constant as a function of the applied rate in units of the maximum shear stress; since $\tau_{\max}$ scales with ΔV, the amplitude of the fluctuations $\delta\tau$ is a linear function of the applied rate. Figure 7.31 shows the values of the full width at half maximum (FWHM) of the velocity distributions reported in the previous figures as a function of the average flow velocity both for the case of rough and smooth walls. We notice how the values for the rough walls are larger than the ones extracted from the flows in smooth channels, but above all we notice that the amplitude of the velocity distribution is a linear function of applied rate with an offset at zero speed. The offset is comparable to our tracking accuracy; in fact the extrapolated values correspond to frame-by-frame displacements of 13 and 19 nm for the smooth and the rough case respectively. Such values are roughly equal to one tenth of a pixel which was previously given [155] as the resolution limit of our particle locating procedure; the slightly larger offset for the rough walls case can be ascribed to additional inaccuracies due to the presence of the larger coating particles (higher polydispersity). The successive linear dependence is instead purely due to the presence of shear; the higher shear implies that particles bump into each other more, increasing the transverse displacements and the spread of the velocity distributions. The linearity suggests once more the link between the presence of stress and displacement fluctuations.

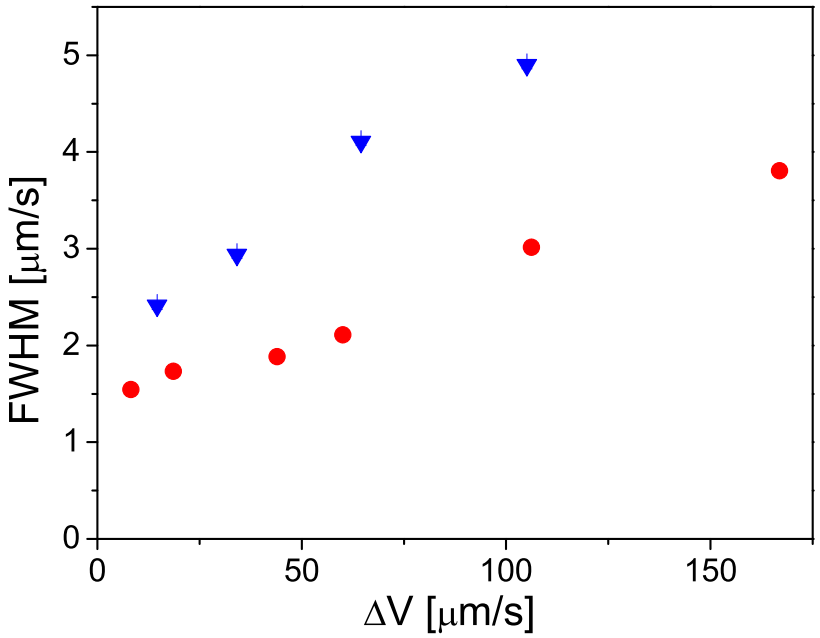

Figure 7.31: FWHM extracted from the distributions reported in Figures 7.29 and 7.30 as a function of flow speed. Bullets correspond to smooth channels, triangles to rough ones.

Figure 7.32 reports the standard deviation of the transverse component of the velocity in the comoving frame (δV_y) normalized by its maximum value (δV_y^{max}) both for the smooth walls (●) and the rough walls (▼) case. We can consider this quantity as a proxy for quantifying the velocity fluctuations in the transverse direction as a function of y/a_{eff}. We have already pointed out in Figure 7.31 that the average amplitude of the velocity fluctuations at a given flow rate is larger for rough-walled channels; by normalizing (δV_y) to its maximum value, we analyse its relative contributions as a function of the distance from the channel walls.

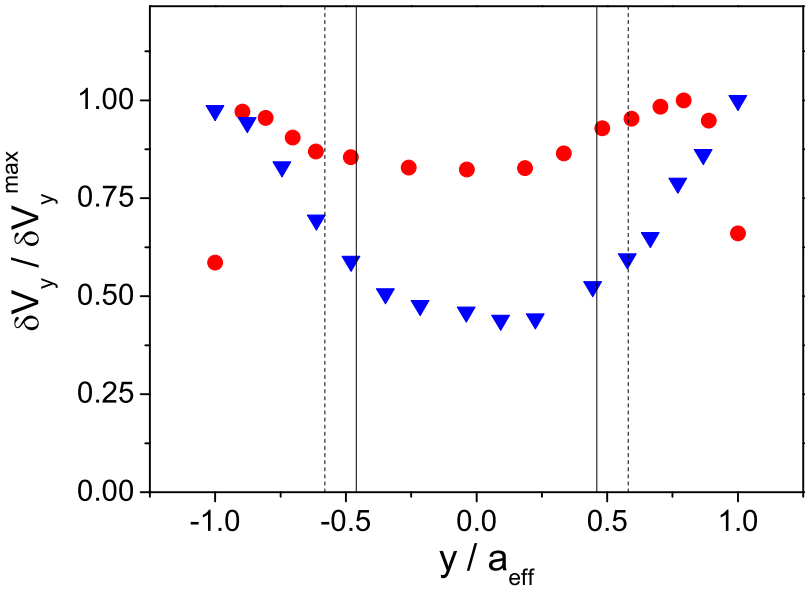

Figure 7.32: Standard deviation of the transverse velocity in the comoving frame (δV_y) normalized by its maximum value δV_y^{max} as a function of y/a_{eff} at $z/a_{eff} = -0.32$. Bullets correspond to smooth channels, triangles to rough ones. Particles have higher mobility close to the walls. Rough walls induce fluctuations with longer decay. The vertical lines mark the average width of the shear zones for smooth (solid) and rough (dashed) boundaries.

We can observe two main features. Firstly we note that the two distributions have a different shape. Starting from the smooth walls case, we observe that the amplitude of the fluctuations rises from the channel walls to reach a maximum and then decays towards the channel centre. The data points at $y/a_{eff} = \pm 1$ correspond to the first layers of particles in contact with the smooth glass walls; since these particles are sliding onto a smooth surface we do not expect to find large fluctuations in the transverse direction. The particles in the second layers second instead bump onto the first ones acquiring large transverse velocity components; as we move away from the wall, the relative motion between adjacent layers decreases and the fluctuations with it. Conversely, for

the rough walls case, the first layer of moving particles already flows onto the rough boundary constituted by the coating particles and therefore the fluctuations only decay towards the centre. The second difference can be found by looking at the the decay length of the fluctuations; in rough-walled channels the fluctuations have a longer decay length compared to the smooth case. The vertical dashed and solid lines highlight the average width of the shear zones for smooth and rough channels respectively. The width of the shear zones is related to the presence and the decay of the velocity fluctuations. We also notice that the difference between the maximum and the value in the centre is also larger in the rough walls case. Similar findings are reported in [95] and references therein.

As a final comment we clarify further the relation between the quantities just discussed and $\Delta\tau$. We remark that $\Delta\tau$ is a measure of *the effective and not of the local* amplitude of the stress fluctuations and is not a function of the transverse position. The local stress fluctuations depend on the relative motion of the particles and therefore, given the non-uniform shear profile, on position. Zones where the fluctuations are larger are more likely to yield and therefore to show up as higher shear regions. The model we used gives instead an effective description of the nature of the shear zones, including the position dependence in the yielding probability distribution.

7.2.7 Summary

To summarize, we have measured the average velocity profiles of the flow of hard-sphere colloids of volume fraction ranging from nearly random close packing to 43% driven by a constant pressure in a micron-sized square channel by tracking the motion of individual particles using fast confocal microscopy. At all flow rates, we observed a central, almost unsheared 'plug', and peripheral shear zones. The width of the shear zone depended on the boundary conditions, the size of the channel and the volume fraction of the flowing suspension. In contrast to the prediction of yield-stress fluid rheology, the size of the shear zone remained constant as the flow rate was increased. We explained this by appealing to a model originally set up for the gravity-driven 'chute flow' of dry granular materials [98]. This model should be applicable in our case if the yield stress, τ_{yield}, is dominated by interparticle contacts and it therefore is valid for the high volume fraction regimes. It predicts that stress fluctuations can bring about yielding even when the average stress is below τ_{yield}. Quantitative fits to our data were obtained. The behaviour of sample at 0.43 volume fraction could be described by a shear-thinning power law model. We also pointed out the differences between our colloidal suspensions and dry grains, the main one being a linear dependence of the shear zones width with the channel size in contrast to what observed for granular

systems. This observation lead to the discussion of the origins of interparticle contacts in colloidal systems highlighting an intrinsic difference with granular media. In the latter the existence of contact networks is independent of the state of flow whilst in the former is caused by the application of an external shear stress leading thus to a full dependence of the flow on the applied stress itself. We finally proposed a microscopic description of the stress fluctuations in terms of the position (velocity) fluctuations.

7.3 Concentration Profiles

The analogy with dry granular flow extends further than the constancy of the shear zone. In the gravity-driven 'chute flow' of dry grains, there exists a density profile across the channel, the 'plug' being $\sim 10\%$ denser than the edge of the shear zone [98]. This feature is also present in our flows. Figure 7.33 shows a typical density profile measured at $z = 17$ μm for a sediment flowing in a rough walls channel ($50\mu\text{m} \times 50\mu\text{m}$). This profile has been obtained by counting particles per unit area and averaging 10^4 frames and it is independent of the overall flow rate. The observed density reduction in the shear zone is not unexpected, since density inhomogeneities are required in flowing particulates (dry or wet) at such high packing fractions within confined geometries. It can be noted how the "density gradient" extends more towards the centre than the extension of the shear zones; this feature is also present in granular flows [98] but its origin remains unclear. Analogous density profiles are found in smooth walls channels, although their determination presents additional complications. As we have remarked several times already in the previous sections, in the presence of flat walls, the flowing suspension presents a high degree of layering, even for the lowest volume fraction studied. An example of this is reported in Figure 7.17. With the particles arranged in sharp, well-defined layers, the calculated concentration profile will strongly depend on the choice of the y-binning, giving rise to the presence of peaks whenever a layer is included in the count. Averaging on larger portions of the image reduces this problem, but also flattens the profile, resulting in a loss of information. The message remains though, that the density of the sheared region has a lower volume fraction than the 'plug' for both boundary conditions.

An alternative approach towards the measurement of concentration profiles is the one followed by [80] and it is based on quantifying particle density by measuring the total fluorescence per unit area. The measured intensity is proportional to the number of particles and therefore calculating concentrations should be a straightforward job. This method does not solve the layering problem, since also the measured intensity will be peaked around the layers and it furthermore incurs additional technical problems. Our confocal microscope does not provide a uniform laser illumination

of the field of view and therefore fluorescence gradients are present also for uniform distributions of particles; furthermore the quality of the image deteriorates slightly close to inner walls of the capillary. These inconveniences can be partly solved by image analysis but this approach did not seem to yield good results for our data. Frank et al. [80] were working with considerably less concentrated suspensions and did not seem to incur these problems; they were interested in studying the development of transverse concentration profiles due to flow (shear induced migration). By subtracting a background fluorescence profile obtained in the absence of motion, they were able to identify any variations induced by the flow. Unfortunately all our data lie in a regime were these effects are not very pronounced.

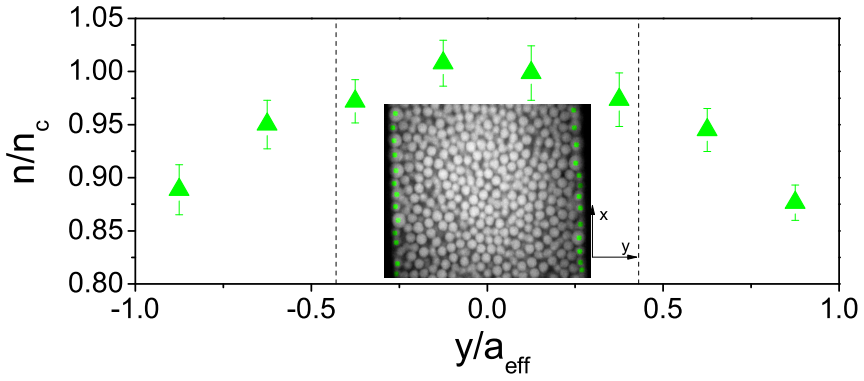

Figure 7.33: Average density profile at $z = 17\mu$m for a sediment flowing in a channel with rough walls. The density n is given in units of the density in the centre, n_c. The plug is $\approx 10\%$ denser than the edge of the shear zone.

7.3.1 Discussion: particle migration and shear-induced density inhomogeneities

Non-uniform concentration profiles are a common feature in particulate flows and, depending on the volume fraction of the flowing suspension, the mechanisms behind their origins are different.

In the low volume fraction regime non-uniform concentration gradients along the transverse direction are due to particle migration [80, 81]. We can intuitively think of shear induced migration in the following way: in channel flows particles immersed in a non-uniform shear flow and experience a higher shear rate on their side closer to the wall due to the parabolic velocity profile. If the local shear is higher the collisions between particles are more frequent and therefore, due to this unbalance in the shear profile, particles are subjected to more "kicks" on one side than the other and thus will be effectively pushed towards the channel centre. A more quantitative analysis uses a

balance between the shear-induced concentration gradient and the osmotic pressure; the equilibrium between the two determines the steady state concentration profile [80]. The build-up of such non-uniform concentration profiles depends on the volume fraction, with more dilute system requiring a larger accumulated strain to establish them [81].

On the other hand, in the high volume fraction regime, the mechanism responsible for a reduction of the volume fraction in the shear zone is the occurrence of shear-induced density inhomogeneities. We have already discussed in Chapter 6 the role played by shear in high density packings flowing within confined geometries. Referring for instance to the concentration profile reported in Figure 7.33 we observe an $\approx 10\%$ difference in the concentration between the boundary and the centre of the channel. In the light of what was discussed above we can try to estimate how much of this non-uniformity is due to particle migration.

In order to do this we can calculate a migration rate by counting how many particles in the shear zone undergo a transverse displacement larger than their diameter in the unit time. Since particles close to the walls are arranged in layers (in particular for smooth walls) the number of particles displaced in the transverse direction by more than their diameter corresponds to particles changing layer. For the case of rough walls this value is ≈ 8 % while in the case of smooth walls there are practically no particles exchanging layers. This fact already excludes particle migration in the latter case with the particles strongly confined in their layer.

A more detailed analysis also excludes it for the rough walls case; we divided the displacements larger than $\bar{D}$ between the ones going towards the channel centre and the ones going towards the walls. The two numbers were equal within experimental errors, showing no preferential motion of the particles towards the channel centre as in the case of shear induced migration. We can therefore conclude that for our flows at the highest density the effect of particle migration is negligible. Particles are mainly confined within their layer and acquire transverse motion by bumping into particles in adjacent layers as previously shown in Figure 7.18.

The question about the origins of non-uniform density gradients at intermediate volume fractions still holds and it is a point of fundamental interest to find a criterion which can give us a clue. Despite the absence of a well-established answer in the present literature, we believe that a crucial point is the occurrence of normal forces. In the case of dilatant flows, geometrical constrictions force the flowing particles into direct contacts giving rise to motion in the direction transverse to flow and therefore to the occurrence and propagation of normal stresses. In the case of shear-induced migration, the overall volume fraction is too low for such chains of particles to occur and therefore there are no normal forces associated to the presence of a density gradient. Normal forces could then act as a beacon for the presence of dilatancy or shear-induced

density inhomogeneities and in fact a number of numerical and experimental studies reported connections between shear thickening, contact networks and normal stresses [60, 17, 192, 61, 182].

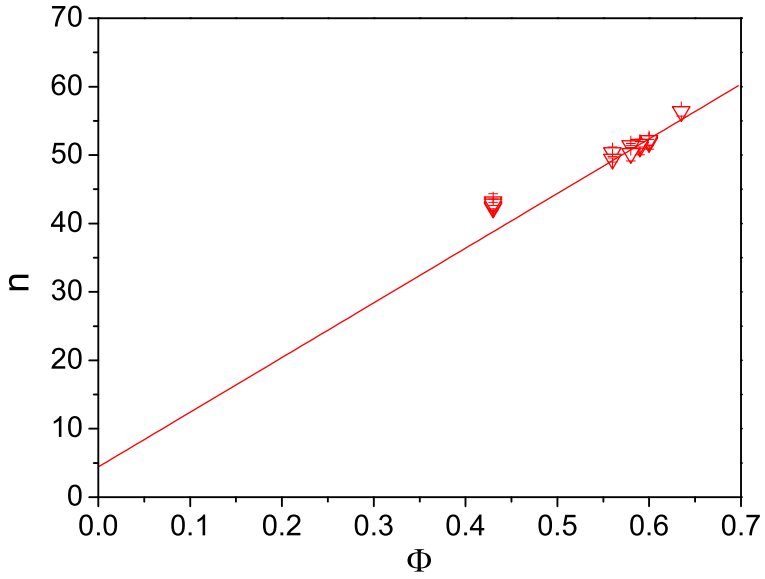

Figure 7.34: Number of particles in a five particles-wide y-bin in the centre of the channel as a function of volume fraction. The straight line is a fit to the high volume fraction points.

Since we cannot measure normal forces in our experiments, we can follow another approach to test the presence of particle migration. We measured the concentration (particle number n) in a five particles-wide bin centred around the channel axis for a series of volume fractions ranging from the sediment to 43%; such a width corresponds to the extension of the central plug for the lowest volume fraction sample defined by our criterion. If the concentration gradients were due to particle migration one could expect, in the high volume fraction regime, the concentration in the centre of channel to be only weakly dependent of the initial bulk Φ. Migration can "squeeze" particles together up to random close packing; the width of the zone where the maximum packing is reached is dependent on the initial bulk Φ but not the value of the maximum concentration. Figure 7.34 shows a different picture; the value of the concentration in the centre scales linearly with the initial volume fraction in the high Φ regime [9]. The data points at 43% deviate from the trend showing a higher concentration which suggests the presence of migration effects. As a last comment we add that in the lowest Φ experiments we were not able to register any dependence of the the concentration profiles on the flow rate as expected for particle migration due to the coverage of a small Péclet number range

[9] The non-zero offset for $\Phi = 0$ is within the fitting errors

compared to other studies [80].

We can finally speculate that, in the presence of shear-thickening, the occurrence of a low-concentration zone close to the channel walls is due to dilatant interparticle contacts. Finally linking this to our previous discussion on the validity of our model for the range of volume fractions we investigated, we can conclude that shear-induced density inhomogeneities play a major role in the build up of non-uniform density profiles for our flows in the high volume fraction regime.

Chapter 8

Time domain

Unlike dilute systems, dense suspensions can exhibit velocity fluctuations when driven into small channels by a constant pressure difference. In this chapter we examine the time behaviour of our colloidal suspensions flowing into square, micron-sized glass capillaries, especially focussing our attention on the flow of sediments ($\Phi \gtrsim 0.635$). We concentrate on complete plug flows, with the aim of finding a relation between the local structure and the flow. We initially present the methods we used to describe and quantitatively analyse the experimental data and we then report the evidence for velocity oscillations. Sections on detailed data analysis follow, accompanied by comments on the effects of boundary roughness, suspension volume fraction and channel size. We conclude this chapter by presenting a quantitative microscopic analysis of the structure of the flowing suspension in the presence of velocity oscillations and with further comments on the nature and origin of the oscillations themselves, focussing on the role played by the solvent.

8.1 Methods

The easiest way of following the flow is of course to look at the time series but for obvious reasons this presents some difficulties on printed paper! A clever way around it, commonly used in representing granular flows [116], consists in reporting what is known as a spatio-temporal diagram. These diagrams are images composed by stacking thin horizontal slices (1 pixel wide) taken from each frame at the same y position. The vertical direction then represents time, with each point corresponding to a frame, and the horizontal one is the x position in each image. If uniform motion in the x direction is present, each point in the slice will be displaced by a certain Δx between two successive frames (Δt); stacking many of these slices will give diagonal 'streaks' corresponding to the traces of the contents of each pixel as a function of time. Since

time is on the ordinate axis, the flow velocity $\Delta x/\Delta t$ is the inverse of the slope of the traces; more horizontal lines correspond to higher velocities and perfectly vertical traces correspond to the absence of flow since each feature is not displaced between successive frames. Figure 8.1 shows two examples of spatio-temporal diagrams of flows with velocity $V_2 > V_1$; the slope of the lines is constant throughout each image, because the flows is uniform in time (the diagrams refer to dilute flows where oscillations are not present, $\Phi \simeq 0.3$). In the original time series positive motion occurs from right to left so the direction of the traces. In the following sections we shall accompany these diagrams with the velocity measured from particle tracking (see Chapter 4). Despite the use of the latter for quantitative analysis, spatio-temporal diagrams offer a useful and quick graphic representation of time series in two-dimensional images.

Most of the data in the following sections refer to complete plug flows and since all the particles move coherently, the velocity of the plug is calculated by averaging the speed of all the particles in the field of view. All the velocity curves reported have been obtained in this way if not stated differently.

The original, frame by frame velocity traces are generally quite noisy due to a number of factors including, for instance, variable image quality, vibrations in the system and inaccuracies in particle tracking. In order to reduce this problem and to discern the genuine features in the velocity signals from instrumental/measurement noise, the signals are averaged over five frames (low pass filter) to eliminate short-time fluctuations. In most of the measurements, this means events with frequency higher than 20 Hz; we shall see in the next sections that the frequencies associated with the velocity oscillations are definitively lower (few Hz maximum) and therefore we are not discarding important parts of the signals. The low-passed signals are the ones reported in the following figures if not stated differently.

In order to characterize quantitatively the oscillations we calculated the power spectra of the velocity signals. The following standard procedure was used: we identified a DC–like offset or a slowly varying component in the low–passed signals (V) by averaging the data on time windows much larger than the oscillation period. This offset signal represents the average flow velocity in the absence of the oscillations ($\langle V \rangle$). We then subtracted the two ($V - \langle V \rangle$) obtaining an oscillating signal centred around zero and shorn of the high frequency noise. We finally calculated the power spectra by performing a Fast Fourier Transform (FFT). The FFT was preceded by triangular windowing of the signals to prevent finite size effects; the use of different windowing functions did not affect the results. Refer to Figure 8.2 for an example.

In the next sections we shall apply these methods to the experimental data and we shall look in detail at the velocity signals and their power spectra in order to characterize the different features emerging from the flows.

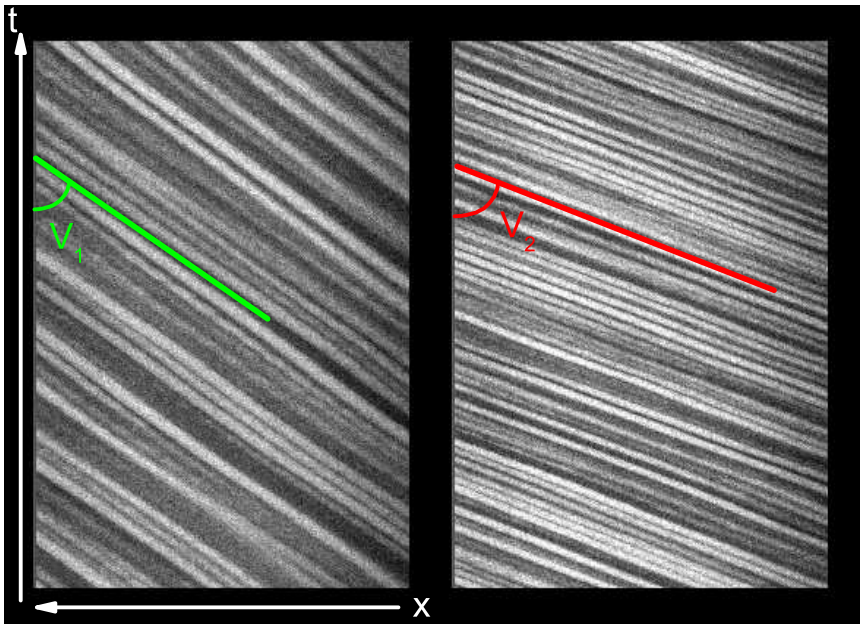

Figure 8.1: Spatio-temporal diagrams relative to two uniform flows $\Phi \simeq 0.3$. The slope of the traces left by the particles gives the flow speed. In this case $V_2 > V_1$. The images were taken at $z/a_{\text{eff}} = 0.32$ and a 50 μm long, 1 pixel wide strip along the centreline of the channel ($y/a_{\text{eff}} = 0$) was extracted.

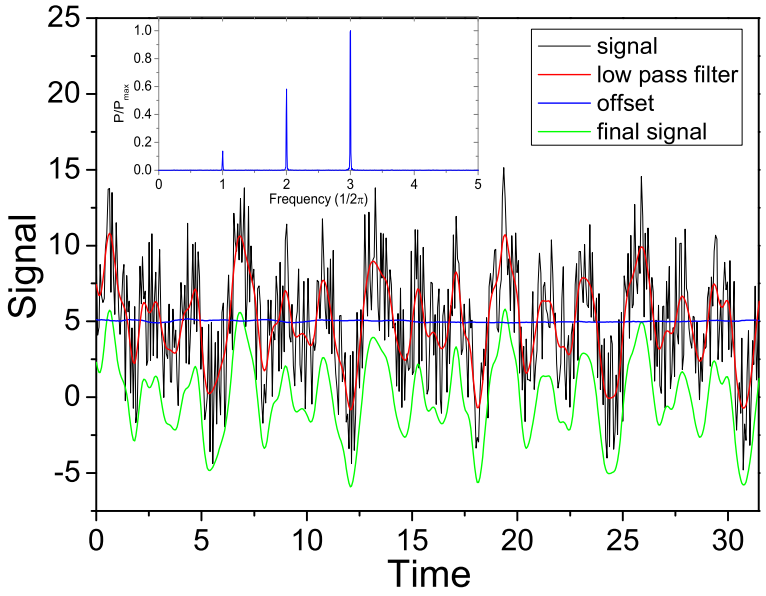

Figure 8.2: Example of the method for signal processing and FFT. The black curve is a signal obtained by superimposing three sine waves of frequency 0.5π, π, 1.5π and different amplitudes and randomly generated noise. The red curve shows the signal after the low pass filtering, the blue one is the DC-like offset and the green one is their difference. Inset: normalized power spectrum of the green curve.

8.2 Velocity oscillations

After introducing the procedures used for analysing the time behaviour of the flows, we now present the measurements. All the data refer to sediments of PMMA particles with $2.6 \pm 0.1 \mu$m diameter, in a buoyancy-matching solvent (see Chapter 5) and flowing into $50\mu\text{m} \times 50\mu\text{m}$ channels with smooth walls if not stated differently. The role played by channel shape will be briefly discussed and qualitative comments on volume fraction dependence will be reported. We shall finally analyse in detail the effect of boundary roughness. Most of the data come from analysing complete plug flows, but we shall also present data taken in different positions along the channel where shear is present.

The main point arising from these measurements is that *a dense suspension driven into a micro-channel with constant force does not flow with constant velocity.* In particular we shall see that, depending on the driving force or on the average local flow rate, the velocity of the suspension can present very regular oscillations; if the driving speed is maintained constant the suspension reaches a steady oscillating state where the frequency of the oscillations remains locked for as long as minutes.

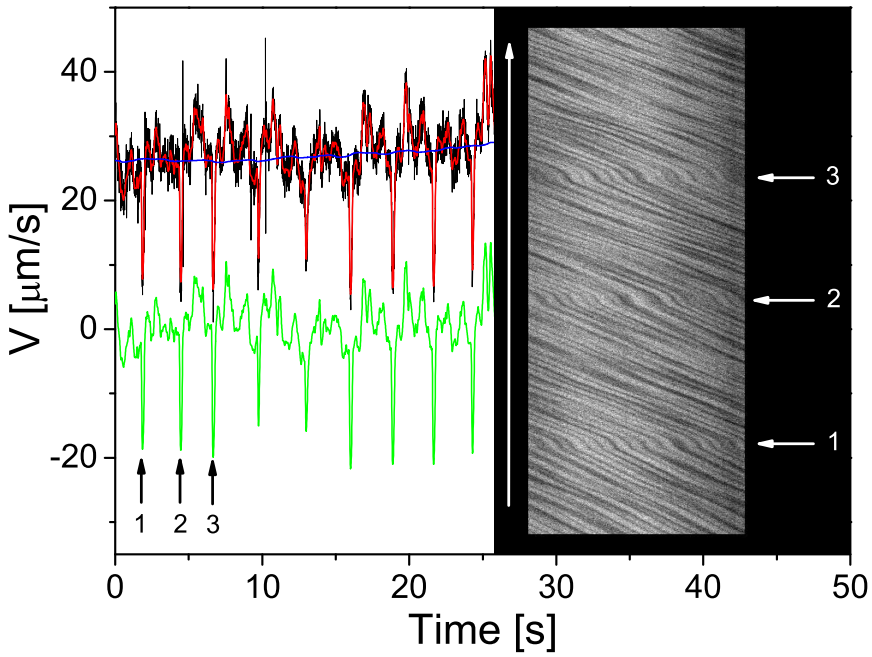

Figure 8.3: Example of oscillating flow for a 0.635 volume fraction suspension. The main body of the figure shows the measured velocity signal and the elaborated ones (colours as in Figure 8.2). Right: spatio-temporal diagram corresponding to the first 9 seconds of flow. The dips in the velocity signal are highlighted on the diagram. The images were taken at $z/a_{\text{eff}} = 0.32$ and a 44 μm long, 1 pixel wide strip along the centreline of the channel ($y/a_{\text{eff}} = 0$) was extracted.

Figure 8.3 shows a clear example. The blue curve gives the average flow while the black one is the measured velocity, obtained by averaging the speed of all the particles in the complete plug. It is clearly observable how the latter is not constant but presents instead regular dips corresponding to an almost complete stoppage of the flow. The spatio-temporal diagram on the right of the figure shows the first nine seconds of flow; the dips in the velocity signal correspond to the changes of slope in the traces. The lines become more vertical as a result of an appreciable slowing down; this constitutes the signature of what we will refer to as "jamming events" (jams); with such nomenclature we refer to events which result in considerable slowing down or in the arrest of the flowing suspension.

8.2.1 Results

We can now start to investigate the dependence of the frequency of the oscillations on the average flow rate. Figure 8.4 portrays the spatio-temporal diagrams for two portions of the flow corresponding to the velocity signal reported in Figure 8.7. The flows are clearly oscillating and we can observe, by comparing the slopes of the traces between the jams, that the left image refers to a slower flow. In addition to the simple presence of jamming events, it is also immediate to observe that they occur more frequently in the right diagram (both diagrams span the same time interval). The inverse frequencies $1/f_{1,2}$ of the velocity oscillations are marked on the diagrams. We can finally note that also the duration of the jam $\Delta t_{1,2}$ depends on the average flow speed, with longer lasting jams for slower flows.

We can give a qualitative description of the dynamics of the velocity oscillations by looking at the traces in the diagrams. We observe, referring for instance to the left image, that, starting from a point between two jams, the flow speed decreases more or less smoothly and then abruptly falls; immediately after the flow quickly accelerates to bring the system back in the same conditions and the whole cycle repeats itself.

The same mechanism can be observed by examining the velocity signals. Figure 8.5 reports a first example. We started to record images at time $t = 0$ and, after roughly 4 seconds, we opened the valve which closes the tubing and applied a constant pressure difference of 10 torr (see Chapter 5). The initial spike marks the start of the flow; the suspension jerks forward and then settles on an oscillating flow regime where the average speed is slowly increasing in time. Figure 8.6 shows blow-ups of two sections of the signal in Figure 8.5. We have highlighted a portion of the signal in the right graph to present again the dynamics of the "jamming cycle" as described above. Starting from the left of the red ellipse, we observe that the flow speed decreases until it rapidly drops when the suspension jams; the flow then suddenly accelerates restoring the speed

roughly at the same level at which it was before the jamming and then the process is repeated. It can already be noted by comparing the two figures, that the frequency of the oscillations increases when the average speed increases, that is to say from left to right. Figure 8.7 reports another example of oscillating flows where it is particularly clear that the speed drops to almost zero during jams.

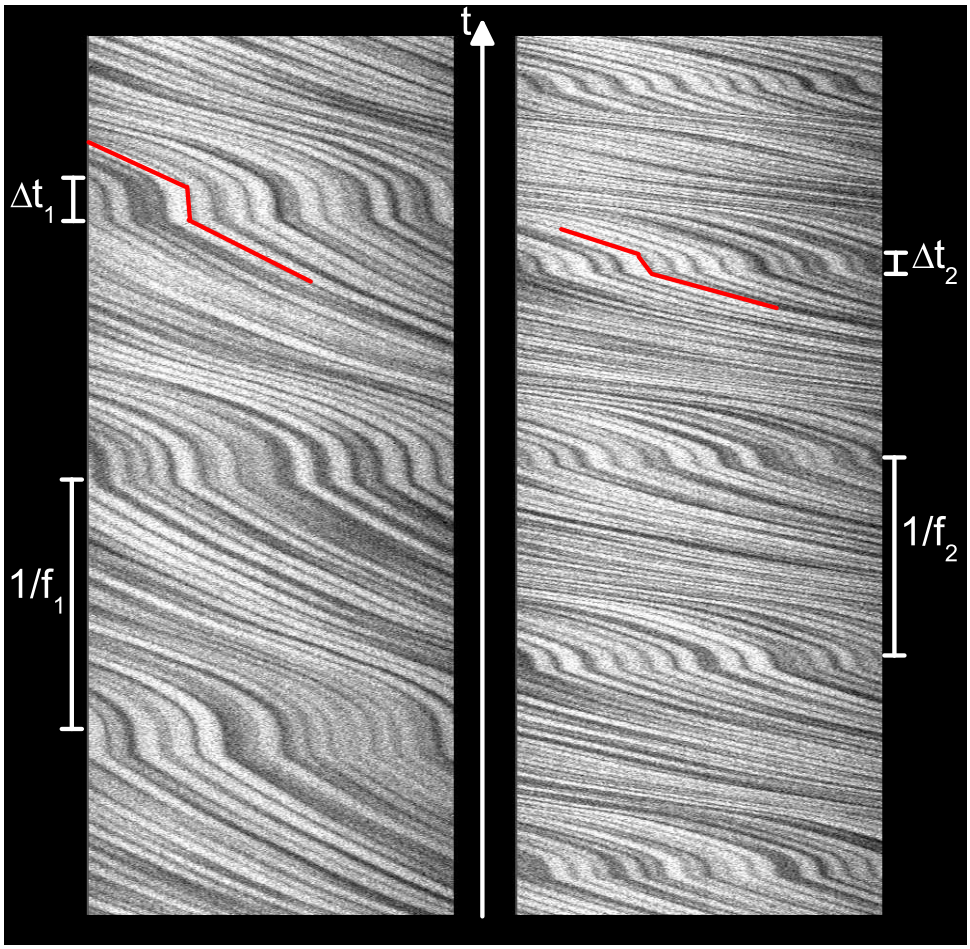

Figure 8.4: Spatio-temporal diagrams for two portions of the flow reported in Figure 8.7 corresponding to the time intervals 10 to 23 s and 50 to 63 s respectively. The average flow speed is lower for the left image. The inverse frequencies $1/f_{1,2}$ mark the time separation between jamming events, while $\Delta t_{1,2}$ are the respective durations of the jams. The images were taken at $z/a_{\text{eff}} = 0.32$ and a 44 μm long, 1 pixel wide strip along the centreline of the channel ($y/a_{\text{eff}} = 0$) was extracted. The initial applied pressure difference was 40 torr and $\Phi = 0.635$.

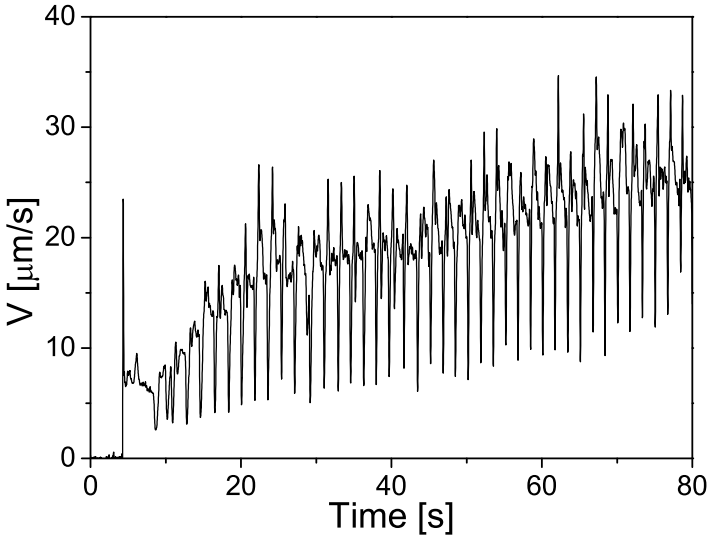

Figure 8.5: Flow velocity as a function of time. The initial applied pressure difference was 10 torr and $\Phi = 0.635$.

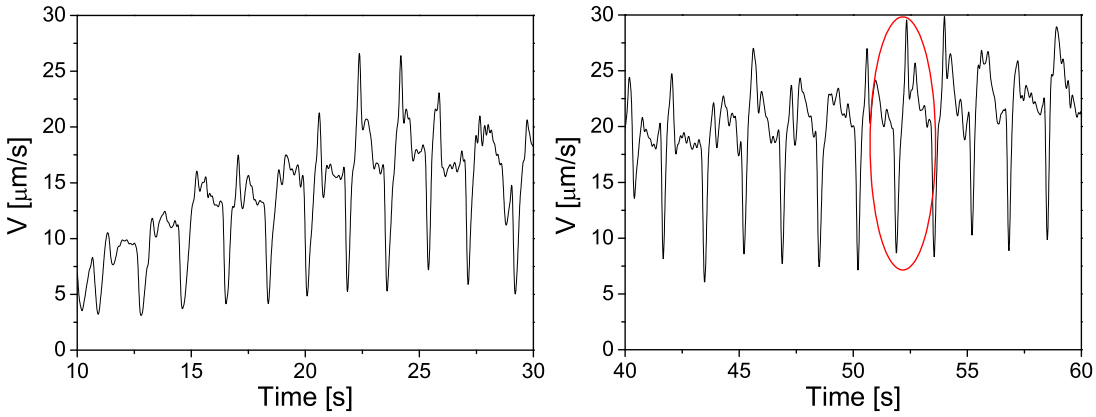

Figure 8.6: Velocity signal for two different time intervals from Figure 8.5. The red ellipse in the right figure highlights the events sequence associated with jamming and subsequent velocity oscillations.

In order to quantify the concepts just discussed, we analysed the power spectrum of the signal in Figure 8.5. The regularity of the oscillations mirrors strikingly into the frequency domain (Figure 8.8). The power spectrum is composed by a fundamental frequency and higher-order harmonics; the spread in the peaks reflects a slight frequency shift according to the average flow speed. In fact by looking at the inset to the figure, we observe how the peaks of the power spectrum move towards higher frequencies as the average flow speed increases from the signal of Figure 8.6-left (blue curve) to the one of Figure 8.6-right (red curve). Also the amplitude of the peaks increases.

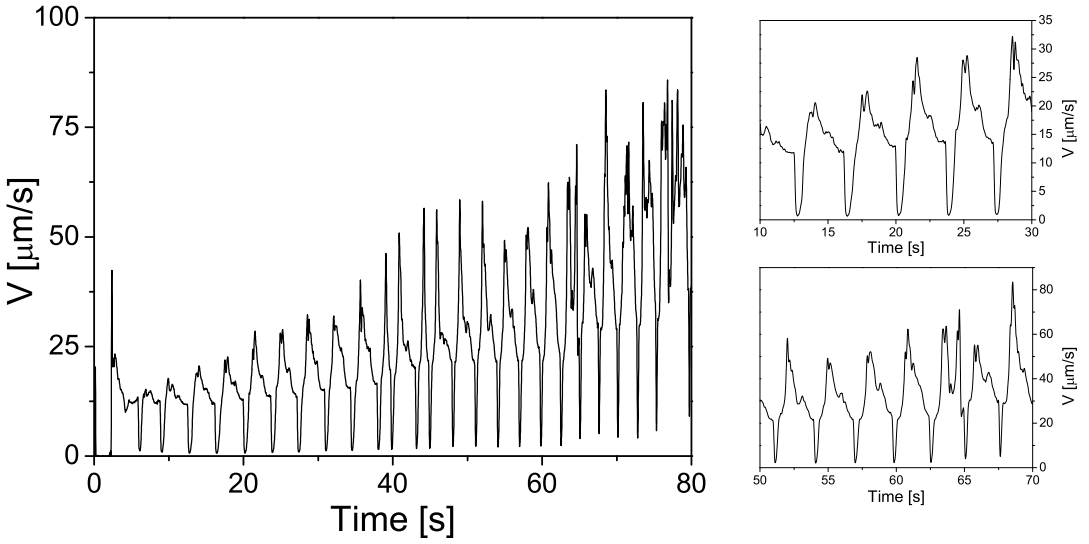

Figure 8.7: Another example of fluctuating velocity signal. The smaller graphs on the side are blow-ups of the main graph; note the different vertical scales. The spatio-temporal diagrams in Figure 8.4 correspond to portions of these signals. The initial applied pressure difference was 40 torr and $\Phi = 0.635$.

Figure 8.9 offers another approach to the information contained in the power spectrum reported in Figure 8.8. A small segment of the offset signal from Figure 8.5 is taken and then fitted using the superposition of pure sine waves with a fundamental frequency and corresponding harmonics. Fit 1 and 2 are obtained using only the first 4 harmonics, Fit 3 includes 6 of them. In Fit 1 and 3 we used the frequencies obtained from the power spectrum in Figure 8.8 (0.604 Hz, 1.216 Hz, 1.809 Hz, 2.420 Hz, 3.026 Hz and 3.625 Hz), in Fit 2 these are left as fit parameters but the calculated values are very close to the previous ones (0.6152 ± 0.0005 Hz, 1.2005 ± 0.0008 Hz, 1.712 ± 0.002 Hz and 2.415 ± 0.003 Hz). Also, two oscillation components are highlighted; the distance between the two main peaks (fundamental frequency) is exactly four times the oscillation between peak and valley (second harmonic). The important point to be taken from this discussion is the fact that the simple superposition of a few sine waves is able to qualitatively reproduce the gross features of the velocity signal.

Such a regular power spectrum is a common property of all the fluctuating velocity signals obtained during complete plug flow, where we reported here some of the clearest examples. We repeat that when the average flow speed was kept constant, regular oscillations were stable for minutes (the whole duration of the measurement).

We have already mentioned on several occasions that both the frequency and amplitude of the fluctuations increase as the average flow velocity increases. We shall now discuss these statements in more details.

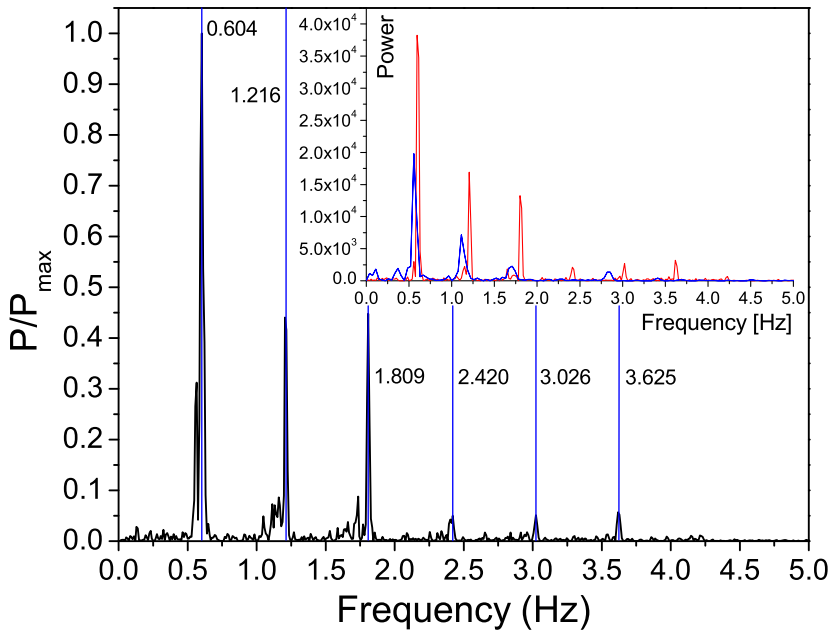

Figure 8.8: Normalized power spectrum for the velocity signal in Figure 8.5. In the inset we report the spectra for the signals in Figure 8.6 where the blue one is relative to lower speed than the red one.

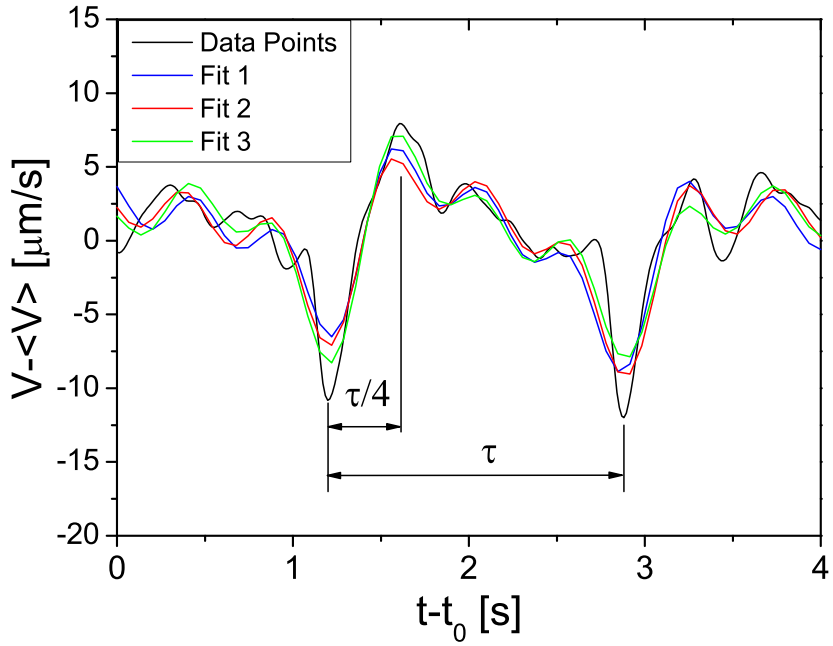

Figure 8.9: Blow up of 4 seconds of the offset velocity signal from Fig.8.5 with the correspondent fits obtained from the superposition of 4 (red and blue) and 6 (green) sine waves. $t_0 = 44$ s.

The driving pressures are applied relative to atmospheric pressure P_{atm}. In the following figure we report both the velocity signal offset by the long time average and the corresponding driving pressure. We started the flow, after applying an initial pressure difference $\Delta P_0 = P_{\text{atm}} - P(0)$ (we recall that $P(t)$ is the pressure at the head of the flowing suspension, see Chapter 5), and synchronized the pressure and velocity signals[1]. The applied pressure difference $\Delta P = P_{\text{atm}} - P(t)$ was varied during the flow. We can observe from Figure 8.10 that for small applied ΔP the offset velocity signal presents only noise while, as the driving pressure is increased above a certain threshold value, oscillations in the flow start to occur. By bringing the ΔP back to a lower level, the amplitude of the fluctuations was reduced, but we notice the presence of some hysteresis. In fact, oscillations in the velocity signal are still present for values of ΔP where previously the signal was flat (apart from noise); these flows are strongly history dependent and the time behaviour changes if the threshold is approached from below or from above. Finally, restoring the pressure difference restores the amplitude of the fluctuations. In other experiments, it was possible to tune finely ΔP so to move in and out of the oscillating regime and study the behaviour close to the threshold. We can lastly note the presence of some delay between the pressure change and the corresponding velocity change which enforces the idea of history dependence.

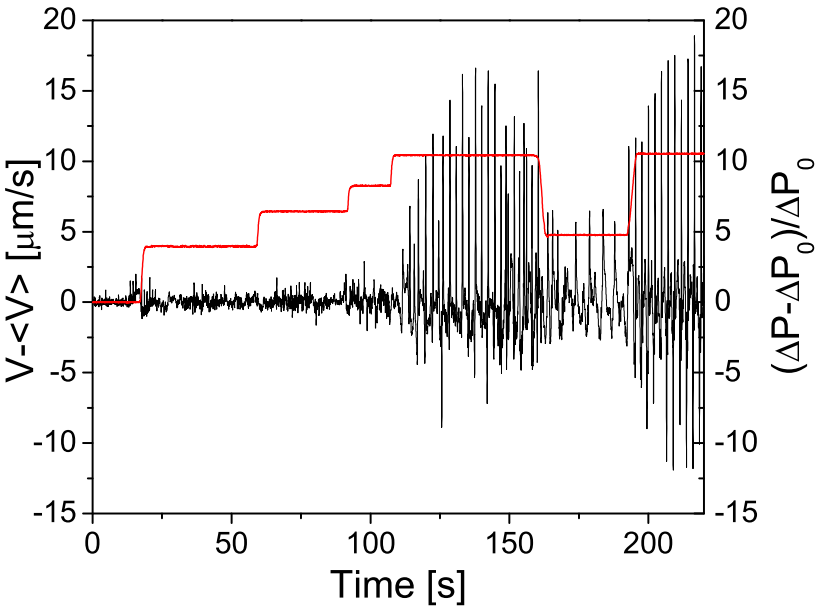

Figure 8.10: A $\Phi \simeq 0.635$ suspension is driven into a $50\mu\text{m} \times 50\mu\text{m}$ uncoated channel by an initial pressure difference $\Delta P_0 = 10$ torr. The driving pressure ΔP was then changed during the experiment and we report here its value normalized to ΔP_0 as a function of time (red) as well as the corresponding offset average speed (black).

[1]This is done *a posteriori* by comparing the confocal images and the pressure signal.

For each experiment we recorded the pressure and calculated the fundamental frequency of the oscillations in the velocity as a function of both the applied ΔP and the local average speed $\langle V \rangle$. We can think of a correspondence between the behaviour as a function of $\langle V \rangle$ and ΔP, i.e. a correspondence between a threshold velocity and a threshold pressure difference, but the relationship between the two is not trivial and depends strongly on the flow history. We chose thus to give the data as function of the speed since $\langle V \rangle$ is calculated locally and represents better the microscopics of the flow; the pressure is only controlled macroscopically and we are not able to access the local ΔP which in turns depends on the flow state (presence of shear, permeation flow, etc.).

The detection of the threshold flow speed is accomplished by examining the power spectra of the signals; in the absence of oscillations they look completely featureless (just noise), while above the threshold they acquire the characteristic shape reported in Figure 8.8. For each experiment we measured the fundamental frequency as a function of speed discarding the points which showed hysteresis. An example is reported in the inset to Figure 8.11; for values of the average flow speed lower than $\sim 10\mu$m/s the flow does not show any oscillation, while they arise above this threshold value. The frequencies f above the threshold are fitted using a curve of the form

$$f(\langle V \rangle) = \alpha_0(\langle V \rangle - V_{\text{thr}})^{\alpha_1} \tag{8.1}$$

where V_{thr} identifies the threshold velocity for which the frequency extrapolates to zero (for the curve in the inset $V_{\text{thr}} = 10.06\mu$m/s) and α_0 and α_1 are fitting parameters. The values of threshold velocities varied from experimental run to experimental run due to history dependence in the flow. By fitting all the data with curves as in 8.1 we obtained V_{thr} for all the flows. Plotting the oscillations fundamental frequency versus $\langle V \rangle - V_{\text{thr}}$ we found that all the data collapsed onto one single curve, which is in turn fitted by a power law with exponent 0.336 ± 0.126.

We can perform the same kind of analysis with respect to the amplitude of the oscillations which we can simply quantify by taking the standard deviation of the offset velocity signal, Figure 8.12. The data collapses on one curve which shows a roughly linear increase in the amplitude (standard deviation) with increasing flow speed above the threshold and with an offset for $\langle V \rangle = V_{\text{thr}}$; the offset marks the standard deviation of the noise in non-oscillating signals, or better its upper limit. We can provide a simple, first order explanation for this: in correspondence to jamming events, the fluctuating velocity signal drops from $\approx \langle V \rangle$ to values which only weakly depend on the flow speed and therefore the amplitude of the fluctuation is roughly $\propto \langle V \rangle - V_{\text{thr}}$.

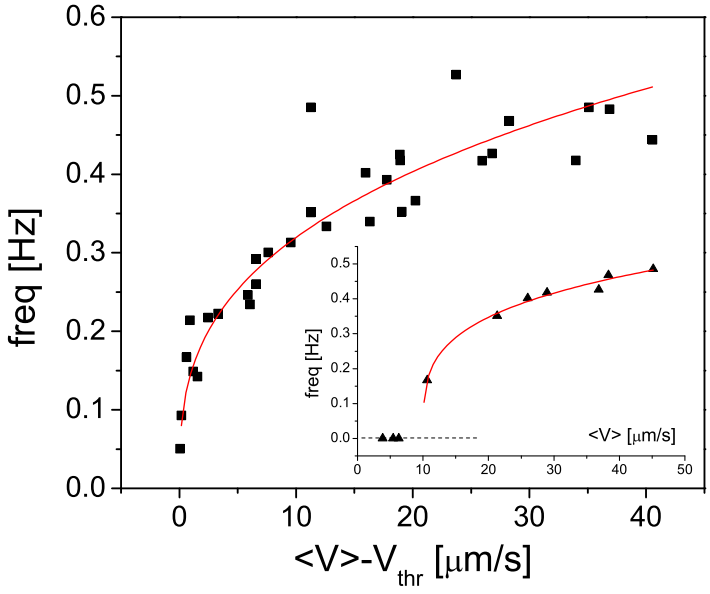

Figure 8.11: Fundamental frequency of the oscillations in the velocity signal as a function $\langle V \rangle - V_{\rm thr}$; the full curve is a fit a power law with exponent 0.336 ± 0.126. Inset: fundamental oscillations frequency as a function of the average flow speed $\langle V \rangle$; the points with non-zero frequency are fitted with Equation 8.1 (full curve). From the fit we obtain the value of $V_{\rm thr} = 10.06 \mu$m/s, corresponding to a pressure difference of 53 torr.

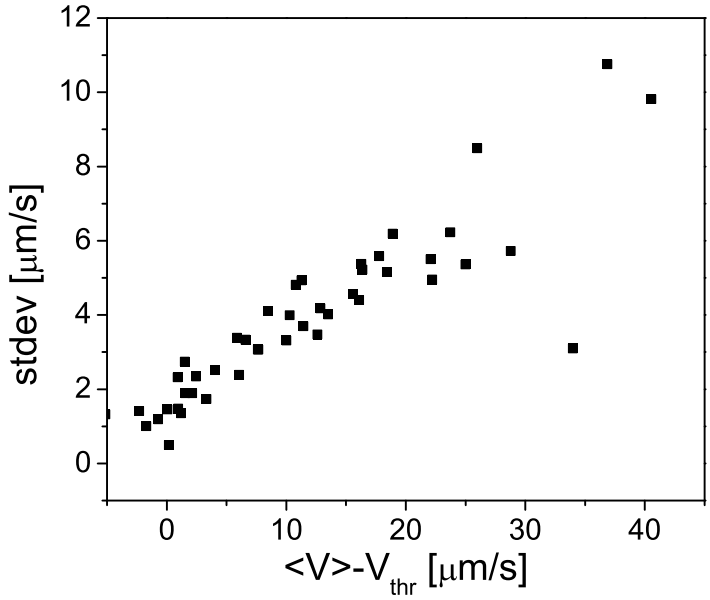

Figure 8.12: Standard deviation of the offset velocity signal versus average $\langle V \rangle - V_{\rm thr}$. The data points to the left of the threshold velocity show the fluctuation level in the noise in the absence of oscillations.

Finally we measure the duration of jamming events as a function of the average flow speed (Figure 8.13). We define *a jam if the oscillating velocity falls below 50% of the average velocity.* In practical terms, we identify those time intervals where the oscillating velocity is lower than 50% of the long time averaged velocity; we plot the duration of these time intervals as a function of $\langle V \rangle$. The trend follows what qualitatively described earlier: the duration of the jams Δt is a decreasing function of the flow speed.

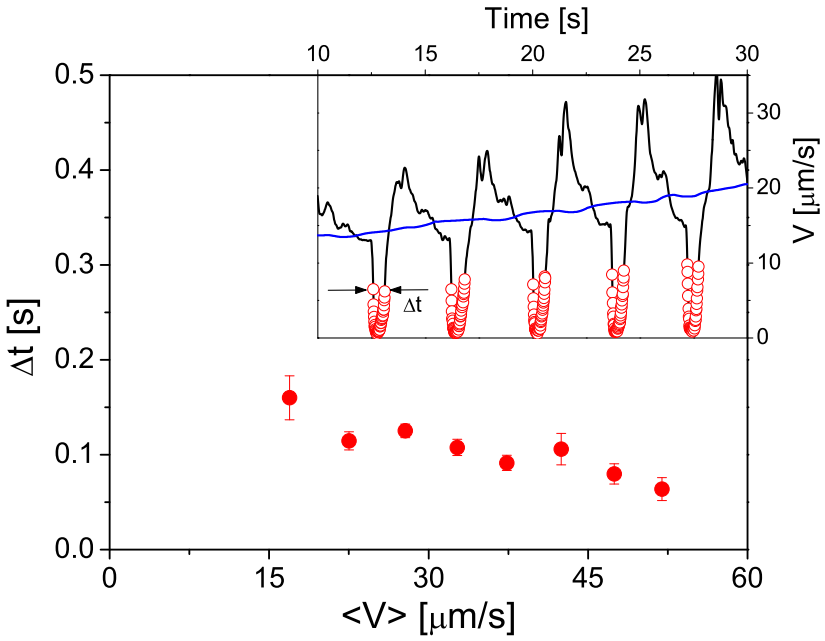

Figure 8.13: Duration of jams as a function of average flow speed. The points have been obtained by calculating and averaging Δt on different data sets. Inset: signal in Figure 8.7(top right). The blue curve is the long time averaged signal $\langle V \rangle$ and the open symbols mark those points whose velocity is lower than $0.5 \times \langle V \rangle$ and therefore jammed according to our definition.

We can summarize stating that *the frequency of jamming events increases with the average flow speed while their duration decreases.*

Sheared flows

The data presented in the previous section referred to complete plug flows. We reported in Chapter 6 that there exists a non-uniform density profile along the flow direction, and that this also affects the local velocity profiles. In particular we are here interested in examining the time behaviour of the velocity in the region upstream of the plug; the dynamics of the formation of the density profile have been also discussed in Chapter

6. We recall that in the aforementioned region the volume fraction is lower than in the plug and shear takes place; details on local velocity profiles have been presented in Chapter 7; We reasonably expect that fluctuations in the velocity will affect the motion in regions upstream; in analogy with traffic jams, the cars before the jam will also experience velocity fluctuations.

We can generally say that *the velocity oscillations "propagate upstream" towards the entrance of the channel*.

If the jam in the plug lasts long enough it can fully back-propagate all the way to the inlet of the channel as in the case reported in Figure 8.14. The spatio-temporal diagram on the right, taken just inside the capillary, depicts 5 seconds of flow and shows the presence of two jams while the signal on the left focusses on the first 1.5 seconds. The two traces reported in the figure are the velocities in the centre of the channel of the downstream part of the image (red curve) and of the upstream one (green curve), respectively; they both show a dip corresponding to a jam, but the red curve drops first and the velocity oscillation then propagates upstream and it is detected in the green curve. We can estimate the speed of the jam propagation by measuring that it takes $\Delta t \approx 0.05$ seconds for the jam to travel $\Delta x \approx 18\mu$m between the centre of the downstream part of the image to the centre of the upstream one yielding a propagation speed of 360 μm/s of the order of 12 times the average flow speed.

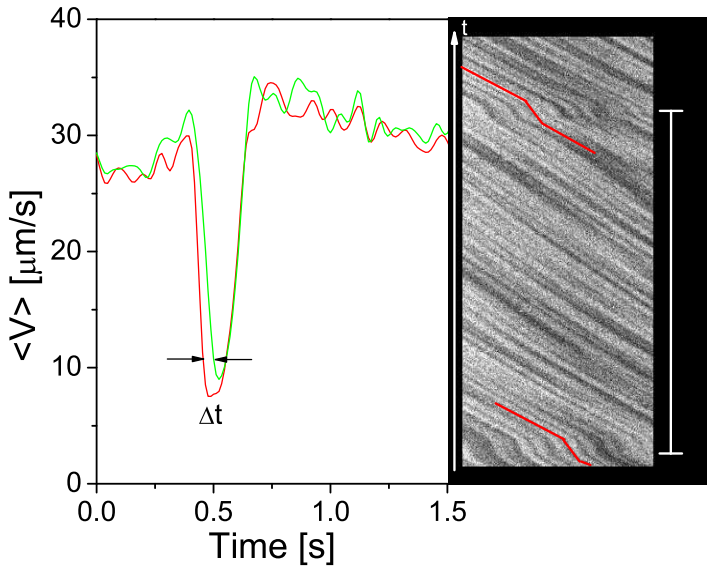

Figure 8.14: Right: spatio-temporal diagram obtained from images collected just inside the channel and showing 5 seconds of flow. From the traces we detect two jams. Left: velocity in the centre of the channel of the downstream (red curve) and upstream (green curve) part of the images as a function of time. The downstream part corresponds to the first 8.5 μm of the field of view and the upstream one to the last 8.5 μm. The jam takes a finite time Δt to travel across the field of view (44 μm).

Figure 8.15 reports the velocity in the centre of the channel as a function of time, measured close to the entrance. We note the same behaviour reported earlier for the complete plug flow; at low speed the flow is regular and at higher rates oscillations appear. We can expect this as a consequence of the velocity oscillations occurring downstream. We note though a difference in the shape of the oscillations; the inset to Figure 8.15 shows a blow up of 10 seconds of signal where this can be appreciated.

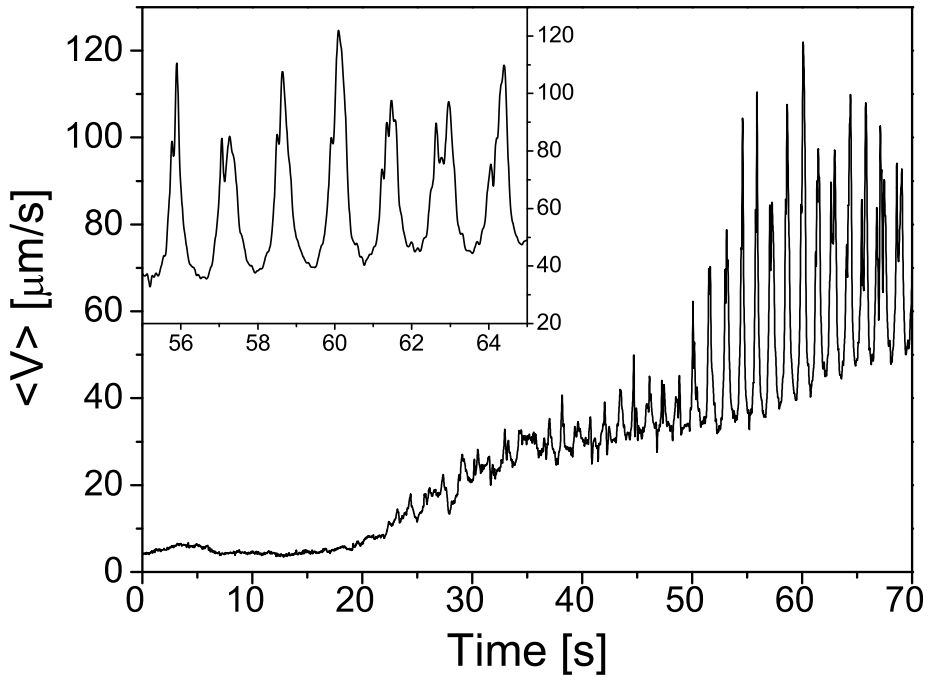

Figure 8.15: Speed as a function of time for shear flow in the centre of a square cross–sectioned capillary with smooth walls and initial applied pressure difference of 10 torr. In the inset 10 seconds of the signal are blown–up to show the shape of the oscillations.

Comments on volume fraction and channel size

All the data reported above refer to flows of sediments into square capillaries with a $50 \times 50\mu$m cross section. We comment here briefly on the effect of changing the volume fraction or the channel size.

Despite the present lack of systematic data on the volume fraction dependence, by analysing the velocity signals measured for the sheared flows in Chapter 7, we can qualitatively state that reducing the volume fraction of the flowing suspension reduces the presence of fluctuations in the velocity, with almost fully regular flows recovered for $\Phi \lesssim 0.43$ within the investigated velocity range. Future systematic investigations are planned.

Another factor which strongly affects the velocity fluctuations is the channel size. Preliminary experiments involved the use 40 × 400 μm rectangular capillaries for which fluctuations in the velocity signal were observed but where the extremely regular behaviour reported above for the 50μm square capillaries was absent. This can be observed in Figure 8.16 where we report the velocity as a function of time for three different runs of increasing average speed in 40 × 400 μm rectangular capillaries with smooth walls. As the average flow rate increases the frequency and the amplitude of the fluctuations in the signals also increase. Therefore the same trend is observed but the regularity of the signal is strongly affected by the different confining geometry. In particular studying the flow in even narrower channels is of great interest; limitations to the available channel sizes are present as the manufacturer of the glass capillaries (Vitrocom) claims that the production of square channels of width lower than 40μm is infeasible as surface tension effects during the solidification of molten glass will round the capillary. In order to go to even smaller aspect ratios other techniques for producing the channels are needed. Discussion on this aspect and future plans will be presented in the outlook of this thesis (Chapter 10).

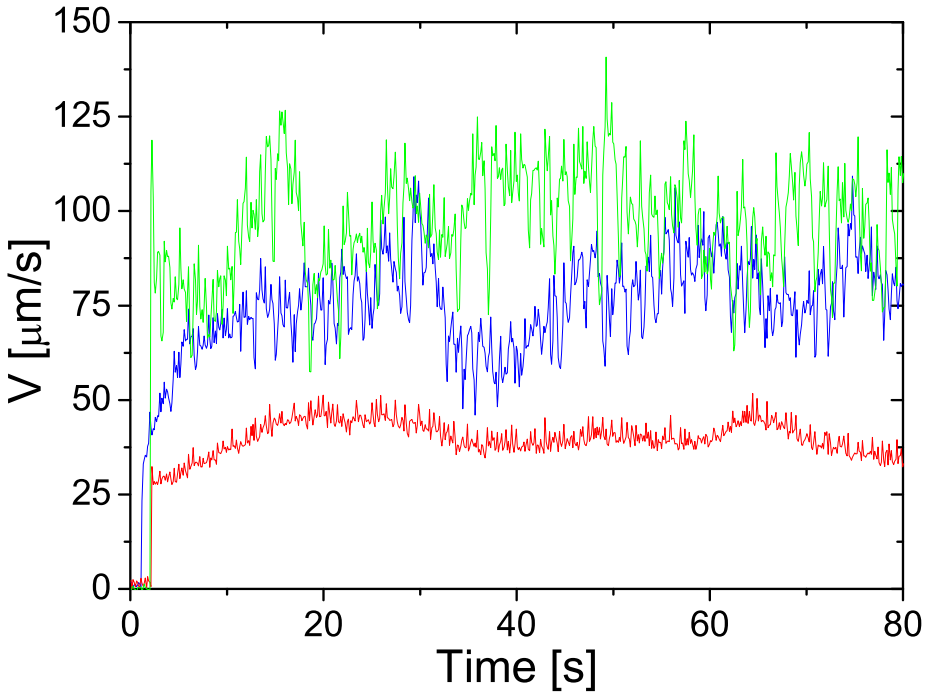

Figure 8.16: Flow velocity as a function of time for three different experiments in a 40 × 400 μm rectangular cross-sectioned, uncoated capillary. The volume fraction of the suspension was $\Phi \simeq 0.635$ and the three applied initial pressure differences were of 10 (red), 30 (blue) and 40 torr (green) respectively. After the flow started ΔP was kept constant in all cases.

Rough walls

We announced in Chapter 5 that it is possible to coat the inner walls of the glass capillaries with a disordered layer of particles and induce roughness on the particle level. We investigated the effect of boundary roughness on the velocity profiles in Chapter 7; for the present discussion it is sufficient to say that the 'bumpiness' of the walls induces transverse motion which destroys the plug. Therefore, *the presence of rough walls prevents the formation of a complete plug that can slide smoothly on the inner surface of the channel.*

Boundary roughness also increases the lifetime of the jams. In our experiments we frequently encountered the case of suspensions that, once arrested, stayed jammed as long as the experiment lasted.

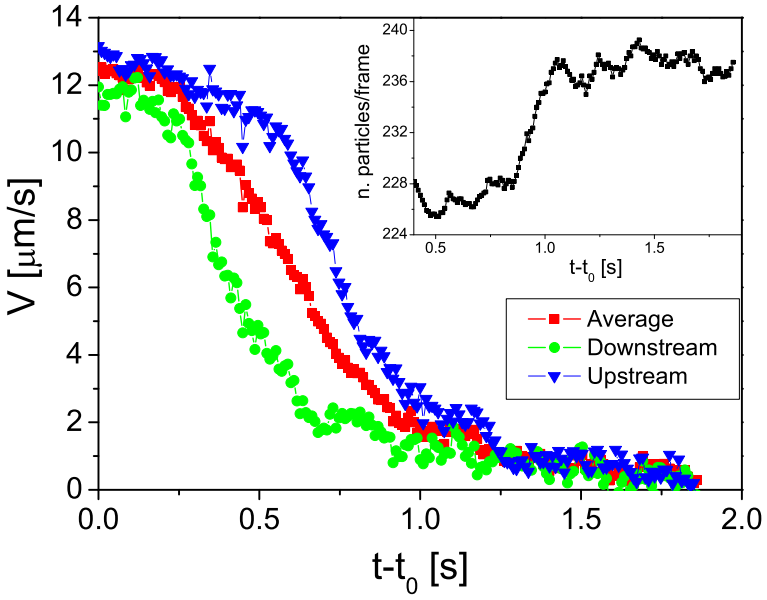

Figure 8.17: Velocity of two sections (upstream and downstream) and of the whole field of view as function of time in correspondence of a jamming event. t_0 is an arbitrary time. The jam takes 0.4 s to travel the 36 μm which separate the two sections of the field of view. Inset: number of particles per frame as function of time. $\Phi \simeq 0.635$.

Figure 8.17 shows the velocity of a flowing suspension as a function of time, respectively for the downstream part of the image (green symbols), the upstream part (blue symbols) and for the whole field of view (red symbols). We observe a drop in the signal from a value of 12μm/s to zero indicating an arrest of the flow while a constant driving pressure difference of 10 torr was applied. If we now compare the green and the blue points, we notice that the jam is propagating upstream , analogously to what reported in Figure 8.14, the difference being that now the flow does not restart

spontaneously. The delay in the arrest between the downstream and the upstream part of the field of view is of roughly 0.4s, yielding a propagation speed for the the jam of $\approx 90\mu$m/s, ≈ 7 times the flow speed. The inset reports the average number of particles per frame as a function of time and we notice that it progressively grows in correspondence of the flow arrest. The suspension jams somewhere further downstream of the field of view and the jam back–propagates upstream leading to arrest and density increase.

Figure 8.19 reports the spatio-temporal diagrams for a flow where the suspension came to arrest under an applied driving pressure difference of 20 torr (the region marked as "jammed" on the diagram); while the suspension was jammed we increased the applied pressure difference up to seven folds before the flow started again in a sequence of discontinuous events (also highlighted in the figure). Figure 8.18 reports the speed as a function of time for the same experiment. We shall explain in the following section the mechanism behind this observation.

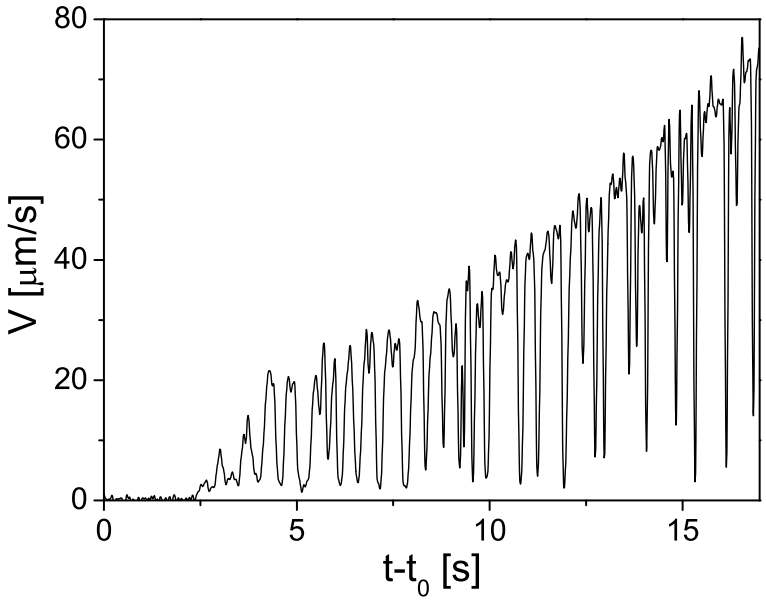

Figure 8.18: Flow velocity in the centre of the channel as a function of time for the flow reported in the diagrams of Figure 8.19. The flow spontaneously stops and is restarted by applying a sevenfold higher pressure difference; once restarted, the flow is highly discontinuous. The time axis is offset by an arbitrary time t_0 previous to the flow recovery.

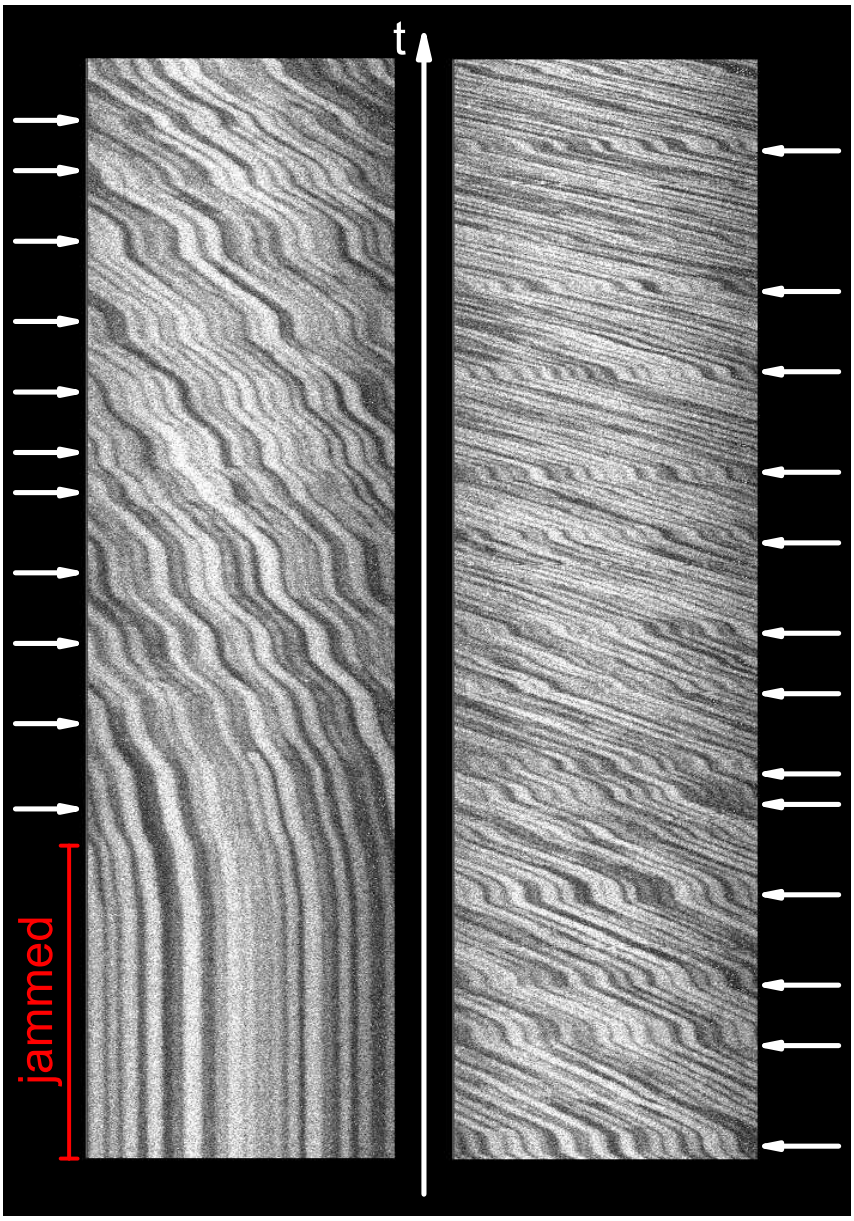

Figure 8.19: Spatio-temporal diagrams for a flow in a $50 \times 50\mu$m channel with rough walls. The images were taken at $z/a_{\text{eff}} = 0.32$ and a 44 μm long, 1 pixel wide strip along the centreline of the channel ($y/a_{\text{eff}} = 0$) was extracted. The initial applied pressure difference was 40 torr and $\Phi = 0.635$. The flow comes to arrest under an applied pressure difference of 20 torr and stays jammed until the applied ΔP reaches 140 torr. At that point, flow starts again in a succession of discontinuous jumps and jams (highlighted with white arrows). The right diagram is the continuation of the left one. The diagrams correspond to the first 18 s of Figure 8.18 .

8.2.2 Discussion

In this section we present some comments and observations on the nature of the velocity fluctuations previously described. We initially give a quantitative description of the micro structure of the flowing suspension in relation to the velocity oscillations and then comment on the role played by the solvent. Comments on the mechanisms and dynamics behind the oscillations conclude the chapter.

A microscopic description

We are in the presence of complete plug flow when shear is totally absent in the transverse direction (y and/or z), i.e. when the whole suspension flows as a rigid body (see Chapter 6). Careful observation of the image sequences though, shows this statement not to be entirely true; in fact the suspension actually flows as a rigid body *for most of the time but local structural rearrangements are observed in the presence of velocity oscillations*. Such rearrangements are mainly located at the boundary and become more and more pronounced as the average flow speed increases.

It is possible to describe quantitatively the rearrangements by looking at the behaviour of individual particles in the comoving frame of reference. In order to set ourselves in the comoving reference, we need to remove the average advective motion from the particle tracks; refer to Chapter 5 and [126] for more details. This operation is particularly simple for complete plug flows since, on average, all the particles move with the same velocity. At high packing fraction and in the absence of local shear, the suspension's structure is frozen and the particles are tightly caged by their neighbours. In the comoving frame, particles will thus only rattle in their cages, but if the local structure is rearranged they can undergo much larger displacements.

The following figures are aimed at describing in a more quantitative manner what stated above.

Figure 8.20 reports the velocity signal in the laboratory frame as a function of time (top) together with the total velocity in the comoving frame, measured at the walls (middle) and in the centre of the channel (bottom). Figure 8.21 is similar, but instead reports the standard deviation of the velocity in the comoving frame.

The goal of this representation is to highlight a link between the "activity" of the particles in the comoving frame and the velocity oscillations in the laboratory frame. Figure 8.20 shows that the total velocity in the comoving reference ($\langle V_{\mathrm{tot}}^{\mathrm{cm}} \rangle = \sqrt{\langle V_{\mathrm{x}}^{\mathrm{cm}} \rangle^2 + \langle V_{\mathrm{y}}^{\mathrm{cm}} \rangle^2})^2$ is not constant as a function of time. In fact we observe peaks in correspondence of velocity oscillations; these peaks are higher and more numerous at

[2]The value is obtained by averaging the velocities of all the particles in a given $y-$bin.

the walls than they are in the centre of the channel. This is telling us that particles move with respect to the average advective motion whenever there are velocity oscillations.

Figure 8.21 highlights the same idea but from a a slightly different perspective; it is in fact reporting the standard deviation of $\langle V_{\rm tot}^{\rm cm} \rangle$ as a function of time. This tells us not only that the particles move more during velocity oscillations but also that they do not move in a coherent way, that is to say that they locally re-arrange according to the local structure.

Figure 8.22 reports the time average of $\langle V_{\rm tot}^{\rm cm} \rangle$ as a function of y for different flow rates. We observe that the rearrangements are peaked at the walls, as already observed from the previous graphs, and that they increase with the average flow rate. In this particular experiment there is an asymmetry of the curves since the rearrangements preferentially took place at one of the side walls; this is a feature of the particular experimental run, other experiments showed more symmetric curves or more rearrangements at the other wall.

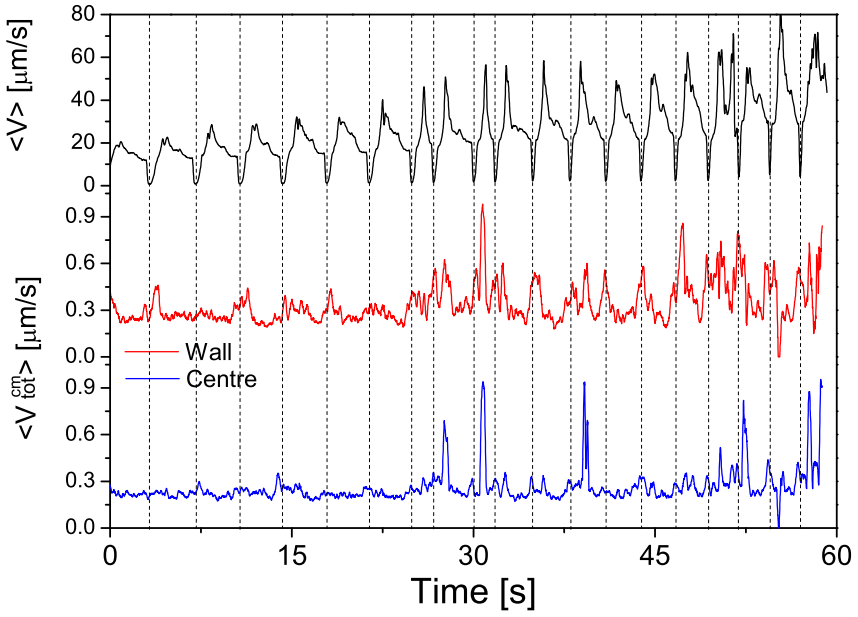

Figure 8.20: Top: average velocity in the laboratory frame as a function of time. Middle-bottom: $\langle V_{\rm tot}^{\rm cm} \rangle$ as a function of time, measured at one of the walls (middle) and in the centre of the channel. The data refer to three-particles-wide y-bins. $z/a_{\rm eff} = -0.32$. $\Phi \simeq 0.635$.

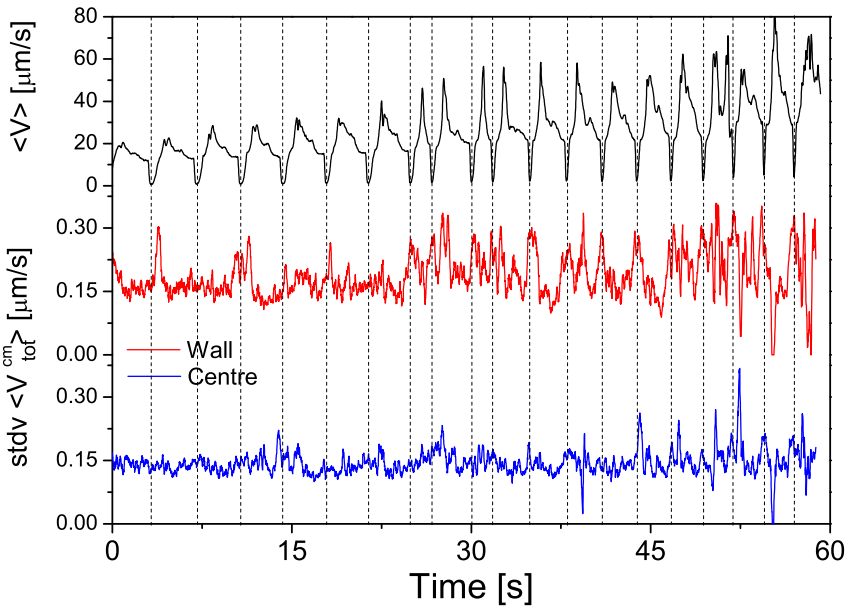

Figure 8.21: Top: average velocity in the laboratory frame as a function of time. Middle-bottom: standard deviation of $\langle V_{\rm tot}^{\rm cm} \rangle$ as a function of time, measured at one of the walls (middle) and in the centre of the channel. The data refer to three-particles-wide y-bins. $z/a_{\rm eff} = -0.32$. $\Phi \simeq 0.635$.

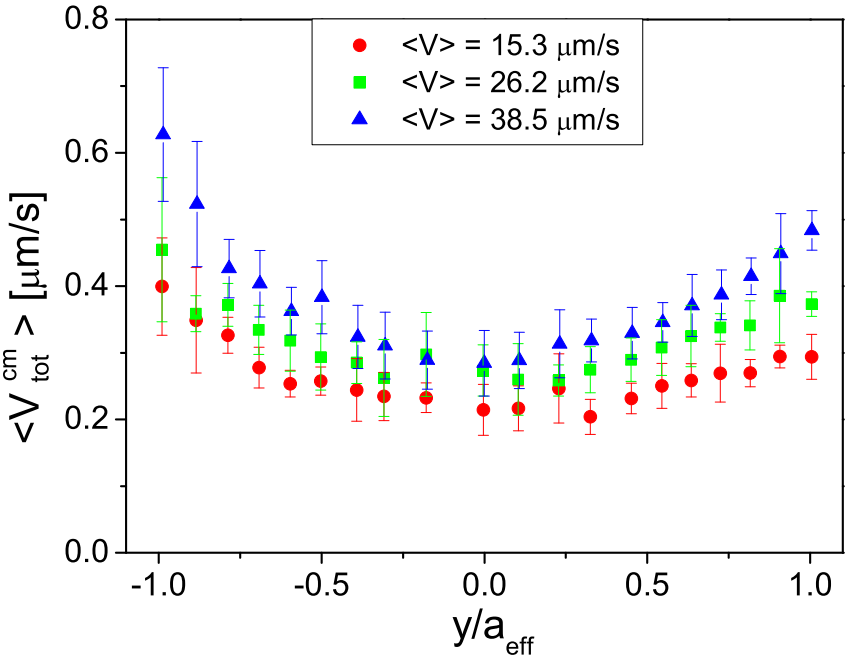

Figure 8.22: $\langle V_{\rm tot}^{\rm cm} \rangle$ as a function of y for three different average flow speeds. The data come from three sections of the same experiment reported in Figure 8.21 and 8.20.

In all the figures the velocities in the comoving frame have been calculated by collecting the displacements of the single particles over 30 frames ($\approx$ 0.4s) in order to rule out the effects of short-time, in cage motion. This has also had the effect of eliminating particles tracked for less than 30 frames, thus improving the quality of the data. We have to make sure, though, that the time interval chosen to get the displacements is shorter than the period between two velocity oscillations, in order to describe the effects of single velocity fluctuations.

We can also give a more detailed microscopic description of these structural rearrangements. In the following two figures we report the histograms of the angles between neighbouring particles in three layers close to one of the lateral walls (Figure 8.23) and in a y-bin of the same size but in the centre of the channel (Figure 8.24). The angles are calculated by performing a Delauney triangulation (see Chapter 5) within a range of two particle diameters. We followed the particles during a velocity fluctuation (in the top left inset to the figures) and reported the angles between *the same* particles before and after the fluctuation in both the positions. Starting with the particles close to the walls, we selected only the particle bonds pointing from the wall towards the centre of the channel and we observed that, in this particular case, the suspension flowing into the field of view presented a very well characterized crystalline order with bonds peaked at -60 and -120 degrees, for first and second nearest neighbours respectively. After the velocity oscillation, the particles have changed the relative positions as highlighted by the now different angles distribution of first and second nearest neighbours (excluding in-layer neighbours), with peaks roughly at -100 and -45 degrees. When we perform the same analysis in the centre of the channel we observe a marked difference. The angular distributions before and after the velocity oscillation are practically identical showing that these particles have not rearranged their relative positions. This is a further proof that structural rearrangements preferentially take place close to the channel walls. Figure 8.25 shows the corresponding confocal images where two sets of particles, one close to a wall and the other in the centre of the channel, are followed through the velocity fluctuation. We can again notice the change in the bond angle for the particles close to the boundary, while the relative positions of the ones in the centre remains unchanged. What we have just shown has to be interpreted carefully though; there is no unique signature of structural changes linked to the velocity fluctuations, but when we observe a velocity fluctuation this carries with it local structural rearrangements which can be experimentally detected. The nature of each rearrangement is embedded in the local structure and we have shown here a particularly clear example.

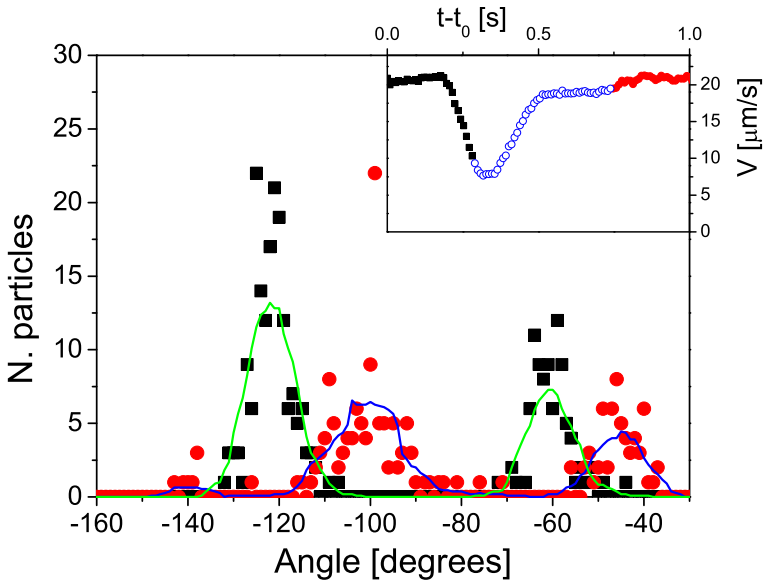

Figure 8.23: Angles between neighbouring particles in the three most external layers close to one of the inner walls before (black points) and after (red points) the velocity fluctuation reported in the left inset. The full lines are an average of the scattered points. Inset: velocity as a function of time (t_0 is an arbitrary time instant); the symbols determine the 'before' and 'after' in the fluctuation.

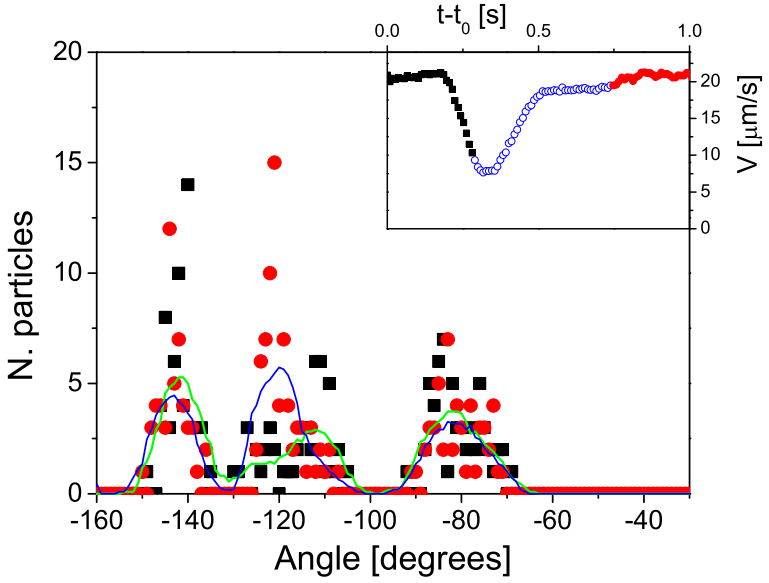

Figure 8.24: Angles between neighbouring particles in a three particles-wide y-bin around the centreline before (black points) and after (red points) the velocity fluctuation reported in the left inset. The full lines are an average of the scattered points. Inset: velocity as a function of time (t_0 is an arbitrary time instant); the symbols determine the 'before' and 'after' in the fluctuation.

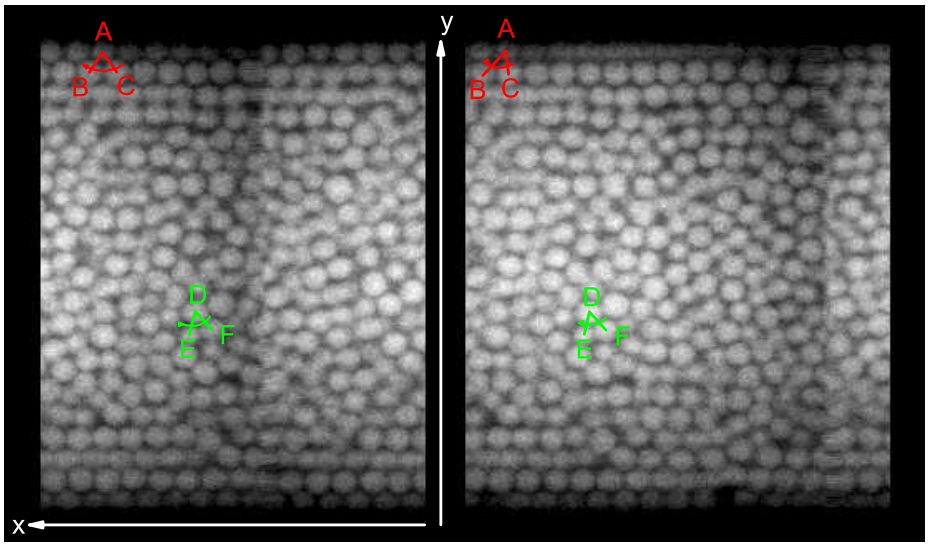

Figure 8.25: Confocal images of the suspension before (left) and after (right) the velocity fluctuation of Figure 8.23 and 8.24. We highlighted the angles between two sets of neighbouring particles close to the walls and in the centre of the channel, following them through the velocity fluctuation. We can appreciate how their relative positions change (at the wall) or stay unchanged (centre).

We therefore presented the evidence of a link between velocity fluctuations and local structure. In particular we can affirm that *in correspondence to velocity oscillations, the particles undergo structural rearrangements; these events happen preferentially close to the boundary and their measure grows with local flow speed.*

The role of solvent

Up to this point we have described the velocity oscillations and the nature of the structural rearrangements which accompany them but we have not yet included the solvent in our description. As seen in Chapter 6 and as for instance reported in [13], the interplay between the suspended colloids and the solvent has vital consequences on determining the local density and shear profiles. In the following we will address the role played by the solvent in the mechanisms at the origin of the suspension's jamming.

In the case of non-Brownian systems (e.g. granular media), once the system is jammed, there are no spontaneous internal fluctuations that can relax the jammed structure and therefore un–jam it. Conversely, in Brownian systems the jam has a finite lifetime since the random motion the particles are subjected to will eventually break up the jammed structure. This corresponds to the definition of *fragile matter* given by [61]; in fact if the system is jammed by applying an external stress, particles or grains will rearrange in *force chains* which oppose and eventually bear the applied

load. In case of shear-induced jamming, the force chains have a precise orientation and are thus only able to bear loads along that direction; applying a small shear stress along another direction will un–jam the system (hence the nomenclature "fragile"). It is now clear why random displacements of particles in a force chain will, with a certain probability (and thus within a given time), lead to the relaxation of the chain itself unjamming thus the system. In the presence of a net flow of solvent through a jammed matrix of particles, the latter are not only subjected to Brownian motion, but they also experience a force due to the interaction with the solvent. The action of the solvent increases particle mobility and reduces therefore the lifetime of the jammed structure. In other words, we suggest that interactions with the solvent translate into an *effective amplified Brownian motion* which accounts for more rapid structural rearrangements and stress relaxations.

We can quantify this mechanism by looking, for instance, at the mean square displacements (msd) of particles in their comoving frame of reference. Figure 8.26 reports the particle msd normalized to the particle radius in the transverse direction in the comoving frame taken in the centre of a channel with smooth walls. We initially recorded the data in the absence of an external pressure difference (black symbols) and we then applied two different ΔP of 10 (red) and 20 (green) torr respectively. The suspension did not flow (only a very slow creep was present) under the first applied ΔP but we notice a clear difference with the former case. When ΔP was increased to 20 torr flow started.

In the 10 torr case the particle mobility is highly enhanced and the msd grows rapidly for intermediate times. At longer times the msd start to plateau since the particles are nonetheless caged by their neighbours; we can observe though that the size of the cage is larger than the one reported in the literature for quiescent systems in the absence of net solvent flow. Our values ($\simeq 0.2$) are one order of magnitude larger than the ones obtained form light scattering on hard-spheres at the glass transitions ($\simeq 0.03$) [193]. By looking at the image series, we notice that the solvent flow allows for collective motions enhancing the space explored by the particles but still holding the presence of a cage in place. The effect is amplified in the higher applied pressure case where the relative net flow is increased consequently.

So, during a velocity fluctuation, the relative velocity difference between particles and solvent increases and solvent flow is responsible for the structural rearrangements discussed above. The localization of these rearrangements close to the inner walls of the channel can be addressed by the fact that, as for instance shown in [194], the shear stresses exerted by a liquid flowing in a channel filled with a porous matrix are higher close to the channel surface.

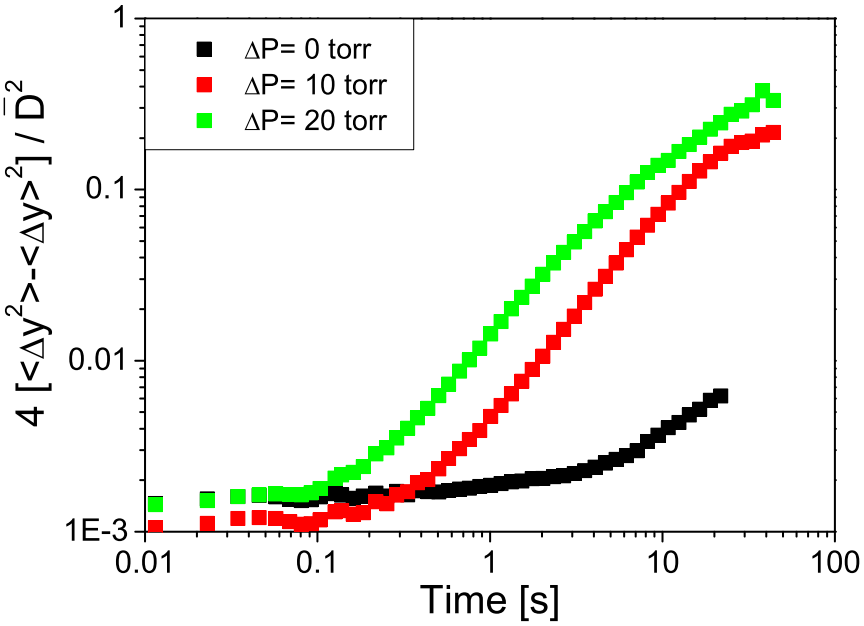

Figure 8.26: y mean square displacements normalized by particle radius for three measurements at different ΔP (black, red and green curve). The data are taken in the centre of a capillary with smooth walls.

Comments

We can finally summarize and comment on the issues raised in the previous discussion.

In the previous paragraphs we have pinpointed the presence of structural rearrangements and the role played by the solvent. We have also described the shape of the velocity signal during an oscillation cycle. We can then qualitatively sketch the following mechanism which governs the dynamics of the velocity oscillations.

Recalling the broader picture reported in Chapter 6, we remind the reader that there exists an interface between the complete plug sliding along the channel and a sheared region downstream of it. We examined properties of this interface highlighting the fact that the complete plug encounters some resistance to flow, mainly due to the removal of the particles attached to the walls in the sheared region. During flow, the complete plug is prevented from moving at its desired speed by such resistance and it is therefore compressed by the permeation flow of the solvent. Associated with the compression, normal forces build up across the suspension and progressively increase the friction with the channel walls additionally slowing down the flow; when the forces overcome a threshold the suspension sticks onto the inner surface and the velocity drops. Once the complete plug is jammed, the relative speed difference between the particles and the

solvent has a sudden increase. In the presence of strong permeation, the interactions between the jammed particles and the solvent rapidly relax the jammed structure and the flow suddenly accelerates. At this point the system is in a situation analogous to the starting point and the cycle is repeated.

This mechanism for instance explains why the duration of the jams in the case of rough walls is increased. Rough boundary can support shear stresses much higher than the smooth ones due to a larger effective friction with the coated walls and therefore the disturbances induced by permeation flow need to be larger to disrupt the jammed structure.

Despite the presence of a microscopic description, a few open questions remain. Why are the oscillations so regular? Which are the typical time and length scales which determine the values of the oscillation frequency? Is it possible to predict the value of the threshold flow rate? Modelling work is currently under way with the hope of finding an answer to these and other questions.

Chapter 9

Conclusions

In this concluding chapter we summarize and review the achievements presented in this thesis.

9.1 Confocal microscopy and particle tracking

Confocal microscopy is now a well-established experimental technique used to study the local, time resolved behaviour of quiescent colloidal systems. In this work we have used a high-speed confocal microscope to investigate for the first time the pressure-driven flow of high volume fraction colloidal suspensions in micro-capillaries at the single particle level. The available procedures to locate and track the particles fail to yield satisfactory results in the presence of strongly non-uniform flow fields. In order to overcome this problem we have designed an algorithm which is able to remove non-uniform advective motion from the particle coordinates and accurately track them in a position-dependent comoving frame of reference. An account of the technique has been recently published [126] and a similar procedure has now been used in a recent publication on planar shear of colloidal glasses [44]. Accurate tracking has allowed us to acquire quantitative information on collective properties, like the flow velocity, by averaging the single particle contributions as well as to obtain a microscopic description at the single particle level. For instance, by calculating the angles between nearest neighbours particles, we have been able to detect the presence of changes in the local structure of the flowing suspension. Finally by collecting two-dimensional slices at different depths in the channel we have been able to three-dimensionally reconstruct the velocity profiles.

9.2 Density gradients and shear profiles

The presence of non-uniform concentration profiles and of permeation effects has already been reported for dense particulate systems. In addition to the existent literature, this thesis reports for the first time, to the best of our knowledge, the presence of a *non-monotonic concentration profile along the flow direction*. Previous experiments have been able to give bulk data on the density of the suspension [13], to show concentration profiles after the cessation of flow [122] or to obtain fluid content contour maps without resolving the microscopic dynamics [195]. Thanks to our experimental technique, we have been able to resolve spatially the flow down to single particle level and relate the local density to the local velocity profiles during flow.

We recall that for the flow of sediments of our colloidal suspensions in smooth channels we observed an initial dense region where the velocity profiles consisted of a central, unsheared plug and lateral shear zones close to the channel walls. The density in this region gradually increases moving away from the channel inlet up to a maximum value. In correspondence to the maximum packing fraction, shear disappears completely and the whole suspension flows as a solid plug sliding along the channel walls. This complete plug region has an extension comparable to several thousands of particles diameters and it flows according to the applied rate. Downstream of the complete plug, there exists a rather sharp interface with another region where shear is present. In this downstream sheared region the density of the suspension decreases considerably reaching values for which parabolic flow profiles are recovered.

Such non-monotonic profiles can be ascribed to the presence of relative velocity differences between the particles and the solvent which lead to permeation flows. Once the flow starts, interactions between the particles slow them down but this effect is absent for the solvent. For large enough initial volume fractions, particles can jam against each other during flow causing other particles to accumulate behind them similarly to what happens in traffic jams; this mechanism leads to the formation of the complete plug region. Under the applied pressure difference the complete plug slides along the channel and in the presence of a net solvent flow, the density of the suspension downstream of the complete plug's head gets progressively more dilute.

9.3 Flow profiles: data and quantitative analysis

One of the most important finding of this thesis, if not the most important one, concerns the measurement and description of the velocity profiles in the initial dense sheared region and it has lead to a recent publication [157]. The flow here consists of a 'plug' in the centre while shear occurs localized adjacent to the channel walls, reminiscent of

yield-stress fluid behaviour. Dense colloidal systems with volume fraction above 0.58 exhibit the presence of a yield stress and are conventionally described by an Herschel-Bulkley (HB) constitutive relation. However, the observed scaling of the velocity profiles with the flow rate strongly contrasts yield-stress fluid predictions. Instead, the velocity profiles can be captured by a theory of stress fluctuations originally developed for two-dimensional chute flow of dry granular media. We have extended the model to a three-dimensional channel and successfully applied it to our systems.

Experiments were carried out for twenty particles-wide square glass channels with different boundary conditions; the inner walls of the glass capillaries were either untreated and therefore smooth, or coated with a disordered layer of larger, polydisperse particles and therefore rough on the particle level. We also performed measurements with suspensions of different initial volume fractions, ranging form sediments ($\Phi \gtrsim 0.635$) to 43%, and for channels with different sizes and shapes.

The main experimental findings are:

- The width of the lateral shear zones is of the order of few particle diameters and it is independent of the applied flow rates contrasting the predictions obtained from the bulk rheological behaviour;

- The width of the shear zones depends on the boundary conditions with rough walls inducing larger shear zones;

- The width of the shear zones grows linearly with the channel size;

- For volume fraction above 58% the size of the shear zones is independent of volume fraction while larger sheared regions are found for $\Phi = 0.56$. The most dilute sample at 43% showed a behaviour compatible with a shear-thinning power law fluid;

- We analysed the width of the shear zones as a function of depth in the channel observing interesting non-monotonic behaviour.

The model we used to account for our experimental observations postulates the occurrence of stress fluctuations induced by the "granularity" of the suspensions and the presence of a Coulomb-type yield stress coming from direct or lubricated particle

contacts. The stress fluctuations can locally bring the applied stress above the yield level and induce local shear; a Boltzmann distribution for the probability of yielding links the fluctuations to the shear rate whose integration gives us a prediction for the velocity profiles. The key quantity is $\Delta\tau$ defined as the typical amplitude of the stress fluctuations; $\Delta\tau$ determiners the decay length of the yielding probability and therefore the width of the shear zones. The main result stemming form the model's analysis is that the amplitude of the fluctuations scales linearly with the maximum applied stress and therefore with the flow rate; as a consequence of this, $\Delta\tau$ is constant in units of the applied stress and therefore determines shear zones of width independent of the flow rate. Moreover we obtained quantitative fits for the velocity profiles and predicted the correct scaling. The model is applicable to our systems if the dynamics are dominated by interparticle contacts. By looking at the traces of particles in the shear zones we demonstrated that the dynamics are indeed determined by particles bumping into their neighbours, justifying the application of the model.

Despite the many similarities with granular media which suggested the use of the model in the first place, we also found important differences. The main distinction between the two cases regards the scaling of the shear zones with channel size; for grains only a weak dependence is found, while we find a linear scaling for our colloidal suspensions. We interpreted such a difference by analysing the nature of the particle contacts. A very recent publication which addresses the problem from a slightly different perspective has also reported linear scaling for granular flows [196].

Moreover we also presented a microscopic description of the flows proposing a link between the predicted stress fluctuations and the measured velocity or displacements ones. Velocity fluctuations are larger in proximity of the channel walls leading to a localization of shear close to the boundary. Additionally the scaling of the velocity fluctuating seems to follow the same trend predicted for $\Delta\tau$.

Finally we reported the presence of non-uniform concentration profiles in the direction transverse to flow, with the volume fraction close to the walls roughly 10% lower than in the channel centre for sediments flowing in rough channels. In the presence of shear and high volume fractions particles are forced to acquire transverse velocity components to flow past each other and locally lower the volume fraction with a mechanism very similar to granular dilation. Comparisons with particle migration found in lower volume fraction systems were made.

9.4 Time behaviour: velocity oscillations and a microscopic description

The last collection of results regards the time behaviour of the flows, with a particular attention to the dynamics of complete plug flows.

We have reported the presence of regular velocity oscillations in the complete plug flows of sediments of colloidal suspensions into twenty particles-wide glass capillaries when driven by a constant pressure difference. Such behaviour has been previously reported for dry grains, but to the best of our knowledge, this thesis is the first detailed study on model colloidal systems. We have found that there exists a threshold flow rate below which velocity oscillations are absent and above which their frequency scales as a power law of the flow rate. The oscillation cycles in the velocity signals consist of a slow speed reduction, followed by a sudden drop and a subsequent rapid acceleration and are repeated at regular intervals. The extreme regularity of the signals shows up in the characteristic power spectra which consist of a fundamental frequency accompanied by as many as six harmonics. The regularity of the oscillation was lost for larger channels and for rough boundaries, with the presence of longer lasting jams in the latter case.

Despite the current absence of a quantitative model we have nonetheless been able to obtain a microscopic description of the phenomenon, linking the oscillations to the local structure. In fact we observed that in the presence of velocity fluctuations the particles undergo structural rearrangements which we ascribed mainly to the presence of a relative flow (permeation) of the solvent. These rearrangements are located preferentially in the proximity of the channel walls. Starting form these observations we proposed a phenomenological interpretation of the mechanisms behind the shape of the velocity oscillations cycles based on the slow build-up and fast relaxation of stresses induced by permeation flow.

Chapter 10

Outlook and future work

The work reported in this thesis led to the finding of new features in the flows of dense colloidal systems; some of questions raised have been answered but many possibilities for further studies have been opened up. We can identify three main broad lines of research which could be followed in the future: sedimentation, additional work on channel flows and systematic comparison with granular media.

10.1 Sedimentation

We have discussed in Chapter 5 that the volume fraction of sediments prepared in similar conditions varies according to the solvent in which the particles are suspended. In particular we observed that the presence of a surface charge results in denser sediments. To the best of our knowledge, a study which systematically characterizes the properties of sediments of colloidal particles according to the interaction potential does not exist at present. The methods we used to characterize our samples appear as a straightforward way to perform such a study. We recall that fluorescently-labelled PMMA suspended in a buoyancy matching (decalin+CHB) acquires a surface charge. The strength of the resulting repulsive potential can be tuned by the addition of different amounts of screening salts. Moreover attraction of varying range and strength can also be induced between the colloids by the addition of polymer to the solution [197]. We believe that a systematic characterization (volume fraction, structure, etc.) of sediments as a function of repulsive and attractive interactions of varying strengths would constitute an extremely interesting investigation.

10.2 Additional work on channel flows

We propose a whole series of possibilities for additional work on channel flows following the results of this thesis.

Despite the division between velocity profiles and time behaviour that we have maintained in this work, these two aspects are closely interconnected. A first interesting line of research involves the study of the effects that changing the interaction potential between the particles has on both of them. Roberts et al. [112] have carried out experiments similar to ours on low volume fraction colloidal gels of silica particles with attractive interactions. They also found discrepancies with the predicted Herschel-Bulkley behaviour. It is of great interest to combine the two ideas and study the flow in the high volume fraction regime in the presence of attractive forces. Bulk rheological studies of attractive colloidal glasses have already been reported [15] and it will be intriguing to compare them once again with the results of channel flows. Moreover we expect that the presence of attraction between the particles will also have an effect on the dynamics of the velocity oscillations.

Another point of interest is to study systematically the effect of channel size on the presence and the characteristics of the velocity oscillations. We have already hinted in the text that the oscillations become less regular for larger channels. We propose to study systematically this aspect and look for the existence of a characteristic length scale for the occurrence of the fluctuations. On the other hand, and perhaps more interesting, we also plan to study the oscillations for smaller channels and investigate the effects of increasingly larger confinement effects. We have already reminded the reader of the practical limitations of finding smaller square glass capillaries. A solution to this inconvenience is offered by soft lithography [198]. Using this procedure we can design and produce channels of specific shapes and of the desired sizes. In preliminary results carried out in collaboration with Dr. Nhan Pham we have been able to obtain channels with $20 \times 20\mu$m and $10 \times 10\mu$m cross sections and a few centimetres in length. The channels are made of the silicon-based organic polymer polydimethylsiloxane (PDMS); this substrate present large advantages thanks to the ease of working with it but has the drawback of being permeable to decalin and therefore it cannot be used with the same PMMA suspensions we employed in this thesis. An alternative is to use water-based PMMA, polystyrene or silica suspensions. Experiments on three particles-wide channels have been performed on suspensions of non-Brownian polystyrene particles and showed the presence of jamming for volume fractions as low as 0.05 [199]. Performing additional experiments for a series of particle to channel size ratios in colloidal suspensions constitutes a promising aim to be pursued.

Working with PDMS microfluidic channels has also the advantage of being able to

study systematically the effects of geometrical constrictions along the flow which offer analogies with blood flows [4] and crowd escaping problems [200]. Studies on the flows of two-dimensional grains at a geometrical constriction have shown the occurrence of arching and subsequent jamming [201]; it is of great interest to perform similar studies in quasi-two-dimensional microfluidic channels for colloidal suspensions. In analogy with the discussion on the origins of the velocity oscillations in our experiments we expect to find interesting results. For a granular material, once the stress bearing arch has formed there is no spontaneous way for that structure to relax and unjam the system; we expect Brownian motion and solvent permeation to introduce a finite lifetime for the arch and regard a detailed study of these effects as a function of the geometry of the constriction as an extremely interesting one. Moreover studies of the time scales of jamming within respect to flow rate and Brownian motion can offer useful comparisons to simulation data on the escape of panicking crowds from narrow exits [200]; even more interesting would be to repeat the experiments with fluorescently-tagged bacteria and examine the effects of crowding in unjamming the flow.

Another line of research could involve the use of Nuclear Magnetic Resonance Imaging [71](NMRI); with such technique it is in fact possible to obtain quantitative information both on the flow of the particles and of the solvent at the same time. It would be then possible to pinpoint the presence and the role played by relative flow in determining the building-up of the non-uniform density profiles and to clarify the role played by permeation in jamming and unjamming the system. NMRI offers also the chance of imaging simultaneously much larger portions of the channels (cm) giving easy access to longitudinal data but above all opening the possibility of correlating the flow and the velocity oscillations at different positions along the channel; this would allow us to gain a better insight on the mechanisms behind the propagations of jams.

Together with the series of experiments mentioned above, we also suggest that numerical simulation will help find answers to the remaining open questions. Working with such high packing fractions should constitute an interesting challenge for the numerical simulator on its own right but above all, the possibility of running batches of calculations varying the external parameters (size ratio or the interactions between the particles) will certainly lead to interesting findings. Moreover stresses measurements will also be available from the numerical calculations offering the possibility of gaining a deeper insight on the relation between the velocity oscillations and stress-induced jamming. A direct measurement of the normal forces at the walls would for instance allow us to find a precise signature of the cause of the jams. Finally simulations on weakly Brownian systems like the ones we used in our experiments, could also directly unveil the presence of stress fluctuations and therefore further justify the application of our model.

10.3 Colloids vs Grains

In this thesis we have made extensive comparisons between the properties of colloidal systems and of granular media, highlighting the similarities and the differences. The issue of what is the actual role played by thermal agitation and what are the contributions of pure grain-like interparticle contacts is an intriguing one. As previously mentioned, there is a large literature on the rheology of the separate cases, but very few systematic comparisons have been carried out. It would be of paramount importance for a number of fundamental issues to be able to draw an accurate comparison and perform a systematic study with the aim of discriminate the behaviour of the two systems.

A large amount of information could be gathered by performing a series of parallel experiments on colloidal and granular systems. To remain in the area of channel flows, we can imagine to perform two parallel experiments with exactly the same system but where one case is Brownian and the other is fully a-thermal. The set-up could be arranged such as the largest number of parameters is kept identical in the two cases. For instance we could work with exactly the same particle to channel size ratio, the same material of the particles and the same solvent, the same boundary conditions and the same volume fraction and therefore be able to address any difference solely to the role played by Brownian motion. A similar approach should also be relatively straightforward to follow for numerical simulations.

Appendix A

Image filtering and particle location

In this appendix we discuss the procedures we used to filter the confocal images and locate the centres of the fluorescent particles. The following discussion is based on the initial work of Crocker and Grier [155] and on successive refinements by Weeks. After the images have been treated and the particles located, the coordinates of the centres are connected as described in Chapter 4 in order to obtain trajectories from which one can extract all the desired quantitative information.

A.1 Image filtering

We will see in the next section that the particle centres are found by determining the locally brightest pixels in the image. Disturbances to the intensity fields then affect the accuracy with which we locate the centre of the features.

Figure A.1 (left) shows a typical raw image from the confocal microscope. We can observe the presence of undesired features in the image, namely contrast gradients and random noise.

The brightness of the image is not uniform in the whole field of view, but the image is brighter in the centre and more shaded towards the edges. Large scale intensity variations across the field of view can be due to different factors in addition to actual contrast gradients given for instance by a different concentration or structure of the fluorescent objects. Non-uniformity of the optical properties of the system can lead to non-uniform brightness. In our case for instance, the quality of the image close to the walls of the glass capillary is worse than in the centre; this is due to the fact that the walls of the channels are not perfectly flat and that the corners between the walls are slightly rounded inducing optical aberrations. Variations of the intensity can

also be due to non-uniform illumination of the laser as in the case of our microscope. This inconvenience depends on the instrument and can be minimized by optimizing the alignment of the optical components in the microscope. In [155] images were collected with a CCD and therefore non-uniform intensity was also due to the varying response of the array of detectors in the CCD.

We can also observe that the image of a particle looks grainy on the pixel scale. This is due to the presence of random noise in the acquisition process. By observing the images we can notice that the noise has a correlation length $\lambda_{\mathrm{n}} \approx 1$ pixel; the fluctuations in the intensity between neighbouring pixels are practically uncorrelated.

We filter the raw images in order to eliminate the effects of the contrast gradients and noise. We describe the image by the function $A(x, y)$ which gives the brightness of pixels of position (x, y) in the image.

Contrast gradients are eliminated by subtracting the background, long wavelength intensity modulations. According to Crocker and Grier, the background can be accurately modelled by an average of the image over a region of extent $2w+1$ provided that the features of interest are small and well separated. w is an integer larger than the particle's radius in pixels but smaller than the typical interparticle separation. In images of dense colloidal systems the separation between features is generally smaller than the feature size so the requirements above are not fulfilled; nonetheless the procedure is robust enough if that the contrast gradients are sufficiently small.

The operation described here corresponds to the following transformation of the image:

$$A_w(x, y) = \frac{1}{(2w+1)^2} \sum_{i,j=-w}^{w} A(x+i, y+j). \tag{A.1}$$

In order to eliminate the high frequency noise, we convolve the image with a Gaussian surface of half width λ_{n}.

$$A_{\lambda_{\mathrm{n}}}(x, y) = \frac{1}{B} \sum_{i,j=-w}^{w} A(x+i, y+j) \exp\left(-\frac{i^2+j^2}{4\lambda_{\mathrm{n}}^2}\right), \tag{A.2}$$

where $B = \left[\sum_{i=-w}^{w} \exp\left(-\frac{i^2}{4\lambda_{\mathrm{n}}^2}\right)\right]^2$ is the normalization factor.

This procedure is preferred to a simple low pass filtering as it successfully suppresses the noise without excessively blurring the image.

The result of the application of these two filters is visible in the central image in Figure A.1. We observe that now the particles appear as distinct bright objects on a black background. The contrast gradients have been eliminated and the pixel by pixel

noise has been considerably reduced.

We note the following problems in the filtered image.

Some of the features are connected by 'bridges'; this problem is related to the finite thickness of the optical sectioning in confocal imaging. In fact particles slightly out of the focal plane are still imaged and as a result the apparent distance between their centres is smaller than the real one. This can also happen if the size of the boxcar averaging is larger than the interparticle separation. Because some features look 'joined', problems in finding the exact centre of each separate particle arise, but we will shortly see how they are overcome and which errors are introduced by bridging (see Figure A.2).

We also observe that close to the vertical edges of the field of view, where the images of some particle are clipped and therefore not spherical any more, the filtering fails to work properly. In particular we notice that two rather bright stripes appear on the sides of the image. This problem is not encountered in the other direction because the size of the field of view is larger than the channel size and therefore the image intensity 'naturally' decays to zero. We will see in the next section that this problem affects locating the particles and so the features close to the edges of the image are discarded.

Finally it is easy to see from the expressions of the filters, that they require to sum the intensity distributions on windows of size $2w+1$; it is therefore impossible to apply the filter to all the pixels at a distance smaller than w from the edges of the image. In order to overcome this problem the images are framed by a black (zero intensity) frame of width larger than w so that the full initial image is filtered. The choice of the frame is not vital since the particles close to the edges are discarded anyway, but it nonetheless affects the filtering of the parts of the image close to the edges; at any rate, we are adding a part of 'fake' image which was not present initially.

A.2 Finding the particle centres

The coordinates of the centres of the features are initially obtained by locating the local intensity maxima in the filtered images. A pixel corresponds to a particle centre if no other pixel has a higher intensity within a distance w to it. The choice of a w sufficiently small that we do not incur the error of including local maxima referring to more than one particle and large enough so that we do not find more than one local maximum within one feature, is crucial.

We can also select the 'mass' of the feature, meaning the total brightness of the image within a distance w to the brightest pixel. This generally allows us to discriminate and eliminate very small or very large features which are not actual particles.

A second, very useful control parameter is the 'threshold' which partly allows to

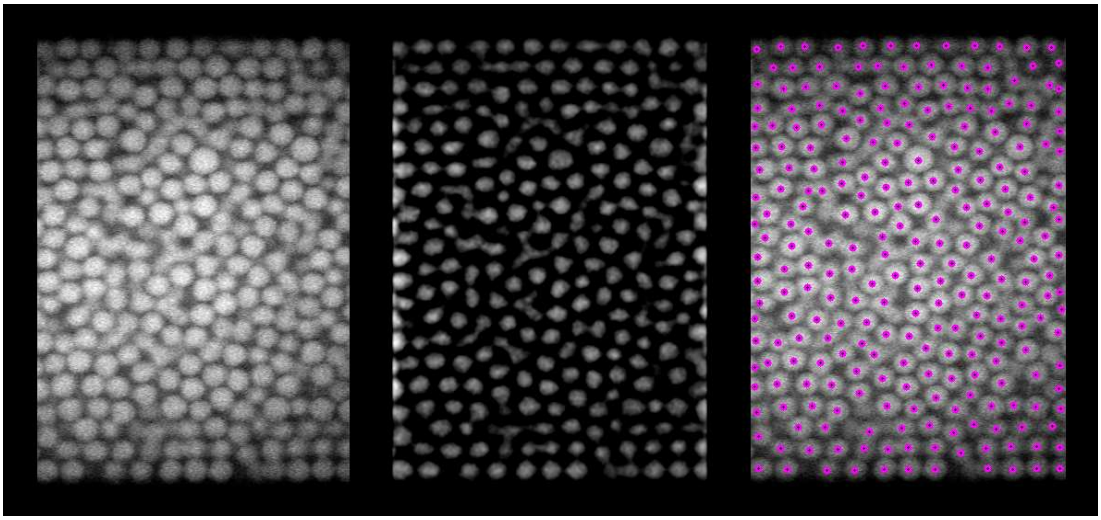

Figure A.1: From left to right. Raw confocal image of a colloidal suspension flowing into a square glass capillary, the same image after the filtering procedure and the superposition of the initial image and the particle centres found by the algorithm described in Section A.2.

solve the 'bridging' problem mentioned earlier. Figure A.2 shows how bridging between to particles occurs in the image. Part (a) shows two separate particles imaged from below by the confocal microscope. One of the particles is fully in the image plane, the other one is slightly above. If the thickness of the optical sectioning of the microscope is larger than the distance between the edge of particle and the image plane, the former will be imaged. Because the projection on the image plane of the distance between the centres of the two particles is smaller than the sum of their radii, the two features will not appear as separate, but the resulting measured intensity will rather look like what reported in part (b). In the top part of the figure we give a more precise description. The blue and the red curves represent the fluorescence intensity profiles of the two separate particles; by effect of the projection onto the image plane the measured intensity will be given by the superposition of the two (green curve). We observe that now a bridge between the two maxima is present. By setting a threshold on the intensity we are able to separate the two objects finding two separate local peaks in the intensity distribution. By adjusting the threshold parameter we are able to successfully locate the centres of particles which initially looked like single, larger objects in the filtered image.

Despite this, a more careful analysis shows that by this procedure we still make a mistake in finding the real position of the particle centres. By looking again at the top part of Figure A.2 we observe that due to the superposition of the two intensity patterns, the positions of the two local maxima in the measured intensity profile do not correspond with the position of the maxima in the single particle distributions; the

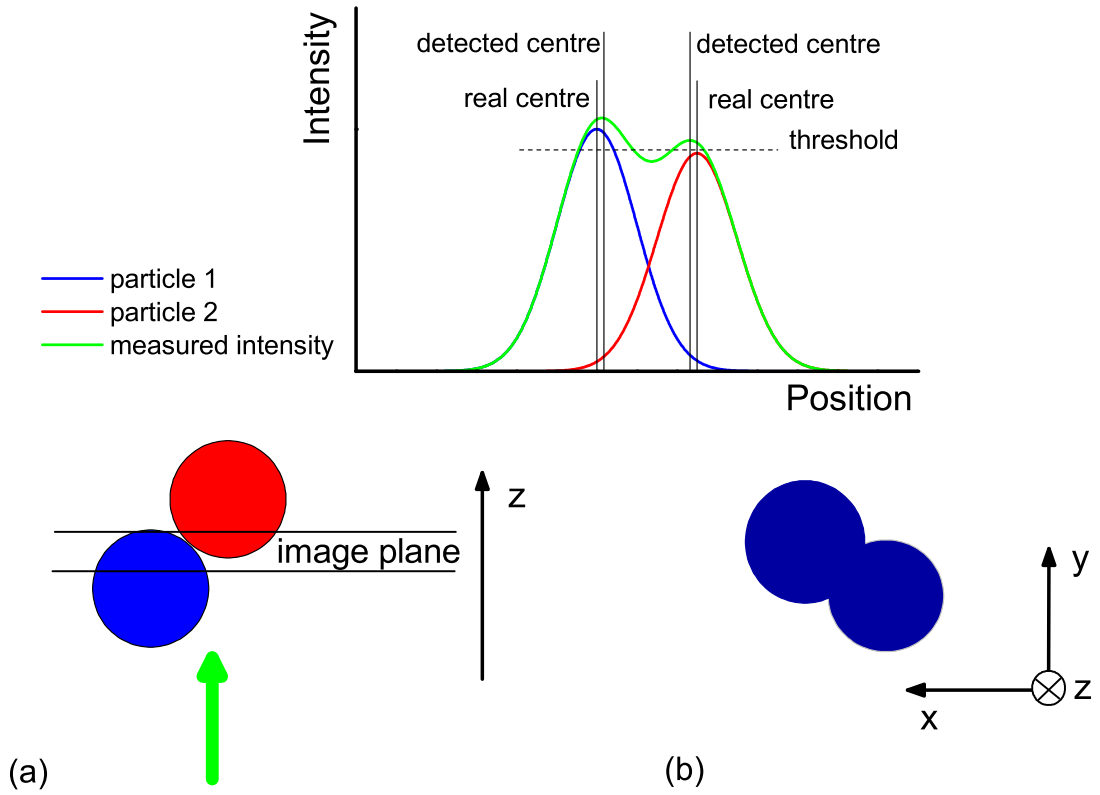

Figure A.2: (a) Lateral view of two particles imaged from below. The finite thickness of the optical section is highlighted and leads to the imaging of both features. (b) Projection onto the xy plane of the measured intensity. Top: Schematics of the single particle intensity distributions (blue and red curves) and of the resulting measured one (green curve). Thresholding separates the local maxima of the total intensity distribution whose positions are different from the single particle ones.

particles look closer to each other than they actually are.

Once we possess the coordinates of the locally brightest pixels, we refine them to get the positions of the particle centres with a higher accuracy. This is achieved by applying a *centroiding* algorithm. We assume that the position of the locally brightest pixel (x, y) is not too far from the position of the geometric centre of the brightness-weighted centre of mass (centroid) of the particle (x_0, y_0).

We calculate the offset (ϵ_x, ϵ_y) between (x, y) and (x_0, y_0) in a region of radius w around (x, y):

$$\epsilon_x = \frac{1}{m_0} \sum_{i^2+j^2 \leq w^2} iA(x+i, y+j) \tag{A.3}$$

$$\epsilon_y = \frac{1}{m_0} \sum_{i^2+j^2 \leq w^2} jA(x+i, y+j) \tag{A.4}$$

where $m_0 = \sum_{i^2+j^2 \leq w^2} A(x+i, y+j)$ is the total brightness of the window.

The new centres' coordinates will now be $(x+\epsilon_x, y+\epsilon_y)$; if the correction to the initial position is larger than 0.5 pixels, the operation is repeated taking as the new initial guess for the centre position the closest integer pixels to $(x+\epsilon_x, y+\epsilon_y)$. With this refinement procedure the coordinates of the particle centres can be obtained with sub pixel resolution down to less than 1/10 of the pixel size [155]. The removal of contrast gradients also ensures that there is no bias in centroiding the particles due to background intensity variations.

This procedure has laid the foundations for very detailed studies of the dynamics and the structure of colloidal systems via confocal microscopy [150]. Locating and tracking objects by a centroiding procedure is also widely used in several fields dealing with image analysis other than colloidal science. The method described here is fairly simple due to the sphericity of the objects, but more advanced centroiding algorithms have been developed to deal with more complicated problems such as the study of bubble dynamics during flows via particle image velocimetry [202], the evolution of waves breaking at a liquid-gas interface [203] and the quantitative analysis of digital images from space telescopes [204].

Once the refinement is completed we obtain a map of the coordinates of the centres of all the detected particles. Figure A.1 (right) shows a superposition of the original image and of the particle centres. As already mentioned, we see that the centre detection becomes inaccurate at the edges of the image, where clipped particles are recognized as full ones.

Figure A.3 shows the histogram of the x (bottom) and y (top) particle positions for a typical experiment in a square glass capillary filled with a dense colloidal suspension. Referring to the comment above, we observe artificial peaks in the x positions corresponding to the edges of the image; to avoid spurious contributions only the particles located between the two vertical dashed lines are considered, while the other ones are discarded. Although the x-distribution of particles is uniform, as mentioned previously, this problem is absent in y since the image is larger than the channel and there are no particles clipped at the edges for the vertical direction. It is worth noting that the presence of a smooth wall induces a strong y-layering in the

colloids. This feature proved to be crucial in the discussion on advection removal.

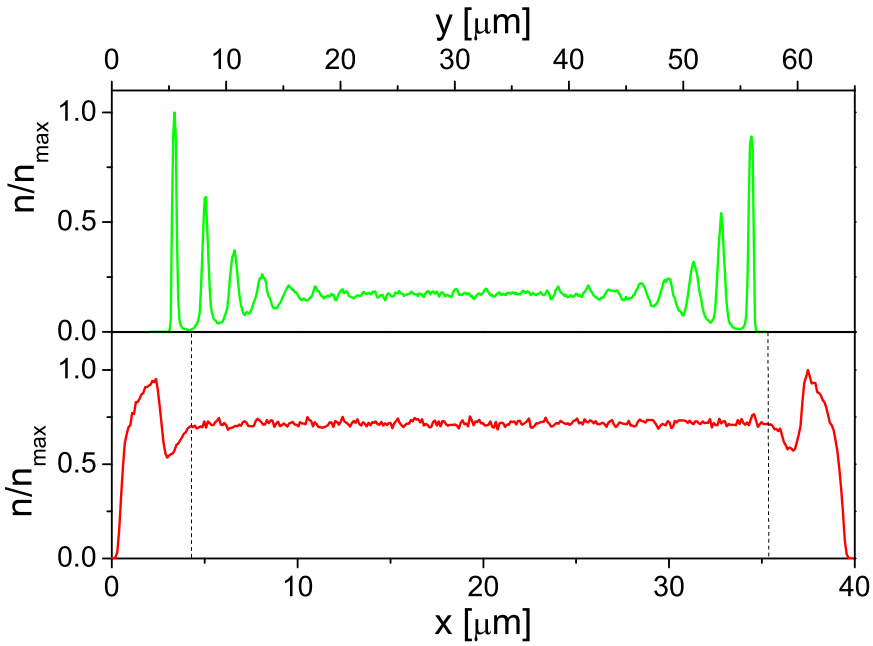

Figure A.3: Normalized histograms of x (bottom) and y (top) particles positions for a typical experiment in a square glass capillary filled with a dense colloidal suspension. The histograms have been calculated by superimposing the coordinates obtained from 5000 frames. The vertical dashed lines in the x histogram mark the range outside which particles are discarded due to spurious locating effects (note the artificial peaks).

Appendix B

Pressure recovery in capillary flows

We present here a derivation of the expression reported in Equation 5.7 describing the time evolution of the pressure recovery signal in capillary flows. Figure B.1 gives a schematic representation of the flow geometry.

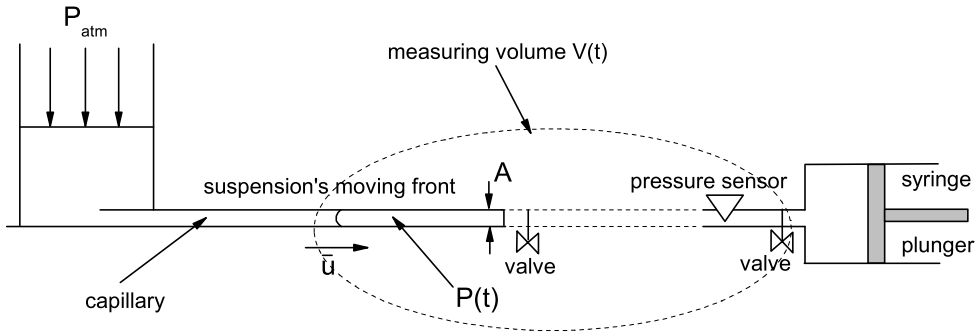

Figure B.1: Schematic representation of the flow set-up highlighting the quantities relevant for the derivation.

We recall the procedure described in Chapter 5. The valve at the end of the capillary is initially closed and the syringe plunger is displaced lowering the pressure of the air downstream of the valve from atmospheric pressure to a value $P(0)$. The syringe plunger is then held is place and it will not be moved for the whole duration of the experiment. Once the valve is opened, the suspension feels a pressure difference $P_{\mathrm{atm}} - P(0)$ and starts flowing with a flow rate $Q(0)$. During the flow the air downstream of the suspension's head undergoes a volume change; we can assume the latter to be isothermal given that the speed at which it takes place is much smaller than the speed of sound and therefore write:

$$P(t)V(t) = constant \implies PdV + VdP = 0 \implies \frac{dP}{dV} = -\frac{P}{V}. \tag{B.1}$$

The volume changes at a rate dictated by the flow and the volume change ΔV due to the fluid moving a distance Δx along a channel with cross section A is

$$\Delta V = -A\Delta x, \tag{B.2}$$

where the minus sign is due to the fact that as the flow progresses in the positive direction along the channel, the volume of the air is reduced.

The expression above can be rewritten in the following way if we introduce the average fluid velocity $\bar{u}$ across the channel's section

$$\Delta V = -A\bar{u}\delta t \implies \frac{dV}{dt} = -\bar{u}A = -Q, \tag{B.3}$$

where we used the definition of flow rate $Q = \int_A u dA = \bar{u}A$ and where Δt is the time interval corresponding to the fluid displacement. We can then look at the rate change of the pressure due to the volume change as a consequence of flow,

$$\frac{dP}{dt} = \frac{dP}{dV}\frac{dV}{dt} = \frac{P}{V}Q. \tag{B.4}$$

Rearranging this equation we can write:

$$\frac{1}{P}\frac{dP}{dt} = \frac{d(\ln P)}{dt} = \frac{Q}{V} = \frac{\bar{u}(t)A}{V}, \tag{B.5}$$

where both pressure and volume are functions of time. By integrating Equation B.3 we obtain:

$$V = V(0) - A\int_0^t \bar{u}(t')dt'. \tag{B.6}$$

The second term of the right side of the equation represents the change in volume due to the suspension flowing into the channel and it is generally much smaller that $V(0)$. The initial available volume $V(0) \approx 5 \times 10^{-6}\mathrm{m}^3$ and in the case of $50 \times 50\mu$m square capillaries with a length of 10 cm, the maximum change of volume corresponding to the complete filling up of the channel is $2.5 \times 10^{-10}\mathrm{m}^3$; this the relative contribution $A\int_0^t \bar{u}(t')dt'/V(0) \lesssim 5 \times 10^{-5}$ and can therefore be neglected.

Assuming a laminar Newtonian flow[1] $\bar{u}(t) = k\nabla P(t)$, where k is a proportionality

[1]Our suspensions are very far from being Newtonian but this assumption allows us to make a simple prediction that can be easily tested via experiments with Newtonian fluids. The assumption of Newtonian flow makes possible to relate velocities and pressure gradients in a simple way; complex fluids show radically different behaviour (see [126]).

constant depending on the fluid viscosity and the channel shape. This can be rearranged in

$$\bar{u}(t) = k\nabla P(t) = k\frac{dP(t)}{dx} \approx k\frac{\Delta P(t)}{L} = k\frac{(P_{\text{atm}} - P(t))}{L} \tag{B.7}$$

if we introduce a constant effective length L over which the pressure gradient acts. The values of L for a given flow geometry can be obtained experimentally by calibrating the system with a fluid of known viscosity.

By substitution, Equation B.5 can then be rearranged into:

$$\frac{d\ln\left(\frac{P(t)}{P_{\text{atm}}}\right)}{t} = t_0^{-1}\left(1 - \frac{P(t)}{P_{\text{atm}}}\right), \tag{B.8}$$

where $t_0 = \dfrac{LV(0)}{kAP_{\text{atm}}}$. Finally by integrating Equation B.8 we obtain

$$\frac{P(t)}{P_{\text{atm}}} = \frac{1}{1 - \left(\frac{P_{\text{atm}}}{P(0)} - 1\right)e^{-t/t_0}} \tag{B.9}$$

equivalent to Equation 5.7.

For a cylindrical channel $t_0 = \dfrac{8\eta LV(0)}{\pi R^4 P_{\text{atm}}}$ where η is the fluid viscosity and R is the radius of the channel. An analogous expression can be obtained for channels of arbitrary shape by substituting the channel radius with the *hydrodynamic radius* R_h defined as:

$$R_h = \frac{2 \times \text{area}}{\text{wetted perimeter}}.$$

For a square channel is then easy to see that $R_h = a/2$ where a is the side of the cross section; substituting then the appropriate quantities we obtain that the lower limit for our $50 \times 50\mu$m channels of $t_0 \gtrsim 1 \times 10^7$ s which justifies the assumption of constant pressure difference previously made in the text[2].

Figure B.2 shows an example of the application of the formula derived here for the case of glycerol flowing into a cylindrical capillary of 1 mm radius. In the case of this larger channel ($A\int_0^t \bar{u}(t')dt'/V(0) \lesssim 0.1$) neglecting the volume occupied by the fluid in integrating Equation B.3 holds strictly only at short times, while deviations from the predicted trend occur at longer times. Figure B.2 (left) shows the calibration measurements obtained using glycerol to find L. The rise of the value of $P(t)/P_0$ corresponds to the pressure recovery in the measuring chamber due to the progressive filling up of the capillary. The measurement ends when the capillary is completely filled

[2]The lower bound comes from the use of the pure solvent viscosity.

up, the valve at the end of the channel is closed again and therefore the pressure then remains constant. If we plot the time necessary for the glycerol to fill up the capillary (t_{fill}) as a function of ΔP_0 (Figure B.2 (right)), we observe the expected behaviour for a Newtonian liquid. As the driving pressure increases, the flow velocity increases as well; therefore t_{fill} decreases with increasing ΔP_0. This trend is no longer valid for dense colloidal suspensions [126].

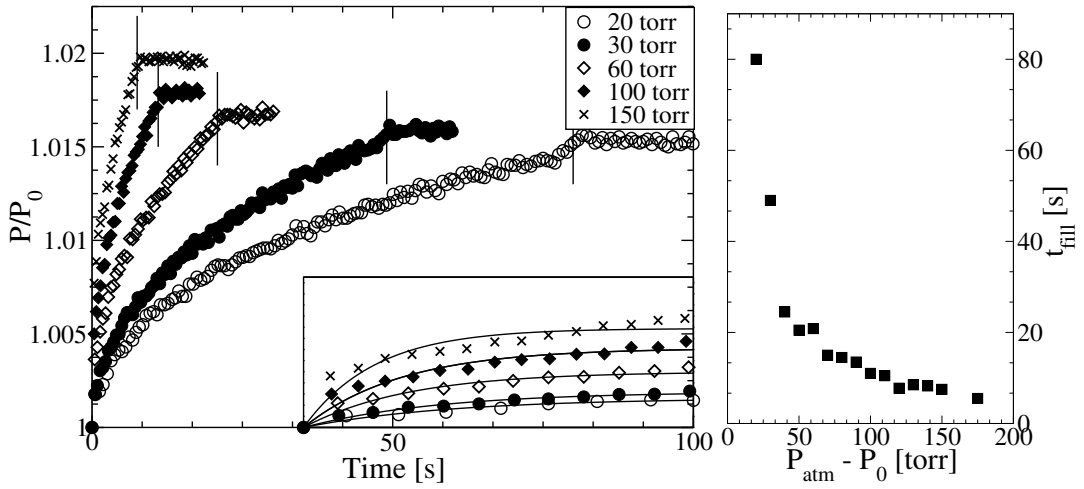

Figure B.2: Calibration measurements with glycerol. Left: pressure signals as function of time. The applied pressure differences ΔP_0 are reported in the legend. All the curves start from 1, but some early–time data points have been omitted for clarity. The flattening of the signals corresponds to the end of the measurement, i.e. when the capillary is completely filled with glycerol. The position of the vertical segments indicates the values of t_{fill}. Inset: first $5s$ of the signals and fits from equation 5.7. Right: t_{fill} as a function of ΔP_0. The data are fitted with the expression reported in the legend. Figure taken from [126].

List of Figures

2.1 a) Schematic representation of a charge-stabilized colloid highlighting the presence of the double layer. b) Schematic representation of a sterically-stabilized colloid highlighting the presence of the polymer layer. 8
2.2 Illustration of the DLVO potential and all its components. 9
2.3 Phase diagram for ideal hard-spheres suspensions. Below a volume fraction of $\Phi_F = 0.494$ the stable phase is a liquid. For volume fractions between 0.494 and 0.545, a coexistence between liquid and crystalline domains is found, while for $\Phi > \Phi_C = 0.545$ the equilibrium phase is a crystalline solid. However for systems denser than $\Phi_G = 0.58$ the system fails to crystallize and is frozen in a disordered, glassy state. The maximum disordered packing fraction $\Phi_{RCP} = 0.64$ and the maximum crystalline close packing fraction $\Phi_{CP} = 0.74$ are also reported. The top part of the figure shows confocal images of colloidal fluid, glassy and crystalline close-packed phases. 11
2.4 Schematic representation of an entropy driven phase transition in two-dimensional discs. In going from a disordered state (a) to an ordered one (b), the system loses configurational but gains free volume entropy; if the gain overcomes the loss, then the system is driven into a crystalline state. 12
2.5 Schematic representation of the repulsive part of the interaction potentials for ideal hard spheres, sterically-stabilized and charge-stabilized colloids. The thickness δ of the polymer layer is highlighted. 13
2.6 Illustration of the procedure for calculating the radial distribution function (right) of an amorphous assembly of discs (left); the colour coding of the discs is relative to the distance from the centre of the black one. Figure taken from Eric Weeks' web page: *http://www.physics.emory.edu/ weeks/idl/gofr.html* 15

3.1 Stress components acting on the faces of a cube of side L. The stresses are decomposed in the normal and tangential components with respect to each face. The vectors on three out of six faces have been omitted for clarity. 20
3.2 Illustration of elongation (a) and shear (b) deformations. 21
3.3 Schematic stress-strain relations for different kinds of solid bodies. 23
3.4 Example of planar shear between two infinite parallel plates. The upper plate is dragged with constant speed V_x and the bottom one is kept fixed; the velocity of the fluid varies linearly from 0 to V_x. 24
3.5 Illustration of constitutive relations for Newtonian and non-Newtonian fluids. The presence of a yield stress is highlighted where necessary. The curves are named in the legend from top to bottom. 25
3.6 Flow curves for PMMA hard-spheres suspensions of diameter D in the glass regime (full symbols) and at concentrated liquid suspensions (open symbols). The normalized stress, $\sigma D^3/k_BT$, is reported as a function of the Péclet number (normalized shear rate). Figure from [14] 28

3.7 Flow curves in the high rate regime for concentrated PMMA suspensions; the volume fractions are reported in the legend. The transition from continuous to discontinuous shear-thickening and jamming is visible as the volume fraction of the suspension increases. The measurements were performed in a cone-plate rheometer by the author of this thesis. 30
3.8 Experimental velocity profiles normalized by the centreline velocity across a cylindrical tube of radius R for a non-Brownian suspension with $\Phi = 0.34$. The different symbols refer to different flow rates; all the curves collapse on one single master curve. Figure from [64]. 32
3.9 Examples of velocity profiles for polyethylene melts in rectangular slits. Left: transverse velocity profiles in a rectangular slit for different applied rates; figure from [87]. Right: three-dimensional reconstruction of the velocity profile in a rectangular slit (open inverted triangles, the full symbols refers to a situation with large wall slip); figure from [88]. 35
3.10 Examples of velocity profiles for 40% starch suspensions in silicon oil (left) and tomato concentrate (right). Figures from [89] and [9] respectively. 35
3.11 Examples of velocity profiles of dry grains flowing into two-dimensional vertical channels with roughened walls with widths of 16 (left) and 28 (right) particle diameters d. Note that the size of the lateral shear bands is of roughly 5 particle diameters irrespective of channel width. Figures from [98]. 37
3.12 Schematics of two-dimensional Newtonian flows between two parallel plates and in a cylindrical channel. 39
3.13 Examples of velocity profiles for shear-thinning power law fluids in a cylindrical channel for different exponents $n \leq 1$. $n = 1$ corresponds to the Hagen-Poiseuille parabolic profile for a Newtonian liquid. The arrows point in the direction of increasing n. 41
3.14 Schematics of 2D Bingham flows. Left: stress distributions for two different applied stresses. No flow is allowed for $\tau_{xy} < \tau_{\text{yield}}$ and therefore the points where the applied stress meets the yield stress determine the size of the unsheared plug. Right: corresponding velocity profiles normalized by the Newtonian profile in the absence of a yield stress (dashed line). The different width of the lateral shear zones b is highlighted; the unsheared plug has a half-width $a - b$. 42
3.15 Examples of velocity profiles calculated for a Bingham fluid in a cylindrical channel. Note that the width of the plug depends on the value of R_0; for a constant yield stress, the width of the plug then depends on the applied pressure gradient ∇p. The arrows point towards increasing R_0/R. 43
3.16 Examples of velocity profiles calculated for an Herschel-Bulkley fluid in a cylindrical channel. Note that the width of the plug depends on the ratio $\tau_{\text{yield}}/\tau_w$ and on the HB exponent n; for a constant yield stress and for a given n (both properties of the material), the width of the plug then depends on the maximum applied stress τ_w. The arrows refer to the curves in the legend from top to bottom. 43
3.17 Flow curves in a-dimensionalised units for a hard-spheres suspension measured by Petekidis [14] (squares) and for a suspension of particles identical to ones used in this thesis but of a smaller size ($D = 280$nm, from light scattering) measured by us in the same conditions (triangles). Both suspensions have a volume fraction of 0.63. The full line is a HB fit to the data from [14] and the fit parameters are reported in th legend in a-dimensionalised units. 46
3.18 Normalized half-width of the central plug in terms of the extension of the lateral shear zones b as a function of the Oldroyd number Od for channels with square cross section and for different constitutive relations. The values of Od in our experiments are to the left of the vertical dashed line, corresponding to a plug of negligible width. Figure from [111]. 46

4.1 Image magnification by a single converging lens. 53
4.2 Diagram of an infinite tube length compound microscope. Image from [141]. . 54
4.3 Effect of immersion oil on the numerical aperture (NA) of the objective and thus on the resolving power r. α is the angle between the cone of light and the optical axis. Image from [141]. 55
4.4 (a) Airy pattern for a single point. (b) Normalized intensity of the Airy pattern on across a diametrical section in the focal plane. Diffraction patterns of two objects not fulfilling the Rayleigh criterion (c) and of two objects which do (d). The brightness of the secondary rings has been artificially increased to make them more clearly visible 57
4.5 Ray diagram of the Köhler illumination set up. Image from [141] 58
4.6 Diagram of a conventional fluorescence microscope. Image from [147] 59
4.7 Diagram of a laser scanning confocal microscope highlighting the main components. The illuminating (light blue) and emitted (green) beams are displayed. . . 61
4.8 Schematics of the principle of out-of-focus light rejection. Only the light coming from the objective focus (green) is successfully passed through the pinhole aperture in front of the detector, while rays coming from other planes are screened (red). 62
4.9 Histograms of x ($\Diamond$) and y (–) displacements after 8000 frames for a typical experiment in the laboratory reference frame before (a) and in the the co–moving reference frame after (b) the advection removal procedure. The y displacements are always smaller as the flow is along x. The histograms show the number of particles which centre moves a certain number of pixels within two consecutive frames. 68
4.10 View of the shifting/correlation procedure. Each particle is displaced by a given (dx_i, dy_i) between frame 1 and frame 2. The whole image is shifted by a $(\Delta x, \Delta y)$ which maximizes the correlation between the two successive images. 69
4.11 View of the non–uniform advection removal procedure. The images are divided in y–bins corresponding to particle layers and the shift/correlation procedure is run separately on each of them producing an array of displacements Δx_i to be subtracted to the particle coordinates. 70

5.1 Schematic representation of a sterically-stabilized colloid highlighting the presence of the polymer layer. 74
5.2 Sample cell. Once the centrifugation is completed, the wooden base is removed and the cell is directly placed onto the confocal microscope stage where the suspension is imaged from below. 80
5.3 Radial distribution functions for sediments in index-matching (decalin-tetralin) and density-matching (decalin-CHB) solvents with or without the screening salt (TBAC). Note the different volume fractions. 81
5.4 Radial distribution functions for suspensions of three volume fractions in the presence (top) and in the absence of screening salt TBAC (bottom). The vertical solid lines mark the positions of the first peak of $g(r)$ in the unscreened case. . . 82
5.5 Example of Delaunay triangulation and Voronoi diagram. The green dots (•) are the positions of the centres of the particles and therefore also the vertices of the Delaunay triangulation (light blue). The red dots (•) are the vertices of the Voronoi cells. Thicker lines mark the bounded cells, while thinner ones delimit the unbounded ones. 88
5.6 Schematic drawing and top view of the sample cell. The capillary, either with a square or rectangular cross section, is not drawn in scale. The construction on the left is placed on the microscope stage plate and the flow is imaged form below with the confocal microscope. 90

5.7 Schematic view of the experimental geometry. The glass coverslide, the sample cell and the microscope stage plate have been omitted from the drawing for clarity. The flow (green arrow) is imaged from below and two-dimensional xy slices are collected at a depth z. The the microscope objective can be translated by a piezoelectric motor, allowing the user to collect images at various depths. The microscope stage can also be translated relative to the microscope objective making it possible to collect images at different positions along the channel. . . 90

5.8 Drawings of microscope stage plates. On the left a conventional design with a circular aperture while on the right a modified one with a rectangular slot. The graded scale allows to keep track of the displacements. 91

5.9 Experimental set-up. 1) Sample cell. 2) Capillary. 3) Pressure gauge. 4) Syringe and syringe motor. 5) and 6) Valves. 7) Microscope objective. The arrow highlights the relative displacement between the microscope objective and the capillary which allows the user to image different locations along the channel. The sample cell is resting on the microscope stage (not in the drawing). 91

5.10 Schematic representation of the flow set-up. The front of the flowing suspension is highlighted. 92

5.11 Confocal image of the Richardson test slide used for calibrating the pixel size. The spacing between the vertical (horizontal) bars is of 2.0, 1.0, 0.5, 0.25, 0.125 and 0.1 μm from top to bottom respectively. Only the first three sets of scale bars are used for the calibration. The x pixel size is ≈ 4 % smaller than the y one. 94

5.12 Confocal image of the first layer of particles in a coated $50 \times 50\mu$m glass capillary. The larger particles are the coating ones while the smaller ones are suspended and flowing. 95

6.1 Average number of particles per frame as a function of the distance from the capillary inlet (0 cm). Red symbols refer to complete plug flow, green ones to the shear case and the blue stars to the presence of crystals. The averages have been performed on 1000 images (collected at 17μm from the bottom surface of the capillary) and the error bars are the standard deviations divided by the square root of the number of frames. The top and the bottom part refer to two different experiments and the latter contains two separate runs. All the measurements were performed in smooth square capillaries (width $2a = 50\mu$m) and the initial volume fraction was $\Phi \gtrsim 0.635$ in all the cases. Top: initial driving pressure $\Delta P_0 = 70$ torr. The data points were collected in the order of the numbers in the figure. Bottom: first run (circles): $\Delta P_0 = 40$ torr, second run (squares and stars): $\Delta P_0 = 40$ torr. The data points (both runs) were collected moving away from the inlet in steps of 0.5 cm. 99

6.2 Velocity profiles relative to the measurements reported in Figure 6.1(top, the numbers in the legend correspond to the order in which the data have been taken). We report here the scaled velocity profiles $[\langle V \rangle - \langle V_s \rangle]/[\langle V_c \rangle - \langle V_s \rangle]$ where $\langle V_c \rangle$ is the velocity in the centre of the channel and $\langle V_s \rangle$ is the velocity of the suspension at the wall or *slip velocity*. The data are obtained by averaging on 1000 frames and are plotted as a function of $y/a_{\rm eff}$ where in this case the effective channel half-size $a_{\rm eff} = a - \bar{D}/2$. The full lines are fits; a constant line for the complete plug (1) and a parabola for the most dilute case (2). The exact ideal profile in a square channel will be reported in Chapter 7 but at the depth where the images were collected ($z = 17\mu$m) it deviates very slightly from a parabola. All complete plug flows show up as flat lines around 0 since $\langle V \rangle = \langle V_s \rangle$ everywhere. 100

6.3 Superposition of particles positions during flow (50 images). In the left part of the image the particles are undergoing shear flow and wall slip is absent (smooth, 50 $\times 50\mu$m square channel). On the right the transition to complete plug flow is visible; note that the full plug "kicks particles off" the walls as it proceeds. The flow direction is from right to left and $\Delta P_0 = 40$ torr. 103
6.4 Average velocity difference for three external layers of particles inside the capillary as a function of time (squares). On the right axis: average number of particles per frame(n) as a function of time (full line). 105
6.5 Normalized mean square displacements in the transverse direction as function of time. The green curve is relative to a sheared suspension (Δt_1) and the red one to complete plug flow in the same position at later times (Δt_2). The straight line has a slope of 1. 105
6.6 Cartoon of non-uniform in a confined geometry leading to the formation of particle contacts. The black arrows represent the flow (x) component of particle velocity and the red dashed ones the transverse (y) component. The blue arrows indicate particles contacts and the red ones the stress exerted onto the walls. . . 107

7.1 Velocity profile for a Newtonian fluid in a square channel of side a (drawn on the side). 110
7.2 Velocity profiles in the lower half of a square capillary (width $2a = 50\mu$m) with smooth walls reconstructed in 3μm steps for PMMA particles with diameter $\bar{D} = 2.6 \pm 0.1\mu$m suspended in a buoyancy-matching solvent ($\Phi \gtrsim 0.635$). The average velocity $\langle V \rangle$ is in units of the average velocity of the central, unsheared 'plug', $\langle V_c \rangle = 20\mu m s^{-1}$. 110
7.3 Examples of averaged velocity profiles as a function of y/a_{eff} for smooth (○) and rough (▽) walls at 17μm from the bottom wall of the capillary ($z/a_{\text{eff}} = -0.32$) for a sediment ($\Phi \gtrsim 0.635$) flowing in a channel with cross section of 50μm$\times 50\mu$m. Full lines: polynomial fits; Vertical lines: extents of shear zones. Inset: width of shear zone in units of particle diameters as a function of ΔV; ▼ rough walls and ● smooth walls. 112
7.4 Averaged velocity profile as a function of y/a_{eff} for a $\Phi \gtrsim 0.635$ suspension in a $50\mu\text{m} \times 50\mu$m square capillary with smooth walls at $z/a_{\text{eff}} = -0.32$. The average has been calculated on 1000 frames. The distribution of velocities in the plug region gives an indication of the error bars for the velocity values. ΔP_0 =10 torr. 113
7.5 Averaged velocity profile as a function of y/a_{eff} for a $\Phi \gtrsim 0.635$ suspension in a $50\mu\text{m} \times 50\mu$m square capillary with rough walls at $z/a_{\text{eff}} = -0.32$. The average has been calculated on 1000 frames. ΔP_0 =20 torr. 113
7.6 Wall slip velocity $\langle V_s \rangle$ as a function of the velocity of the plug $\langle V_c \rangle$ for rough (▼) and smooth walls (●). The points correspond to the data reported in the inset of Figure 7.3. 114
7.7 Averaged velocity profile as a function of y/a_{eff} for a channel where only one side walls (the left one) is coated (smooth side(○), rough side (▽)) at $z = 17\mu$m. Full lines: polynomial fits; dashed lines: extents of sheared zones. Note that the value of a_{eff} is different on the two sides of the channel. Red line: histogram of particle y positions normalized to its maximum value. The outermost histogram peak to the left corresponds to the coating layer and therefore the measured speed is zero. 115
7.8 Values of the width of the shear zone b normalized to the effective channel size a_{eff} as a function of the applied rate ΔV for different values of the suspension volume fraction Φ. The solid and the dashed lines give the respective size of the shear zones for an ideal Newtonian liquid and for a shear-thinning power law fluid with $n = 0.65$ according to our criterion. The data refer to smooth-walled channels. 116

7.9 Normalized velocity profile for a 0.43 volume fraction suspension flowing into a 50μm $\times$ 50μm smooth capillary. The solid line is a fit where the shear-thinning power law exponent is left as a free parameter. A value of $n = 0.65 \pm 0.02$ is found. 117

7.10 Normalized velocity profile for a 0.635 volume fraction suspension flowing into a 50μm $\times$ 50μm smooth capillary at $z/a_{\text{eff}} = -0.32$. The plug (bullets) and the shear zone (squares) are highlighted. The solid line is a HB fit to the profile in the shear zone performed using Equation 7.1, with $Od = 0.22$ and $n = 0.456 \pm 0.018$. 118

7.11 Top: size of the shear zone in units of particle diameters as a function of ΔV for sediments flowing into capillaries of 50μm $\times$ 50μm (●), 80μm $\times$ 80μm (■) and 100μm $\times$ 100μm (▼) cross sections respectively. Bottom: same data in units of relative effective channel width. 119

7.12 Size of the shear zone relative to the effective channel size as a function of z/a_{eff} for a series of suspensions of different volume fractions. The right axis reports the data in units of particle diameters. The horizontal line with the open symbols represents the size of the shear zone calculated with our criterion for a fully developed Newtonian flow. 120

7.13 Size of the shear zone relative to the effective channel size as a function of z/a_{eff} for the flows of a sediment in channels with cross section of 50μm $\times$ 50μm for rough and smooth walls. 121

7.14 Size of the shear zone relative to the effective channel size as a function of z/a_{eff} for a sediment flowing into smooth channels with cross sections of 50μm $\times$ 50μm and 80μm $\times$ 80μm, respectively. 122

7.15 Velocity profile calculated for a Newtonian fluid in a rectangular channel with an aspect ratio of 10. Note that the profile in y rapidly becomes independent of z, giving a situation analogous to a 2-dimensional channel. 123

7.16 Examples of measured velocity profiles in a 40μm$\times$$400\mu$m smooth wall channel for a $\Phi \approx 30\%$ ($a_{\text{eff}} = 40\mu$m). The solid lines are parabolic fits to the points corresponding to moving particles. 123

7.17 Example of measured velocity profile (●) in a 40μm$\times$$400\mu$m smooth wall channels for a suspension with $\Phi \gtrsim 63.5\%$. The solid lines are fits to the data. The histogram of y particle positions, normalized to its maximum value, is also reported (right axis). Inset: value of the width of the shear zone b in units of particle diameters as a function of ΔV. 124

7.18 Normalized transverse fluctuations of particles in the shear zone for the smooth (–) and rough (–) boundary conditions, versus normalized time t/τ_B or *local* accumulated strain $t \cdot \partial\langle V(y)\rangle/\partial y = t \cdot \dot{\gamma}(y)$, top axis. The traces show larger fluctuations for rough walls. 126

7.19 Analytical expressions (▽) and quadratic fits (solid lines) for τ_{xy}/τ_0 in a square channel as a function of y/a_{eff} for different values of z/a_{eff}. The curved arrow points from the wall to the centre and the numbers on the right are the depths. Remember that $z/a_{\text{eff}} = 0$ is the centre. 130

7.20 (Top) Fitted fluctuating stress amplitude $\Delta\tau$ in units of $\tau_{\max}$ as a function of the 'net shear', ΔV; ■ and ● two runs for smooth walls, ▲ and ▼ two runs for rough walls. (Bottom) Schematic of the fluctuating shear stress superimposed on the continuum τ_{xy}. The dashed line shows the quadratic fit used for the integration of equation 7.11. In the zone where the fluctuating stress overcomes τ_{yield}, flow results. 131

7.21 Examples of averaged velocity profiles as a function of $y/a_{\rm eff}$ for smooth (○) and rough (▽) walls at $z = 17\mu$m ($z/a_{\rm eff} = -0.32$) for a sediment flowing in a channel with cross section of $50\mu\text{m} \times 50\mu\text{m}$. Full lines: fits obtained from equation 7.13; Vertical dashed lines: extents of shear zones. Inset: width of shear zone in units of particle diameters as a function of ΔV. ■ and ● two runs for smooth walls, ▲ and ▼ two runs for rough walls. 132
7.22 Normalized velocity profiles at $z = 17\mu$m as a function of $y/a_{\rm eff}$. We use the fitting profiles from Eq. 7.13 instead of the raw data for clarity; the typical spread of the measured profiles in each case is indicated by the error bar ($\pm 2\sigma$). 133
7.23 Inset: data from [45] giving the velocity profiles as a function of the normalized radial distance ($(R - R_i)/d_c(V_i)$), with R_i inner cylinder radius and d_c extent of sheared material) in a Couette experiment. The sheared system is a dense suspension of non-Brownian particles. The solid line is an exponential and the dotted one a power law fit. Body: ● data points from the inset corresponding to ▲. The solid lines are fits to the data with the Newtonian profile (ideal), an exponential profile (exp) and a profile calculated from Eq. 7.15 (fluct). 135
7.24 Mean value of stress fluctuations in units of the stress at walls as a function of the volume fraction of the flowing suspension. 137
7.25 Size of shear zones b in units of particle diameters as a function of channel size for our data, for the data measured by Pouliquen [98] and from the modelling in [94]. 138
7.26 Example of normalized velocity profiles (polynomial fits) for the three channels sizes. Inset: $\Delta\tau/\tau_{\rm max}$ as a function of channel size. 140
7.27 Sketch of the "bumpy" motion of a particle (in grey) flowing in the proximity of rough walls. The particles attached on the bottom wall induce fluctuations in both y and z positions. 141
7.28 Confocal images of the first layer of particles in a $50\mu\text{m} \times 50\mu\text{m}$ smooth channel; $\Phi \simeq 0.43$ (left) and $\Phi \gtrsim 0.635$ (right). 141
7.29 Normalized distribution of the absolute values of the transverse component of the velocity $V_{\rm y}^{\rm cm}$ of all the particles in the field of view calculated in the comoving frame for different the average flow velocities reported in the legend at $z/a_{\rm eff} = -0.32$. The data refer to smooth channels. 143
7.30 Normalized distribution of the absolute values of the transverse component of the velocity $V_{\rm y}^{\rm cm}$ of all the particles in the field of view calculated in the comoving frame for different the average flow velocities reported in the legend at $z/a_{\rm eff} = -0.32$. The data refer to rough channels. 143
7.31 FWHM extracted from the distributions reported in Figures 7.29 and 7.30 as a function of flow speed. Bullets correspond to smooth channels, triangles to rough ones. 144
7.32 Standard deviation of the transverse velocity in the comoving frame ($\delta V_{\rm y}$) normalized by its maximum value $\delta V_{\rm y}^{\rm max}$ as a function of $y/a_{\rm eff}$ at $z/a_{\rm eff} = -0.32$. Bullets correspond to smooth channels, triangles to rough ones. Particles have higher mobility close to the walls. Rough walls induce fluctuations with longer decay. The vertical lines mark the average width of the shear zones for smooth (solid) and rough (dashed) boundaries. 145
7.33 Average density profile at $z = 17\mu$m for a sediment flowing in a channel with rough walls. The density n is given in units of the density in the centre, n_c. The plug is $\approx 10\%$ denser than the edge of the shear zone. 148
7.34 Number of particles in a five particles-wide y-bin in the centre of the channel as a function of volume fraction. The straight line is a fit to the high volume fraction points. 150

8.1 Spatio-temporal diagrams relative to two uniform flows $\Phi \simeq 0.3$. The slope of the traces left by the particles gives the flow speed. In this case $V_2 > V_1$. The images were taken at $z/a_{\text{eff}} = 0.32$ and a 50 μm long, 1 pixel wide strip along the centreline of the channel ($y/a_{\text{eff}} = 0$) was extracted. 155
8.2 Example of the method for signal processing and FFT. The black curve is a signal obtained by superimposing three sine waves of frequency 0.5π, π, 1.5π and different amplitudes and randomly generated noise. The red curve shows the signal after the low pass filtering, the blue one is the DC-like offset and the green one is their difference. Inset: normalized power spectrum of the green curve. 155
8.3 Example of oscillating flow for a 0.635 volume fraction suspension. The main body of the figure shows the measured velocity signal and the elaborated ones (colours as in Figure 8.2). Right: spatio-temporal diagram corresponding to the first 9 seconds of flow. The dips in the velocity signal are highlighted on the diagram. The images were taken at $z/a_{\text{eff}} = 0.32$ and a 44 μm long, 1 pixel wide strip along the centreline of the channel ($y/a_{\text{eff}} = 0$) was extracted. 156
8.4 Spatio-temporal diagrams for two portions of the flow reported in Figure 8.7 corresponding to the time intervals 10 to 23 s and 50 to 63 s respectively. The average flow speed is lower for the left image. The inverse frequencies $1/f_{1,2}$ mark the time separation between jamming events, while $\Delta t_{1,2}$ are the respective durations of the jams. The images were taken at $z/a_{\text{eff}} = 0.32$ and a 44 μm long, 1 pixel wide strip along the centreline of the channel ($y/a_{\text{eff}} = 0$) was extracted. The initial applied pressure difference was 40 torr and $\Phi = 0.635$. 158
8.5 Flow velocity as a function of time. The initial applied pressure difference was 10 torr and $\Phi = 0.635$. 159
8.6 Velocity signal for two different time intervals from Figure 8.5. The red ellipse in the right figure highlights the events sequence associated with jamming and subsequent velocity oscillations. 159
8.7 Another example of fluctuating velocity signal. The smaller graphs on the side are blow-ups of the main graph; note the different vertical scales. The spatio-temporal diagrams in Figure 8.4 correspond to portions of these signals. The initial applied pressure difference was 40 torr and $\Phi = 0.635$. 160
8.8 Normalized power spectrum for the velocity signal in Figure 8.5. In the inset we report the spectra for the signals in Figure 8.6 where the blue one is relative to lower speed than the red one. 161
8.9 Blow up of 4 seconds of the offset velocity signal from Fig.8.5 with the correspondent fits obtained from the superposition of 4 (red and blue) and 6 (green) sine waves. $t_0 = 44$ s. 161
8.10 A $\Phi \simeq 0.635$ suspension is driven into a $50\mu\text{m} \times 50\mu\text{m}$ uncoated channel by an initial pressure difference $\Delta P_0 = 10$ torr. The driving pressure ΔP was then changed during the experiment and we report here its value normalized to ΔP_0 as a function of time (red) as well as the corresponding offset average speed (black). 162
8.11 Fundamental frequency of the oscillations in the velocity signal as a function $\langle V \rangle - V_{\text{thr}}$; the full curve is a fit a power law with exponent 0.336 ± 0.126. Inset: fundamental oscillations frequency as a function of the average flow speed $\langle V \rangle$; the points with non-zero frequency are fitted with Equation 8.1 (full curve). From the fit we obtain the value of $V_{\text{thr}} = 10.06\mu$m/s, corresponding to a pressure difference of 53 torr. 164
8.12 Standard deviation of the offset velocity signal versus average $\langle V \rangle - V_{\text{thr}}$. The data points to the left of the threshold velocity show the fluctuation level in the noise in the absence of oscillations. 164

8.13 Duration of jams as a function of average flow speed. The points have been obtained by calculating and averaging Δt on different data sets. Inset: signal in Figure 8.7(top right). The blue curve is the long time averaged signal $\langle V \rangle$ and the open symbols mark those points whose velocity is lower than $0.5 \times \langle V \rangle$ and therefore jammed according to our definition. 165

8.14 Right: spatio-temporal diagram obtained from images collected just inside the channel and showing 5 seconds of flow. From the traces we detect two jams. Left: velocity in the centre of the channel of the downstream (red curve) and upstream (green curve) part of the images as a function of time. The downstream part corresponds to the first 8.5 μm of the field of view and the upstream one to the last 8.5 μm. The jam takes a finite time Δt to travel across the field of view (44 μm). 166

8.15 Speed as a function of time for shear flow in the centre of a square cross–sectioned capillary with smooth walls and initial applied pressure difference of 10 torr. In the inset 10 seconds of the signal are blown–up to show the shape of the oscillations. 167

8.16 Flow velocity as a function of time for three different experiments in a 40×400 μm rectangular cross-sectioned, uncoated capillary. The volume fraction of the suspension was $\Phi \simeq 0.635$ and the three applied initial pressure differences were of 10 (red), 30 (blue) and 40 torr (green) respectively. After the flow started ΔP was kept constant in all cases. 168

8.17 Velocity of two sections (upstream and downstream) and of the whole field of view as function of time in correspondence of a jamming event. t_0 is an arbitrary time. The jam takes 0.4 s to travel the 36 μm which separate the two sections of the field of view. Inset: number of particles per frame as function of time. $\Phi \simeq 0.635$. 169

8.18 Flow velocity in the centre of the channel as a function of time for the flow reported in the diagrams of Figure 8.19. The flow spontaneously stops and is restarted by applying a sevenfold higher pressure difference; once restarted, the flow is highly discontinuous. The time axis is offset by an arbitrary time t_0 previous to the flow recovery. 170

8.19 Spatio-temporal diagrams for a flow in a $50 \times 50 \mu$m channel with rough walls. The images were taken at $z/a_{\rm eff} = 0.32$ and a 44 μm long, 1 pixel wide strip along the centreline of the channel ($y/a_{\rm eff} = 0$) was extracted. The initial applied pressure difference was 40 torr and $\Phi = 0.635$. The flow comes to arrest under an applied pressure difference of 20 torr and stays jammed until the applied ΔP reaches 140 torr. At that point, flow starts again in a succession of discontinuous jumps and jams (highlighted with white arrows). The right diagram is the continuation of the left one. The diagrams correspond to the first 18 s of Figure 8.18 171

8.20 Top: average velocity in the laboratory frame as a function of time. Middle-bottom: $\langle V_{\rm tot}^{\rm cm} \rangle$ as a function of time, measured at one of the walls (middle) and in the centre of the channel. The data refer to three-particles-wide y-bins. $z/a_{\rm eff} = -0.32$. $\Phi \simeq 0.635$. 173

8.21 Top: average velocity in the laboratory frame as a function of time. Middle-bottom: standard deviation of $\langle V_{\rm tot}^{\rm cm} \rangle$ as a function of time, measured at one of the walls (middle) and in the centre of the channel. The data refer to three-particles-wide y-bins. $z/a_{\rm eff} = -0.32$. $\Phi \simeq 0.635$. 174

8.22 $\langle V_{\rm tot}^{\rm cm} \rangle$ as a function of y for three different average flow speeds. The data come from three sections of the same experiment reported in Figure 8.21 and 8.20. . . 174

8.23 Angles between neighbouring particles in the three most external layers close to one of the inner walls before (black points) and after (red points) the velocity fluctuation reported in the left inset. The full lines are an average of the scattered points. Inset: velocity as a function of time (t_0 is an arbitrary time instant); the symbols determine the 'before' and 'after' in the fluctuation. 176
8.24 Angles between neighbouring particles in a three particles-wide y-bin around the centreline before (black points) and after (red points) the velocity fluctuation reported in the left inset. The full lines are an average of the scattered points. Inset: velocity as a function of time (t_0 is an arbitrary time instant); the symbols determine the 'before' and 'after' in the fluctuation. 176
8.25 Confocal images of the suspension before (left) and after (right) the velocity fluctuation of Figure 8.23 and 8.24. We highlighted the angles between two sets of neighbouring particles close to the walls and in the centre of the channel, following them through the velocity fluctuation. We can appreciate how their relative positions change (at the wall) or stay unchanged (centre). 177
8.26 y mean square displacements normalized by particle radius for three measurements at different ΔP (black, red and green curve). The data are taken in the centre of a capillary with smooth walls. 179

A.1 From left to right. Raw confocal image of a colloidal suspension flowing into a square glass capillary, the same image after the filtering procedure and the superposition of the initial image and the particle centres found by the algorithm described in Section A.2. 194
A.2 (a) Lateral view of two particles imaged from below. The finite thickness of the optical section is highlighted and leads to the imaging of both features. (b) Projection onto the xy plane of the measured intensity. Top: Schematics of the single particle intensity distributions (blue and red curves) and of the resulting measured one (green curve). Thresholding separates the local maxima of the total intensity distribution whose positions are different from the single particle ones. 195
A.3 Normalized histograms of x (bottom) and y (top) particles positions for a typical experiment in a square glass capillary filled with a dense colloidal suspension. The histograms have been calculated by superimposing the coordinates obtained from 5000 frames. The vertical dashed lines in the x histogram mark the range outside which particles are discarded due to spurious locating effects (note the artificial peaks). 197

B.1 Schematic representation of the flow set-up highlighting the quantities relevant for the derivation. 199
B.2 Calibration measurements with glycerol. Left: pressure signals as function of time. The applied pressure differences ΔP_0 are reported in the legend. All the curves start from 1, but some early–time data points have been omitted for clarity. The flattening of the signals corresponds to the end of the measurement, i.e. when the capillary is completely filled with glycerol. The position of the vertical segments indicates the values of t_{fill}. Inset: first $5s$ of the signals and fits from equation 5.7. Right: t_{fill} as a function of ΔP_0. The data are fitted with the expression reported in the legend. Figure taken from [126]. 202

List of Tables

5.1 Physical properties of interest of PMMA and the solvents used. 77

Bibliography

[1] J Choi, A Kudrolli, and M Z Bazant. Velocity profile of granular flows inside silos and hoppers. *Journal of Physics: Condensed Matter*, 17:S2533–S2548, 2005.

[2] M M Denn. Extrusion instabilities and wall slip. *Annual Review of Fluid Mechanics*, 33:265–287, 2001.

[3] D N Ku. Blood flow in arteries. *Annual Review of Fluid Mechanics*, 29:399–434, 1997.

[4] H B Li, H P Fang, Z F Lin, et al. Lattice Boltzmann simulation on particle suspensions in a two-dimensional symmetric stenotic artery. *Annual Review of Fluid Mechanics*, 69(3):031919, 2004.

[5] J G Riess. Fluorous micro- and nanophases with a biomedical perspective. *Tetrahedron*, 58(20):4113–4131, 2002.

[6] S M Moghimi, A C Hunter, and J C Murray. Long-circulating and target-specific nanoparticles: Theory to practice. *Pharmacological Reviews*, 53(2):283–318, 2001.

[7] T G Mason and J Bibette. Shear rupturing of droplets in complex fluids. *Langmuir*, 13(17):4600–4613, 1997.

[8] S L Rough, J Bridgwater, and D I Wilson. Effects of liquid phase migration on extrusion of microcrystalline cellulose pastes. *International Journal of Pharmaceutics*, 204:117–126, 2000.

[9] Y J Choi, R R Milczarek, C E Fleck, T C Garvey, K L McCarthy, and M J McCarthy. In-line monitoring of tomato concentrate physical properties during evaporation. *Journal of Food Process Engineering*, 29:615–632, 2006.

[10] J Bent et al. Neutron-mapping polymer flow: Scattering, flow visualization, and molecular theory. *Science*, 301:1691, 2003.

[11] J A Lewis. Colloidal processing of ceramics. *J. Am. Ceramic Soc.*, 83(10):2341, 2000.

[12] D I Wilson and S L Rough. Exploiting the curious characteristics of dense solid-liquid pastes. *Chem. Engin. Sci.*, 61:4147–54, 2006.

[13] M D Haw. Jamming, two–fluid behaviour and 'self–filtration' in concentrated particulate suspensions. *Phys. Rev Lett.*, 92:185506, 2004.

[14] G Petekidis, D Vlassopoulos, and P N Pusey. Yielding and flow of sheared colloidal glasses. *J. Phys.–Condens. Mat.*, 16(38):S3955–S3963, 2004.

[15] K N Pham, G Petekidis G, D Vlassopoulos, S U Egelhaaf, P N Pusey, and W C K Poon. Yielding of colloidal glasses. *Europhys. Lett.*, 75:624–630, 2006.

[16] W J Frith, P d'Haene, R Buscall, and J Mewis. Shear thickening in model suspensions of sterically stabilized particles. *J. Rheo.*, 40(4):531–548, 1996.

[17] D Lootens, H van Damme, and P Hebraud. Giant stress fluctuations at the jamming transition. *Phys. Rev. Lett.*, 90(17):178301, 2003.

[18] D Psaltis, S R Quake, and C H Yang. Developing optofluidic technology through the fusion of microfluidics and optics. *Nature*, 442:381–386, 2006.

[19] M Fuchs and M E Cates. Theory of nonlinear rheology and yielding of dense colloidal suspensions. *Phys. Rev. Lett.*, 89:248304, 2002.

[20] A Einstein. Über die von der molekularkinetischen Theorie der Wärme geforderte Bewegung von in ruhenden Flüssigkeiten suspendierten Teilchen. *Annalen der Physik*, 17:549–560, 1905.

[21] P N Pusey. *Liquids, Freezing and the Glass Trnasition*, chapter 10. Elsevier, 1991.

[22] W C K Poon. Colloids as big atoms. *Science*, 304:830–831, 2004.

[23] J Perrin. *Journal de Physique*, 9:5, 1910.

[24] D G A L Aarts, M Schmidt, and H N W Lekkerkerker. Direct visual observation of thermal capillary waves. *Science*, 301:1691, 2004.

[25] P N Pusey and W van Megen. Phase behaviour of concentrated suspensions of nearly hard colloidal spheres. *Nature*, 320:340–342, 1986.

[26] E R Weeks, J C Crocker, A C Levitt, A Schofield, and D A Weitz. Three–dimensional direct imaging of structural relaxation near the colloidal glass transition. *Science*, 287:627–631, 2000.

[27] J N Israelachvili. *Intramolecular and Surface Forces*. Academic Press, London, 2nd edition, 1991.

[28] B W Ninham. On progress in forces since the DLVO theory. *Advances in Colloid and Interface Science*, 83:1–17, 1999.

[29] H Sedgwick. *Colloidal Metastability*. PhD thesis, School of Physics, The University of Edinburgh, 2003.

[30] W W Wood and J D Jacobson. Preliminary results from a recalculation of the Monte Carlo equation of state of hard spheres. *Journal of Chemical Physics*, 27(5):1207–1208, 1957.

[31] W G Hoover and F H Ree. Melting transition and communal entropy or hard spheres. *Journal of Chemical Physics*, 49(8):3609–3617, 1968.

[32] J X Zhu, M Li, R Rogers, W Meyer, R H Ottewill, W B Russell, and P M Chaikin. Crystallization of hard-sphere colloids in microgravity. *Nature*, 387(6636):883–885, 1997.

[33] N B Simeonova and W K Kegel. Gravity-induced aging in glasses of colloidal hard spheres. *Physical Review Letters*, 93(3):035701, 2004.

[34] J D Bernal. The bakerian lecture, 1962: The structure of liquids. *Proceedings of the Royal Society*, A280:290–321, 1964.

[35] J D Bernal. A geometrical approach to the structure of liquids. *Nature*, 183:141:147, 1959.

[36] J D Bernal and J Mason. Co-ordination of randomly packed spheres. *Nature*, 188:910:911, 1960.

[37] E B Sirota, H D Ou-Yang, S K Sihna, and P M Chaikin. Complete phase diagram of a charged colloidal system - a synchrotron and x-ray scattering study. *Physical Review Letters*, 62:1524–1527, 1989.

[38] D J Fairhurst. *Polydispersity in Colloidal Phase Transitions*. PhD thesis, School of Physics, The University of Edinburgh, 1999.

[39] P Linder and T Zemb, editors. *Neutrons, X-rays and Light: Scattering Methods Applied to Soft Condensed Matter*. North-Holland, 2002.

[40] A Evilevitch, V Lobaskin, U Olsson, P Linse, and P Schurtenberger. Structure and transport properties of a charged spherical microemulsion system. *Langmuir*, 17(4):1043–1053, 2001.

[41] C P Royall, M E Leunissen, A-P Hynninen, M Dijkstra, and A van Blaaderen. Re-entrant melting and freezing in a model system of charged colloids. *The Journal of Chemical Physics*, 124(24):244706, 2006.

[42] P Coussot and C Ancey. Rheophysical classification of concentrated suspensions and granular pastes. *Physical Review E*, 59(4):4445–4457, 1999.

[43] W van Megen and S M Underwood. Glass transition in colloidal hard spheres: Measurement and mode coupling theory analysis of the coherent intermediate scattering function. *Physical Review E*, 49(5):4206–4220, 1994.

[44] R Besseling, E R Weeks, A B Schofield, and W C K Poon. Three-dimensional imaging of colloidal glasses under steady shear. *Physical Review Letters*, 99:028301, 2007.

[45] N Huang, G Ovarlez, F Bertrand, S Rodts, P Coussot, and D Bonn. Flow of wet granular materials. *Phys. Rev. Lett.*, 94:028301, 2005.

[46] P Pierrat and H S Caram. Tensile strength of wet granular materials. *Powder Technology*, 91(2):83–93, 1997.

[47] R Albert, I Albert, D Hornbaker, P Schiffer, and A L Barabasi. Maximum angle of stability in wet and dry spherical granular media. *Physical Review E*, 56(6):R6271–R6274, 1997.

[48] J C Geminard, W Losert, and J P Gollub. Frictional mechanics of wet granular material. *Physical Review E*, 59(5):5881–5890, 1999.

[49] R G Larson. *The Structure and Rheology of Complex Fluids*. Oxford University Press, Oxford, 1999.

[50] M Fuchs and M E Cates. Theory of nonlinear rheology and yielding of dense colloidal suspensions. *Physical Review Letters*, 89(24):248304, 2002.

[51] P Sollich, F Lequeux, P Hèbraud, and M E Cates. Rheology of soft glassy materials. *Journal of Rheology*, 78(10):2020–2023, 1997.

[52] M Fuchs and M E Cates. Non-Newtonian viscosity of interacting Brownian particles: comparison of theory and data. *Journal of Physics: Condensed Matter*, 15:S401–S406, 2003.

[53] C B Holmes, M E Cates, M Fuchs, and P Sollich. Glass transitions and shear thickening suspension rheology. *Journal of Rheology*, 49(1):237–269, 2005.

[54] L E Silbert, D Ertas, G S Grest, T C Halsey, and D Levine. Analogies between granular jamming and the liquid-glass transition. *Physical Review E*, 65(5):051307, 2002.

[55] Emanuel Bertrand, Jerome Bibette, and Veronique Schmitt. From shear thickening to shear–induced jamming. *Physical Review E*, 66:060401, 2002.

[56] V T O'Brien and M E Mackay. Stress components and shear thickening of concentrated hard sphere suspensions. *Langmuir*, 16:7931–7938, 2000.

[57] D Lootens, H van Damme, Y Hemar, and P Hebraud. Dilatant flow of concentrated suspensions of rough particles. *Phys. Rev. Lett.*, 95:268302, 2005.

[58] R L Hoffman. Explanations for the cause of shear thickening in concentrated colloidal suspensions. *Journal of Rheology*, 42(1):111–123, 1998.

[59] G Bossis and J F Brady. The rheology of Brownian suspensions. *Journal of Chemical Physics*, 91(3):1866–1874, 1989.

[60] J R Melrose and R C Ball. "Contact networks" in continuously shear thickening colloids. *Journal of Rheology*, 48(5):961–978, 2004.

[61] M E Cates et al. Jamming, force chains and fragile matter. *Phys. Rev. Lett.*, 81(9):1841–1844, 1998.

[62] M E Cates, M D Haw, and C B Holmes. Dilatancy, jamming, and the physics of granulation. *Journal of Physics: Condensed Matter*, 17:S2517–S2531, 2005.

[63] D A Head, A Ajdari, and M E Cates. Rheological instability in a simple shear-thickening model. *Europhysics Letters*, 57(1):120–126, 2002.

[64] R G Cox and S G Mason. Suspended particles in fluid flow through tubes. *Annual Review of Fluid Mechanics*, 3:291–316, 1971.

[65] F Durst, A Melling, and J H Whitelaw. *Principles and practice of laser-Doppler anemometry*. Academic Press, New York, 1981.

[66] C J Koh, P Hookham, and L G Leal. An experimental investigation of concentrated suspension flows in a rectangular channel. *Journal of Fluid Mechanics*, 266:1–32, 1994.

[67] A Averbakh, A Shauly, A Nir, and R Semiat. Slow viscous flows of highly concentrated suspensions. Part 1. Laser-Doppler velocimetry in rectangular ducts. *International Journal of Multiphase Flow*, 23(3):409–424, 1997.

[68] A Shauly, A Averbakh, A Nir, and R Semiat. Slow viscous flows of highly concentrated suspensions. Part 2. Particle migration, velocity and concentration profiles in rectangular ducts. *International Journal of Multiphase Flow*, 23(4):613–629, 1997.

[69] M K Lyon and L G Leal. An experimental study of the motion of concentrated suspensions in two-dimensional channel flow. Part 1. Monodisperse systems. *Journal of Fluid Mechanics*, 363:25–56, 1998.

[70] P R Nott and J F Brady. Pressure-driven flow of suspensions: simulation and theory. *Journal of Fluid Mechanics*, 275:157–199, 1994.

[71] E Fukushima. Nuclear magnetic resonance as a tool to study flow. *Annual Review of Fluid Mechanics*, 31:95–123, 1999.

[72] S W Sinton and A W Chow. NMR flow imaging of fluids and solid suspensions in Poiseuille flow. *Journal of Rheology*, 35(5):735–772, 1991.

[73] R E Hampton, A A Mammoli, A L Graham, N Tetlow, and S A Altobelli. Migration of particles undergoing pressure-driven flow in a circular conduit. *Journal of Rheology*, 41(3):621–640, 1997.

[74] J F Morris and J F Brady. Pressure-driven flow of a suspension: Buoyancy effects. *International Journal of Multiphase Flow*, 24(1):105–130, 1998.

[75] J R Abbott, N Tetlon, A L Graham, S A Altobelli, E Fukushima, L A Mondy, and T S Stephens. Experimental observations of particle migration in concentrated suspensions: Couette flow. *Journal of Rheology*, 35(5):773–795, 1991.

[76] D Leighton and A Acrivos. The shear-induced migration of particles in concentrated suspensions. *Journal of Fluid Mechanics*, 181:415–439, 1987.

[77] S R Subia, M S Ingber, L A Mondy, S A Altobelli, and A L Graham. Modelling of concentrated suspensions using a continuum constitutive equation. *Journal of Fluid Mechanics*, 373:193–219, 1998.

[78] R M Miller and J F Morris. Normal stress-driven migration and axial development in pressure-driven flow of concentrated suspensions. *Journal of Non-Newtonian Fluid Mechanics*, 135(2-3):149–165, 2006.

[79] Y A Buyevich and S K Kapbsov. Segregation of a fine suspension in channel flow. *Journal of Non-Newtonian Fluid Mechanics*, 86:157–184, 1999.

[80] M Frank, D Anderson, E R Weeks, and J F Morris. Particle migration in pressure–driven flow of a Brownian suspension. *J. Fluid Mech.*, 493:363–378, 2003.

[81] D Semwogerere, J F Morris, and E R Weeks. Development of particle migration in pressure-driven flow of a Brownian suspension. *Journal of Fluid Mechanics*, 581:437–451, 2007.

[82] T A Kowalewski. Concentration and velocity measurements in the flow of droplet suspensions through a tube. *Experiments in Fluids*, 2:213–219, 1984.

[83] X Li and C Pozrikidis. Wall-bounded shear flow and channel flow of suspensions of liquid drops. *International Journal of Multiphase Flow*, 26:1247–1279, 2000.

[84] R H Somani, L Yang, L Zhu, and B S Hsiao BS. Flow-induced shish-kebab precursor structures in entangled polymer melts. *Polymer*, 46(20):8587–8623, 2005.

[85] S. Nigen, N El Kissi, J-M Piau, and S Sadun. Velocity field for polymer melts extrusion using particle image velocimetry. Stable and unstable flow regimes. *Journal of Non-Newtonian Fluid Mechanics*, 112:177–202, 2003.

[86] M W Collis, A K Lele, M R Mackley, R S Graham, D J Groves, A E Likhtman, T M Nicholson, O G Harlen, T C B McLeish, L R Hutchings, C M Fernyhough, and R N Young. Constriction flows of monodisperse linear entangled polymers: Multiscale modeling and flow visualization. *Journal of Rheology*, 49(2):501–522, 2005.

[87] H Munstedt, M Schmidt, and E Wassner. Stick and slip phenomena during extrusion of polyethylene melts as investigated by laser-doppler velocimetry. *Journal of Rheology*, 44(2):413–427, 2000.

[88] L Robert, Y Demay, and B Vergnes. Stick-slip flow of high density polyethylene in a transparent slit die investigated by laser doppler velocimetry. *Rheological Acta*, 43:89–98, 2004.

[89] B Ouriev and E J Windhab. Rheological study of concentrated suspensions in pressure-driven shear flow using a novel in-line ultrasound doppler method. *Experiments in Fluids*, 32(2):204–211, 2002.

[90] C S Campbell. Granular material flows — an overview. *Powder Techol.*, 162:208–229, 2006.

[91] I Goldhirsch. Rapid granular flows. *Annual Review of Fluid Mechanics*, 35:267–293, 2003.

[92] P Jop, Y Forterre, and O Pouliquen. A constitutive law for dense granular flows. *Nature*, 441(8):727–729, 2006.

[93] S B Savage. Analyses of slow high-concentration flows of granular materials. *Journal of Fluid Mechanics*, 377:1–26, 1998.

[94] O Pouliquen, Y Forterre, and S Ledizes. Slow dense granular flows as a self-induced process. *Advances in Complex Systems*, 4(4):441–450, 2001.

[95] G D R MiDi. On dense granular flows. *Eur. Phys. J. E*, 14:341–365, 2004.

[96] S B Savage. Gravity flows of cohesionless granular materials in chutes and channels. *Journal of Fluid Mechanics*, 92:53, 1979.

[97] V V R Natarajan, M L Hunt, and E D Taylor. Local measurements of velocity fluctuations and diffusion coefficients for a granular material flow. *Journal of Fluid Mechanics*, 304:1–25, 1995.

[98] O Pouliquen and R Gutfraind. Stress fluctuations and shear zones in quasistatic granular chute flows. *Phys. Rev. E*, 53(1):552–561, 1996.

[99] R Gutfraind and O Pouliquen. Study of the origin of shear zones in quasi-static vertical chute flows by using discrete particle simulations. *Mech. Mater.*, 24:273–285, 1996.

[100] C Denniston and H Li. Dynamics and stress in gravity-driven granular flow. *Physical Review E*, 59(3):3289–3292, 1999.

[101] J-C Tsai, W Losert, G A Voth, and J P Gollub. Two-dimensional granular Poiseuille flow on an incline: Multiple dynamical regimes. *Physical Review E*, 65:011306, 2001.

[102] S P Meeker, R T Bonnecaze, and M Cloitre. Slip and flow in pastes of soft particles: Direct observation and rheology. *Journal of Rheology*, 48(6):1295–1320, 2004.

[103] U Yilmazer and D M Kaylon. Slip effects in capillary and parallel disk torsional flows of highly filled suspensions. *Journal of Rheology*, 33(8):1197–1212, 1989.

[104] Y Zhu and S Granick. Rate-dependent slip of Newtonian liquid at smooth surfaces. *Physical Review Letters*, 87(9):096105, 2001.

[105] Y Zhu and S Granick. Limits of the hydrodynamic no-slip boundary condition. *Physical Review Letters*, 88(10):106102, 2002.

[106] S P Salvatore and R Skalak. The history of Poiseuille's law. *Annual Review of Fluid Mechanics*, 25:1–19, 1993.

[107] F M White. *Viscous Fluid Flow*. McGraw-Hill, second edition, 1991.

[108] J F Steffe. *Rheological methods in food processing engineering*. Freeman Press, East Lansing, MI, USA, 1996.

[109] E Mitsoullis and R R Huilgol. Entry flow of Bingham plastics in expansions. *Journal of Non–Newtonian Fluid Mechanics*, 122:45–54, 2004.

[110] M A Moyers-Gonzalez and I A Frigaard. Numerical solutions of duct flows of multiple visco-plastic fluids. *Journal of Non–Newtonian Fluid Mechanics*, 122:227–241, 2004.

[111] R R Huilgol and Z You. Application of the augmented Lagrangian method to steady pipe flows of Bingham, Casson and Herschel–Bulkley fluids. *J. Non-Newton. Fluid Mech.*, 128:126–143, 2005.

[112] M T Roberts, A Morhaz, K T Christensen, and J A Lewis. Direct flow visualization of colloidal gels in microfluidic channels. *Langmuir*, 23(17):8726–8731, 2007.

[113] X-L Wu, K J Måløy, A Hansen, M Ammi, and D Bideau. Why hour glasses tick. *Physical Review Letters*, 71(9):1363–1366, 1993.

[114] T Le Pennec, K J Måløy, A Hansen, M Ammi, D Bideau, and X L Wu. Ticking hour glasses: Experimental analysis of intermittent flow. *Physical Review E*, 53(3):2257–2264, 1996.

[115] T Raafat, J P Hulin, and H J Herrmann. Density waves in dry granular media falling through a vertical pipe. *Physical Review E*, 53(5):4345–4350, 1996.

[116] J-L Aider, N Sommier, T Raafat, and J-P Hulin. Experimental study of a granular flow in a vertical pipe: A spatiotemporal analysis. *Physical Review E*, 59(1):778–786, 1999.

[117] Y Bertho, F Giorgiutti-Dauphine, and JP Hulin. Intermittent dry granular flow in a vertical pipe. *Physics of Fluids*, 15(11):3358–3369, 2003.

[118] S Luding, J Duran, E Clement, and J Rajchenbach. Simulations of dense granular flow: Dynamic arches and spin organization. *Journal de Physique*, 6(6):823–836, 1996.

[119] S Horluck, M van Hecke, and P Dimon. Shock waves in two-dimensional granular flow: Effects of rough walls and polydispersity. *Physical Review E*, 67:021304, 2003.

[120] S Horluck and P Dimon. Statistics of shock waves in a two-dimensional granular flow. *Physical Review E*, 60(1):671–686, 1999.

[121] S Horluck and P Dimon. Grain dynamics in a two-dimensional granular flow. *Physical Review E*, 63(3):031301, 2001.

[122] P Yaras et al. Flow instabilities in capillary flow of concentrated suspensions. *Rheol. Acta*, 33:48–59, 1994.

[123] H Suwardie, R Yazici, D M Kalyon, and S Kovenklioglu. Capillary flow behaviour of microcrystalline wax and silicon carbide suspension. *Journal of Materials Science*, 33(20):5059–5067, 1998.

[124] R B Lukner and R T Bonnecaze. Piston-driven flow of highly concentrated suspensions. *Journal of Rheology*, 43(3):735–751, 1999.

[125] L Robert, B Vergnes, and Y Demay. Flow birefringence study of the stick–slip instability during extrusion of high–density polyethylenes. *Journal of Non–Newtonian Fluid Mechanics*, 112:27–42, 2003.

[126] L Isa, R Besseling, E R Weeks, and W C K Poon. Experimental studies of the flow of concentrated hard sphere suspensions into a constriction. *J. Phys.–Conference Series*, 40:124–132, 2006.

[127] J D Jackson. *Classical electrodynamics*. Wiley, New York, 3rd edition, 1999.

[128] B J Berne and R Pecora. *Dynamic Light Scattering*. Wiley, New York, 1976.

[129] P N Segré, V Prasad, A B Schofield, and D A Weitz. Glasslike kinetic arrest at the colloidal-gelation transition. *Physical Review Letters*, 86(26):6042–6045, 2001.

[130] P N Pusey and W van Megen. Observation of a glass transition in suspensions of spherical colloidal particles. *Physical Review Letters*, 59:2083–2086, 1987.

[131] K Schatzel, M Drewel, and J Ahrens. Suppression of multiple scattering in photon correlation spectroscopy. *Journal of Physics: Condensed Matter*, 2:SA393–SA398, 1990.

[132] P N Segré, W van Megen, P N Pusey, K Schatzel, and W Peters. Two-colour dynamic light scattering. *Journal of Modern Optics*, 42(9):1929–1952, 1995.

[133] A Moussaid and P N Pusey. Multiple scattering suppression in the static light scattering by cross-correlation spectroscopy. *Physical Review E*, 60(5):5670–5676, 1999.

[134] D J Pine, D A Weitz, P M Chaikin, and E Herbolzheimer. Diffusing-wave spectroscopy. *Physical Review Letters*, 60(12):1134–1137, 1988.

[135] K N Pham et al. Multiple glassy states in a simple model system. *Science*, 296:104–106, 2002.

[136] K N Pham, S U Egelhaaf, P N Pusey, and W C K Poon. Glasses in hard spheres with short-range attraction. *Physical Review E*, 69:011503, 2004.

[137] L Cipelletti, H Bissig, V Trappe, P Ballesta, and S Mazoyer. Time-resolved correlation: a new tool for studying temporally heterogeneous dynamics. *Journal of Physics: Condensed Matter*, 15:S257–S262, 2003.

[138] A Duri and L Cipelletti. Length scale dependence of dynamical heterogeneity in a colloidal fractal gel. *Europhysics Letters*, 76(5):972–978, 2006.

[139] E Hecht. *Optics*. Addison Wesley, San Francisco, 2002.

[140] M Pluta. *Advanced Light Microscopy*, volume 1. Elsevier, Amsterdam, 1988.

[141] W Abramovitz. *Microscope. Basics and beyond.* Olympus America Inc., Melville, NY, 2003.

[142] M S Elliot and W C K Poon. Conventional optical microscopy of colloidal suspensions. *Advances in Colloid and Interface Science*, 92:133–194, 2001.

[143] S Inoué. *Video Microsocpy*. Plenum Press, New York, 1986.

[144] M Gu. *Principles of Three-Dimensional Imaging in Confocal Microscopes*. World Scientific, Singapore, 1996.

[145] N S Claxton, T J Fellers, and M W Davidson. *Laser Scanning Confocal Microscopy*. http://www.olympusconfocal.com/theory/LSCMIntro.pdf.

[146] M Jenkins. *Quantitative Confocal Microscopy of Dense Colloidal Systems*. PhD thesis, School of Physics, The University of Edinburgh, 2005.

[147] Various Authors. *Optical Microscopy Primer*. http://micro.magnet.fsu.edu/primer/–index.html.

[148] P J Lu, P A Sims, H Oki, J B Macarthur, and D A Weitz. Target-locking acquisition with real-time confocal (tarc) microscopy. *Optics Express*, 15(14):8703, 2007.

[149] T Wilson. *Confocal Microscopy*. Academic Press, San Diego, 1990.

[150] V Prasad, D Semwogerere, and E R Weeks. Confocal microscopy of colloids. *Journal of Physics: Condensed Matter*, 19:113102, 2007.

[151] D Semwogerere and E R Weeks. *Encyclopedia of Biomaterials and Biomedical Engineering*. Taylor and Francis, 2005.

[152] M Minsky. Memoir on inventing the confocal scanning microscope. *Scanning*, 10:128–138, 1988.

[153] W Denk, J H Strickler, and W W Webb. Two-photon laser scanning fluorescence microscopy. *Science*, 248(4951):73–76, 1990.

[154] K Konig. Multiphoton microscopy in life science. *Journal of Microscopy*, 200:83–104, 2000.

[155] J C Crocker and D G Grier. Methods of digital video microscopy for colloidal studies. *J. Colloid Interface Sci.*, 179:298, 1996.

[156] D Derks, H Wisman, A van Blaaderen, and A Imhof. Confocal microscopy of colloidal dispersions in shear flow using a counter-rotating cone-plate shear cell. *Journal of Physics: Condensed Matter*, 16:S3917–S3927, 2004.

[157] L Isa, R Besseling, and W C K Poon. Shear zones and wall slip in the capillary flow of concentrated colloidal suspensions. *Physical Review Letters*, 98(18):198305, 2007.

[158] H Xu, A P Reeves, and M Y Louge. Measurement error in the mean and fluctuation velocities of spherical grains form a computer analysis of digital images. *Review of Scientific Instruments*, 75(4):811–819, 2004.

[159] L Antl, J W Goodwin, R D Hill, R H Ottewill, S M Owens, S Papworth, and J A Waters. The preparation of poly(methyl methacrylate) lattices in non-aqueous media. *Colloids and Surfaces*, 17(1):67–78, 1986.

[160] R S Jardine and P Bartlett. Synthesis of non-aqueous fluorescent hard-sphere polymer colloids. *Colloids and Surfaces A–Physicochemical and Engineering Aspects*, 211(2–3):127–132, 2002.

[161] A I Campbell and P Bartlett. Fluorescent hard-sphere polymer colloids for confocal microscopy. *Journal of Colloid and Interface Science*, 256:325–330, 2002.

[162] A D Dinsmore, E R Weeks, V Prasad, A C Levitt, and D A Weitz. Three–dimensional confocal microscopy of colloids. *App. Optics*, 40:4152–4159, 2001.

[163] B A de L Costello, P F Luckham, and Th F Tadros. Investigation of the interaction forces of polymer-coated surfaces using force balance, rheology, and osmotic pressure results. *Langmuir*, 8:464–468, 1992.

[164] G Bryant, S R Williams, L Qian, I K Snook, E Perez, and F Pincet. How hard is a colloidal hard-sphere interaction? *Physical Review E*, 66:060502, 2002.

[165] K N Pham, G Petekidis, D Vlassopoulos, S U Egelhaaf, P N Pusey, and W C K Poon. Yielding of colloidal glasses. *Europhysics Letters*, 75:624–630, 2006.

[166] B J Ackerson and P N Pusey. Shear–induced order in suspensions of hard–spheres. *Physical Review Letters*, 61(8):1033–1036, 1988.

[167] A Yethiraj and van Blaaderen A. A colloidal model system with an interaction tunable from hard sphere to soft and dipolar. *Nature*, 421(6922):513–517, 2003.

[168] E R Weeks and D A Weitz. Subdiffusion and the cage effect studied near the colloidal glass transition. *Chemical Physics*, 284:361–367, 2002.

[169] P J Lu, J C Conrad, H M Wyss, A B Schofield, and D A Weitz. Fluids of clusters in attractive colloids. *Physical Review Letters*, 96:028306, 2006.

[170] P Bartlett and A I Campbell. Three-dimensional binary superlattices of oppositely charged colloids. *Physical Review Letters*, 95:128302, 2005.

[171] C P Royall, M E Leunissen, and A van Blaaderen. A new colloidal model system to study long-range interactions quantitatively in real space. *Journal of Physics–Condensed Matter*, 15(48):S3581–S3596, 2003.

[172] M E Leunissen, C G Christova, A P Hynninen, C P Royall, A I Campbell, A Imhof M Dijkstra, R van Roij, and A van Blaaderen. Ionic colloidal crystals of oppositely charged particles. *Nature*, 437(7056):235–240, 2005.

[173] A B Schofield. private communication.

[174] A van Blaaderen and P Wiltzius. Real-space structure of colloidal hard-sphere glasses. *Science*, 270(5239):1177–1179, 1995.

[175] J Groenewold and W K Kegel. Anomalously large equilibrium clusters of colloids. *Journal of Physical Chemistry B*, 105(47):11702–11709, 2001.

[176] F P Preparata and M I Shamos. *Computational Geometry: An Introduction*. Springer–Verlag, New York, 1993.

[177] R D Deegan, O Bakajin, T F Dupont, G Huber, S R Nagel, and T A Witten. Capillary flow as the cause of ring stains from dried liquid drops. *Nature*, 389(6653):827–829, 1997.

[178] A Poitou and G Racineux. A squeezing experiment showing binder migration in concentrated pastes. *Journal of Rheology*, 45(3):609–625, 2001.

[179] O Reynolds. On the dilatancy of media composed of rigid particles in contact. with experimental illustrations. *Philosophical magazine*, 20:479, 1885.

[180] M. D. Haw, W. C. K. Poon, and P. N. Pusey. Direct observation of oscillatory-shear-induced order in colloidal suspensions. *Phys. Rev. E*, 57(6):6859–6864, Jun 1998.

[181] M. D. Haw, W. C. K. Poon, and P. N. Pusey. Colloidal glasses under shear strain. *Phys. Rev. E*, 58(4):4673–4682, Oct 1998.

[182] G Y Onoda and E G Liniger. Random loose packing of uniform spheres and the dilatancy onset. *Physical Review Letters*, 64(22):2727–2730, 1990.

[183] R C Ball and J R Melrose. Lubrication breakdown in hydrodynamic simulations of concentrated colloids. *Adv. Colloid Interfac.*, 59:19–30, 1995.

[184] C Goldenberg and I Goldhirsch. Small and large scale granular statics. *Granular Matter*, 6(2-3):87–96, 2004.

[185] C H Liu, S R Nagel, D A Schecter, S N Coppersmith, S Majumdar, O Narayan, and T A Witten. Fluctuations in bead packs. *Science*, 269(5223):513–515, 1995.

[186] D L Blair, N W Mueggenburg, A H Marshall, H M Jaeger, and S R Nagel. Force distributions in three-dimensional granular assemblies: Effects of packing order and interparticle friction. *Physical Review E*, 63(4):041304, 2001.

[187] T S Majmudar and R P Behringer. Contact force measurements and stress-induced anisotropy in granular materials. *Nature*, 435(7045):1079–1082, 2005.

[188] D M Mueth, G F Debregeas, G S Karczmar, P J Eng, S R Nagel, and J P Gollub. Signatures of granular microstructure in dense shear flows. *Nature*, 406:385–388, 2000.

[189] W Losert, L Bocquet, T C Lubensky, and J P Gollub. Particle dynamics in sheared granular matter. *Phys. Rev. Lett.*, 85:1428, 2000.

[190] A V Tkachenko and T A Witten. Stress in frictional granular material: Adaptive network simulations. *Physical Review E*, 62(2):2510–2516, 2000.

[191] H Herrmann. private communication.

[192] M Lee, M Alcoutlabi, J J Magda, C Dbble, M J Solomon, X Shi, and G B McKenna. The effect of the shear-thickening transition of model colloidal spheres on the sign of N_1 an thee radial pressure profile in torsional shear flows. *Journal of Rheology*, 50(3):293–311, 2006.

[193] W van Megen, T C Mortensen, S R Williams, and J Müller. Measurements of the self–intermediate scattering function of suspensions of hard spherical particles near the glass transition. *Physical Review E*, 58(5):6073–6085, 1998.

[194] N Scales and R N Tait. Modelling electroosmotic and pressure-driven flows in porous microfluidic devices: Zeta potentials and porosity changes near the channel walls. *Journal of Chemical Physics*, 125:094714, 2006.

[195] A B Yu, J Bridgewater, A S Burbridge, and Z Saracevic. Liquid maldistribution in particulate flow extrusion. *Powder Technology*, 103:103–109, 1999.

[196] R Artoni, A Santomaso, and P Canu. Shear bands in granular flow through a mixing–length model. *European Physics Letters*, 80:3004, 2007.

[197] W C K Poon. The physics of a model colloid–polymer mixture. *Journal of Physics: Condensed Matter*, 14:R859–R880, 2002.

[198] Y N Xia and G M Whitesides. Soft lithography. *Angewandte Chemie-International Edition*, 37(5):551–575, 1998.

[199] K V Sharp and R J Adrian. On flow-blocking particle structures in microtubes. *Microfluid Nanofluid*, 1:376–380, 2005.

[200] D Helbing, I Farkas, and T Vicsek. Simulating dynamical features of escape panic. *Nature*, 407:487–490, 2000.

[201] K To, P-Y Lai, and H K Pak. Jamming of granular flow in a two-dimensional hopper. *Physical Review Letters*, 86(1):71–74, 2001.

[202] A T Jessup and K R Phadnis. Measurement of the geometric and kinematic properties of microscale breaking waves from infrared imagery using a piv algorithm. *Measurement Science and Technology*, 16:1961–1969, 2005.

[203] P Tho, R Manasseh, and A Ooi. Cavitation microstreaming patterns in single and multiple bubble systems. *Journal of Fluid Mechanics*, 576:191–233, 2007.

[204] K Suhling, R W Airey, and B L Morgan. Optimization of centroiding algorithms for photon event counting imaging. *Nuclear Instruments and Methods in Physics Research A*, 437:393–418, 1999.

Publications

L Isa, R Besseling, E R Weeks, and W C K Poon. "Experimental studies of the flow of concentrated hard sphere suspensions into a constriction". *J. Phys.–Conference Series*, 40:124–132, 2006.

L Isa, R Besseling, and W C K Poon. "Shear zones and wall slip in the capillary flow of concentrated colloidal suspensions". *Physical Review Letters*, 98(18) 198305, 2007.

L Isa, R Besseling and W C K Poon. "Velocity oscillations in the confined flows of dense colloidal suspensions". *In preparation.*

L Isa, R Besseling and W C K Poon. "Capillary flows of dense colloidal suspensions". *In preparation.*

L Isa, R Besseling and W C K Poon. "Imaging and particle tracking of dense colloidal flows". *In preparation.*

R Besseling, P Ballesta, **L Isa**, G Petekidis and W C K Poon. "Slip and flow of glassy hard-sphere colloidal suspensions". *In preparation.*

R Besseling, P Ballesta, **L Isa**, G Petekidis and W C K Poon.. "Shear localization in Hard-Sphere colloidal glasses". *In preparation*